

University of Southampton Research Repository ePrints Soton

Copyright © and Moral Rights for this thesis are retained by the author and/or other copyright owners. A copy can be downloaded for personal non-commercial research or study, without prior permission or charge. This thesis cannot be reproduced or quoted extensively from without first obtaining permission in writing from the copyright holder/s. The content must not be changed in any way or sold commercially in any format or medium without the formal permission of the copyright holders.

When referring to this work, full bibliographic details including the author, title, awarding institution and date of the thesis must be given e.g.

AUTHOR (year of submission) "Full thesis title", University of Southampton, name of the University School or Department, PhD Thesis, pagination

UNIVERSITY OF SOUTHAMPTON
FACULTY OF ENGINEERING, SCIENCE AND
MATHEMATICS

School of Engineering Sciences

Processing of Aluminium and Titanium Alloys by
Severe Plastic Deformation

by

Saleh Naser Alhajeri

Thesis for the degree of Doctor of Philosophy

February 2010

UNIVERSITY OF SOUTHAMPTON

ABSTRACT

FACULTY OF ENGINEERING, SCIENCE & MATHEMATICS

SCHOOL OF ENGINEERING SCIENCE

Doctor of Philosophy

PROCESSING OF ALUMINIUM AND TITANIUM ALLOYS BY
SEVERE PLASTIC DEFORMATION

by Saleh Naser Alhajeri

Severe plastic deformation (SPD) techniques are applied to polycrystalline materials to significantly refine their grain sizes which lead normally to an enhancement of the material properties. Equal-channel angular pressing (ECAP) and high pressure torsion (HPT) were considered as very important SPD techniques. Very high deformation is applied to the samples in ECAP and HPT which refines the grain size and enhances the properties of materials.

In the present research, the evolution of homogeneity in microhardness measurements in the aluminium alloys was investigated after processing by ECAP and HPT. In the ECAP experiments, billets of Al-1050 alloy were processed by ECAP at room temperature using route B_C for up to six passes. The results of the microhardness measurements show that the hardness increases significantly after the first pass and continues to increase by smaller amounts in the subsequent passes. There are regions of lower hardness near the top and bottom surfaces of the billet after one pass. The hardness of the alloy becomes homogeneous along the longitudinal and cross-sectional planes after six passes of ECAP except in a very small region with lower hardness near the lower surface. Better results were achieved when processing the same material by HPT. The HPT experiments were conducted at room temperature at a pressure of 6 GPa and for up to five turns. The hardness was completely homogeneous across the entire surface after five turns of HPT. A comparison between the results performed by processing Al-1050 alloy by ECAP

and by HPT shows clearly that better homogeneity and higher hardness was achieved by using the HPT process. Another aluminium alloy (Al-1%Mg) was processed by HPT under similar conditions of processing as for Al-1050. The results illustrate that there is still a small region of lower hardness at the centre of Al-1%Mg disk after five turns. It was clear that the Al-1%Mg alloy needs more than five turns under the pressure of 6.0 GPa to become totally homogeneous.

A series of [114] convergent beam electron diffraction (CBED) zone axis patterns were obtained at 148.7 kV with a 20 nm diameter electron probe from dislocation-free regions close to and away from the grain boundaries in the billets processed by ECAP through two and four passes after cooling to 80 K. The results show that there were no detectable strains in the centre of the grains of both billets. Near the grain boundaries, compressive and shear strains were detected. The compressive strain was constant in both billets with a value of $\sim 0.1\%$ and the shear strain at the two passes sample was $\sim 0.044\%$ and increased at the four passes sample to reach a value of $\sim 0.177\%$. Similar patterns from the billet processed through eight passes were difficult to be analyzed due to the higher dislocation density which led to a blurring of the HOLZ lines.

Processing of commercial purity titanium alloy by ECAP at room temperature proved the feasibility to perform this when the die channel angle increased and the pressing speed decreased. The experiments were performed at an angle of 135 deg and pressing speeds of 0.5 and 0.05 mm/s. A maximum of one pass were reached by processing under the speed of 0.5 mm/s whereas two passes were successfully performed under the speed of 0.05 mm/s without experiencing any visible cracks in the billet.

Finally, HPT experiments were performed monotonically (m-HPT) and cyclically (c-HPT) on two aluminium alloys (Al-1050 and Al-1%Mg) and two titanium alloys (CP Ti and Ti-6Al-4V). The results show that the rate of the evolution towards the homogeneity of microhardness along the diameter of the disks in the aluminium alloys is higher when the disks are processed by m-HPT rather than processing by c-HPT. Opposing results were found at the titanium alloys where the rate was higher when the disks are processed by c-HPT rather than processing by m-HPT.

DECLARATION OF AUTHORSHIP

I, Saleh Naser Alhajeri, declare that the thesis entitled:

Processing of Aluminium and Titanium Alloys by Severe Plastic Deformation

and the work presented in the thesis are both my own, and have been generated by me as the result of my own original research. I confirm that:

- this work was done wholly or mainly while in candidature for a research degree at this University;
- where any part of this thesis has previously been submitted for a degree or any other qualification at this University or any other institution, this has been clearly stated;
- where I have consulted the published work of others, this is always clearly attributed;
- where I have quoted from the work of others, the source is always given. With the exception of such quotations, this thesis is entirely my own work;
- I have acknowledged all main sources of help;
- where the thesis is based on work done by myself jointly with others, I have made clear exactly what was done by others and what I have contributed myself;
- parts of this work have been published as:
 1. Alhajeri SN, Gao N, Langdon TG. The Evolution of Homogeneity during Processing of Commercial Purity Aluminium by ECAP; (2008) Mater Sci Forum, 584-586: 446.
 2. Alhajeri SN, Fox AG, Vincent R, Langdon TG. A convergent beam electron diffraction HOLZ line symmetry-breaking study of the homogenous strain in aluminium processed by equal-channel angular pressing; (2010) To be submitted to Acta Mater.

3. Cao Y, Wang YB, Alhajeri SN, Liao XZ, Zheng WL, Ringer SP, Langdon TG, Zhu YT. A visualization of shear strain in processing by high-pressure torsion; (2010) J Mater Sci, 45:765.
4. Ni S, Wang YB, Liao XZ, Alhajeri SN, Li HQ, Zhao YH, Lavernia EJ, Ringer SP, Langdon TG, Zhu YT. Strain hardening and softening in a nanocrystalline Ni–Fe alloy induced by severe plastic deformation; (2010) Submitted to Acta Mater.

Signed:

Date:.....

ACKNOWLEDGEMENT

I would like to express my sincere appreciation to the following people whom without their support this thesis would not have been possible. It is a pleasure to recognize and thank those who supported me.

Firstly, a huge thanks to my supervisors Professor Terence G. Langdon and Dr. Nong Gao for their invaluable guidance, support and advise through the course of my research. Their leadership and supervision became the building blocks which helped me to gain a great learning experience during my scientific research.

My sincere acknowledgment is due to Professor Michael E. Kassner, University of Southern California, USA, for his supervision during part of my scholarship. He has added a huge amount to my development for which I will always be grateful.

I would like to thank the Public Authority for Applied Education and Training (PAAET) - Kuwait for their financial support throughout the duration of my study.

I sincerely thank Prof. Alan Fox, Asian University, Thailand, and Dr. Roger Vincent, University of Bristol, for their invaluable help in the TEM and CBED. I sincerely thank Yue Zhang, Nanjing University of Science & Technology, China, for her contribution in chapter 5.

I sincerely acknowledge all the staff and students in the Engineering Materials Research Group at the University of Southampton for their support during my study.

Finally, I would like to thank my mother for always believing in me. Without her support and love I would never achieved this. I would also like to thank my dear wife for her unconditional love and patience. Her sacrifices have been greatly appreciated.

LIST OF CONTENTS

	Abstract	ii
	Declaration of authorship	iv
	Acknowledgment	vi
	List of contents	vii
	List of Figures	x
	List of Tables	xvi
1	INTRODUCTION	1
1.1	Introduction	1
1.2	1.2 Aims and Objectives	3
1.3	1.3 Thesis Structure	4
2	FUNDAMENTALS OF THE ECAP AND HPT PROCESSES	5
2.1	Introduction	5
2.2	Equal-Channel Angular Pressing (ECAP)	5
2.2.1	The strain imposed in ECAP	8
2.2.2	The processing routes in ECAP	10
2.2.3	Slip planes for the different processing routes	12
2.2.4	Influence of the processing route on the microstructure	14
2.2.5	Significance of the channel angle (Φ)	15
2.2.6	Influence of the pressing speed	16
2.2.7	Influence of the pressing temperature	17
2.2.8	Incorporation of ECAP in continuous production	18
2.2.9	Evolution of the microhardness homogeneity during processing by ECAP	20
2.2.10	Processing of titanium alloys by ECAP	24
2.2.11	Twinning in titanium alloys after processing by ECAP	27
2.3	High Pressure Torsion (HPT)	29
2.3.1	Calculation of the strain imposed in HPT	30
2.3.2	Constrained and unconstrained HPT	32
2.3.3	Variation in homogeneity across the HPT disk	33
2.3.4	Influence of the applied pressure on microstructural evolution	35
2.3.5	Influence of the number of revolutions	36
2.3.6	New technique in evaluating the microhardness evolution	37
2.3.7	Strain reversal in HPT	40
2.4	Microstructure - Microhardness Relation	42

3	THE EVOLUTION OF HOMOGENEITY DURING PROCESSING OF COMMERCIAL PURITY ALUMINIUM BY ECAP	44
3.1	Introduction	44
3.2	Experimental Material and Procedures	45
3.3	Experimental Results	51
3.4	Discussion	67
3.5	Summary and Conclusions	69
4	STRAIN MEASUREMENTS BY CONVERGENT BEAM ELECTRON DIFFRACTION IN ALUMINIUM PROCESSED BY ECAP	70
4.1	Introduction	70
4.2	Experimental Material and Procedures	71
4.3	Experimental Results	73
4.3.1	Al-1050 in the as-received condition	73
4.3.2	Al-1050 after ECAP through two passes	74
4.3.3	Al-1050 after ECAP through four passes	76
4.3.4	Al-1050 after ECAP through eight passes	77
4.4	Discussion	80
4.5	Summary and Conclusions	82
5	PROCESSING OF COMMERCIAL PURITY TITANIUM BY ECAP AT ROOM TEMPERATURE	83
5.1	Introduction	83
5.2	Experimental Material and Procedures	83
5.3	Experimental Results	88
5.4	Discussion	104
5.5	Summary and Conclusions	107
6	THE EVOLUTION OF HOMOGENEITY IN ALUMINIUM DURING PROCESSING BY HPT	108
6.1	Introduction	108
6.2	Experimental Materials and Procedures	109
6.3	Experimental Results	116
6.3.1	Al-1% Mg alloy	116
6.3.2	Al-1050 alloy	124
6.4	Discussion	131
6.5	Summary and Conclusions	133
7	THE EFFECT OF STRAIN REVERSAL ON ALUMINIUM AND TITANIUM ALLOYS DURING PROCESSING BY HPT	135
7.1	Introduction	135
7.2	Experimental Materials and Procedures	136

7.3	Experimental Results	139
7.3.1	The existence of slippage	139
7.3.2	The microhardness measurements	139
7.3.2.1	Al-1050 alloy	140
7.3.2.2	Al-1%Mg alloy	150
7.3.2.3	CP Ti alloy	160
7.3.2.4	Ti - 6Al - 4V alloy	170
7.4	Discussion	181
7.5	Summary and Conclusions	184
<hr/>		
8	SUMMARY AND FUTURE WORK	185
8.1	Summary and Conclusions	185
8.1.1	The evolution of homogeneity after processing by ECAP and HPT	185
8.1.2	Strain measurements by CBED in Al-1050 processed by ECAP	186
8.1.3	Processing of CP Ti by ECAP at room temperature:	188
8.1.4	The effect of strain reversal in Al and Ti alloys during processing by HPT	189
8.2	Future work	189
<hr/>		
	REFERENCES	191
<hr/>		

LIST OF FIGURES

Fig. 2.1	Schematic illustration of a typical ECAP facility showing the three orthogonal planes X, Y and Z	7
Fig. 2.2	Schematic illustration of a typical ECAP facility showing the channel angle (Φ) and the angle at the outer arc of curvature (Ψ)	7
Fig. 2.3	The principle of ECAP process showing the shearing plane between the two adjacent elements labelled 1 and 2	8
Fig. 2.4	Principle of ECAP where Φ is the channel angle and Ψ is the angle the outer arc of curvature: (a) $\Psi = 0^\circ$, (b) $\Psi = (\pi - \Phi)^\circ$ and (c) $0^\circ < \Psi < (\pi - \Phi)^\circ$	9
Fig. 2.5	Variation of strain with the angles Φ and Ψ after ECAP for a single pass	11
Fig. 2.6	The four basic processing routes used in ECAP	11
Fig. 2.7	The slip planes associated with the four processing routes	12
Fig. 2.8	The distortions of cubic elements on the X, Y and Z planes when pressed for up to 8 passes for different processing routes	13
Fig. 2.9	The microstructures on the X plane for polycrystalline aluminium after ECAP through 4 passes using routes A, B _A , B _C and C together with the associated SAED patterns	14
Fig. 2.10	Microstructures and SAED patterns after ECAP for an imposed strain of ~4 using dies having channel angles (Φ) of 90° , 112.5° , 135° and 157.5°	16
Fig. 2.11	Variation of the yield stress with the pressing speed of Al-1%Mg alloy after ECAP through 1, 2, 3 and 4 passes	17
Fig. 2.12	Variation of the grain size with the pressing temperature after ECAP of different aluminium alloys	18
Fig. 2.13	Schematic illustration of the DCAP process which was used in continuous production operations	19
Fig. 2.14	Schematic illustration of the process of ECAP-Conform	19
Fig. 2.15	Colour-coded contour maps of the microhardness through the cross-sectional planes of pure aluminium billets in the unpressed condition and after ECAP through 1, 2, 3, 4 and 8 passes	22
Fig. 2.16	Colour-coded contour maps of the microhardness through the cross-sectional planes of an Al-6061 alloy in the unpressed condition and after ECAP through 1, 2, 3, 4 and 6 passes	23
Fig. 2.17	Colour-coded contour maps of the microhardness through the longitudinal planes of Al-6061 alloy after ECAP through 1, 2, 4, and 6 passes	24
Fig. 2.18	Samples of CP Ti billets after pressing at room temperature using pressing speeds of 0.025, 0.25 and 25.0 mm/s	26
Fig. 2.19	CP Ti billets after pressing at room temperature with dies having channel angles (Φ) of (a) 90° and (b) 120°	27
Fig. 2.20	Illustration of the HPT facility showing the sample under pressure and rotation	30
Fig. 2.21	Parameters used in estimating the total strain in HPT	31

Fig. 2.22	Schematic illustration of HPT process for (a) unconstrained, (b) constrained and (c) quasi-constrained conditions	33
Fig. 2.23	The average Hv microhardness versus distance from the centre of the disk after processing by HPT: (a) under a pressure of 1.25 GPa, (b) under a pressure of 6.0 GPa and (c) after five turns using different pressures	34
Fig. 2.24	Three-dimensional meshes of microhardness of Ni processed by HPT under applied pressures of (a) 1 GPa, (b) 3 GPa, (c) 6 GPa and (d) 9 GPa	35
Fig. 2.25	Three-dimensional meshes of microhardness in Ni processed by HPT under a pressure of 6.0 GPa for (a) 1/2 turn, (b) 1 turn, (c) 3 turns and (d) 7 turns	36
Fig. 2.26	Colour-coded contour maps showing Hv microhardness across the surface of high purity Al processed by HPT at a pressure of 1.25 GPa for (a) 1, (b) 3 and (c) 5 turns	38
Fig. 2.27	Colour-coded contour maps showing Hv microhardness across the surface of high purity Al processed by HPT at a pressure of 6.0 GPa for (a) 1, (b) 3 and (c) 5 turns	39
Fig. 2.28	Schematic illustration of HPT facility showing the two directions of rotation; A and B	41
Fig. 2.29	(a) Change in microhardness, (b) change in internal microstructure for armco-iron and the pearlitic rail steel S900A	42
Fig. 3.1	Photographs of the experimental facility used in the ECAP experiments showing the die and the plunger	47
Fig. 3.2	Drawing for the die used in the experiments showing the dimensions in mm and angles of the channel	48
Fig. 3.3	As-Received and as-pressed billets after 1, 2, 4 and 6 passes	49
Fig. 3.4	Billets after sectioning, mounting and polishing	50
Fig. 3.5	The linear traverses used for taking microhardness measurements	50
Fig. 3.6	Individual measurements of the microhardness, Hv, recorded along the vertical longitudinal plane after 1, 2, 4 and 6 passes along (a) the traverse located at 1.0 mm from the top surface, (b) the central traverse and (c) the traverse located at 1.0 mm from the bottom surface	55
Fig. 3.7	Individual measurements of the microhardness, Hv, recorded along the vertical longitudinal plane at the central traverse and the traverses at 1.0 mm from the top and bottom surfaces after (a) one pass, (b) two passes, (c) four passes and (d) six passes	57
Fig. 3.8	Colour-coded contour maps of the microhardness, Hv, recorded along the vertical longitudinal plane after ECAP for (a) one pass, (b) two passes, (c) four passes and (d) six passes	59
Fig. 3.9	Three-dimensional representations of the microhardness measurements, Hv, along the vertical longitudinal plane after ECAP for (a) one pass, (b) two passes, (c) four passes and (d) six passes	61
Fig. 3.10	Individual measurements of the microhardness, Hv, recorded on the cross-sectional plane along the central traverse and the traverses at 1.0 mm from the top and bottom surfaces after (a) one pass, (b) two passes, (c) four passes and (d) six passes	63

Fig. 3.11	Colour-coded contour maps of the microhardness, Hv, along the cross-sectional plane after (a) one pass, (b) two passes, (c) four passes and (d) six passes	65
Fig. 4.1	Photographs of the TEM facility located at the University of Bristol	72
Fig. 4.2	The observed and the simulated HOLZ patterns taken from the material in the as-received condition	73
Fig. 4.3	TEM image of the grain used for acquiring the HOLZ patterns from the billet processed by ECAP through 2 passes	75
Fig. 4.4	The observed and the simulated HOLZ patterns taken from the centre of the grain after ECAP through two passes	75
Fig. 4.5	The observed and the simulated HOLZ patterns taken near the grain boundary after ECAP through two passes. The arrows show the break in the symmetry after increasing the magnification of the patterns	76
Fig. 4.6	TEM image of the grain used for taking the HOLZ pattern at the billet pressed through 4 passes	78
Fig. 4.7	The observed and the simulated HOLZ patterns taken from the centre of the grain after ECAP through four passes	78
Fig. 4.8	The observed and the simulated HOLZ patterns taken near the grain boundary after ECAP through four passes. The arrows show the break in the symmetry	79
Fig. 4.9	TEM image of a single grain in the billet processed through 8 passes showing a dislocation network inside a typical grain	79
Fig. 5.1	Schematic illustration of a CP Ti billet after ECAP showing the cutting method and dimensions	85
Fig. 5.2	Schematic illustrations of the cross-sectional plane showing the two lines defined for the microhardness measurements and the positions of the data points	87
Fig. 5.3	Schematic illustrations of the vertical longitudinal plane showing the three lines defined for the microhardness measurements and the positions of the data points	87
Fig. 5.4	Appearance of CP Ti billets after ECAP through one and two passes at room temperature using pressing speeds of 0.5 and 0.05 mm/s	88
Fig. 5.5	Individual measurements of the microhardness, Hv, recorded on the cross-sectional plane after 1 and 2 passes at a pressing speed of 0.5 mm/s along (a) the vertical line which is laying from the top to bottom surfaces and (b) the horizontal line which is laying from the right to left sides	90
Fig. 5.6	Individual measurements of the microhardness, Hv, recorded along the vertical longitudinal plane at the central traverse and the traverses at 1.0 mm from the top and bottom surfaces after ECAP through (a) one pass at a speed of 0.5 mm/s, (b) two passes at a speed of 0.5 mm/s, (c) one pass at a speed of 0.05 mm/s and (d) two passes at a speed of 0.05 mm/s	92
Fig. 5.7	Optical micrograph of the microstructure of CP Ti in as annealed unpressed condition	94

Fig. 5.8	Optical micrographs of the microstructure on the cross-sectional plane after ECAP at room temperature through (a) one pass at a pressing speed of 0.5 mm/s, (b) two passes at a pressing speed of 0.5 mm/s, (c) one pass at a pressing speed of 0.05 mm/s and (d) two passes at a pressing speed of 0.05 mm/s	95
Fig. 5.9	Optical micrographs of the microstructure on the vertical longitudinal plane after ECAP at room temperature through (a) one pass at a pressing speed of 0.5 mm/s, (b) two passes at a pressing speed of 0.5 mm/s, (c) one pass at a pressing speed of 0.05 mm/s and (d) two passes at a pressing speed of 0.05 mm/s	98
Fig. 5.10	Statistical distributions of twinning growth direction determined from the cross-sectional OM observations after pressing for (a) one pass at a pressing speed of 0.5 mm/s, (b) two passes at a pressing speed of 0.5 mm/s, (c) one pass at a pressing speed of 0.05 mm/s and (d) two passes at a pressing speed of 0.05 mm/s	100
Fig. 5.11	Statistical distributions of twinning growth direction determined from the vertical longitudinal OM observations after pressing for (a) one pass at a pressing speed of 0.5 mm/s, (b) two passes at a pressing speed of 0.5 mm/s, (c) one pass at a pressing speed of 0.05 mm/s and (d) two passes at a pressing speed of 0.05 mm/s	102
Fig. 6.1	HPT facility showing the two sets: the control panel and the high pressure press	110
Fig. 6.2	The control panel and the pressure gauges for the HPT facility.	110
Fig. 6.3	The high pressure torsion facility showing the upper and lower anvil	111
Fig. 6.4	Illustration of the HPT facility showing the sample under pressure and rotation	111
Fig. 6.5	Illustration of the process used for taking the data points along the diameter of the disks after HPT	113
Fig. 6.6	Individual measurements of the microhardness, Hv, recorded along the diameter of Al-1%Mg disk after HPT under a pressure of 6.0 GPa for (a) 1/4, (b) one and (c) five turns	119
Fig. 6.7	Individual microhardness measurements recorded along the diameter of Al-1%Mg disks after HPT under a pressure of 6.0 GPa for 1/4, 1 and 5 turns	120
Fig. 6.8	Colour-coded contour maps of the microhardness measurements along the surface of Al-1% Mg disk after HPT under a pressure of 6.0 GPa for (a) 1/4, (b) one and (c) five turns	121
Fig. 6.9	Three-dimensional representations of the hardness measurements on the surface of Al-1%Mg disk after HPT under a pressure of 6.0 GPa for (a) 1/4, (b) one and (c) five turns	122
Fig. 6.10	Individual measurements of the microhardness, Hv, recorded along the diameter of Al-1050 disk after HPT under a pressure of 6.0 GPa for (a) 1/4, (b) one and (c) five turns	126
Fig. 6.11	Individual microhardness measurements recorded along the diameter of Al-1050 disks after HPT under a pressure of 6.0 GPa for 1/4, 1 and 5 turns	127
Fig. 6.12	Colour-coded contour maps of the microhardness measurements along the surface of Al-1050 disk after HPT under a pressure of 6.0 GPa for (a) 1/4, (b) one and (c) five turns	128

Fig. 6.13	Three-dimensional representations of the hardness measurements on the surface of Al-1050 disk after HPT under a pressure of 6.0 GPa for (a) 1/4, (b) one and (c) five turns	129
Fig. 7.1	Illustration of the HPT facility showing the sample under pressure and cyclic rotation	137
Fig. 7.2	The average of the microhardness measurements, Hv, recorded along the diameter of Al-1050 disks after m-HPT under a pressure of 6.0 GPa for (a) 1/2, (b) 3/4, (c) one and (d) two turns	143
Fig. 7.3	The average of the microhardness measurements, Hv, recorded along the diameter of Al-1050 disks after c-HPT under a pressure of 6.0 GPa for (a) +1/4-1/4, (b) +1/4-1/4+1/4, (c) +1/4-1/4+1/4-1/4 and (d) +1-1 turns	145
Fig. 7.4	The average of the microhardness measurements, Hv, recorded along the diameter of Al-1050 disks after m-HPT and c-HPT under a pressure of 6.0 GPa for (a) 1/2, (b) 3/4, (c) one and (d) two turns	147
Fig. 7.5	The average microhardness measurements, Hv, recorded along the diameter of Al-1050 disks after (a) m-HPT and (b) c-HPT under a pressure of 6.0 GPa for totals of 1/2, 3/4, 1 and 2 turns	149
Fig. 7.6	The average of the microhardness measurements, Hv, recorded along the diameter of Al-1%Mg disks after m-HPT under a pressure of 6.0 GPa for (a) 1/2, (b) 3/4, (c) one and (d) two turns	153
Fig. 7.7	The average of the microhardness measurements, Hv, recorded along the diameter of Al-1%Mg disks after c-HPT under a pressure of 6.0 GPa for (a) +1/4-1/4, (b) +1/4-1/4+1/4, (c) +1/4-1/4+1/4-1/4 and (d) +1-1 turns	155
Fig. 7.8	The average of the microhardness measurements, Hv, recorded along the diameter of Al-1%Mg disks after m-HPT and c-HPT under a pressure of 6.0 GPa for (a) 1/2, (b) 3/4, (c) one and (d) two turns	157
Fig. 7.9	The average microhardness measurements, Hv, recorded along the diameter of Al-1%Mg disks after (a) m-HPT and (b) c-HPT under a pressure of 6.0 GPa for totals of 1/2, 3/4, 1 and 2 turns	159
Fig. 7.10	The average of the microhardness measurements, Hv, recorded along the diameter of CP Ti disks after m-HPT under a pressure of 6.0 GPa for (a) 1/2, (b) 3/4, (c) one and (d) two turns	163
Fig. 7.11	The average of the microhardness measurements, Hv, recorded along the diameter of CP Ti disks after c-HPT under a pressure of 6.0 GPa for (a) +1/4-1/4, (b) +1/4-1/4+1/4, (c) +1/4-1/4+1/4-1/4 and (d) +1-1 turns	165
Fig. 7.12	The average of the microhardness measurements, Hv, recorded along the diameter of CP Ti disks after m-HPT and c-HPT under a pressure of 6.0 GPa for (a) 1/2, (b) 3/4, (c) one and (d) two turns	167
Fig. 7.13	The average microhardness measurements, Hv, recorded along the diameter of CP Ti disks after (a) m-HPT and (b) c-HPT under a pressure of 6.0 GPa for totals of 1/2, 3/4, 1 and 2 turns	169
Fig. 7.14	The average of the microhardness measurements, Hv, recorded along the diameter of Ti-6Al-4V disks after m-HPT under a pressure of 6.0 GPa for (a) 1/2, (b) 3/4, (c) one and (d) two turns	174

- Fig. 7.15 The average of the microhardness measurements, H_v , recorded 176
along the diameter of Ti-6Al-4V disks after c-HPT under a
pressure of 6.0 GPa for (a) $+1/4-1/4$, (b) $+1/4-1/4+1/4$, (c) $+1/4-$
 $1/4+1/4-1/4$ and (d) $+1-1$ turns
- Fig. 7.16 The average of the microhardness measurements, H_v , recorded 178
along the diameter of Ti-6Al-4V disks after m-HPT and c-HPT
under a pressure of 6.0 GPa for (a) $1/2$, (b) $3/4$, (c) one and (d)
two turns
- Fig. 7.17 The average microhardness measurements, H_v , recorded along 180
the diameter of Ti-6Al-4V disks after (a) m-HPT and (b) c-HPT
under a pressure of 6.0 GPa for totals of $1/2$, $3/4$, 1 and 2 turns

LIST OF TABLES

Table 2.1	Mechanical properties of CP Ti before and after ECAP	27
Table 3.1	The chemical composition of Al-1050 in wt. %	45
Table 5.1	The chemical composition of CP Ti in wt. %	84
Table 5.2	The hardness of CP Ti at this and earlier investigations	105
Table 6.1	The factor (t) used in calculating the error bars	115

CHAPTER 1

INTRODUCTION

1.1 Introduction

The mechanical and physical properties of polycrystalline materials are generally enhanced by a decrease in the average size of the material grains. Examples of these properties include the strength and the resistance of plastic deformation. The Hall-Petch equation illustrates the relation between the strength of polycrystalline materials and the average grain size [1,2]. In this equation the yield stress, σ_y , is given by

$$\sigma_y = \sigma_o + k_y d^{-1/2} \quad (1.1)$$

where σ_o is the friction stress, k_y is a constant of yielding and d is the average grain size. The Hall-Petch equation illustrates clearly that the strength increases with the reduction in grain size of the polycrystalline material. Another important advantage of the small grain sizes materials is their enhanced superplastic properties at elevated temperatures compared with the coarse-grained materials [3]. These facts have increased the interest in producing materials with extremely small grain sizes.

The conventional procedures using thermomechanical treatments are usually used to enhance the grain sizes of polycrystalline materials and hence to improve the properties of these materials. In these procedures, specified regimes of temperature and strain are normally applied to the materials to refine the grains. However, the ability of these procedures in refining the grain sizes is limited to the order of a few micrometers only. Therefore, the development of new techniques to produce materials with grain sizes in the submicrometer and nanometer range was very important. The materials having grain sizes in the range of 0.1-1 μm are called

submicrometer structured materials while the materials having grain sizes less than 100 nm are called nanocrystalline materials. Bulk ultrafine-grained materials (UFG) are defined as polycrystals having grains with average sizes less than $\sim 1 \mu\text{m}$. Bulk UFG materials require homogeneous and reasonably equiaxed microstructures with a majority of grain boundaries having high angles of misorientation [4].

Materials with UFG microstructures can be produced using two different approaches [5]. In the first approach, which is known as the "bottom- up" approach, the individual atoms or the nano-particles are assembled together to form bulk UFG materials. Examples of some techniques using this approach to form UFG materials include inert gas condensation [6], electrodeposition [7] and ball milling with subsequent consolidation [8]. The advantage of this approach is the capability of producing materials with exceptionally small grain sizes. However, this approach has many limitations such as the sizes of the finished products which are very small, introducing some contaminations during processing and the residual porosity in the materials after processing.

In the second approach, which is known as the “top-down” approach, the bulk solid which has a relatively coarse grain size initially is processed to produce a material having an UFG microstructure through the application of heavy straining. The limitations of the “bottom-up” approach such as the small product sizes and the contamination or residual porosity were avoided by the application of the “top-down” approach. Examples of this approach include equal-channel angular pressing (ECAP) [9], accumulative roll-bonding (ARB) [10] and high-pressure torsion (HPT) [11]. All these processes are based on the introduction of severe plastic deformation (SPD) into the materials, so these processes are termed the SPD processes.

To convert a solid with coarse grains into an ultrafine-grained material (UFG), it is necessary to impose an extremely high strain on the solid. Two conditions should result from imposing the high strain: first, introducing a high density of dislocations and second, re-arranging these dislocations to form an array of grain boundaries. This conversion into UFG materials can be attained by applying severe plastic deformation to the coarse-grained materials, where extremely high strains are

imposed on the solid at relatively low temperatures without introducing any significant changes in the overall dimensions of the solid [12].

The first development in using SPD in processing materials was in the 1940s by Bridgman [13]. In the 1970s and 1980s, many developments and investigations of UFG materials produced by the use of SPD techniques were achieved by Segal and coworkers [14,15]. However, the interest in the production of UFG materials by using the SPD techniques has increased significantly during the last two decades. Some of these SPD techniques are already well-established processes for producing UFG materials. Leading examples of these well-established processes are the ECAP and the HPT processes.

1.2 Aims and Objectives

The aim of the present research is to gain the experience on processing materials by severe plastic deformation (SPD) techniques. In particular, using ECAP and HPT processes as an SPD techniques to process some aluminium and titanium alloys.

The main objectives of this research are as follows:

- Investigate the evolution of the microhardness homogeneity in aluminium alloys during processing by ECAP and HPT.
- Perform strain measurements by convergent beam electron diffraction (CBED) on commercial purity aluminium (Al-1050) alloy after processing by ECAP.
- Perform ECAP on commercial purity titanium (CP Ti) at room temperature.
- Investigate the effect of strain reversal on two aluminium alloys (Al-1050 and Al-1%Mg) and two titanium alloys (CP Ti and Ti-6Al-4V) during processing by HPT.

- Examine the existence of slippage between the surfaces of the processed disks and the surfaces of the upper or lower anvils during processing by HPT.

1.3 Thesis Structure

The thesis consists of eight chapters. Chapter 2 presents the fundamentals of the ECAP and HPT processes. Chapter 3 illustrates the evolution of the homogeneity in commercial purity aluminium (Al-1050) alloy during processing by ECAP. Chapter 4 contains the strain measurements by convergent beam electron diffraction (CBED) in commercial purity aluminium (Al-1050) alloy after processing by ECAP. Chapter 5 illustrates the feasibility of processing of commercial purity titanium (CP Ti) by ECAP at room temperature. In this chapter the work was cooperated with a group from China consisting of Prof. Jingtao Wang and his student Yue Zhang. The ECAP experiments were performed at Southampton but the microhardness measurements and the micrographs were taken in China. Chapter 6 illustrates the evolution of the homogeneity in aluminium alloys during processing by HPT. Chapter 7 presents the effect of strain reversal on aluminium and titanium alloys during processing by HPT. Finally, chapter 8 summarizes all conclusions and findings from the previous chapters and highlights of the future work are presented.

CHAPTER 2

FUNDAMENTALS OF THE ECAP AND HPT PROCESSES

2.1 Introduction

Equal channel angular pressing (ECAP) and high pressure torsion (HPT) are termed as leading severe plastic deformation (SPD) processes. In the present chapter, the fundamentals and a literature review of some applications of both processes will be reviewed. The relation between the microhardness measurements and the internal microstructure of the materials which processed by ECAP or HPT will be discussed at the end of the chapter.

2.2 Equal-Channel Angular Pressing (ECAP)

The process of ECAP is an SPD process in which a material in the form of square or circular billet is deformed through a process of simple shear. This process was first introduced by Segal and his co-workers in the 1970s and 1980s [14,15]. The purpose of this process was introducing severe plastic strain into the material billets without changing the cross-sectional dimensions of the billets. The constancy of the cross-sectional dimensions provides an opportunity for repeating the pressing for many passes. Accordingly, different slip systems can be introduced by rotating the billet in different ways between the different passes [16]. In the early 1990s the process of ECAP as an SPD technique was further developed and the potential for using the process to fabricate UFG materials with grain sizes in the submicrometer and the nanometer range have increased significantly [17,18].

Many reasons have made the ECAP process one of the basic and most attractive processing techniques over the other SPD techniques [9]. First, processing by this

technique can produce quite large billets and it is possible to produce materials that may be used in some structural applications. Second, the process is relatively simple and it uses equipment that is available in most laboratories except the relative difficulty in constructing the die. Third, it can be applied to materials with different crystal structures. Fourth, processing for sufficient numbers of passes can lead to reasonably homogeneous microstructures. Fifth, there is a possibility for scaling up the process where it can be incorporated in commercial metal-processing procedures. These reasons and advantages of the processing by ECAP have increased the attention in the process in the last two decades.

The principle of the process of ECAP is illustrated schematically in Fig. 2.1 [19]. There are two angles in the die shown in the figure, the internal channel angle, Φ , which is equal to 90° in this die and the angle of the outer arc of curvature where the two channels intersect, Ψ , which is equal to 0° in this die. The channel angle, Φ , and the angle at the outer arc of curvature, Ψ , are illustrated schematically in Fig. 2.2 [20]. The three orthogonal planes in Fig. 2.1 X, Y and Z are defined as follows: X is the transverse plane which is perpendicular to the flow direction, Y is the flow plane which is parallel to the side face at the point of exit from the die and Z is the longitudinal plane which is parallel to the top surface at the point of exit from the die. In the process of ECAP, the sample which is having a square or circular cross-section is placed within the die channel then pressed by a plunger using some form of press and this process can be repeated for several passes to reach the required strain. The die and the plunger are made from material having higher strength than the sample. When the sample passes through the die channel angle, it experiences a simple shear as shown schematically in Fig. 2.3 [21]. The dimensions of the sample's cross-section remain constant despite the severe imposed strain when it passes through the shear plane and this is defined as the most important characteristic of the process of ECAP. There are several fundamental parameters governing the ECAP process such as the imposed strain in each pass, the processing route, the operated slip planes during the process and many other parameters.

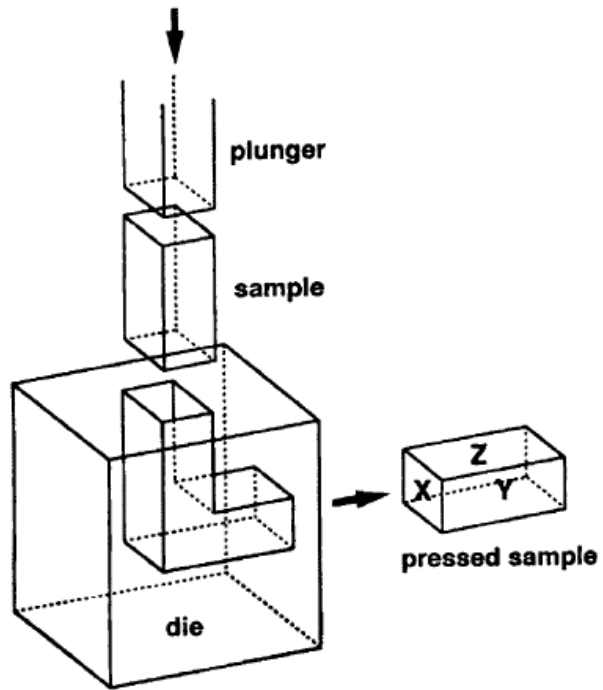


Fig. 2.1: Schematic illustration of a typical ECAP facility showing the three orthogonal planes X, Y and Z [19].

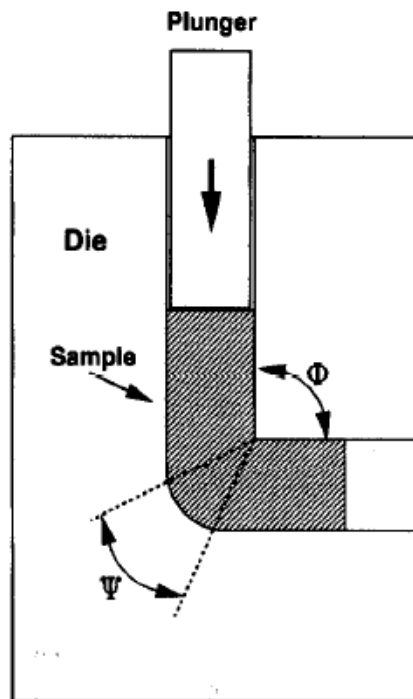


Fig. 2.2: Schematic illustration of a typical ECAP facility showing the channel angle (Φ) and the angle at the outer arc of curvature (Ψ) [20].

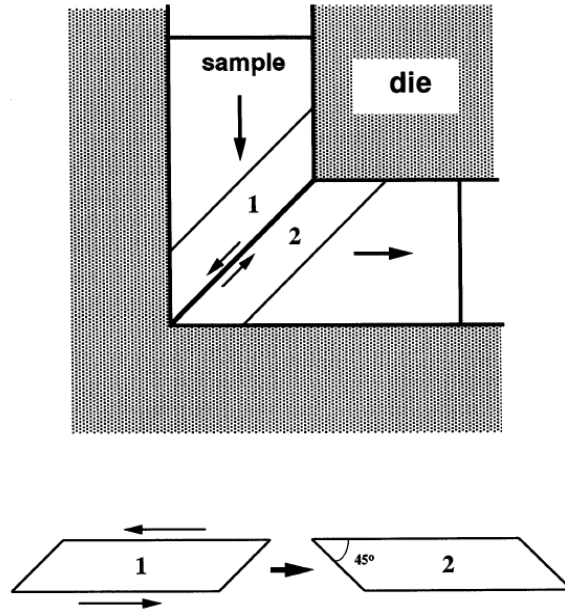


Fig. 2.3: The principle of ECAP process showing the shearing plane between the two adjacent elements labelled 1 and 2 [21].

2.2.1 The strain imposed in ECAP

The magnitude of the strain which is imposed on the sample in each pass during the ECAP process may be estimated using analytical calculations based on the different die configurations illustrated schematically in Fig. 2.4 [22]. Two angles are shown in the figure; the channel angle (Φ) and the angle of the outer arc of curvature (Ψ). There are three conditions corresponding to the situation of the angle of the outer arc of curvature (Ψ) which are shown in Fig. 2.4. These situations are: Fig. 2.4(a) where $\Psi = 0^\circ$, Fig. 2.4(b) where $\Psi = (\pi - \Phi)^\circ$ and Fig. 2.4(c) where $0^\circ < \Psi < (\pi - \Phi)^\circ$. The strain is estimated where the frictional effects are neglected.

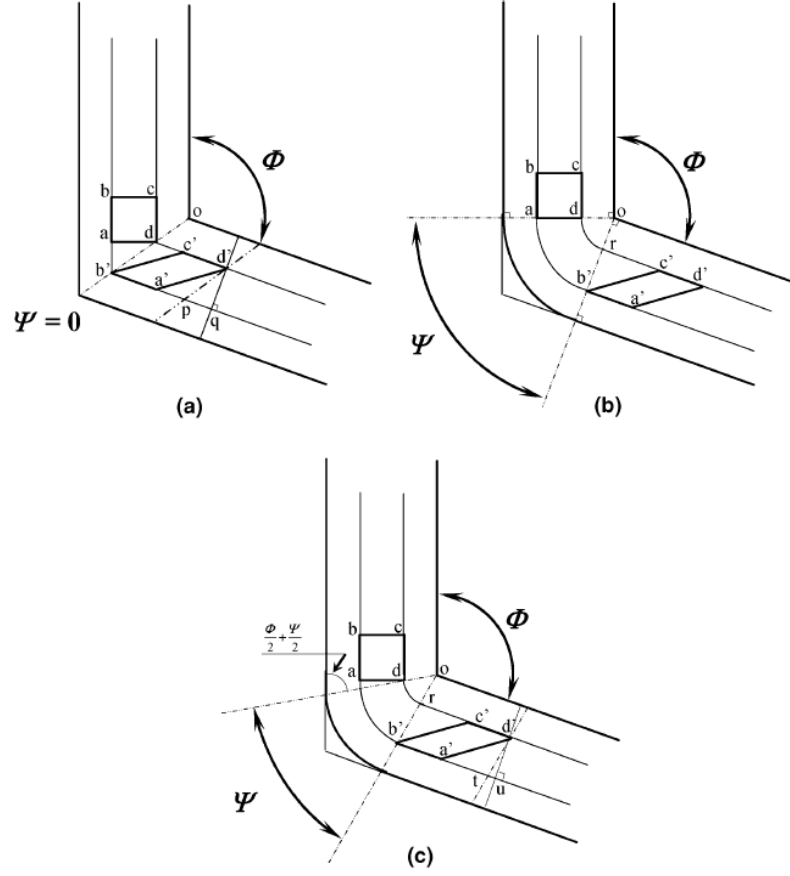


Fig. 2.4: Principle of ECAP where Φ is the channel angle and Ψ is the angle the outer arc of curvature: (a) $\Psi = 0^\circ$, (b) $\Psi = (\pi - \Phi)^\circ$ and (c) $0^\circ < \Psi < (\pi - \Phi)^\circ$ [22].

For the situation where $\Psi = 0^\circ$, it was shown in a previous study [22] that the shear strain, γ , is given by

$$\gamma = 2 \cot\left(\frac{\phi}{2}\right) \quad (2.1)$$

For the situation where $\Psi = (\pi - \Phi)^\circ$, the shear strain, γ , is given by

$$\gamma = \psi \quad (2.2)$$

and for the general situation where $0^\circ < \Psi < (\pi - \Phi)^\circ$, the shear strain, γ , is given by the general solution

$$\gamma = 2 \cot\left(\frac{\Phi}{2} + \frac{\Psi}{2}\right) + \Psi \operatorname{cosec}\left(\frac{\Phi}{2} + \frac{\Psi}{2}\right) \quad (2.3)$$

The general solution in Eq. (2.3) reduces to Eq. (2.1) if $\Psi = 0^\circ$ and reduces to Eq. (2.2) if $\Psi = (\pi - \Phi)^\circ$.

Generally, the equivalent strain imposed during processing by ECAP after N passes, ϵ_N , may be expressed in a general form by the relationship [22],

$$\epsilon_N = \frac{N}{\sqrt{3}} \left[2 \cot\left(\frac{\Phi}{2} + \frac{\Psi}{2}\right) + \Psi \operatorname{cosec}\left(\frac{\Phi}{2} + \frac{\Psi}{2}\right) \right] \quad (2.4)$$

Take into considerations that the same strain is accrued after each pass. Two modeling experiments revealed excellent agreement with Eq. (2.4), except for the regions near the cell walls or adjacent to the lower surface of the billets [23,24]. The significance of the die angles Φ and Ψ are shown in Fig. 2.5 [20]. The equivalent strain will increase with decreasing channel angle (Φ) while the angle at the arc of curvature (Ψ) has a relatively small effect on the equivalent strain. The equivalent strain in the conventional dies with a channel angle of 90° is approximately ~ 1 for each single pass and this strain is independent of the angle of the outer arc of curvature (Ψ).

2.2.2 The processing routes in ECAP

Four essential processing routes are defined for processing materials by ECAP which are termed as routes A, B_A, B_C and C. In route A the sample is pressed without rotation between the repeated passes, in route B_A the sample is rotated by 90° in alternate directions between the repeated passes, in route B_C the sample is rotated by 90° in the same direction after each pass, and in route C the sample is rotated by 180° between the repeated passes. The four different processing routes are illustrated in Fig. 2.6 [21]. Different slip systems will be introduced when using various routes

during the pressing. Therefore, different microstructures may be produced by ECAP through using different routes [25-27].

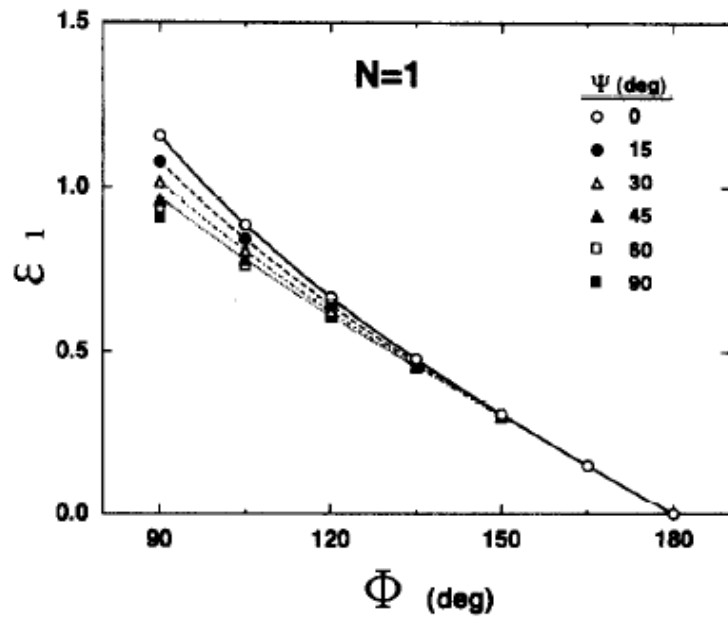


Fig. 2.5: Variation of strain with the angles Φ and Ψ after ECAP for a single pass [20].

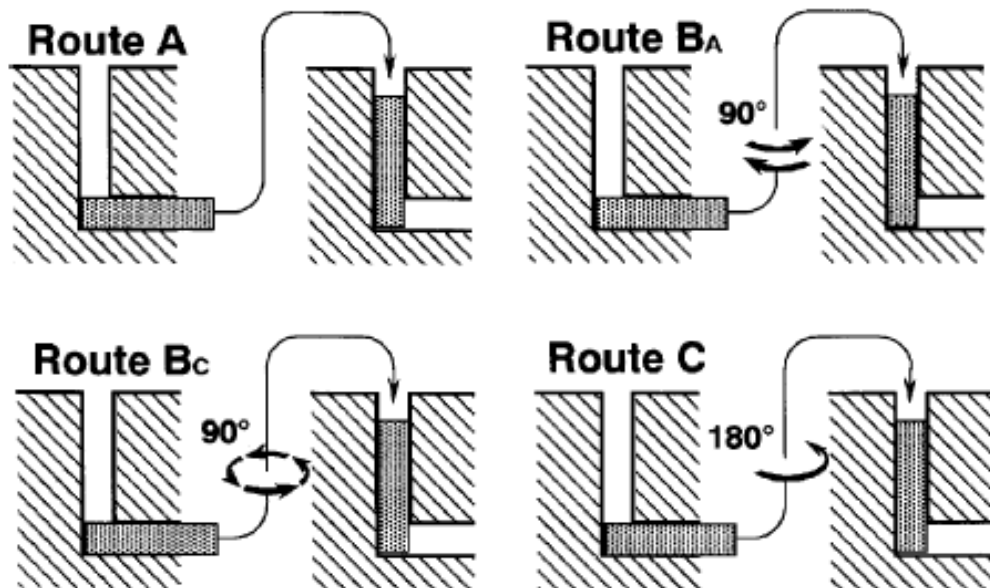


Fig. 2.6: The four basic processing routes used in ECAP [21].

2.2.3 Slip planes for the different processing routes

Different slip planes are introduced when processing materials by ECAP using different processing routes. Fig. 2.7 illustrates schematically the slip planes introduced by each processing route [28]. In the figure, the planes X, Y and Z correspond to the three orthogonal planes shown previously in Fig. 2.1 and the slip planes labeled 1, 2, 3 and 4 correspond to the first 4 passes of ECAP for the different processing routes.

In route A, there are two separate shearing planes intersecting at an angle of 90° . In route B_A , there are four separate shearing planes intersecting at angles of 120° . In route B_C , the slip in the first and second passes are cancelled by the slip in the third and fourth passes, respectively. In route C, the shearing occurs on the same plane in each consecutive pass with reversing the direction of the shear in each pass. Routes C and B_C are called redundant strain processes because the strain is restored after every two and four passes, respectively. Routes A and B_A are not redundant strain processes and there is an additional buildup of strain on each separate pass through the die.

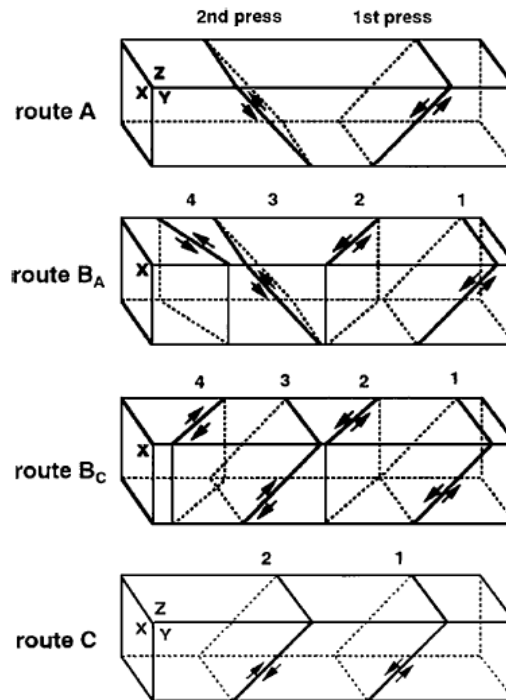


Fig. 2.7: The slip planes associated with the four processing routes [28].

The distortions introduced into a cubic element due to the different processing routes are illustrated in Fig. 2.8 [29]. The cube elements are viewed on the X, Y and Z planes for processing routes A, B_A, B_C, and C after pressing through 1–8 passes. In Route A, the distortions of the cube element increase on the X and Y planes with increasing number of passes. There is no distortion on the Z plane in route A. In route B_A, the distortions increase in all planes with increasing number of passes. In route B_C, the cubic element is restored every four passes. In route C, the cubic element is restored every two passes but there is no distortion on the Z plane. It is concluded from Fig. 2.8 that route B_C is better than the other routes because the evolution of the microstructure occurs most rapidly when using this processing route in which the sample is rotated by 90° in the same direction after each pass.



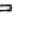
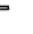

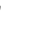







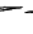
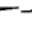
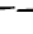
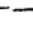








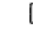



























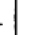




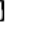


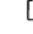





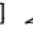
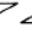








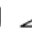





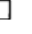



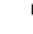
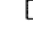

















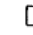

Route	Plane	Number of pressings								
		0	1	2	3	4	5	6	7	8
A	X									
	Y									
	Z									
B _A	X									
	Y									
	Z									
B _C	X									
	Y									
	Z									
C	X									
	Y									
	Z									

Fig. 2.8: The distortions of cubic elements on the X, Y and Z planes when pressed for up to 8 passes for different processing routes [29].

2.2.4 Influence of the processing route on the microstructure

The microstructures formed in pure aluminium on the X plane after ECAP through four passes using (a) route A [30], (b) route B_A [31], (c) route B_C [30] and (d) route C [30] are shown in Fig. 2.9 together with the selected area electron diffraction (SAED) patterns. It is clearly evident from these photomicrographs that pressing for four passes using route B_C leads to an array of reasonably equiaxed ultrafine grains. It is also evident that after pressing for four passes using routes A, B_A, and C the grains become elongated. The SAED patterns show that processing through route B_C led to a high fraction of boundaries having high angles of misorientation, while processing routes A, B_A and C led to high fraction of boundaries having low angles of misorientation.

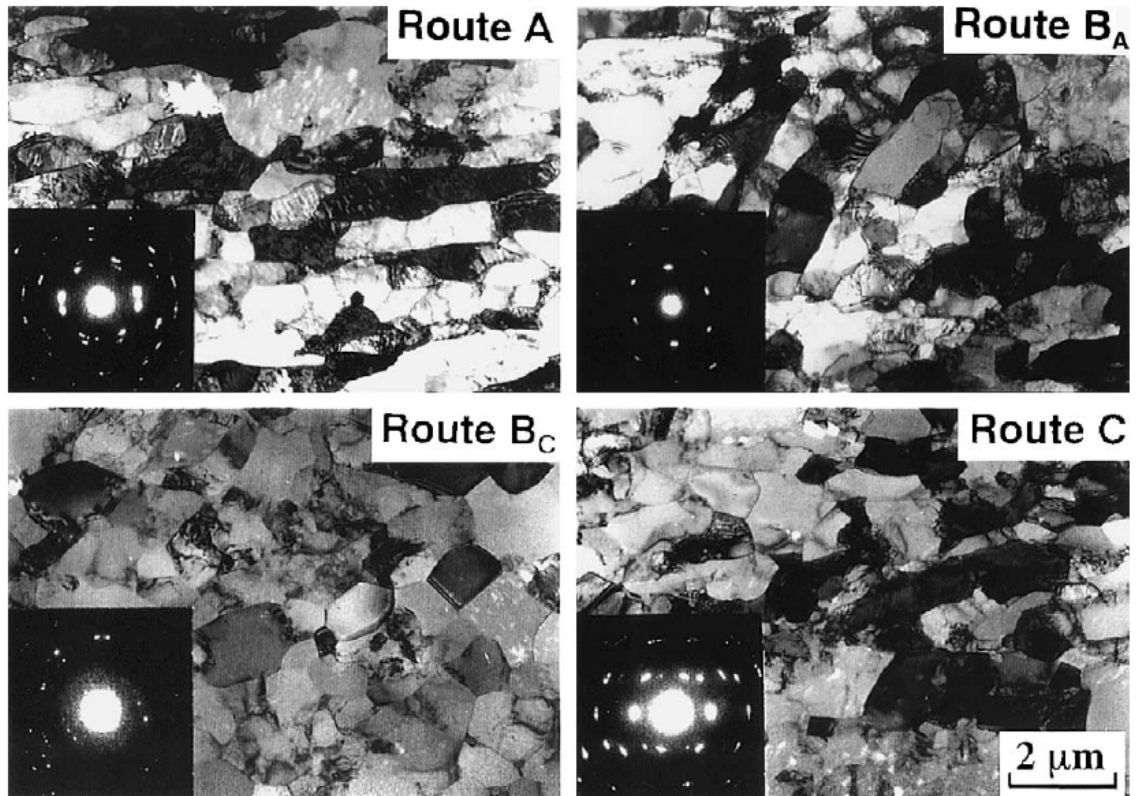


Fig. 2.9: The microstructures on the X plane for polycrystalline aluminium after ECAP through 4 passes using routes A [30], B_A [31], B_C [30] and C [30] together with the associated SAED patterns.

2.2.5 Significance of the channel angle (Φ)

As stated in equation (2.4) and presented by the plot in Fig. 2.5, the channel angle (Φ) is one of two factors significantly affecting the imposed strain on the sample during processing by ECAP. The second factor is the total number of passes. To investigate the effect of the channel angle (Φ) on the microstructure, experiments were performed on pure aluminium using four different dies having channel angles of 90° , 112.5° , 135° and 157.5° [32]. The total imposed strain on each sample was approximately 4. The samples were pressed using route Bc, in which the sample was rotated by 90° in the same direction after each pass of ECAP, for 4, 6, 9 and 19 passes giving total strains of 4.22, 4.27, 4.21 and 4.33 for the dies having channel angles of 90° , 112.5° , 135° and 157.5° , respectively. The microstructure and selected area electron diffraction (SAED) pattern of each sample are shown in Fig. 2.10. It is clear from the figure that the microstructure after pressing using a die with a channel angle of 90° consists of ultrafine equiaxed grains with boundaries having high angles of misorientation. With increasing the channel angle, the microstructure becomes less regular and the fraction of boundaries having low angles of misorientation increased. It is shown from these results that, although the total imposed strain on the four samples was almost equal, the resultant microstructures were different. It is concluded that the factor of the channel angle and hence the imposed strain in each separate pass is more important than the total imposed strain after ECAP through many passes. It is concluded also that increasing the imposed strain in each separate pass enhances the resultant microstructure. However, increasing the die channel angle is required in processing some hard or difficult-to-work materials such as titanium and tungsten at low temperatures to prevent cracking or segmented failures [33,34].

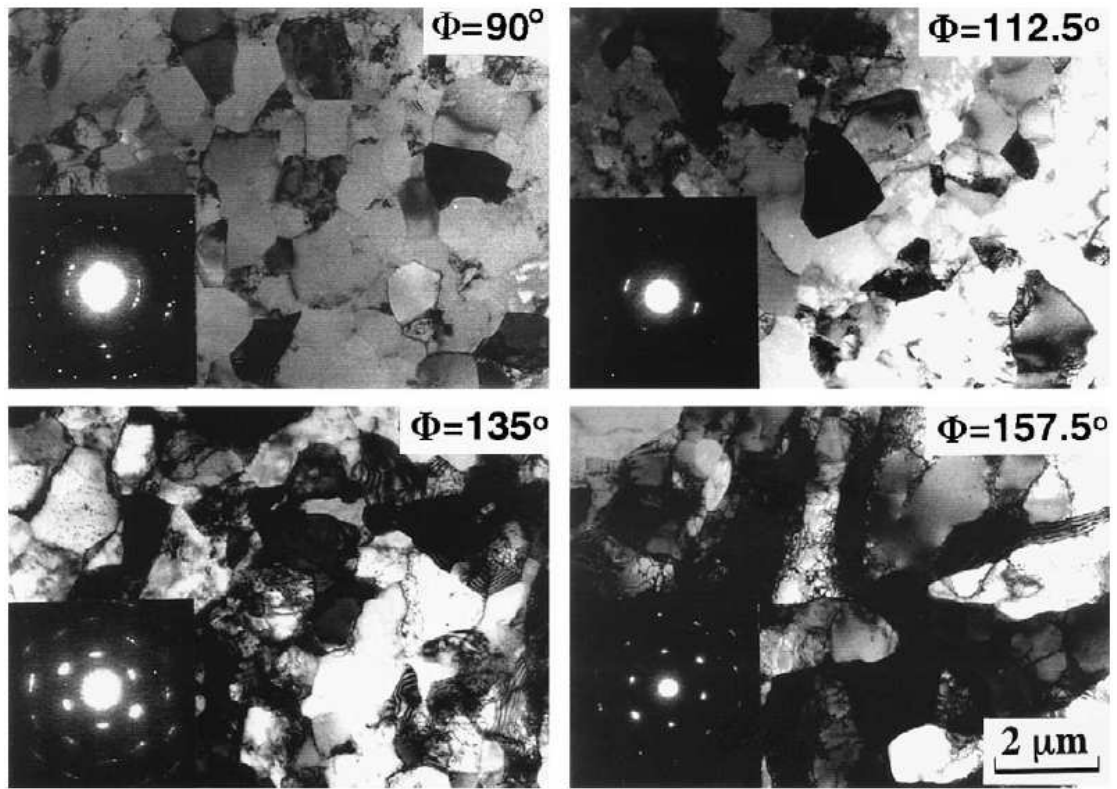


Fig. 2.10: Microstructures and SAED patterns after ECAP for an imposed strain of ~ 4 using dies having channel angles (Φ) of 90° , 112.5° , 135° and 157.5° [32].

2.2.6 Influence of the pressing speed

Usually, the processing by ECAP is conducted at relatively high speeds using high-capacity hydraulic presses. It was confirmed by many investigations that the equilibrium size of the ultrafine grains which are formed through processing by ECAP is not influenced significantly by changing the pressing speeds [19,35,36]. Fig. 2.11 illustrates the variation of the yield stress with changing the pressing speed for Al-1%Mg alloy after ECAP through 1, 2, 3 and 4 passes [19]. It is clearly evident from the figure that the pressing speed has no significant effect on the resultant yield stress. However, in processing hard or difficult-to-work materials such as titanium at relatively low temperatures, it is always required to decrease the pressing speed in order to prevent cracking [33,37].

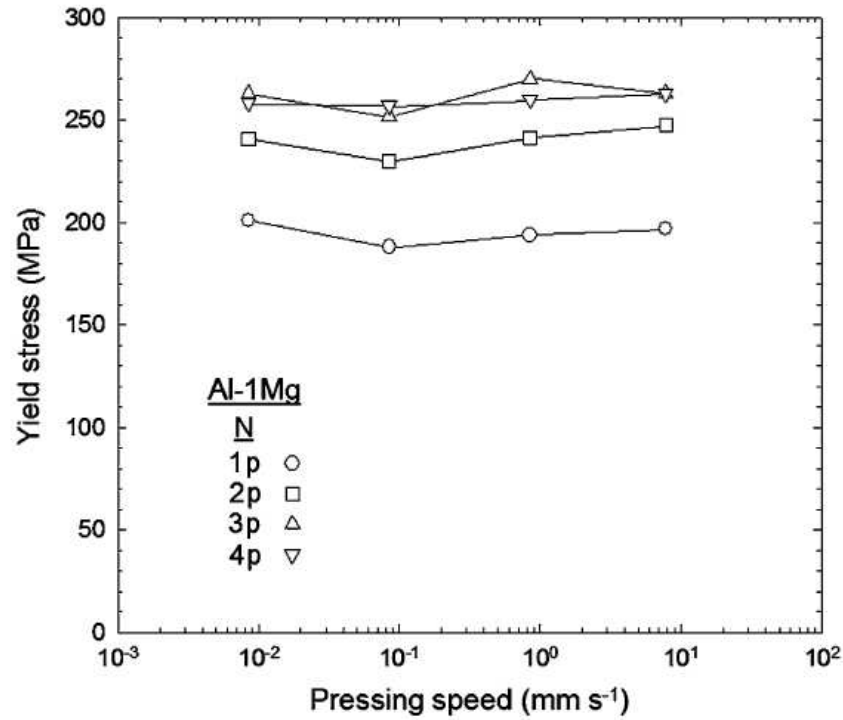


Fig. 2.11: Variation of the yield stress with the pressing speed of Al-1%Mg alloy after ECAP through 1, 2, 3 and 4 passes [19].

2.2.7 Influence of the pressing temperature

The pressing temperature has a great effect on the grain size, thus it is termed as a key factor in any use of the ECAP process. Fig. 2.12 illustrates the influence of the pressing temperature on the grain size for different aluminium alloys after ECAP through several numbers of passes at different pressing temperatures [38]. It is clearly evident from the figure that the equilibrium grain size of all materials increases with increasing temperature. With increasing pressing temperature, the fraction of low-angle grain boundaries increases because the rates of recovery become faster. Consequently, this leads to an increasing in the annihilation of dislocations within the grains which in turn leads to a decrease in the numbers of dislocations absorbed into the subgrain walls.

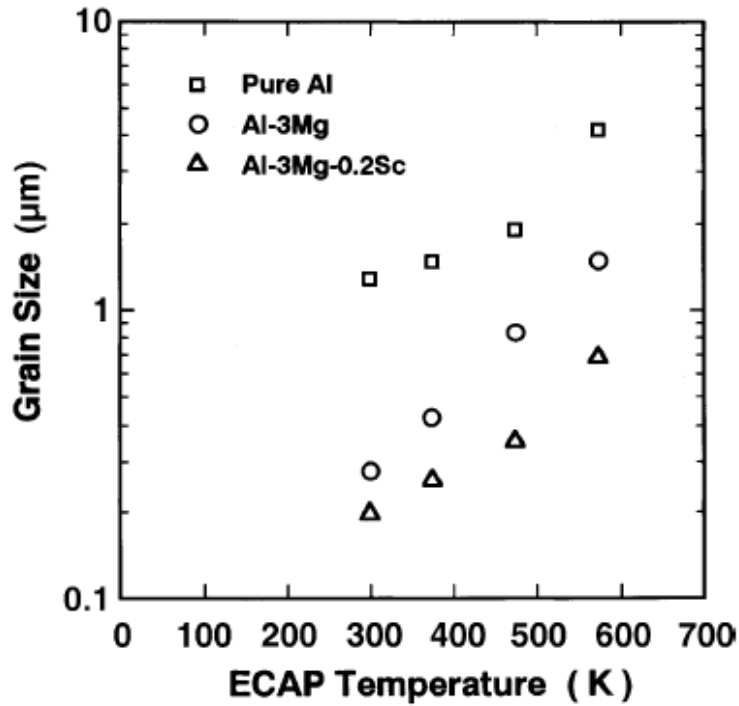


Fig. 2.12: Variation of the grain size with the pressing temperature after ECAP of different aluminium alloys [38].

2.2.8 Incorporation of ECAP in continuous production

As is known, ultra-fine grains (UFG) materials with exceptional physical and mechanical properties can be achieved by processing using the ECAP process. These materials may have important applications in the industry. There is some effort to incorporate ECAP technique in continuous processing operations [39-50]. Fig. 2.13 illustrates an example of incorporating a process termed the dissimilar-channel angular pressing (DCAP) in continuous production operation [45]. Another example of incorporating ECAP in continuous production operations is illustrated in Fig. 2.14 where a process termed ECAP-Conform was incorporated in a continuous production operation [49].

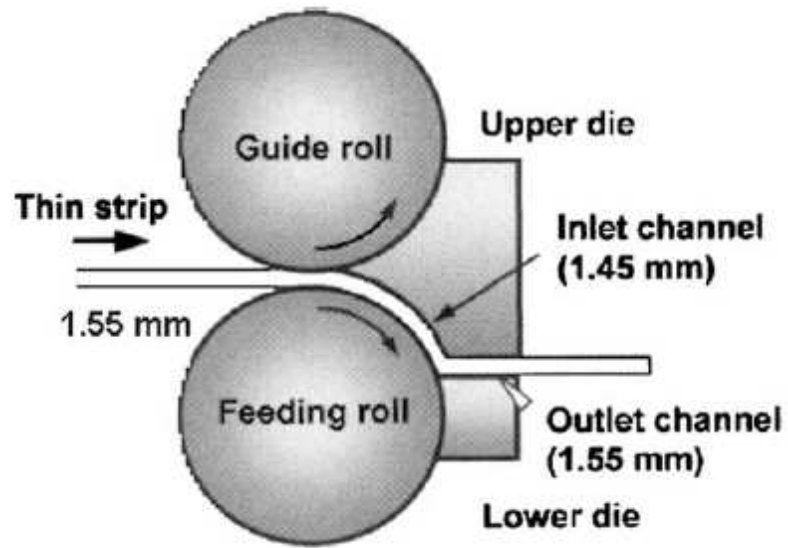


Fig. 2.13: Schematic illustration of the DCAP process which was used in continuous production operations [45].

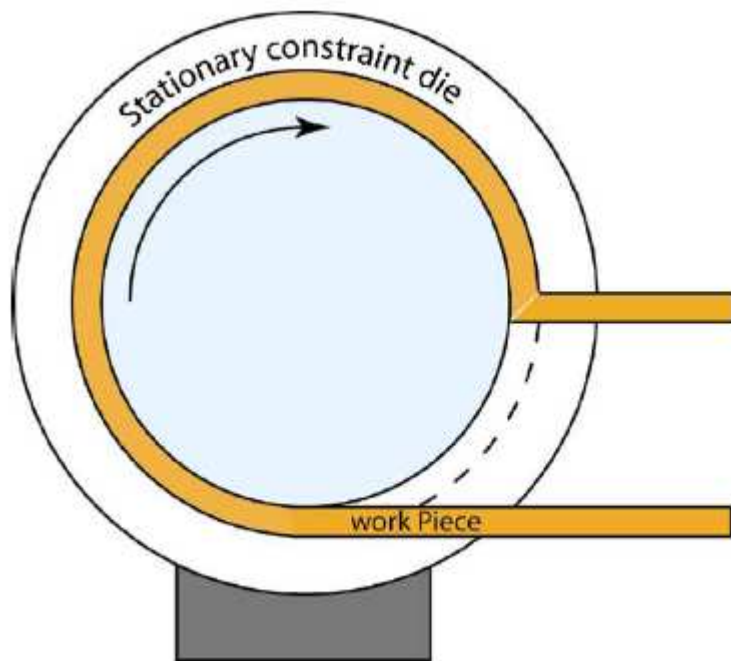


Fig. 2.14: Schematic illustration of the process of ECAP-Conform [49].

2.2.9 Evolution of the microhardness homogeneity during processing by ECAP

Since the sample pressed through the ECAP die experiences a homogeneous simple shear strain, it is suggested theoretically that the microstructure will be homogeneous. However, practically the applied strain during ECAP is inhomogeneous. The frictional forces between the sample and the die walls, for example, may affect the strain distributions especially near the die walls. The lack of contact between the sample and the lower surface when the sample passes through the outer arc is another example of the effect on the strain distribution. However, the experimental data available to date suggests that a reasonable homogeneity of the microstructure can be achieved after sufficient number of passes.

ECAP experiments were conducted on pure Al and Al-6061 alloy to investigate the evolution of homogeneity after pressing for several passes [51]. In these experiments, the billets were pressed for up to four passes at room temperature using route B_C. Microhardness measurements were taken following a regular rectilinear grid pattern over the cross-sectional planes of the billets. The results were presented in the form of contour maps representing the individual microhardness values. The results show that the hardness on both materials became inhomogeneous after one pass with lower hardness regions near the bottom surface. With increasing numbers of passes, the microhardness values became more homogeneous. After four passes, the hardness values of the pure Al became homogeneous while the homogeneity of the microhardness values of the Al-6061 alloy gradually improved.

A new technique was developed recently by recording the microhardness measurements in a rectilinear grid pattern across the different planes of the ECAP billets. These measurements were then plotted in the form of colour-coded contour maps to provide a visual representation of the variations in the microhardness across these planes [52,53]. Examples for the colour-coded contour maps for pure aluminium and Al-6061 alloy subjected to ECAP are shown in Figs. 2.15 [52], 2.16 [52] and 2.17 [53]. In Fig. 2.15, the microhardness measurements were recorded on the cross-sectional plane of pure aluminium in the as-received unpressed condition and after pressing through one, two, three, four and eight passes of ECAP at room temperature using route B_C. In Fig. 2.16, the microhardness measurements were

recorded on the cross-sectional plane of Al-6061 alloy in the as-received unpressed condition and after pressing through one, two, three, four and six passes of ECAP at room temperature using route B_C. In Fig. 2.17, the microhardness measurements were recorded on the vertical longitudinal plane of Al-6061 alloy after pressing through one, two, four and six passes of ECAP at room temperature using route B_C. The results of these experiments show that the material became inhomogeneous after one pass, although the hardness remarkably increased after this pass. With increasing numbers of passes, the hardness continued to increase in small amounts and at the same time the homogeneity of the microhardness values increased significantly.

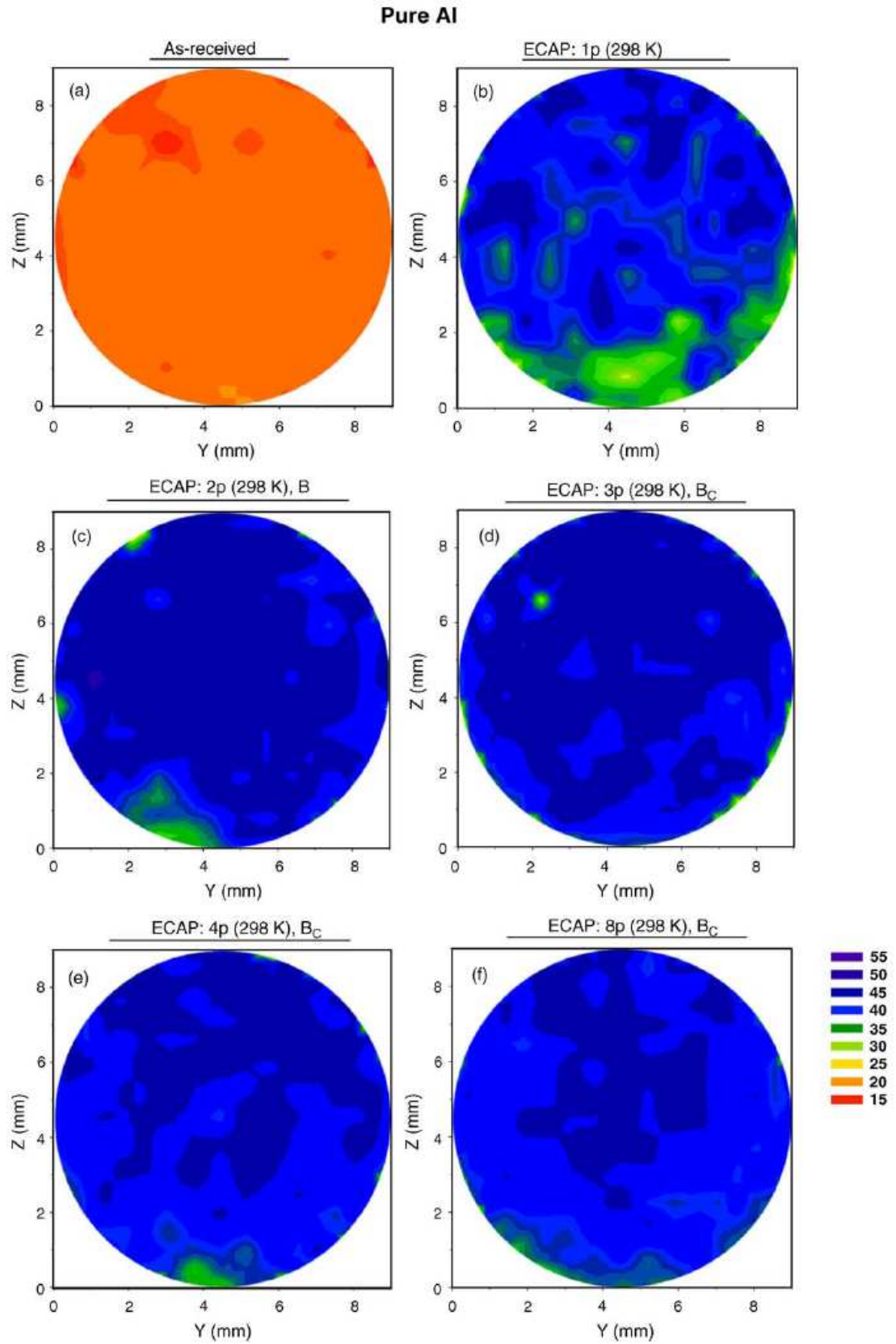


Fig. 2.15: Colour-coded contour maps of the microhardness through the cross-sectional planes of pure aluminium billets in the unpressed condition and after ECAP through 1, 2, 3, 4 and 8 passes [52].

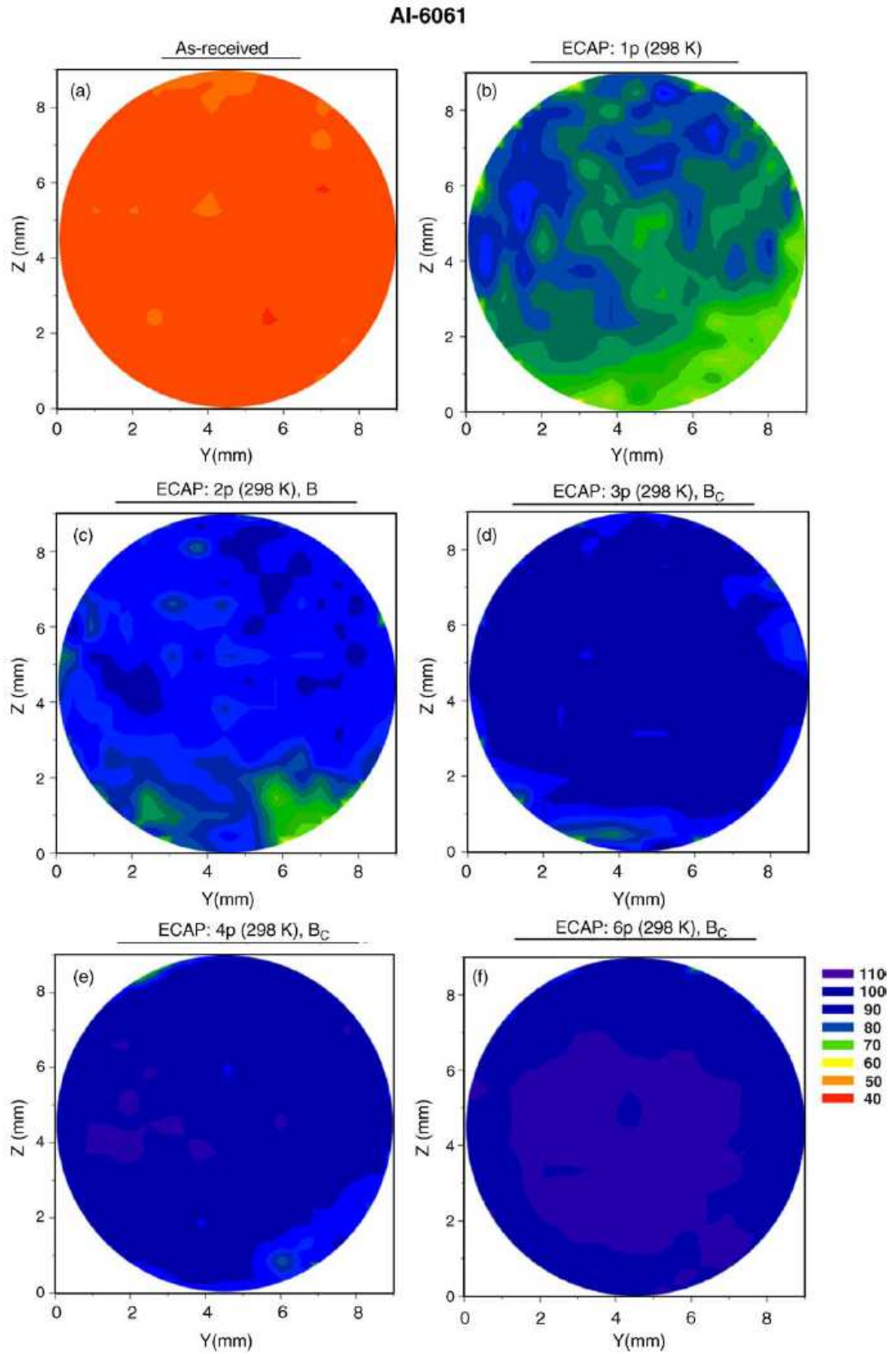


Fig. 2.16: Colour-coded contour maps of the microhardness through the cross-sectional planes of an Al-6061 alloy in the unpressed condition and after ECAP through 1, 2, 3, 4 and 6 passes [52].

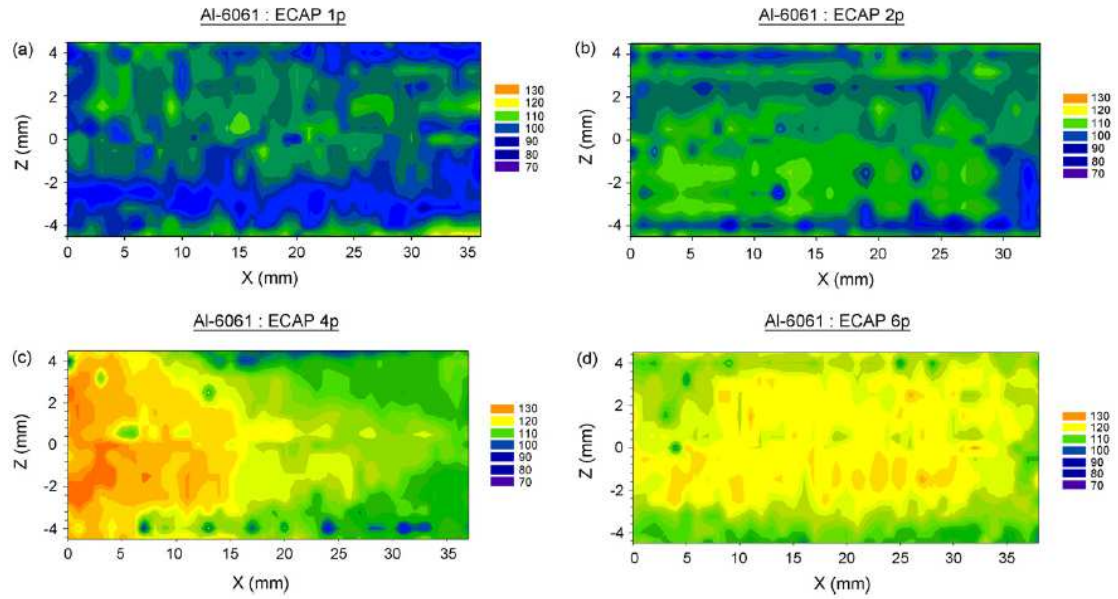


Fig. 2.17: Colour-coded contour maps of the microhardness through the longitudinal planes of Al-6061 alloy after ECAP through 1, 2, 4, and 6 passes [53].

2.2.10 Processing of titanium alloys by ECAP

It is known that processing by ECAP at low temperatures; such as room temperature, leads to the optimum ultrafine-grained microstructures. Pressing at low temperatures results in smaller grain sizes and higher fractions of high-angle boundaries [38]. However, it is not easy to perform ECAP processing on hard metals such as titanium at low temperatures due to the high loads needed for pressing which may exceed the capacity of the press or lead to the formation of cracks and segmentations. Therefore, most of the low temperature ECAP investigations are carried out on relatively soft metals such as aluminium and copper. One of the early investigations for processing titanium by ECAP was in 1999 by Semiatin et al. [33]. In this study, ECAP pressing was performed on commercial purity titanium (CP Ti) using a conventional die with an angle of 90° between the two channels. It was found that the CP Ti billet experiences segmented failure at room temperature using many pressing speeds (25, 0.25 and 0.025 mm/s) as illustrated in Fig. 2.18. Furthermore, CP Ti experiences the same failure at temperatures of ~ 400 K and ~ 500 K using a pressing speed of 0.25 mm/s. By contrast, CP Ti experiences a uniform flow when pressed at a temperature of ~ 550 K using a pressing speed of 0.25 mm/s. At temperature of ~ 600 K, CP Ti

experiences a uniform flow at the pressing speeds of 0.25 and 0.025 mm/s but it experiences segmented failure again at a pressing speed of 25 mm/s.

All subsequent experiments of ECAP of CP Ti were performed at elevated temperatures with only one exception of performing the experiment at room temperature. Most of these experiments were performed at temperatures in the range of 623 - 773 K [36,54-65]. Only one investigation successfully performed ECAP on CP Ti at a temperature of 473 K [66]. The dies used in all these investigations were having an angle of 90° between the two channels.

Up to date, there is only one investigation showing ECAP of CP Ti at room temperature successfully [37]. In this study, billets of CP Ti were pressed in two different dies; one having an angle of 90° between the two channels and the second having an angle of 120° between the two channels. For both dies, the angle of the outer arc of curvature was 20°. Using the calculation written by Iwahashi et al. [22], it is found that the equivalent strain imposed on the billet in each pass is ~1 for the 90° die and ~0.6 for the 120° die. All billets were pressed for a single pass at room temperature using a pressing speed of 0.5 mm/s. As shown in Fig. 2.19, the billets pressed using the 90° die start to have cracks along the direction of the shear and if the pressing is continued the billet will experience segmented failure similar to the failure reported by Semiatin et al. [33]. By contrast, the billet pressed using the 120° die shows a uniform and smooth flow without having any visible surface cracking. Furthermore, as shown in Table 2.1, the yield stress, σ_{ys} , the ultimate tensile strength, σ_{UTS} , and the Vickers microhardness, Hv, of the billet pressed by ECAP at room temperature for one pass by 120° die shows a significant increase compared to the billet in the initial unpressed condition. In addition, the elongation to failure in the billet pressed at room temperature remains reasonably high. The comparison between those mechanical properties in the billet pressed at room temperature for one pass with those in the billets pressed for multiple passes at elevated temperatures show that the values are reasonably similar or even the room temperature billets show slightly better values in some cases. Finite element modelling predictions on hard and difficult-to-work materials performed by Figueiredo et al. [67] show that the increase in the angle of the die distributes the deformation zone within the shearing

region and this prevents the shear localization which in turn leads to reducing the tendency for cracking and segmented failures.

A conclusion from the previous mentioned studies, especially [33,37], is that there are two important parameters in processing by ECAP for the hard or difficult-to-work materials at room temperature. The first parameter is increasing the channel angle (Φ) within the ECAP die to an angle equal or above 120° . The second parameter is reducing the pressing speed to slow speeds (in the range of 0.5 mm/s or less). Those two important parameters manage the fracture behaviour and controlling them can prevent the failure by segmentation and lead to a uniform flow in the ECAP process.

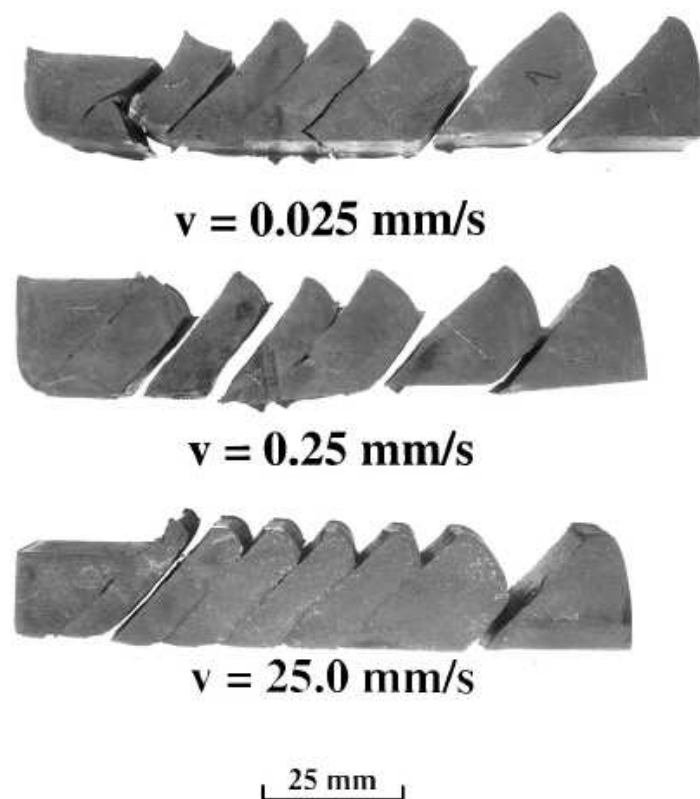


Fig. 2.18: Samples of CP Ti billets after pressing at room temperature using pressing speeds of 0.025, 0.25 and 25.0 mm/s [33].

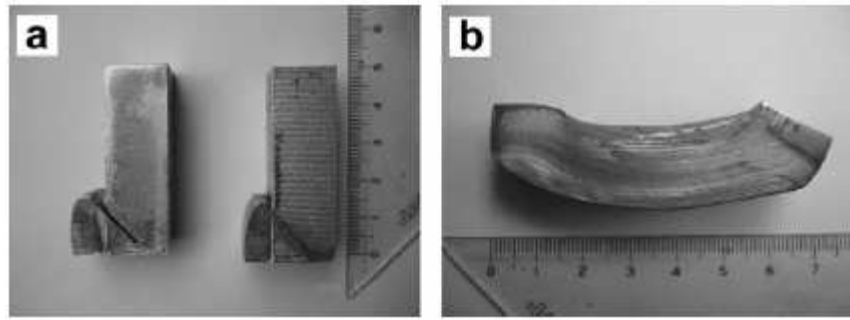


Fig. 2.19: CP Ti billets after pressing at room temperature with dies having channel angles (Φ) of (a) 90° and (b) 120° [37].

Table 2.1: Mechanical properties of CP Ti before and after ECAP [37]

	ECAP conditions				Mechanical properties			
	Angle Φ	T (K)	N	Ram Speed (mm/s)	Hv(MPa)	σ_{ys} (MPa)	σ_{UTS} (MPa)	δ (%)
<i>This investigation</i>								
Initial material	-	-	-	-	1550	405	530	41
After ECAP	120°	R.T.	1	0.5	2430	680	780	14
<i>Earlier investigations</i>								
Stolyarov et al. [5]	90°	723-773	7	-	2350	520	540	16
Stolyarov et al. [7]	90°	673-723	8	6	-	640	710	14
Stolyarov et al. [8]	90°	673-723	8	-	2700	640	710	14

2.2.11 Twinning in titanium alloys after processing by ECAP

Slip and the activated slip systems in the materials processed by ECAP play a critical role in the introduced structure of the material [9]. It has been found by von Mises (1928) and Taylor (1938) that the minimum required number of independent slip systems for a material to experience a homogeneous deformation by slip is five [68]. For face-centered cubic (FCC) metals and body-centered cubic (BCC) metals, this condition exists and the required five independent systems for slipping are available. On the contrary, the number of the independent active slip systems in the hexagonal close-packed (HCP) metals such as titanium (Ti) is limited. This limitation in the number of the slip systems makes the processing by ECAP of the h.c.p. metals and alloys very difficult. Due to this limitation in the slip systems, deformation twinning

plays a critical role in the processing of h.c.p. metals such as Ti by ECAP. The formation of deformation twins in titanium alloys was reported in many investigations [37,55,59,60,66].

Commercial purity titanium (CP Ti) was processed by ECAP for one pass at a temperature of 623 K [55]. The analysis of the microstructure showed that the deformed structure was covered by multiple micro twins. It was shown that the twins occurred on $\{10\bar{1}1\}$ planes despite of the grain orientation with respect to the shear direction. Depending on this result, it was confirmed that, in CP Ti alloys, the $\{10\bar{1}1\}$ twinning plays a critical role in the plastic deformation accrued through the processing by ECAP. A similar investigation was performed on CP Ti at the same temperature of 623 K for one and two passes, then microstructural observations were made on the specimens [60]. It was observed that CP Ti during the first pass deformed mainly by $\{10\bar{1}1\}$ deformation twinning, as proved by Kim et al. [55]. However, during the second pass, CP Ti deformed mainly by slip rather than by deformation twinning. This is due to the microstructural changes such as grain size refinement and texture formation which occurred during the first pass. These changes increase the critical resolved shear stress (CRSS) for deformation twinning over that for dislocation slip.

At room temperature, it was shown that processing of CP Ti for one pass using 120 degree die led to the formation of shear bands and $\{10\bar{1}1\}$ deformation twins [37]. It was suggested that the limited slip systems in the hexagonal close-packed (hcp) metal such as titanium are assisted by the formation of $\{10\bar{1}1\}$ deformation twins and this leads to the formation of a microstructure containing both the shear bands and the deformation twins.

2.3 High Pressure Torsion (HPT)

The concept of high pressure torsion (HPT) was first introduced by Bridgman in the 1940s when he combined the torsion with compression in his experiments [13]. In the 1980s, the principles of HPT were applied on several metallic alloys by a research group in Russia [69]. After that the process of high pressure torsion was considered as a method of processing of nanostructured materials [70]. Homogeneous nanostructures with high-angle grain boundaries were successfully formed using this method of severe plastic deformation [71].

When compared to HPT, ECAP is relatively simple procedure where, except only for the construction of the die, it uses equipment that is readily available in most laboratories. However, HPT became an attractive processing technique because it leads to a greater refinement of the microstructure and to a higher fraction of high-angle boundaries compared to ECAP. For example, experiments on Al-3% Mg alloy led to grain sizes of ~270 nm in ECAP [72] and ~90 nm in HPT [73], experiments on Al-5% Fe alloy led to grain sizes of ~300 nm in ECAP and ~100 nm in HPT [74] and experiments on high-purity Ni led to grain sizes of ~350 nm in ECAP and ~170 nm in HPT [75]. Subjecting pure Ti to HPT after ECAP reduces the grain size from ~300 nm after ECAP only to ~200 nm after ECAP then HPT [54]. In addition, experiments on high-purity Ni showed that the ratio of high-angle boundaries was higher after HPT compared with ECAP [75,76].

In HPT, a sample in the form of a disk is held between two anvils termed the lower and upper anvils. High compressive pressure, P , is applied up to several GPa and then the disk is concurrently strained in torsion by rotation of the lower anvil. Illustration of the HPT method is shown in Fig. 2.20. Due to the applied pressure and torsion, surface frictional forces deform the disk by shear. The deformation of the disk continues under a condition of quasi-hydrostatic pressure.

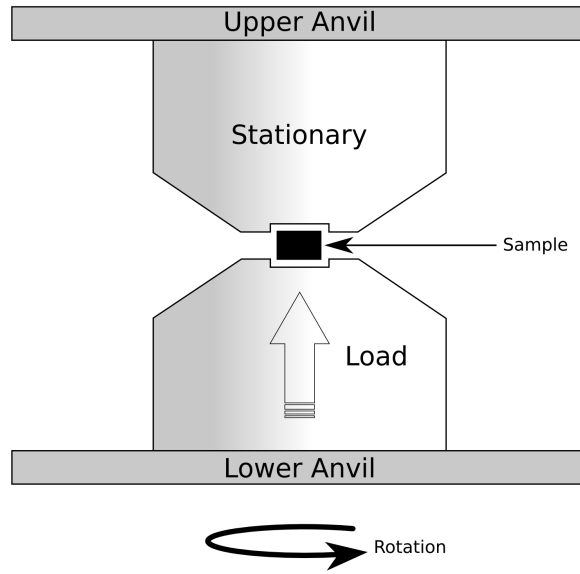


Fig. 2.20: Illustration of the HPT facility showing the sample under pressure and rotation.

2.3.1 Calculation of the strain imposed in HPT

Different relationships were used to calculate the strain imposed on the disk in high pressure torsion (HPT). Fig. 2.21 illustrates the variables used in estimating the strain [71]. For an infinitely small rotation, $d\theta$, the displacement, dl , is calculated as $dl = rd\theta$ where r is the radius of the disk. Therefore, the incremental shear strain, $d\gamma$, is given by

$$d\gamma = \frac{dl}{h} = \frac{rd\theta}{h} \quad (2.5)$$

where h is the disk thickness.

Since $\theta = 2\pi N$, where N is the number of revolutions, and by assuming that the thickness of the disk, h , is independent of the rotation angle, θ , it follows from formal integration that the shear strain, γ , is given by

$$\gamma = \frac{2\pi N \cdot r}{h} \quad (2.6)$$

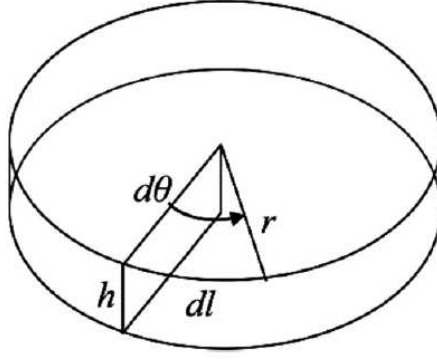


Fig. 2.21: Parameters used in estimating the total strain in HPT [71].

Finally, the equivalent strain is calculated according to the von Mises criterion using the relationship [77-79]

$$\varepsilon = \gamma / \sqrt{3} = \frac{2\pi N \cdot r}{h\sqrt{3}} \quad (2.7)$$

Eq. (2.7) can be used for small imposed shear strains only. For large strains, where $\gamma \geq 0.8$, the equivalent strain is given by [80]

$$\varepsilon = (2/\sqrt{3}) \ln \left[(1 + \gamma^2/4)^{1/2} + \gamma/2 \right] \quad (2.8)$$

An alternative relationship for calculating the equivalent strain was developed to incorporate the decrease in the thickness of the disk which is resulting from the application of large values of pressure. For this condition, the equivalent strain is given by [81]

$$\varepsilon = \ln \left[1 + \left(\frac{\theta \cdot r}{h} \right)^2 \right]^{1/2} + \ln \left(\frac{h_o}{h} \right) \quad (2.9)$$

where h_o and h are the initial and final thickness of the disk, respectively. Since $(\theta \cdot r)/h \gg 1$, Eq. (2.9) may be simplified to the following expression [82,83]

$$\varepsilon = \ln \left(\frac{\theta \cdot r}{h} \right) + \ln \left(\frac{h_o}{h} \right) = \ln \left(\frac{\theta \cdot r \cdot h_o}{h^2} \right) = \ln \left(\frac{2\pi N \cdot r \cdot h_o}{h^2} \right) \quad (2.10)$$

All these equations provide different theoretical relationships which may be used to calculate approximately the total strains imposed on HPT disks. However, the equivalent strain values calculated by the above relationships are only approximately equal to the real strain values. It is more realistic to consider the number of revolutions imposed on the disk and not the strain value calculated by the analytical equations while studying the evolution of the microstructure during HPT [77].

2.3.2 Constrained and unconstrained HPT

When processing by HPT, two different types of processing can be used based on the method of insertion of the disk sample between the two anvils. These types are called constrained and unconstrained HPT as illustrated schematically in Fig. 2.22 [84].

In unconstrained HPT, as illustrated in Fig. 2.22(a), the disk is placed on the lower anvil and it is free to flow outwards under the applied pressure and torsion. A minor back-pressure is introduced on the disk due to the frictional forces between the disk and the surface of the anvils. Unconstrained HPT was used in some experiments such as pure Ni experiments [71].

In the second condition where the disk is processed under constrained HPT, as shown in Fig. 2.22(b), the disk is placed in a cavity in the lower anvil, so there is no material flow outside the cavity after applying the pressure and torsion. In this type of HPT processing, the disk is strained under a condition of full back-pressure. The idealized constrained HPT is difficult to achieve and normally the experiments are conducted under a quasi-constrained condition, as illustrated in Fig. 2.22(c). In this case, there are two cavities in the upper and lower anvils and the disk is fitted in these cavities. The flow of the material outside the anvils is limited.

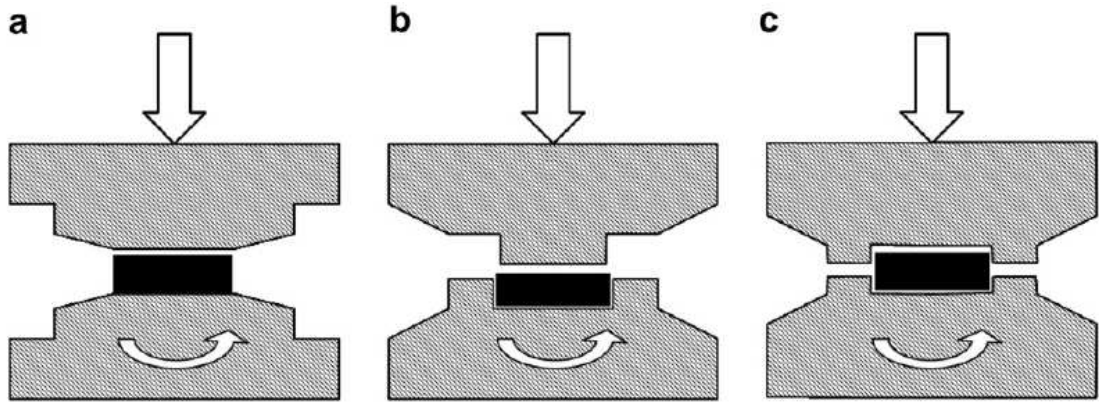


Fig. 2.22: Schematic illustration of HPT process for (a) unconstrained, (b) constrained and (c) quasi-constrained conditions [84].

2.3.3 Variation in homogeneity across the HPT disk

In principle, the theoretical imposed strain on the HPT disks is given by $(2 \pi N r / h)$ where N , r and h are the number of turns, the radial distance from the centre and the thickness of the disk, respectively. As a result of this expression, the strain must be zero at the centre and increases linearly to reach a maximum near the edges. So, it is theoretically suggested that the microstructure produced by HPT should be inhomogeneous. This homogeneity was proven by studying the microhardness evolution of the HPT disk. Some reports have proved this inhomogeneity and show that the values of the microhardness along the diameter of disks processed by HPT vary significantly with low values in the centre and high values near the edge of the disks [85-87]. However, most of the experimental data available to date suggests that a reasonable homogeneity of the microstructure can be achieved when processing under sufficient pressure and revolutions [71,88-95].

A clear contradiction with the theoretical strain relationship was shown by Xu et al. [95] where high purity aluminium disks were processed by HPT at room temperature under pressures of 1.25, 2.5 and 6.0 GPa for 1, 3 and 5 turns. As shown in Fig. 2.23, at the early stages of pressing, the hardness at the centre of the disks under different pressures is higher than near the edge of the disk and with increasing number of turns the hardness becomes homogeneous along the diameter of the disk.

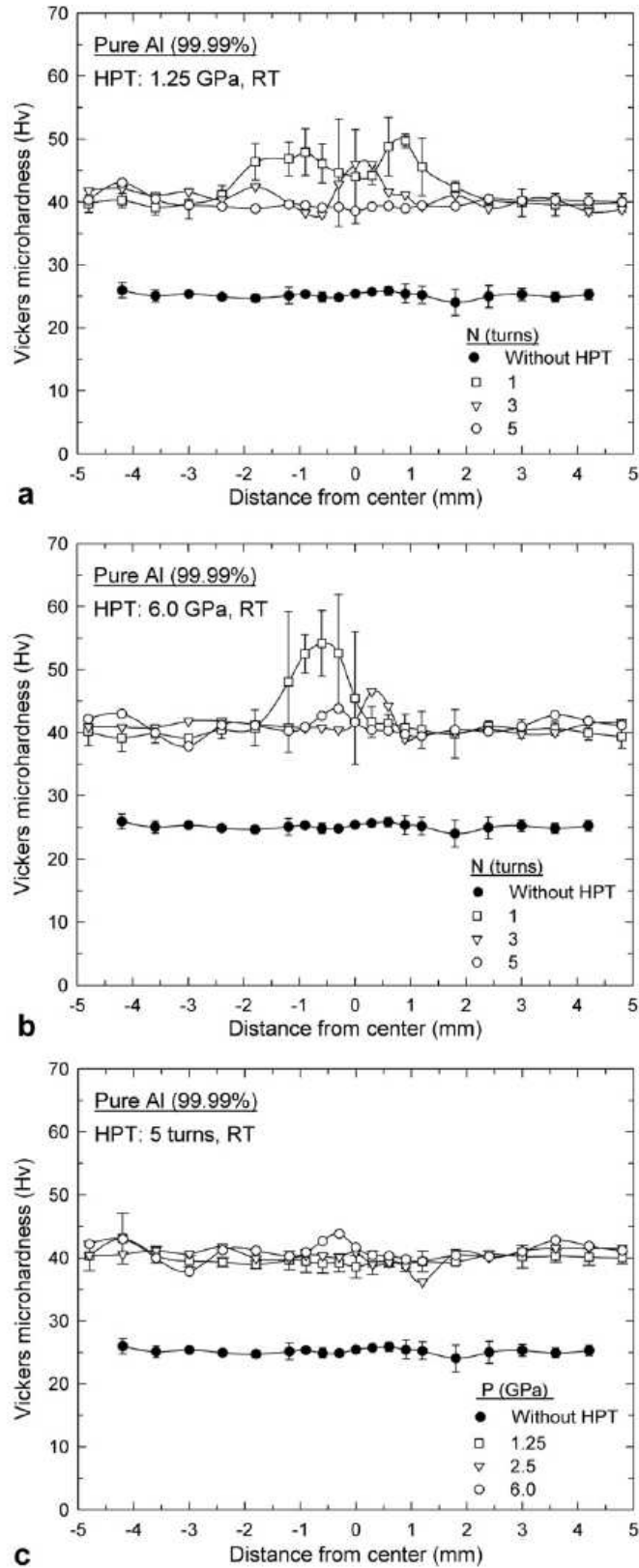


Fig. 2.23: The average Hv microhardness versus distance from the centre of the disk after processing by HPT: (a) under a pressure of 1.25 GPa, (b) under a pressure of 6.0 GPa and (c) after five turns using different pressures [95].

2.3.4 Influence of the applied pressure on microstructural evolution

The applied load or pressure is an important factor in processing by HPT. Fig. 2.24 illustrates the influence of the applied pressure on the microhardness values for Ni disks processed by HPT for 5 turns under applied pressures of (a) 1 GPa, (b) 3 GPa, (c) 6 GPa and (d) 9 GPa [71].

The figure shows the three-dimensional meshes for microhardness data and the projected hardness values. The initial hardness of the material in the unpressed condition was ~ 1.4 GPa. The microhardness increased after pressing under a pressure of 1 GPa inhomogeneously where the hardness near the edges of the disk is larger than near the centre. With an increase in the applied pressure, the microhardness values over the surfaces of the disks increased especially in the centres of the disks and all values were more than 3 GPa after pressing under a pressure of 9 GPa. Increasing the applied pressure led to an increase in the homogeneity of the microhardness values.

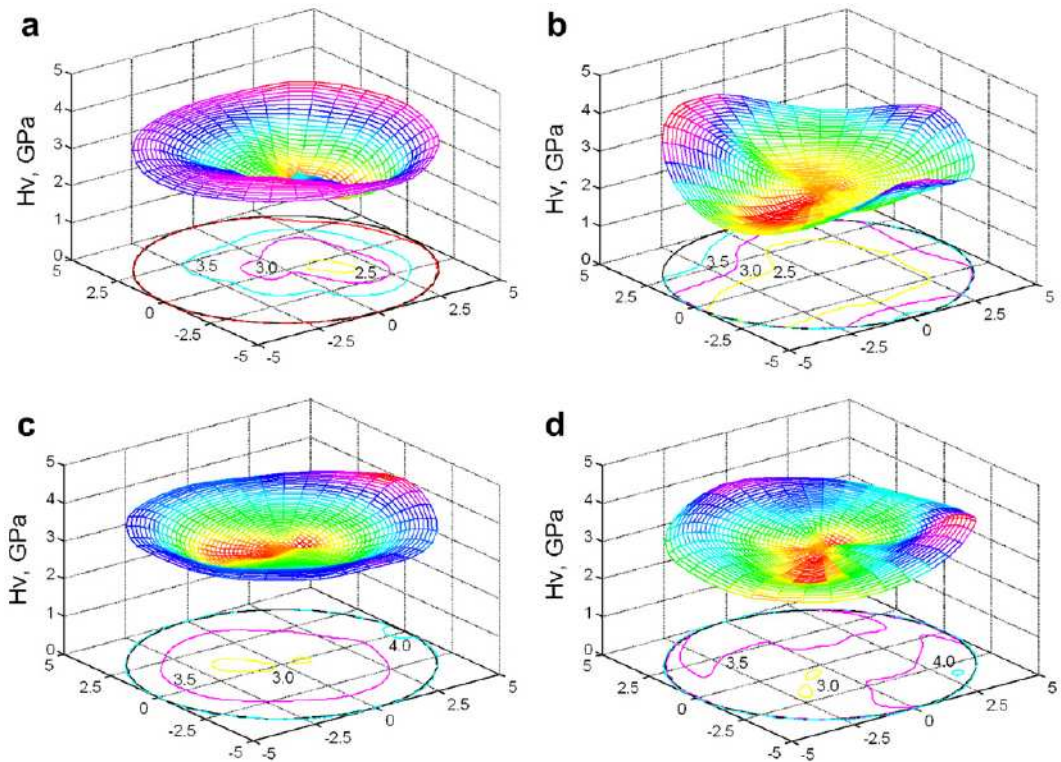


Fig. 2.24: Three-dimensional meshes of microhardness of Ni processed by HPT under applied pressures of (a) 1 GPa, (b) 3 GPa, (c) 6 GPa and (d) 9 GPa [71].

2.3.5 Influence of the number of revolutions

The second important factor in the HPT process is the total imposed strain which is measured by the number of revolutions. Fig. 2.25 illustrates the influence of the total number of revolutions on the microhardness values for Ni disks processed by HPT under a pressure of 6.0 GPa for (a) 1/2, (b) 1, (c) 3 and (d) 7 turns [71]. After 1/2 turn, the microhardness increased inhomogeneously where the centre of the disk shows lower hardness than the edges. With increasing number of revolutions, the higher microhardness regions near the edges became larger. After seven turns, the microhardness values became reasonably homogeneous. Increasing the number of revolutions led to an increase in the homogeneity of the microhardness values.

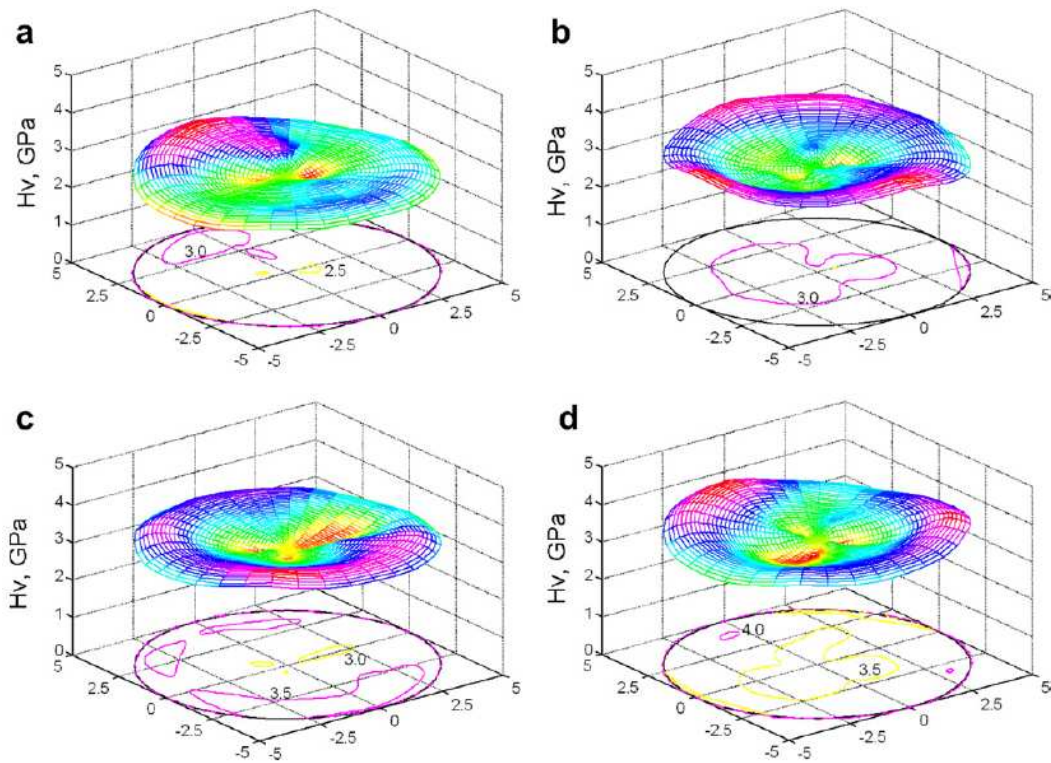


Fig. 2.25: Three-dimensional meshes of microhardness in Ni processed by HPT under a pressure of 6.0 GPa for (a) 1/2 turn, (b) 1 turn, (c) 3 turns and (d) 7 turns [71].

2.3.6 New technique in evaluating the microhardness evolution

To evaluate the evolution of homogeneity in the microhardness measurements, a new technique was developed recently by recording the microhardness measurements in a rectilinear grid pattern across the surface of the HPT disks. These measurements were then plotted in the form of colour-coded contour maps to provide a visual representation of the variations in the microhardness across the surface of the disks [95].

Examples for the colour-coded contour maps for high purity aluminium are shown in Figs. 2.26 and 2.27. The material in both figures were processed for 1, 3 and 5 turns. Fig. 2.26 shows the maps under a pressure of 1.25 GPa while Fig. 2.27 shows the maps under a pressure of 6.0 GPa [95]. Fig. 2.26 shows that the homogeneity of the microhardness after processing under a pressure of 1.25 GPa increases with increasing numbers of revolutions. A similar trend is shown in Fig. 2.27 for the disks subjected to a pressure of 6.0 GPa. Conflicting all other HPT reports, both figures show that the microhardness at the centre of the disks is higher than near the edges. This is related to the high value of the stacking fault energy in the pure aluminium. High purity aluminium has a high stacking fault energy and a high recovery rate. The diameter of the area of higher microhardness at the centre of both disks decreases with increasing number of turns and pressure. On the other hand, evaluation of the figures shows that optimal homogeneity for pure Al is achieved after five turns when using the lowest pressure of 1.25 GPa.

The results of this investigation show that the development of homogeneity in HPT depends upon two factors: the numbers of revolutions which reflect the values of the imposed strain and the values of the applied pressure.

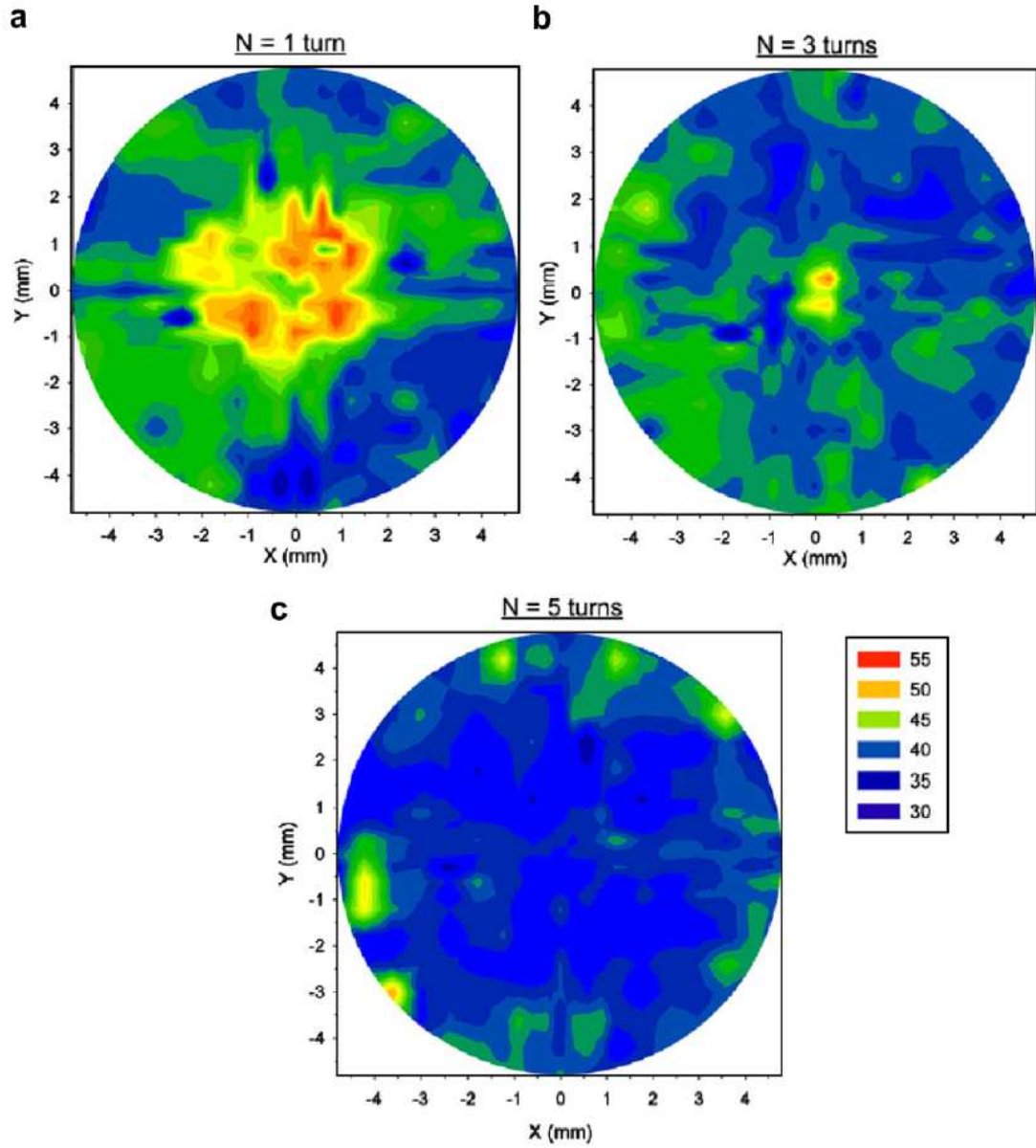


Fig. 2.26: Colour-coded contour maps showing Hv microhardness across the surface of high purity Al processed by HPT at a pressure of 1.25 GPa for (a) 1, (b) 3 and (c) 5 turns [95].

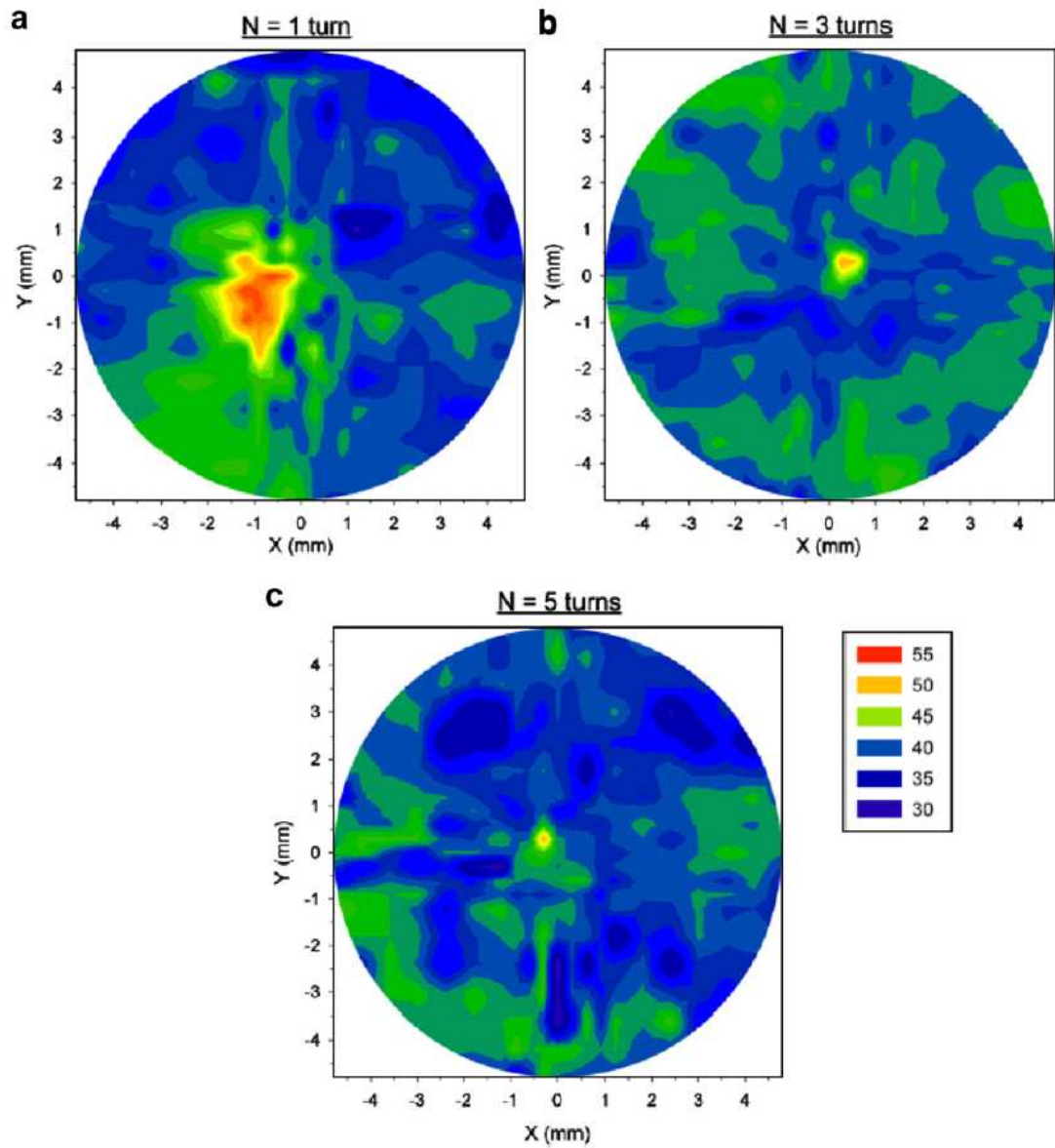


Fig. 2.27: Colour-coded contour maps showing Hv microhardness across the surface of high purity Al processed by HPT at a pressure of 6.0 GPa for (a) 1, (b) 3 and (c) 5 turns [95].

2.3.7 Strain reversal in HPT

One of the essential differences between ECAP and HPT is the continuity of the processing operation. In ECAP, the process is discontinuous where the processed billet is removed from the die after each pass and this discontinuity allows changing the pressing route between consecutive passes. Four different processing routes were established that lead to activating different slip systems giving different shear patterns for each route [29,96]. On the contrary, HPT is a continuous process where the sample remains between the two anvils during the entire experiment. The only way to change the route of the HPT processing operation is by altering the path or direction of rotation. As shown in Fig. 2.28, two directions of rotation are available in the HPT operations; A and B, where the rotation in the same direction is called the monotonic HPT (m-HPT) and altering between A and B directions is called the cyclic HPT (c-HPT) [97].

There are only a few reports to date investigating the effect of strain reversal on the structure and the mechanical properties of some materials. In the first investigation, c-HPT were conducted on an Al-3% Mg-0.2% Sc alloy at a pressure of 6 GPa for two turns; one in A direction and one in B direction, and it was compared to the same alloy strained for two turns by m-HPT [90]. The results of the hardness across the diameter of the disks showed the same trend where the hardness is low at the centre and higher near the edge. However, the rate of hardening was higher in the disk processed by m-HPT than that processed by c-HPT. Later, Armco iron, high-purity Ni and 900A pearlitic rail steel were processed by c-HPT by estimating the strain by cycle ranging from 0.5 to 4 at a radius distance of 3 mm from the centre of the disk up to a total strain deformation of 64 at the radius distance of 3 mm [98,99]. The results of these investigations were similar to that found in the previous study by Horita and Langdon [90].

Commercial purity Ti (CP Ti) and a low carbon steel (Fe-0.03C) were processed for up to 50 turns using m-HPT and c-HPT [100]. The results of the hardness measurements for the low carbon steel were similar to the other materials discussed previously; i.e. the rate of increase of the hardness was higher in m-HPT than in c-

HPT. However, contradicting all other studies, the rate of increase of hardness in CP Ti was higher in c-HPT than in m-HPT.

High-purity Al was processed using m-HPT and c-HPT at room temperature for up to 4 turns under a pressure of 6.0 GPa [97]. The measurements of the microhardness were recorded over the surface of the disks and colour-coded contour maps were constructed. The results showed that, as in all other materials investigated in reversal straining except CP Ti, the microstructural homogeneity occurs more slowly in c-HPT than in m-HPT.

The evolutions of microstructures in high-purity aluminium were studied in m-HPT and c-HPT for strains up to 8 which is equivalent to rotation for 96° at the outer edge of the disk [101]. Reversal straining was performed by alternating rotation in A and B directions for 12° in each direction. The results showed that there were no significant differences between m-HPT and c-HPT for the grain refinement and the final grain size. However, it was shown that processing by c-HPT significantly slowed down the formation of high angle grain boundaries. The same group studied the microstructure and the texture of the same material using the same procedure [102]. The results showed that the microstructural and textural developments were similar for m-HPT and c-HPT in the early stages of the deformation (strain of ~ 1) but significantly different at higher strain levels.

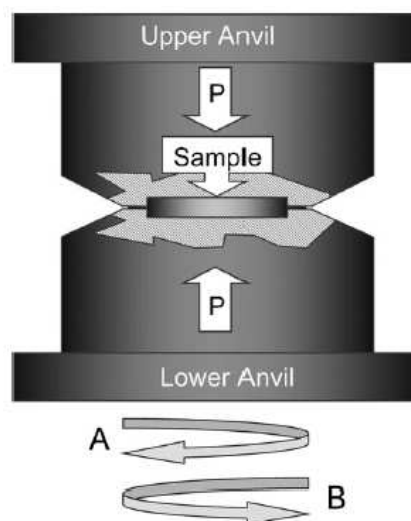


Fig.2.28: Schematic illustration of HPT facility showing the two directions of rotation; A and B [97].

2.4 Microstructure - Microhardness Relation

The relation between the internal microstructure of the materials and the microhardness measurements were reported in many studies. Those studies concluded that there is a direct relation between the internal microstructure and the microhardness measurements where the materials show increase in the microhardness with the decrease in the size of the materials grains.

The results of some studies guarantee this direct relation. First, there is a report for armco-iron and the pearlitic rail steel S900A [78] showing the variation of both the microhardness measurements and the grain size for the armco-iron or the cementite lamellae distance for the pearlitic rail steel S900A after deforming both materials by HPT under a pressure of 5 GPa and for an equivalent strain of up to 32. It was shown by this study, as illustrated in Fig. 2.29, that the microhardness increases with the decrease in the grain size in the armco-iron and in the pearlitic rail steel S900A the microhardness increased with the decrease in the cementite lamellae distance.

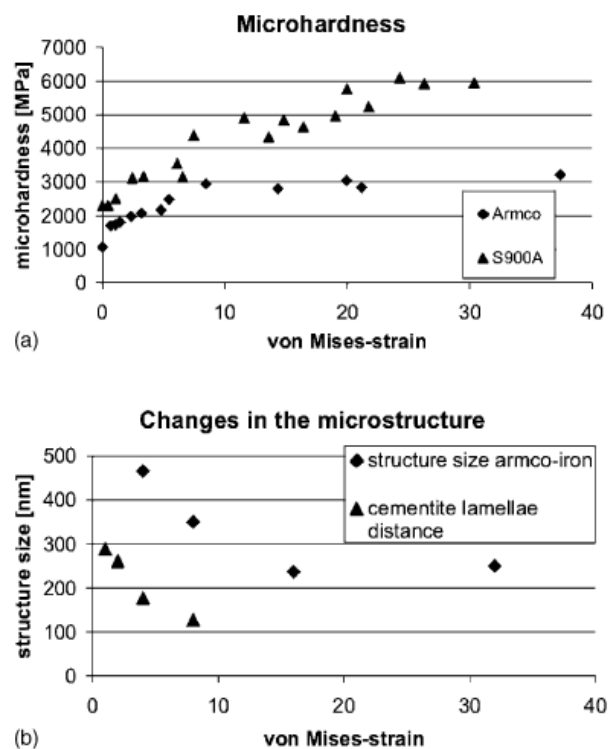


Fig. 2.29: (a) Change in microhardness, (b) change in internal microstructure for armco-iron and the pearlitic rail steel S900A [78].

In the second report, the microhardness measurements which were taken across the cross-section of pure aluminium processed by ECAP for one pass show higher values in the central region of the billet than at the vicinity of the bottom surface [52]. Studying the microstructure at both regions shows that the microstructure at the central region consists of ~50% elongated grains and ~50% equiaxed grains whereas the microstructure at the vicinity of the bottom surface consists of ~90% elongated grains and ~10% equiaxed grains. Hence, the increase in the fraction of the equiaxed grains in the pure aluminium increases the microhardness. In the third report, similar results were found when processing pure aluminium by ECAP for one pass using a back pressure of 50 MPa [103]. Microhardness measurements were recorded across the cross-sectional plane which show a region of lower values adjacent to the bottom surface. Photomicrographs were taken at three different positions on the cross-section; (a) near the upper surface, (b) at the centre and (c) near the lower surface. Well-defined sub-grains having reasonably equiaxed configurations were found near the upper surface and at the centre of the plane. On the other hand, there were no well-defined equiaxed sub-grains near the lower surface.

In the fourth report, the same results were also found when processing high purity aluminium by HPT for one turn with a pressure of 1.25 GPa [95]. Microhardness measurements show high values in the centre of the disk and lower values near the edge of the disk. The microstructures in the centre and near the edge of the disk were recorded by TEM. The micrographs show that the grains in the centre of the disk are smaller compared to that near the edge; the average grain sizes in the central area were ~0.8 μm and near the edge of the disk were ~1.2 μm . All these investigations show that the microhardness measurements increase with the decrease in the grain sizes of the materials. The previous results guarantee a direct relation between the internal microstructure of the materials and the microhardness measurements.

An investigation on commercial purity aluminium (Al-1050) processed by ECAP for one pass showed that the microhardness was highest at the centre of the cross-section of the billet while the grain size was smallest at the edges [104]. It was suggested that the contribution of dislocations in the increase in the microhardness values near the edges was higher than that of the grain size.

CHAPTER 3

THE EVOLUTION OF HOMOGENEITY DURING PROCESSING OF COMMERCIAL PURITY ALUMINIUM BY ECAP

3.1 Introduction

In this chapter, the evolution of the microhardness homogeneity of commercial purity aluminium alloy during processing by ECAP will be investigated. As mentioned previously, the degree of homogeneity of the microhardness measurements reveal the homogeneity of the internal microstructure of metals as stated in many previous reports [52,78,95,103].

Theoretically, the imposed shear strain on the billet during ECAP is homogeneous [16,22,23]. However, in practice, the strain is affected by many factors that lead to inhomogeneities in the internal microstructure. The frictional forces between the billet and the die walls are a source of inhomogeneities. Another source is the lack of contact between the billet and the lower surface at the dead zone when the billet passes through the outer arc [23,24,105,106].

In this chapter, the changes in the microhardness with increasing number of passes will be studied on two planes; the longitudinal and the cross-sectional planes. The required number of passes to reach a reasonable homogeneity in the microhardness measurements when processing Al-1050 alloy will be investigated.

3.2 Experimental Material and Procedures

A commercial purity aluminium alloy Al-1050 with a weight percent of at least 99.5% aluminium was used in the ECAP experiments. The chemical composition of the alloy in weight percent (wt. %) is shown in Table 3.1. The alloy was supplied in the form of a long bar having a diameter of 9.45 mm. Billets having a diameter of 9.45 mm and length of 65.0 mm were cut from the bar for the ECAP experiments.

Table 3.1: The chemical composition of Al-1050 in wt. %:

Maximum composition in wt.%								
Al	Fe	Si	Mg	Cu	Mn	Zn	V	Ti
(Min.)								
99.50	0.40	0.25	0.05	0.05	0.05	0.05	0.05	0.03

The ECAP experiments were conducted in air at room temperature using a facility connected to a computer to control the pressing speed during the experiments. Photographs of the experimental facility used in the ECAP experiments are shown in Fig. 3.1. The experiments were conducted by fabricating a solid die made from H13 tool steel material with dimensions of 101.6×152.4×82.6 mm as shown in Fig. 3.2. The solid die contains a circular cross-section channel which is bent into an L-shaped configuration. The entrance portion of the channel has a diameter of 9.7 mm and the exit portion of the channel has a diameter of 9.5 mm. The diameter of the exit portion of the channel increased to 9.9 mm near the exit of the channel to ease the removal of the billets from the die. The channel has two angles, one is the die internal angle between the entrance and exit portions of the channel (Φ) and the second is the angle of the outer arc of curvature at the point of intersection of the two portions (Ψ). The values used in this investigation for the two angles were 90 deg for the channel angle (Φ) and 20 deg for the angle of the outer arc of curvature (Ψ). For the die configuration and the values of the two angles Φ and Ψ used in this investigation, it has been shown previously that the equivalent strain accumulated on each separate

pass is ~ 1 [22]. Before testing, billets were coated by a lubricant containing a suspension of molybdenum disulfide in a mineral oil. Pressure was applied to the billets using a plunger made from H13 tool steel material attached to a hydraulic press having a capacity of 200 tons.

Billets were pressed for 1, 2, 4 and 6 passes giving a maximum total strain of ~ 1 , 2, 4 and 6, respectively. All billets were pressed using a pressing speed of 0.5 mm/s and processing route B_C , in which the billet was rotated by 90° in the same direction between each consecutive pass [29]. This processing route was selected because, for the die configuration used in these experiments, it leads most rapidly to an array of equiaxed ultrafine grains separated by an array of boundaries having high angles of misorientation [31]. Also a previous investigation shows that pressing Al-1050 alloy using route B_C leads to higher hardness and yield strength values when pressing up to eight passes compared to route C, in which the billet is rotated by 180° between each consecutive pass [107]. Limited inherent back-pressure was applied on the billets in this investigation because each billet is pressed against the preceding billet which stays in the die after pressing. An as-received billet and as-pressed billets through 1, 2, 4 and 6 passes are illustrated in Fig. 3.3.



Fig. 3.1: Photographs of the experimental facility used in the ECAP experiments showing the die and the plunger.

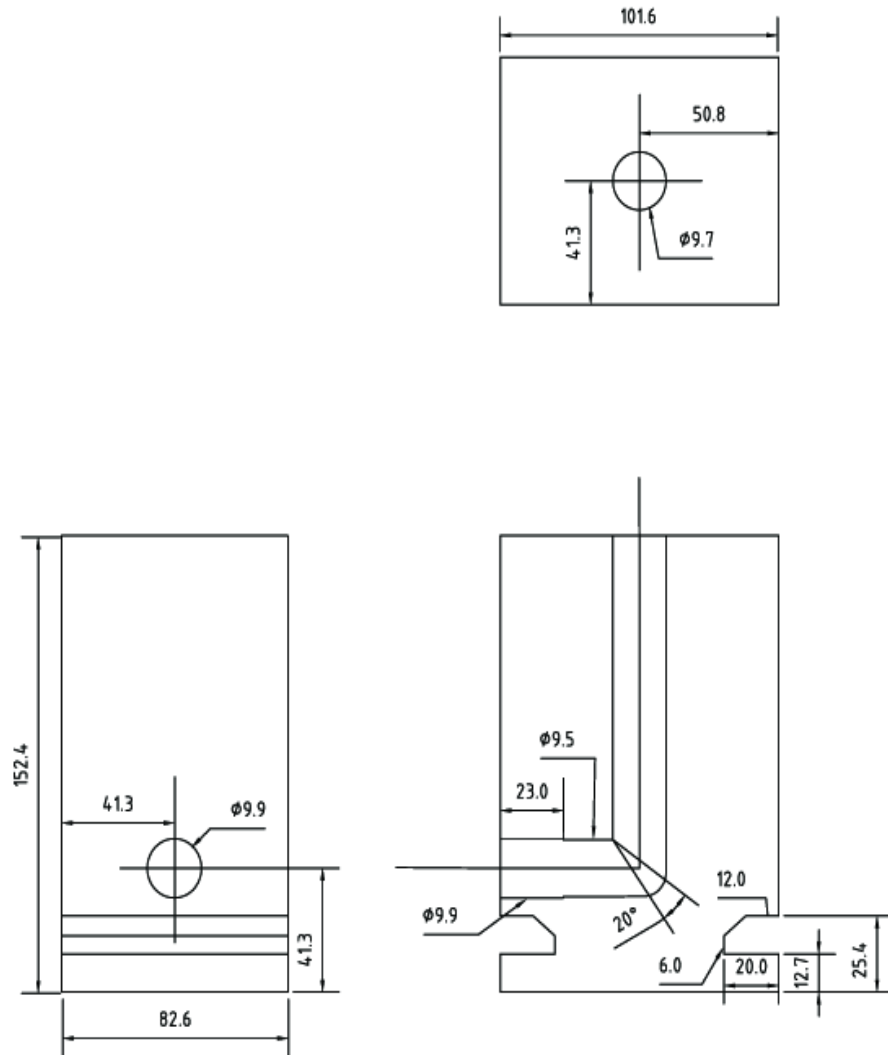


Fig. 3.2: Drawing for the die used in the experiments showing the dimensions in mm and angles of the channel.

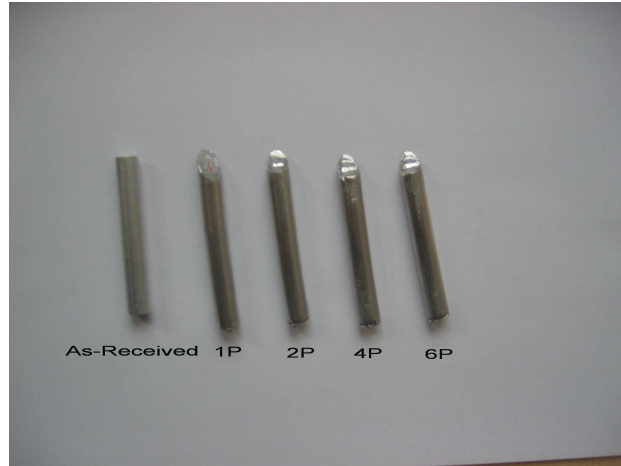


Fig. 3.3: As-Received and as-pressed billets after 1, 2, 4 and 6 passes.

After pressing, two groups of billets were selected. Each group consists of four billets after pressing through 1, 2, 4 and 6 passes, respectively. The billets from one group were carefully sectioned into two halves along the central line of the billets, perpendicular to the upper surface, using 0.25 mm brass wire erosion with an electro-discharge machine. All microhardness measurements of this group were then taken on the vertical longitudinal (XZ) planes of one half of each billet. The billets from the second group were sectioned perpendicular to their longitudinal axes using the same method of sectioning and a small disk was chosen from the middle of each billet, i.e. away from the front and rear edges. All microhardness measurements of this group were then taken on the cross-sectional (YZ) planes of each disk. The orthogonal notation used in this investigation, as in earlier ECAP studies [9], is: the X or transverse plane perpendicular to the flow direction, the Y or flow plane parallel to the side face at the point of exit from the die and the Z or longitudinal plane parallel to the top surface at the point of exit from the die, respectively. One half of each billet of the first group and a small disk from each billet of the second group were mounted using a cold-setting resin based on two fluid epoxy components and then carefully polished using 120, 600, 1200 and 4000 grit to a mirror-like finish. Fig. 3.4 illustrates the billets of the first group after sectioning, mounting and polishing.

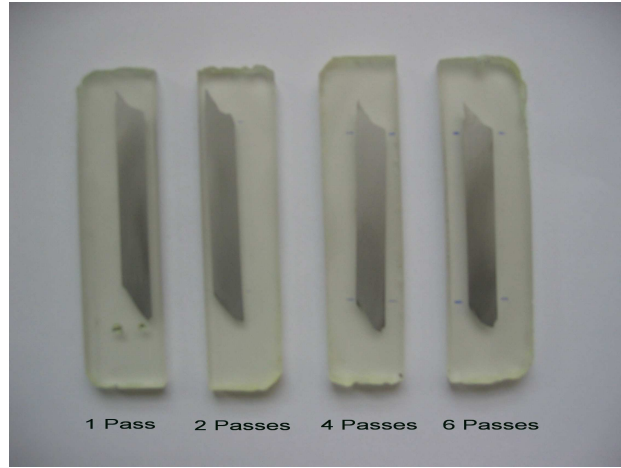


Fig. 3.4: Billets after sectioning, mounting and polishing.

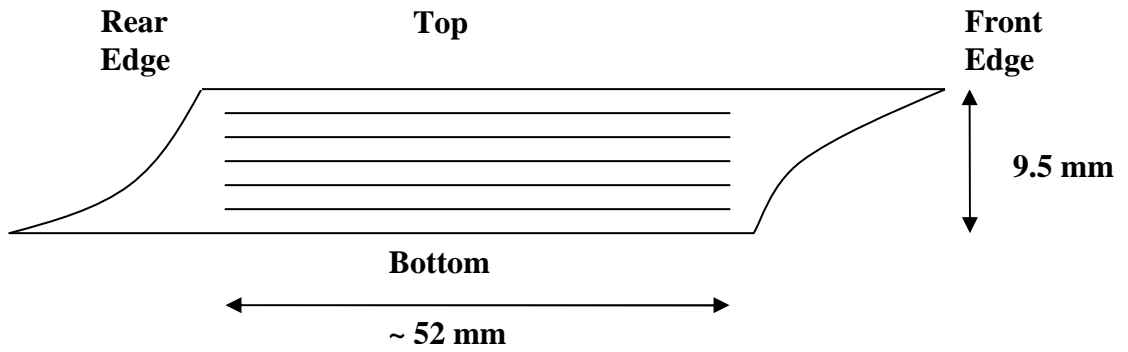


Fig. 3.5: The linear traverses used for taking microhardness measurements.

Microhardness measurements, H_v , were then recorded on the surface of each sample of the two groups using a Matsuzawa Seiki MHT-1 microhardness tester equipped with a Vickers indenter. For each measurement, a load of 300 gf was applied for a dwell time of 15 s. For the first group, five traverses were chosen at distances of 1.0 and 3.0 mm from the top surface, at the centre, and at distances of 1.0 and 3.0 mm from the bottom surface as shown in Fig. 3.5. The length of each traverse of these five traverses was 52 mm and the microhardness measurements were taken at an increment of 1.0 mm giving a total number of 52 data points for each traverse. So the total number of data points for each sample of this group was 260 data points. As illustrated in Fig. 3.5, all measurements were taken over a rectangular section in the centre of the surface avoiding the areas adjacent to the front and rear edges due to the

severe distortion of the billets at these areas. For the second group, the microhardness measurements were taken on the cross-sectional plane with an increment of 1.0 mm between the data points through Y and Z axes giving a total number of 57 data points for each sample.

The individual microhardness measurements were then plotted against the X axis for the first group and against the Y axis for the second group. For the first group, the individual measurements were plotted in the form of colour-coded contour maps to show the variation of hardness along the longitudinal plane then it was plotted as a three-dimensional representation. For the second group, the individual measurements were plotted in the form of colour-coded contour maps to show the variation of hardness over the cross-sectional area. The microhardness of the alloy in the as-received unpressed condition was measured and recorded in the graphs to provide a comparison with the as-pressed billets.

3.3 Experimental Results

In this investigation, the values of the Vickers microhardness measurements, H_v , were recorded on both the vertical longitudinal plane and the transverse plane. For the vertical longitudinal plane, five separate traverses were recorded for each sample, as shown in Fig. 3.5. These traverses are located at 1.0 and 3.0 mm from the top surface, the centre, and at 1.0 and 3.0 mm from the bottom surface. For each traverse there was a total of approximately 52 individual measurements which gave a total number of 260 data points for each vertical longitudinal plane. For the transverse plane, the microhardness measurements were taken with an increment of 1.0 mm between the data points through Y and Z axes giving a total number of 57 data points for each transverse plane. For simplicity, only three traverses were recorded on each plane. These traverses were located at 1.0 mm from the top surface, the centre traverse, and the traverse located at 1.0 mm from the bottom surface.

Fig. 3.6 shows the individual microhardness measurements recorded along the longitudinal axis after ECAP for one pass, two passes, four passes, and six passes along (a) the traverse located at 1.0 mm from the top surface, (b) the central traverse, and (c) the traverse located at 1.0 mm from the bottom surface, respectively. The microhardness measurements for the as-received unpressed alloy are also shown and the front edge of the billets lies on the right of the graphs. As shown in Fig. 3.6, the hardness increases after processing by ECAP through one pass from an initial value of ~25 to values larger than ~42 for all traverses which is an increment of ~70% from the initial hardness. The hardness values at the central traverse after one pass are larger than 50 which is ~100% of the initial hardness. The hardness at the central traverse is larger than that near the top surface which is in turn larger than that near the bottom surface. The hardness continues to increase by smaller amounts in the subsequent passes. The hardness values after ECAP through six passes are larger than 47 for all traverses, even close to the bottom surface, which is ~90% of the initial hardness. The hardness values near the top surface ranging from ~44 after one pass to ~54 after six passes. These values ranging from ~40 after one pass to ~52 after six passes near the bottom surface, where it is ranging from ~50-56 at the central traverse. As shown in Fig. 3.6, the hardness measurements along all traverses are consistent especially along the central traverse.

Fig. 3.7 shows the individual microhardness measurements along the longitudinal axis for the ECAP after (a) one pass, (b) two passes, (c) four passes, and (d) six passes, respectively. The microhardness measurements for the as-received unpressed alloy are also shown and the front edge of the billets lies on the right of the graphs. As mentioned previously from Fig. 3.6, Fig. 3.7(a) also shows that the microhardness increased after one pass from 25 to ~50 at the centre traverse of the billet which is an increment of ~100% from the initial hardness. The microhardness near the top surface showed lower values where the microhardness was ~45 and it was lower near the bottom surface where it was ~42. The microhardness values increased by smaller amounts after two passes for all traverses and this small increasing continues after four passes and after six passes as shown in Figs. 3.7(b), (c), and (d). After six passes, the lower values of microhardness at the area near the top surface are not evident while the lower values of microhardness at the area near the bottom surface are still evident, although it becomes less evident. The difference between the

microhardness values at the centre traverse and the traverses near the top and bottom surfaces decreased after six passes and the homogeneity of the microhardness of the alloy increased.

Fig. 3.8 shows the colour-coded contour maps of the microhardness measurements along the vertical longitudinal plane of the billets after ECAP for (a) one pass, (b) two passes, (c) four passes and (d) six passes, respectively. The significance of the colours is shown by the scale lying on the right of the figures where the increments of the microhardness values are 2 and the front edge of the billets lying on the right. In these figures, the bottom axis represents the *X* component and the vertical axis represents the *Z* component and the microhardness measurements were recorded along the *Y* plane. After ECAP for one pass, as shown in Fig. 3.8(a), the microhardness measurements are consistent on the *X* axis but on the *Z* axis the variation of the microhardness measurements are clearly evident and the values ranging between ~40 near the top and bottom surfaces and ~52 at the centre of the billet. There are regions of lower microhardness near the top and bottom surfaces of the billet, although the region near the bottom surface is bigger. After ECAP for two passes, as shown in Fig. 3.8(b), the region of lower microhardness near the top surface disappeared while that near the bottom surface is still visible although it becomes less evident. The microhardness measurement along the *X* axis is still consistent. After ECAP for two and four passes, as shown in Figs. 3.8(b) and (c), the plots show that the microhardness measurements near the front edge are lower than that near the rear edge. The reason for this is due to the inherent back-pressure introduced when using a solid die. In the solid die configuration, the billet remains in the die after pressing and each billet will be pressed against the preceding billet which causes a back pressure on the pressed billet. This variation continues after ECAP for six passes, as shown in Fig. 3.8(d), although it becomes less evident. After ECAP for six passes, as shown in Fig. 3.8(d), the microhardness measurements are homogeneous over the surface of the billet and the microhardness values ranging between ~50 and ~56 except the region of lower microhardness within a distance of ~1.0 mm near the bottom surface and mainly toward the front edge of the billet.

Fig. 3.9 shows the three dimensional representations of the microhardness measurements after ECAP for (a) one pass, (b) two passes, (c) four passes, and (d)

six passes, respectively. The plots record the microhardness values against the X and Z axes. The significance of the colours is shown by the scale lying on the right of the figures where the increments of the microhardness values are 5. In these graphs, the top surface lies to the right and the front edge lies at the far edge from the viewer. After ECAP for one pass, as shown in Fig. 3.9(a), the regions near the top and bottom surfaces show lower microhardness values than the regions away from these surfaces. With increasing number of passes, as shown in Figs. 3.9(b), (c), and (d), the region of lower microhardness values near the top surface disappeared while that near the bottom surface is still evident, although it becomes less evident. After ECAP for six passes, as shown in Fig. 3.9(d), the microhardness values becomes homogeneous except the small region near the bottom surface.

Fig. 3.10 shows the individual microhardness measurements recorded on the cross-sectional planes for the ECAP after (a) one pass, (b) two passes, (c) four passes, and (d) six passes, respectively. The graphs show the microhardness measurements of three lines only for simplicity; the line located at 1.0 mm from the top surface, the line at the centre, and the line located at 1.0 mm from the bottom surface. The microhardness measurements for the as-received unpressed alloy are also shown in the graphs for comparison. After ECAP for one pass, as shown in Fig. 3.10(a), the microhardness measurements increased from an initial value of ~ 25 to values larger than ~ 44 which is an increment of $\sim 75\%$ from the initial hardness. The microhardness values at the centre line are larger than the values near the top and bottom surfaces. At the centre line, the hardness increased as the distance from the edges increased then it decreased at the centre of the billet. The reason for this decrease is unknown. This decrease becomes less evident with increasing number of passes, as shown in Figs. 3.10(b), (c), and (d). The hardness continues to increase by small amounts in the subsequent passes and the surface becomes more homogeneous after six passes, as shown in Fig. 3.10(d).

Fig. 3.11 shows the colour-coded contour maps of the microhardness measurements along the cross-sectional plane of the billets after ECAP for (a) one pass, (b) two passes, (c) four passes and (d) six passes, respectively. The significance of the colours is shown by the scale lying on the right of the figures where the increments of the microhardness values are 2. After ECAP for one pass, as shown in Fig.

3.11(a), the hardness was low near the top and bottom surfaces and at the centre of the billet. The hardness increased with increasing number of passes, as shown in Figs. 3.11(b), (c), and (d), and the low hardness regions near the top and bottom surfaces and at the centre of the billet became less evident and the surface became more homogeneous.

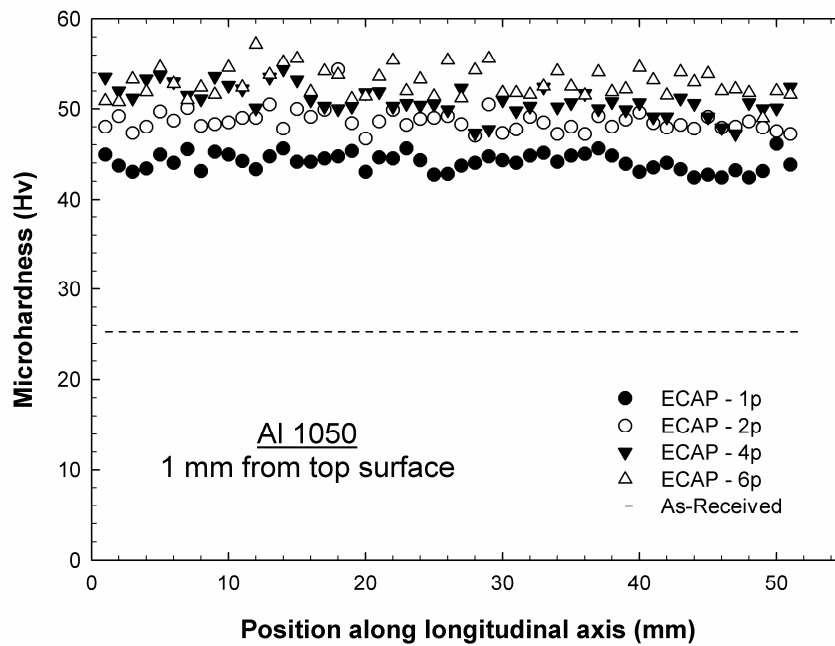


Fig. 3.6(a): Individual measurements of the microhardness, Hv, recorded along the vertical longitudinal plane at 1.0mm from the top surface after 1, 2, 4, and 6 passes. The front edge lies on the right of the graphs.

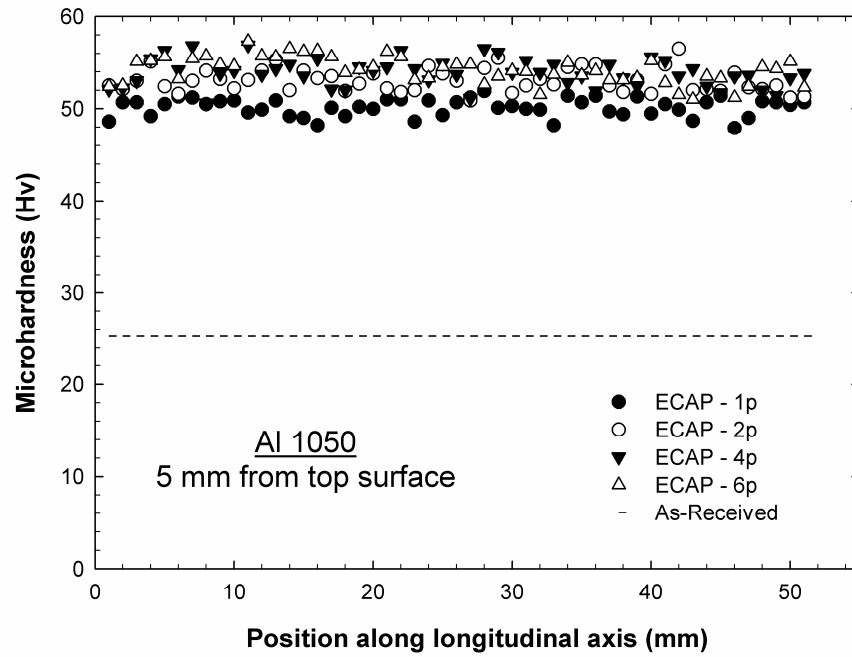


Fig. 3.6(b): Individual measurements of the microhardness, Hv, recorded along the vertical longitudinal plane at the centre traverse after 1, 2, 4, and 6 passes. The front edge lies on the right of the graphs.

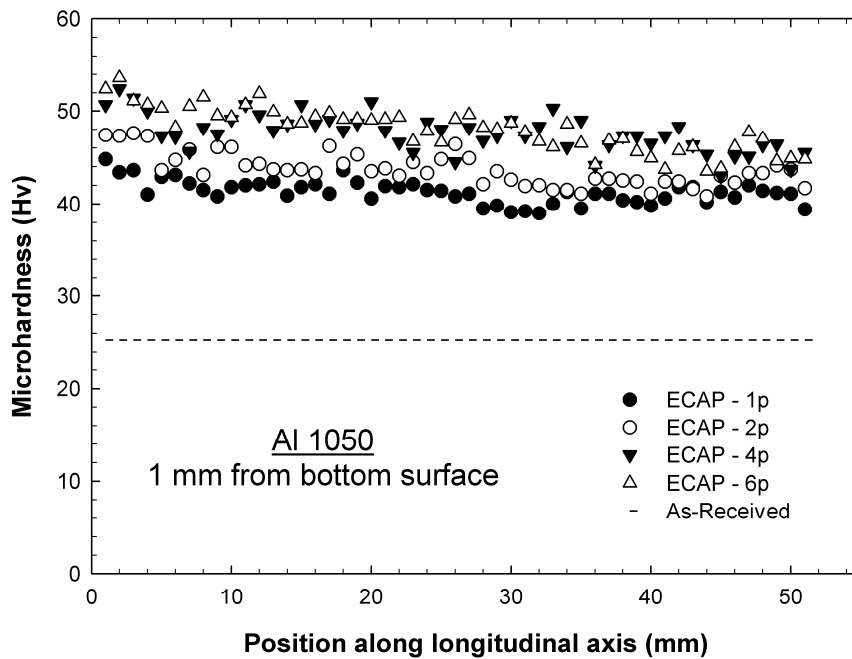


Fig. 3.6(c): Individual measurements of the microhardness, Hv, recorded along the vertical longitudinal plane at 1.0mm from the bottom surface after 1, 2, 4, and 6 passes. The front edge lies on the right of the graphs.

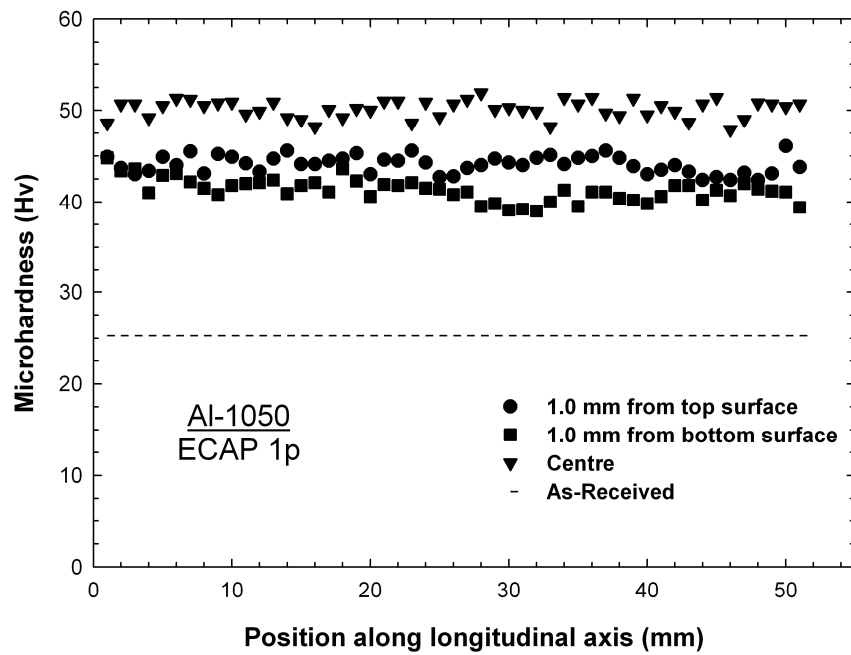


Fig. 3.7(a): Individual measurements of the microhardness, Hv, recorded along the vertical longitudinal plane at the central traverse and the traverses at 1.0mm from the top and bottom surfaces after one pass. The front edge lies on the right of the graphs.

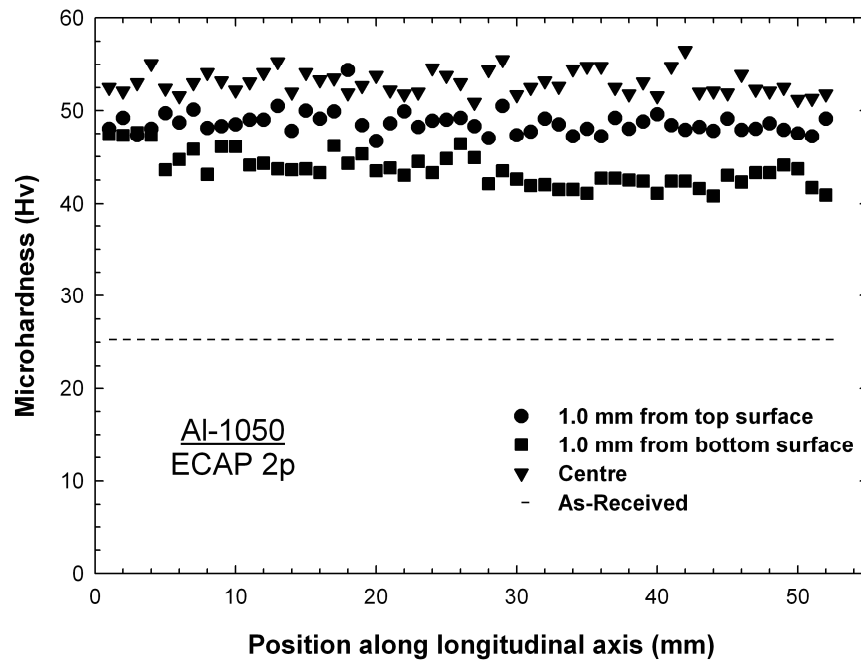


Fig. 3.7(b): Individual measurements of the microhardness, Hv, recorded along the vertical longitudinal plane at the central traverse and the traverses at 1.0mm from the top and bottom surfaces after two passes. The front edge lies on the right of the graphs.

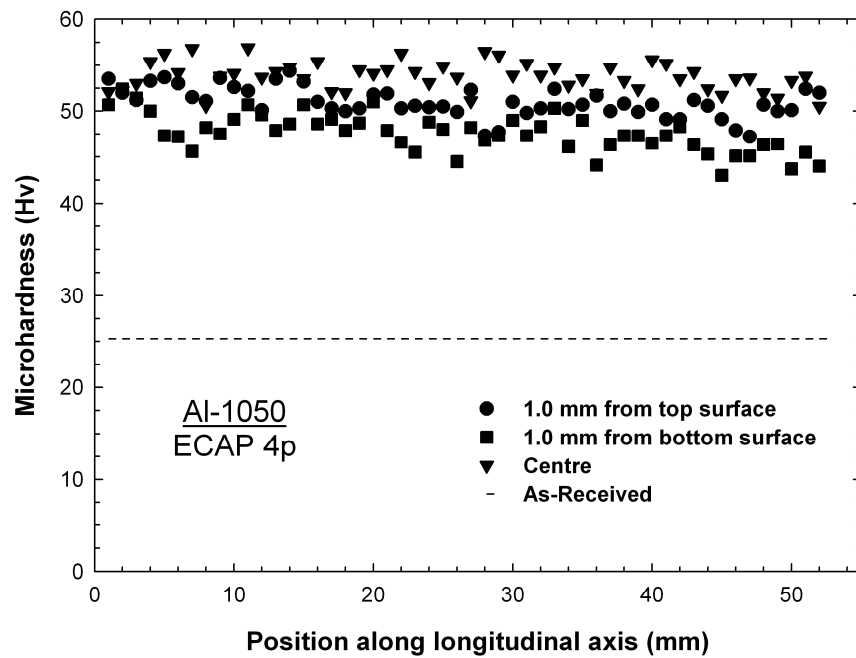


Fig. 3.7(c): Individual measurements of the microhardness, Hv, recorded along the vertical longitudinal plane at the central traverse and the traverses at 1.0mm from the top and bottom surfaces after four passes. The front edge lies on the right of the graphs.

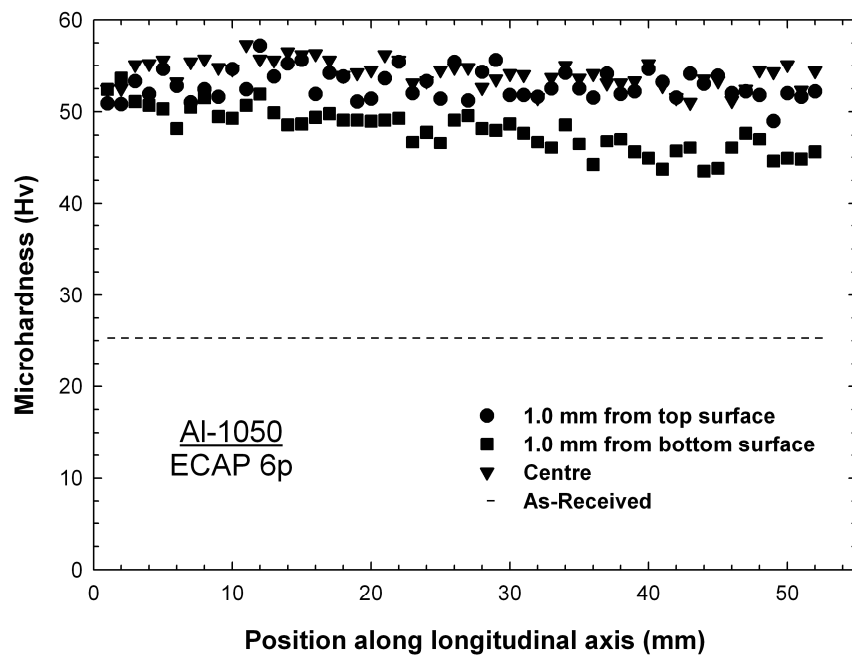


Fig. 3.7(d): Individual measurements of the microhardness, Hv, recorded along the vertical longitudinal plane at the central traverse and the traverses at 1.0mm from the top and bottom surfaces after six passes. The front edge lies on the right of the graphs.

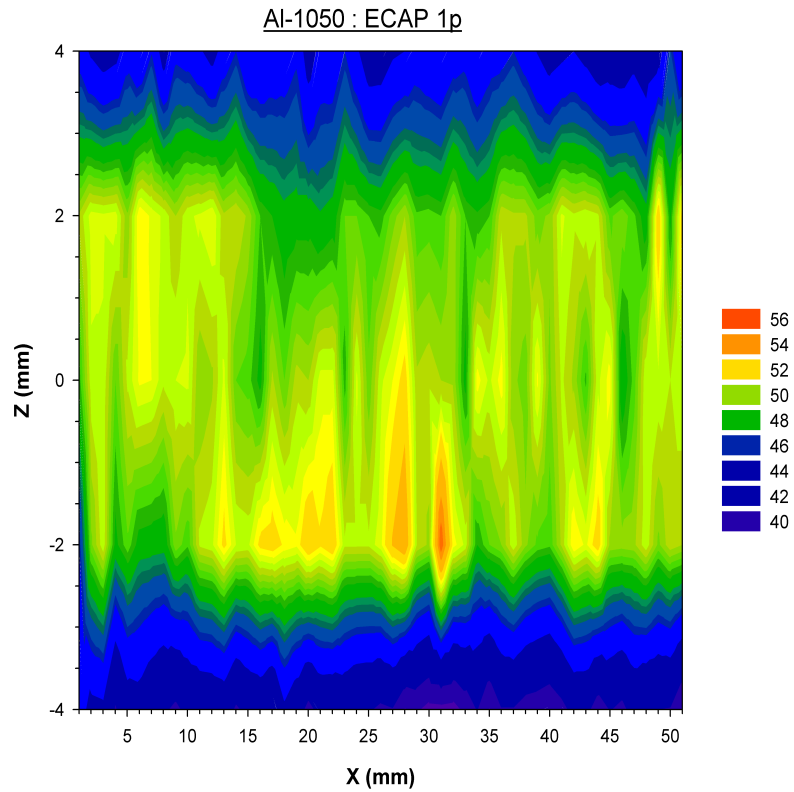


Fig. 3.8(a): Colour-coded contour map of the microhardness, Hv, recorded along the vertical longitudinal plane after one pass: the significance of the colours is shown on the right. The front edge lies on the right of the figure.

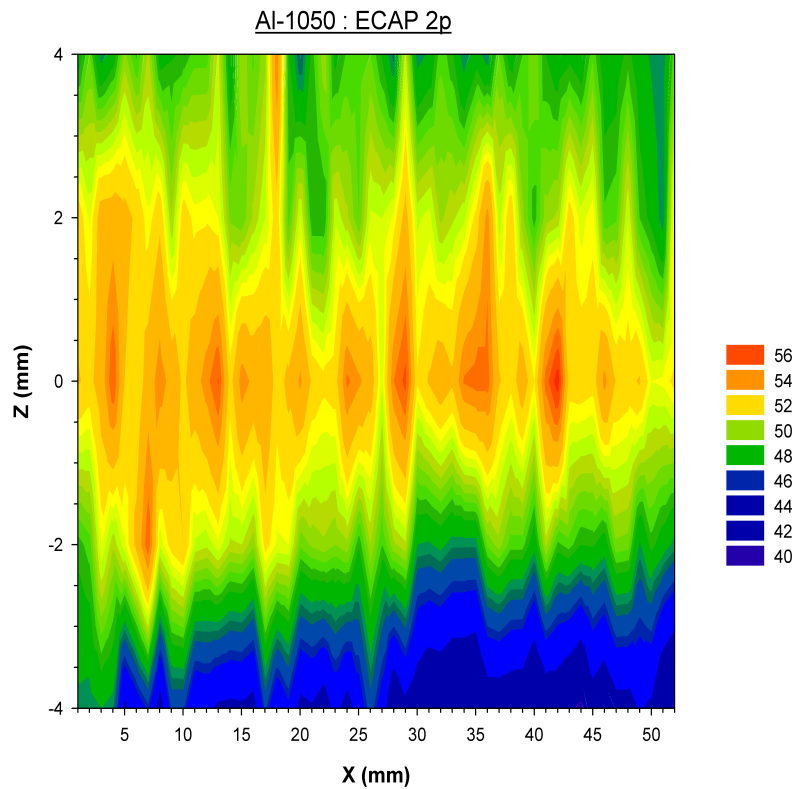


Fig. 3.8(b): Colour-coded contour map of the microhardness, Hv, recorded along the vertical longitudinal plane after two passes: the significance of the colours is shown on the right. The front edge lies on the right of the figure.

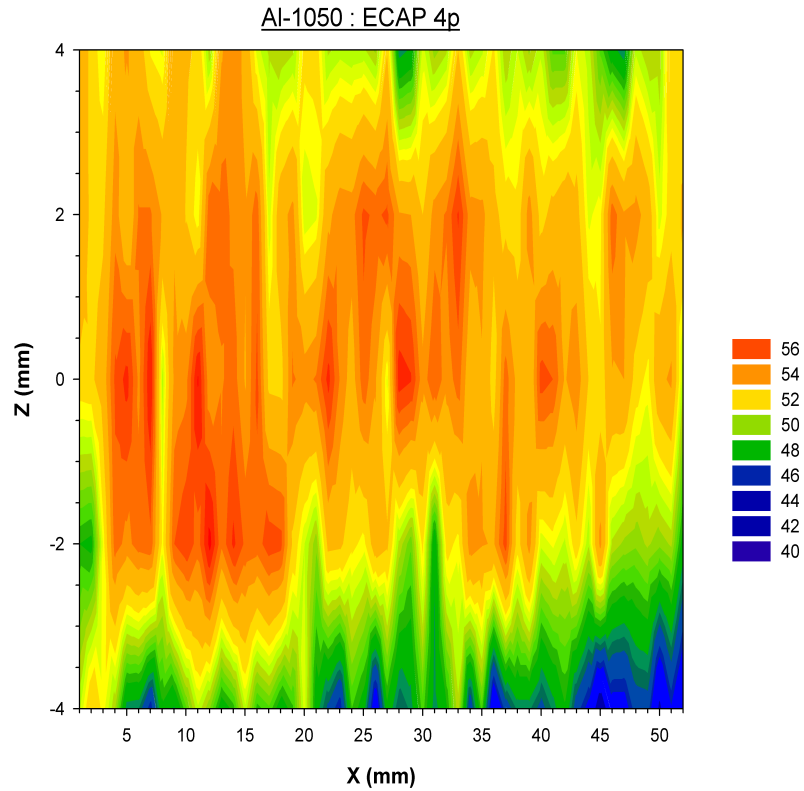


Fig. 3.8(c): Colour-coded contour map of the microhardness, Hv, recorded along the vertical longitudinal plane after four passes: the significance of the colours is shown on the right. The front edge lies on the right of the figure.

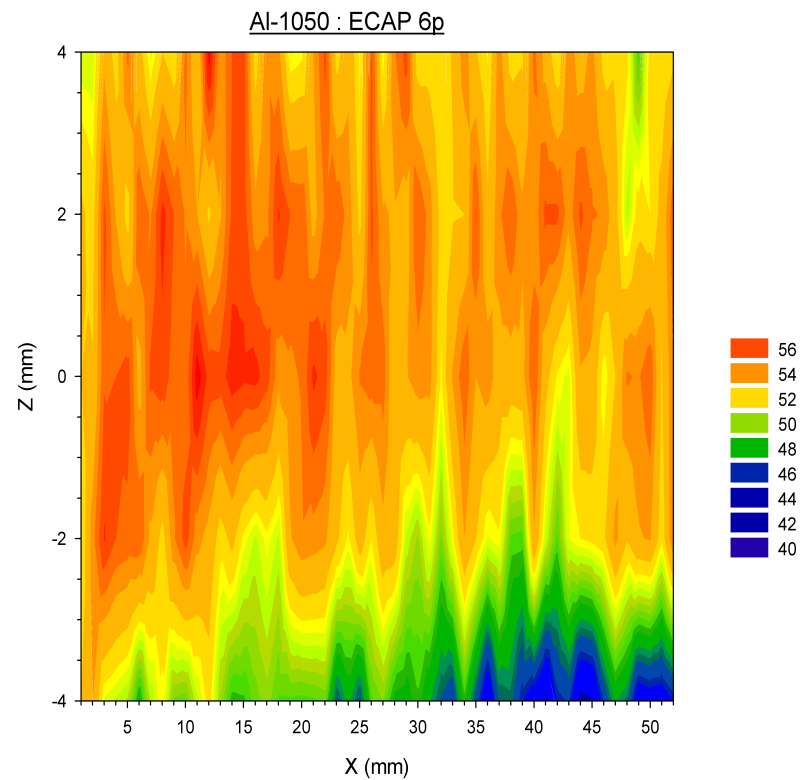


Fig. 3.8(d): Colour-coded contour map of the microhardness, Hv, recorded along the vertical longitudinal plane after six passes: the significance of the colours is shown on the right. The front edge lies on the right of the figure.

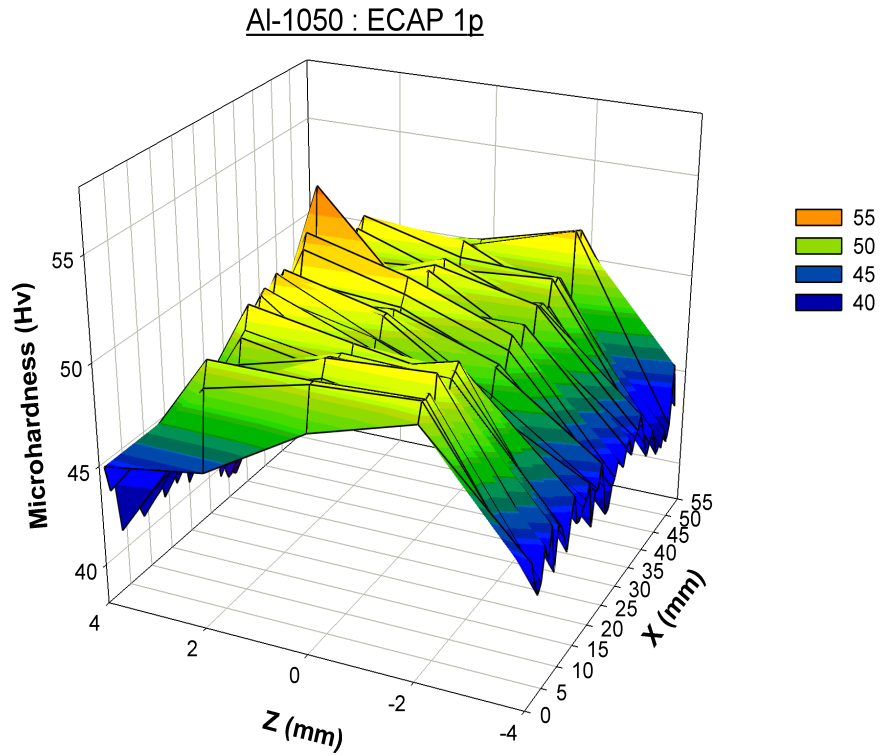


Fig. 3.9(a): Three-dimensional representation of the microhardness measurements, Hv, along the vertical longitudinal plane after one pass: the significance of the colours is shown on the right.

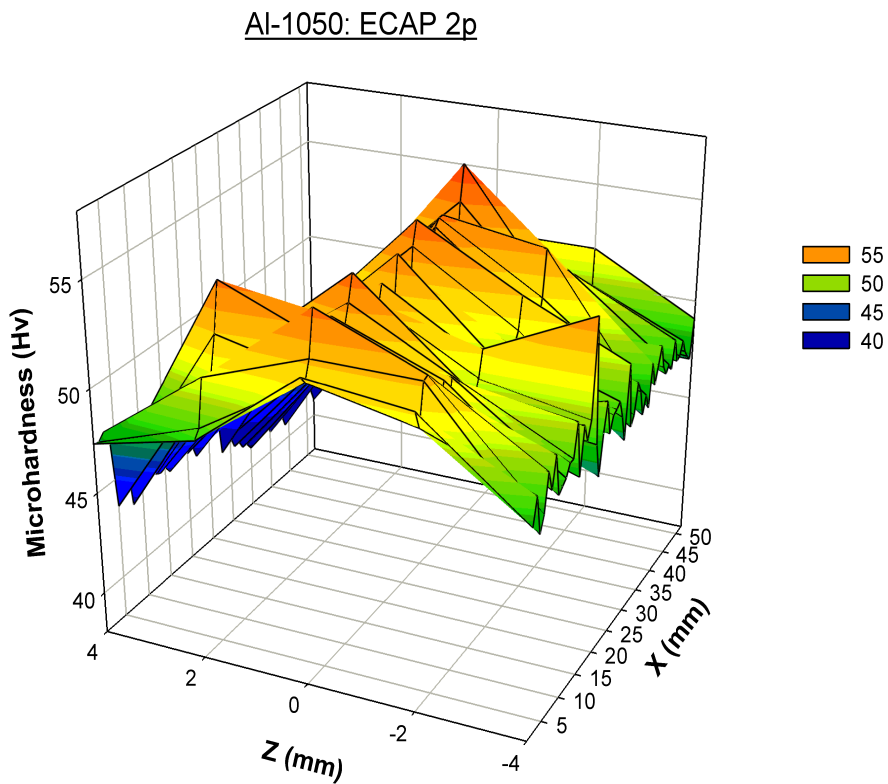


Fig. 3.9(b): Three-dimensional representation of the microhardness measurements, Hv, along the vertical longitudinal plane after two passes: the significance of the colours is shown on the right.

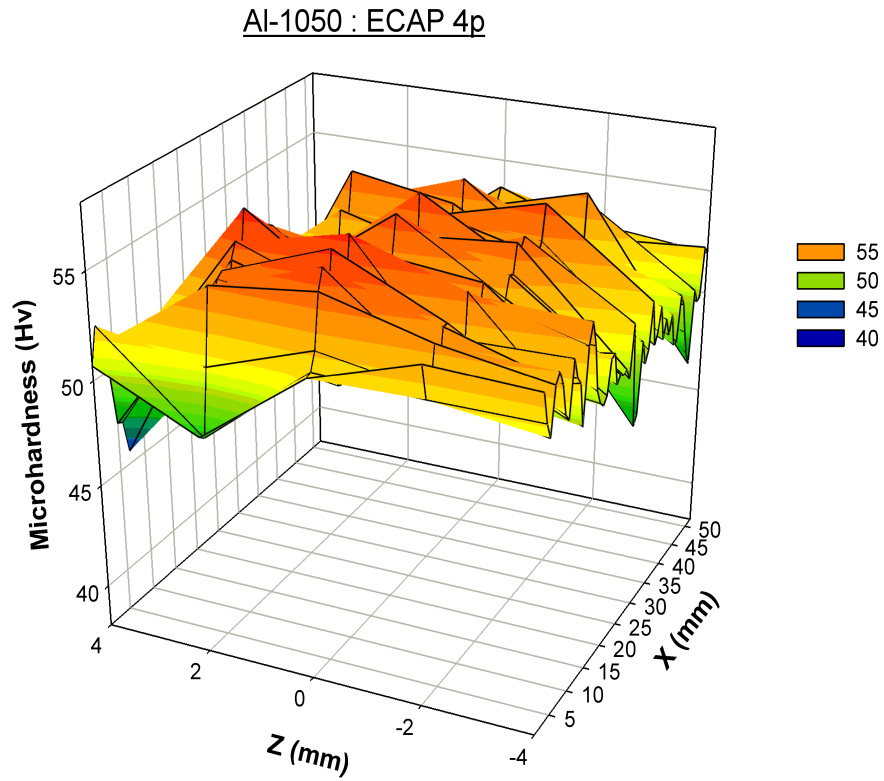


Fig. 3.9(c): Three-dimensional representation of the microhardness measurements, Hv, along the vertical longitudinal plane after four passes: the significance of the colours is shown on the right.

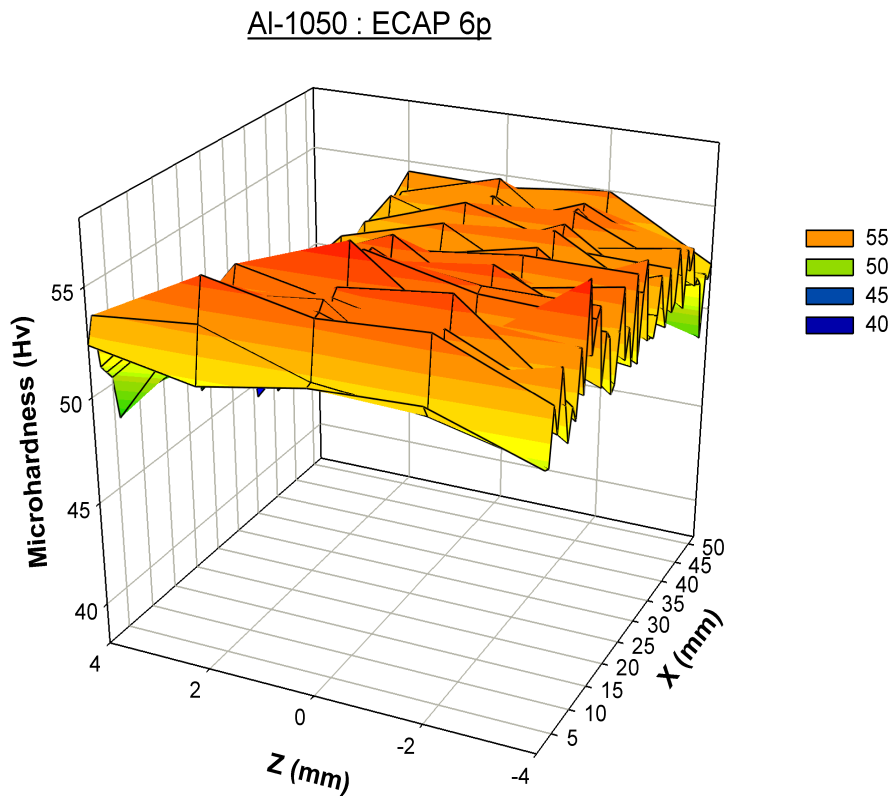


Fig. 3.9(d): Three-dimensional representation of the microhardness measurements, Hv, along the vertical longitudinal plane after six passes: the significance of the colours is shown on the right.

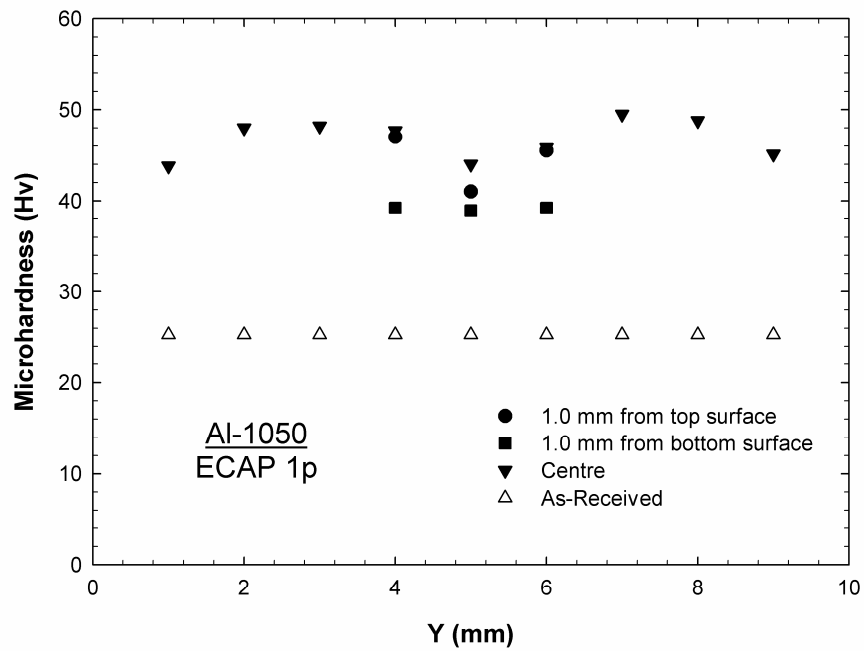


Fig. 3.10(a): Individual measurements of the microhardness, Hv, recorded on the cross-sectional plane along the central traverse and the traverses at 1.0mm from the top and bottom surfaces after one pass.

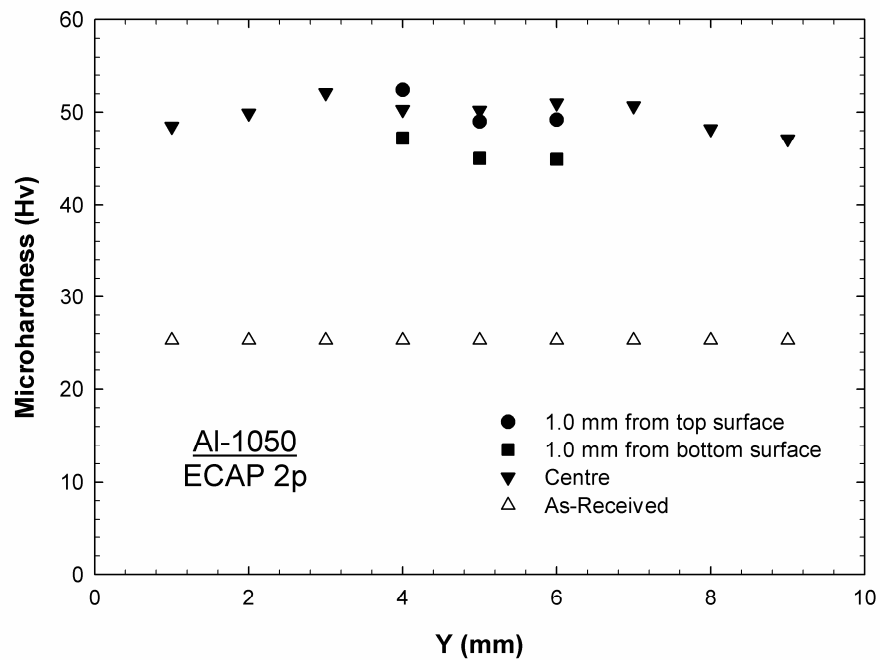


Fig. 3.10(b): Individual measurements of the microhardness, Hv, recorded on the cross-sectional plane along the central traverse and the traverses at 1.0mm from the top and bottom surfaces after one pass.

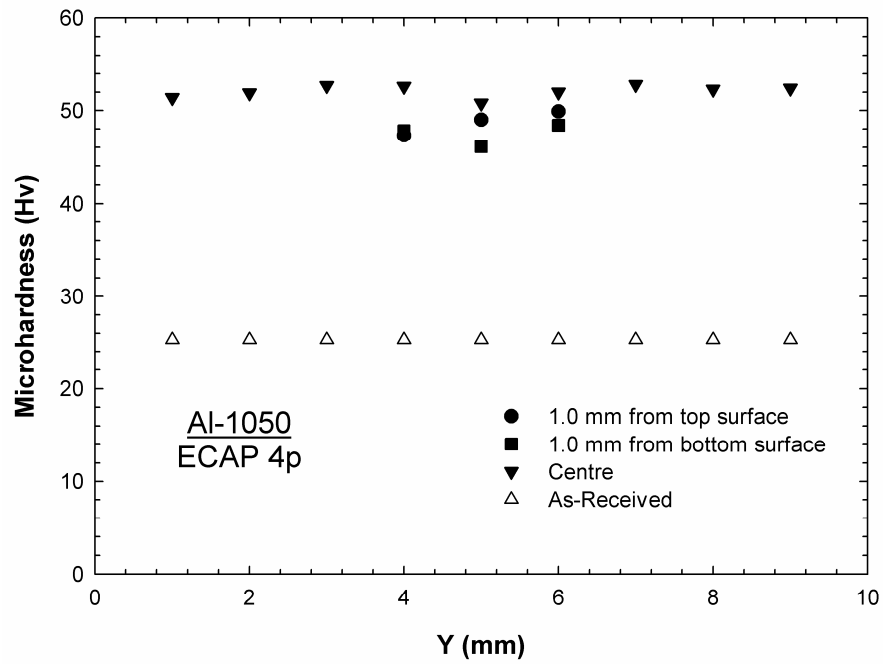


Fig. 3.10(c): Individual measurements of the microhardness, Hv, recorded on the cross-sectional plane along the central traverse and the traverses at 1.0mm from the top and bottom surfaces after one pass.

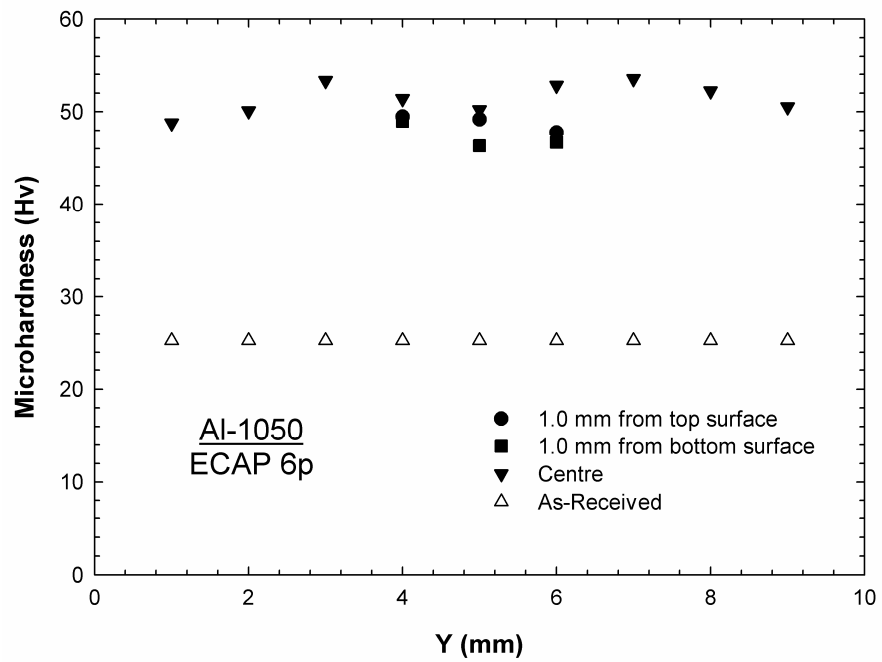


Fig. 3.10(d): Individual measurements of the microhardness, Hv, recorded on the cross-sectional plane along the central traverse and the traverses at 1.0mm from the top and bottom surfaces after one pass.

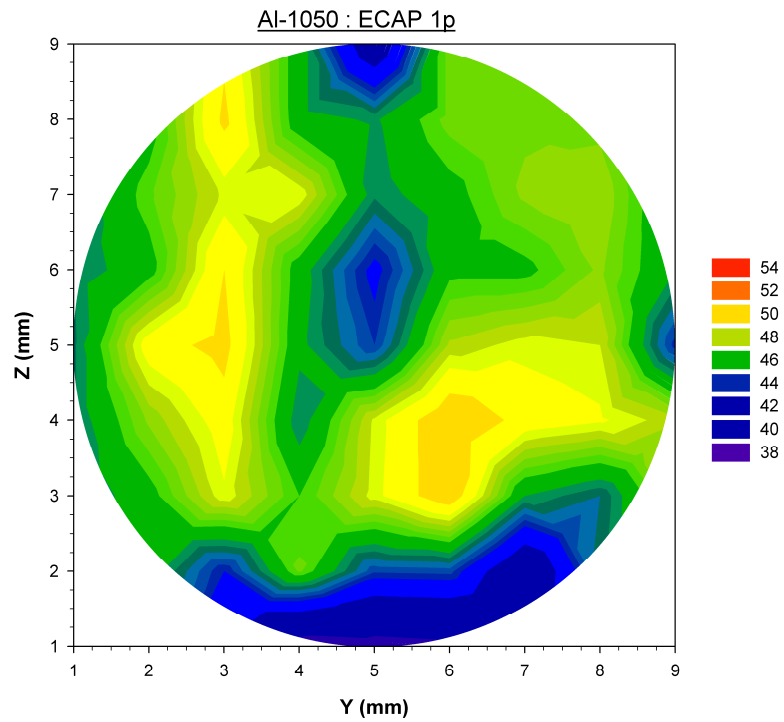


Fig. 3.11(a): Colour-coded contour map of the microhardness, Hv, along the cross-sectional plane after one pass: the significance of the colours is shown on the right.

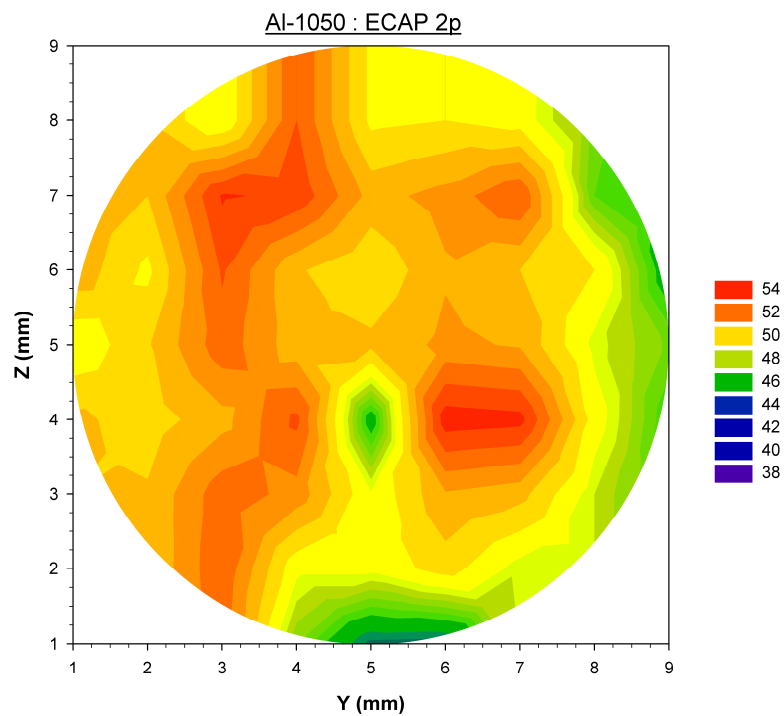


Fig. 3.11(b): Colour-coded contour map of the microhardness, Hv, along the cross-sectional plane after two passes: the significance of the colours is shown on the right.

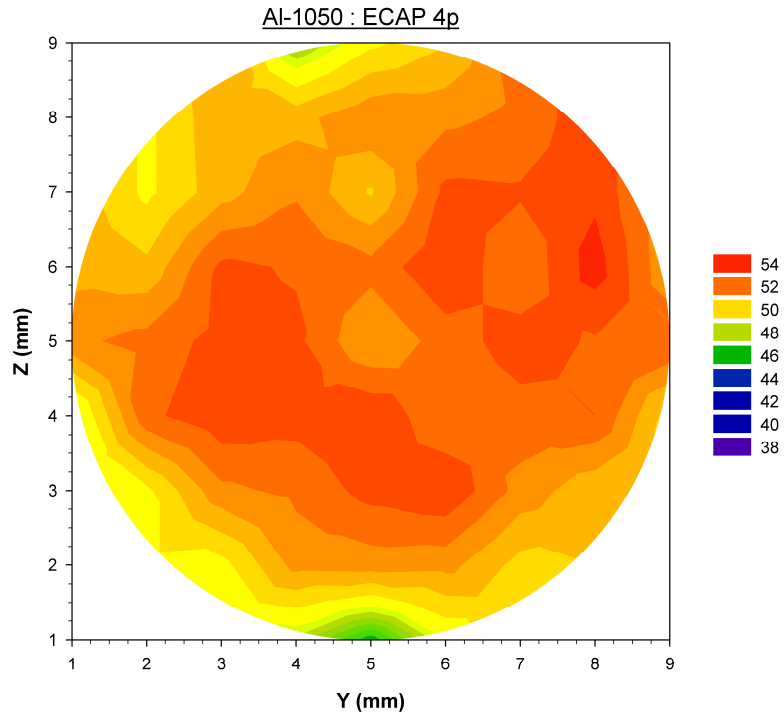


Fig. 3.11(c): Colour-coded contour map of the microhardness, Hv, along the cross-sectional plane after four passes: the significance of the colours is shown on the right.

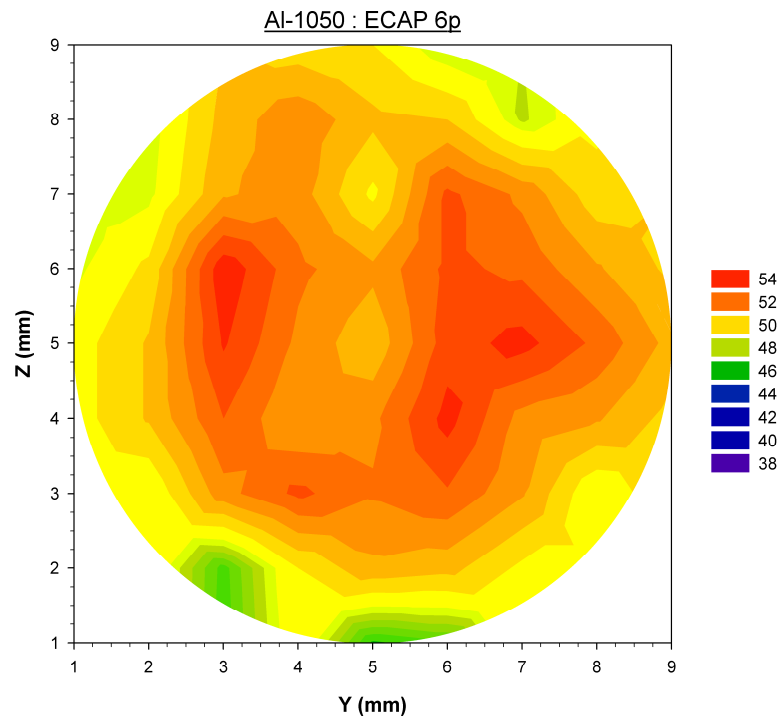


Fig. 3.11(d): Colour-coded contour map of the microhardness, Hv, along the cross-sectional plane after six passes: the significance of the colours is shown on the right.

3.4 Discussion

As suggested previously in various reports [52,78,95,103], the microhardness measurements reveal the internal microstructure of metal alloys. The most important conclusion of the present investigation is that the microhardness measurements of Al-1050 alloy on both the vertical longitudinal plane and the cross-sectional plane become homogeneous after six passes. Hence, the internal microstructure for Al-1050 alloy become homogeneous after sufficient number of passes, e.g. six passes, of ECAP using a pressing speed of 0.5 mm/s and processing route B_C.

In the present investigation, the number of the individual microhardness measurements used was very large, i.e. approximately 260 individual measurements on each vertical longitudinal plane and 57 individual measurements on each cross-sectional plane. This number of individual measurements minimized the error in the investigation results. Before starting the experiments, all billets were well-lubricated to minimize the frictional effect between the billets and the die wall. As stated in previous study, the friction between the billets and the die wall has minor effect on the well-lubricated billets [108].

As in all other ECAP studies, the present investigation showed that most of the increase in the microhardness measurements is achieved after the first pass. Although, the microhardness values and hence the internal microstructure is not homogeneous after this pass. With increasing number of passes, up to six passes for Al-1050 alloy, the increase in the microhardness is relatively small but on the other hand the increase in the homogeneity is large. The additional pressing is a key factor in increasing the homogeneity of the microhardness values and hence the internal microstructure, although the increase in the microhardness values is relatively small. This result proves that the ECAP technique, if it is used for a sufficient number of passes, can be incorporated successfully in the continuous processing techniques for the production of metal sheets or wires.

The microhardness values recorded near the top and bottom surfaces after one pass are lower than the average. This is more evident for the bottom surface. With

increasing number of passes, the lower microhardness measurements near the top surface stops and that near the bottom surface continues, although it becomes less evident. The reason for forming of the lower hardness area near the bottom surface was the lack of contact between the billet and the channel at the outer arc of curvature and the formation of a gap at that area. It was shown in previous reports that a gap is formed and a dead zone is initiated in the die at the area of the outer arc when using a die having arc angle (ψ) of 0° [22-24,105]. It was shown previously that there is no effect for changing the arc angle from 0° to 20° on the homogeneity of hardness measurements and the dead zone was formed at a die having arc angle of 20° [109]. Previous study showed that the size of the corner gap between the billet and the die depend on the strain hardening rate of the billet material [110]. It was shown that the corner gap in materials with higher strain hardening rate is bigger. The hardening rate decreases with increasing applied total strain and this lead to decrease in size of the corner gap and hence the size of the lower hardness area near the bottom surface. This is clearly shown in the colour-coded maps where the area of lower hardness decreases with increasing number of turns. The lack of contact and the gap formation between the upper surface of the billet and the die was noticed in many finite element analysis researches [105, 111].

After six passes, which was the maximum number of passes used in this investigation, the microhardness values and hence the internal microstructure became homogeneous except the small distance near the bottom surface especially toward the front edge of the billet. The decrease in the hardness near the front edge is due to the inherent back-pressure which is introduced to the billet when it is pressed against the preceding billet which stays in the die after pressing. The inherent back pressure is introduced on the pressed billet while the front of the billet passes through the angle of the die. After approximately pressing half of the billet, the preceding billet passes the smaller diameter of the exit portion of the channel to the higher diameter of the exit portion and the back-pressure become zero. Previous study shows that the lower hardness region near the bottom surface increases with increasing back-pressure [103].

The results demonstrated in the present investigation are consistent with the results demonstrated in previous studies for the cross-sectional planes of Al-6061 alloy [52] and for the vertical longitudinal planes of Al-6061 alloy [53].

3.5 Summary and Conclusions

1. Microhardness measurements were recorded along the vertical longitudinal planes and the cross-sectional planes of Al-1050 alloy billets after pressing by ECAP through 1, 2, 4 and 6 passes at a pressing speed of 0.5 mm/s using route B_C.
2. 260 data points were taken on each vertical longitudinal plane and 57 data points were taken on each cross-sectional plane after processing by ECAP. Using of this large numbers of individual microhardness measurements of Hv minimized the error in the results.
3. There is a significant increase in the average microhardness measurements, reaching approximately 70%, after ECAP pressing through one pass, although there are regions of lower hardness near the top and bottom surfaces due to the lack of contact between the billet and the die at the inner and outer corners at the die angle. There are additional but smaller increases in hardness in subsequent passes.
4. Good homogeneity in the hardness was achieved after processing by ECAP through six passes throughout the vertical longitudinal plane and the cross-sectional plane although the region of the lower hardness near the bottom surface remains, especially towards the front edge, but it was less evident while the region of lower hardness near the top surface disappeared.
5. These results prove that the ECAP technique can be incorporated successfully in the continuous processing techniques for the production of metal sheets or wires if it is used for a sufficient number of passes.

CHAPTER 4

STRAIN MEASUREMENTS BY CONVERGENT BEAM ELECTRON DIFFRACTION IN ALUMINIUM PROCESSED BY ECAP

4.1 Introduction

The location and nature of the internal stresses in the microstructure of strained metals has been the subject of considerable discussion for many years. The convergent beam electron diffraction (CBED) technique provides a quantitative tool in measuring the existence of these internal stresses by probing the grains to determine the changes in the lattice parameters [112-115]. For this TEM technique the microscope is operated in convergent beam nanoprobe mode in which convergent electron probes of several nanometers in diameter are focused onto the region of interest when the sample is oriented in a crystallographic zone axis at which a large number of sharp higher order Laue zone (HOLZ) lines are present in the CBED pattern. It is well known that such patterns can allow the determination of any lattice parameter changes that are associated with strains. The nature of the strain can be either inhomogeneously or homogeneously distributed in the regions of interest. Dislocation strain fields are an example of the former type where it is difficult to measure these strains quantitatively by using the HOLZ lines in CBED. On the other hand, homogeneous strains are associated with changes in lattice parameters and such changes can be measured from the changes in the position of the HOLZ lines in the CBED patterns for quite small levels of strain (e.g. 0.1% or even less). In addition, these lattice parameter changes can be associated with a distortion of the usual unit cell to one of a different Bravais lattice and this can be known from the broken symmetry in the HOLZ CBED pattern.

In the present investigation, the CBED HOLZ method was used to look for homogenous strains that may be present inside the grains and near grain boundaries in commercial purity aluminium (Al-1050) alloy processed by equal-channel angular pressing (ECAP) at room temperature.

4.2 Experimental Material and Procedures

A commercial purity aluminium alloy Al-1050 with a weight percent of at least 99.5% aluminium was used in the present experiments. The chemical composition of the alloy and the dimensions of the billets were illustrated in chapter 3. The ECAP experiments were described in detail in chapter 3. Billets were pressed repetitively for 2, 4 and 8 passes giving a maximum total strain of ~2, 4 and 8, respectively. All billets were pressed using a pressing speed of 0.5 mm/s and processing route B_C, in which the billet is rotated by 90° in the same direction between each consecutive pass [29]. After pressing, a disk was cut from the cross-sectional plane of each billet using 0.25 mm brass wire erosion with an electro-discharge machine. Another disk was cut from the material in the as-received condition. The thickness of the each disk was 0.8 mm and it was reduced to 0.2 mm by mechanical polishing using 1200 and 4000 grit. TEM samples having a diameter of 3.0 mm were cut from the centre of each disk. All TEM samples were electropolished with a twin jet electropolisher using a solution consisting of 30% HNO₃ + 70% Methanol and a voltage of 20-30 V. The temperature of the solution during the polishing process was ranging between -20°C and -30°C and the resulting polished surfaces were shiny. The TEM was conducted using a Philips EM 430 T transmission electron microscope (TEM) located at the University of Bristol. Photographs of the TEM facility are shown in Fig. 4.1. Convergent-beam electron diffraction (CBED) patterns on the <114> zone axis were taken for each sample and it was compared with simulated patterns. The patterns were taken at a temperature of ~80 K and at a voltage of 148.7 kV using a probe size of 20 nm. A JECP “Java Electron Crystallography Package” was used to find the simulated patterns. The package was designed and written by Dr. X.Z. Li from University of Nebraska-Lincoln at USA to study the crystalline structures by using electron diffraction [116]. To find the accurate voltage used in the experiment

which was 148.7 kV, the pattern from the material in the as-received condition was compared with the simulated pattern when the lattice parameter at the experiment temperature (80 K) was 0.40329 nm and all lattice angles were 90° [117].



Fig. 4.1: Photographs of the TEM facility located at the University of Bristol.

4.3 Experimental Results

4.3.1 Al-1050 in the as-received condition:

The microstructure of the Al-1050 alloy in the as-received condition consists from equiaxed grains having an average grain size of approximately $\sim 44 \mu\text{m}$. The material was free from dislocations inside the grains. The HOLZ pattern was taken from the centre of a grain. The lines of the pattern were sharp, as shown in Fig. 4.2 where the observed HOLZ pattern is compared to the simulated pattern. As shown in the figure, the symmetry was preserved in the centre of a grain from the material in the as-received condition. The symmetry continued when probing the grain from the centre to the grain boundary by 20 nm steps which was the probe size. The lattice parameters used in the simulation to get the same pattern as in the observed one were: $a = b = c = 0.40329 \text{ nm}$ and $\alpha = \beta = \gamma = 90^\circ$. This pattern was considered as the reference pattern for the other patterns taken from the samples after ECAP through two, four and eight passes.

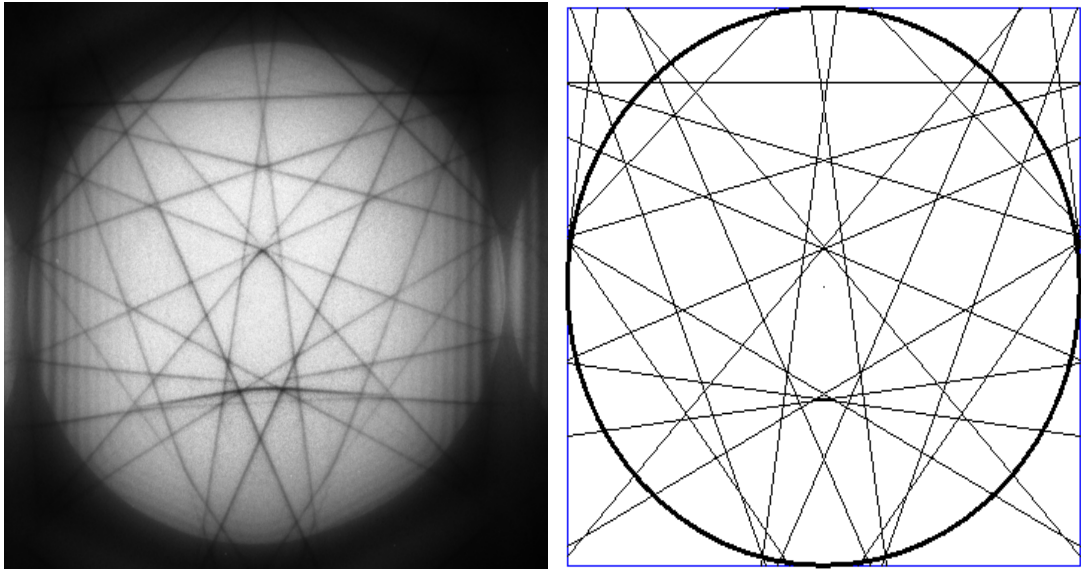


Fig. 4.2: The observed and the simulated HOLZ patterns taken from the material in the as-received condition.

4.3.2 Al-1050 after ECAP through two passes:

After ECAP through two passes, the microstructure consists of elongated low-angle subgrain boundaries with relatively few dislocations present within the subgrains. These elongated grains had average widths of approximately $\sim 0.66 \mu\text{m}$ and lengths of approximately $\sim 1.0 \mu\text{m}$. A micrograph taken from a region oriented approximately at right angle to the direction of ECAP is shown in Fig. 4.3. Two patterns were taken from the sample after ECAP through two passes. One at the centre of a grain and one near the grain boundary. At the centre of the grain, as shown in Fig. 4.4, the lines of the HOLZ pattern were sharp to some extent but they were less sharp than the pattern of the as-received condition. As noticed from the figure, the symmetry of the pattern was preserved. The observed HOLZ pattern was compared to the simulated pattern which was used in the as-received condition with the same lattice parameters and they were identical. The lattice parameters were: $a = b = c = 0.40329 \text{ nm}$ and $\alpha = \beta = \gamma = 90^\circ$.

The observed pattern near a grain boundary shows a break in the symmetry. Fig. 4.5 shows the observed and the simulated patterns near the grain boundary of a grain taken from the billet which was pressed by ECAP through two passes. It is noticed from the figure that the lines of the observed pattern were reasonably sharp and the two patterns are in good agreement. The arrows in Fig. 4.5 show the shift of the intersection of the two lines towards the left by the same amount for the observed and the simulated patterns. In the simulated pattern, the lattice parameter c was reduced from 0.40329 nm to 0.40289 nm which indicates a compression strain of approximately 0.1% . In addition, the angles α and β were changed to 89.95° and 90.05° , respectively. This change in the angles indicates a shear strain of approximately 0.044% and -0.044% , respectively. The other three parameters were set to $a = b = 0.40329 \text{ nm}$ and $\gamma = 90^\circ$.

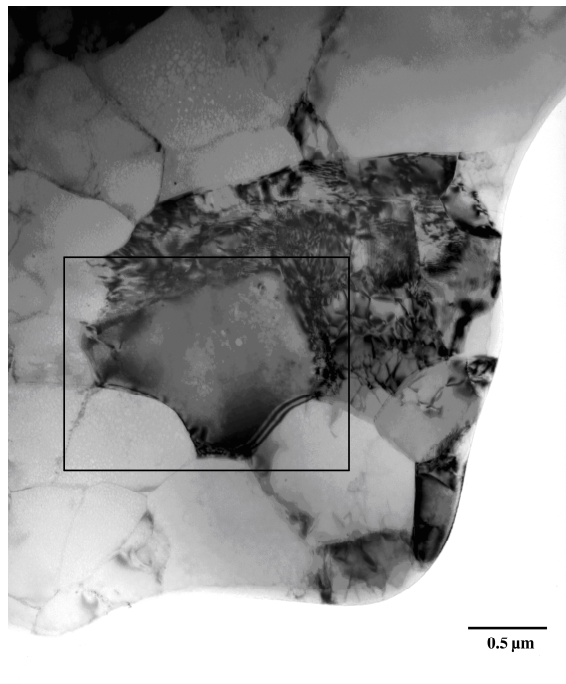


Fig. 4.3: TEM image of the grain used for acquiring the HOLZ patterns from the billet processed by ECAP through 2 passes.

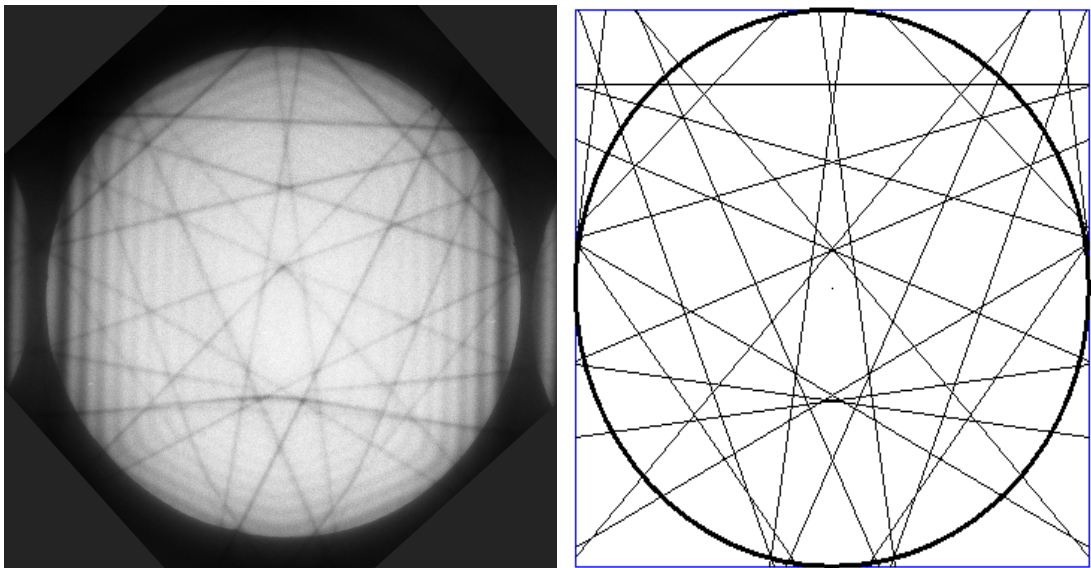


Fig. 4.4: The observed and the simulated HOLZ patterns taken from the centre of the grain after ECAP through two passes.

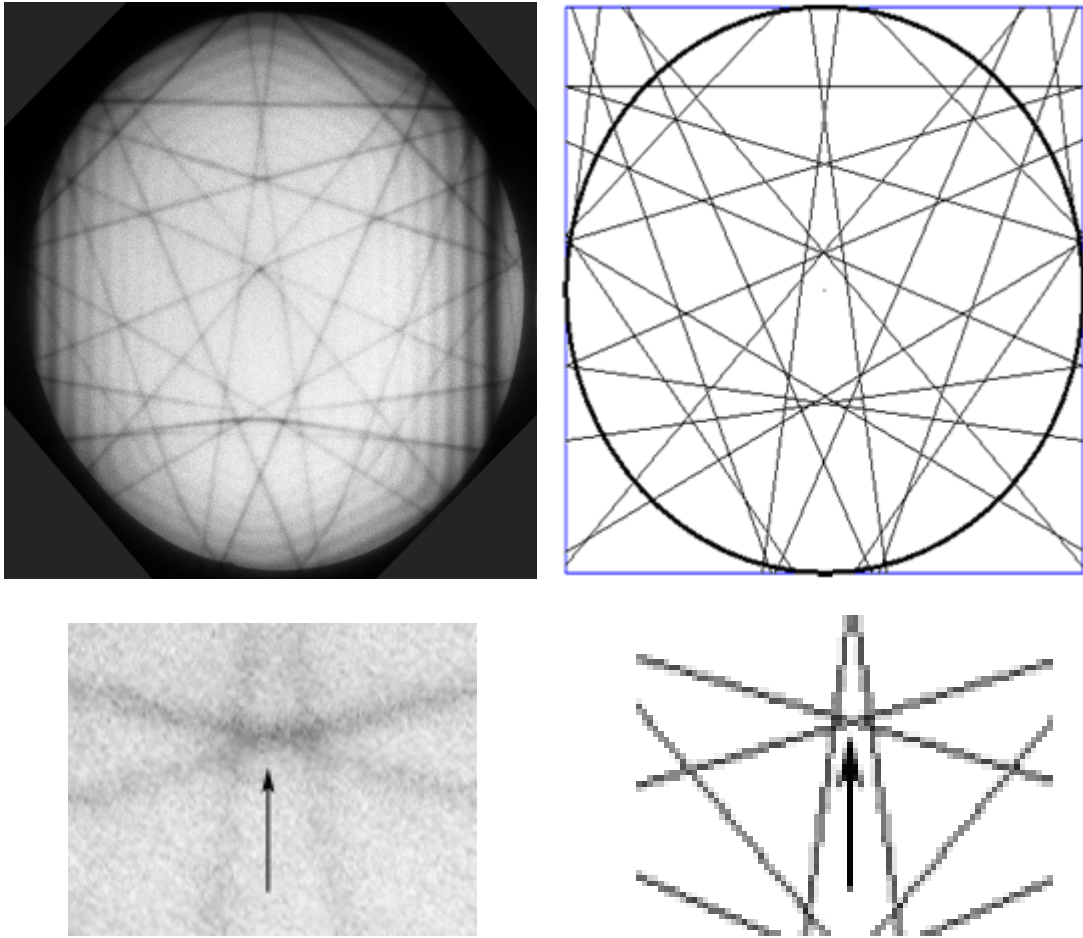


Fig. 4.5: The observed and the simulated HOLZ patterns taken near the grain boundary after ECAP through two passes. The arrows show the break in the symmetry after increasing the magnification of the patterns.

4.3.3 Al-1050 after ECAP through four passes:

After ECAP through four passes, the microstructure consists of equiaxed grains having an average grain size of approximately $\sim 0.9 \mu\text{m}$. A micrograph taken from a region oriented approximately at right angle to the direction of the ECAP after processing through 4 passes is shown in Fig. 4.6. Two patterns were taken from this sample, one at the centre of a grain and one near the grain boundary. The symmetry in the pattern which was taken from the centre of the grain was preserved as shown in Fig. 4.7 and the lattice parameters were: $a = b = c = 0.40329 \text{ nm}$ and $\alpha = \beta = \gamma = 90^\circ$ which are similar to the parameters of the material in the as-received condition. The lines of the pattern were blurred and less sharp compared to that in the sample

pressed through two passes. Fig. 4.8 shows the observed and the simulated patterns near the grain boundary. As shown in the figure, the blurring of the lines in the pattern increased compared to the pattern taken from the centre of the grain. It is clearly shown that the symmetry was broken and the arrows in both graphs indicate the shifting of some points from its original positions. The arrows in both graphs are in a good agreement. The lattice parameter a , b and c did not change from the sample which was pressed for two passes; i.e. $a = b = 0.40329$ nm and $c = 0.40289$ nm. The change in the angles α and β increased over that for the two-pass sample. The angle α became approximately 89.8° and the angle β became approximately 90.2° . The other three parameters were set to $a = b = 0.40329$ nm and $\gamma = 90^\circ$. This indicates that the shear strain increased after four passes and became 0.175% and -0.175% for the angles α and β , respectively.

4.3.4 Al-1050 after ECAP through eight passes:

The microstructure of the billet pressed by ECAP through eight passes consists of equiaxed grains having an average grain size of approximately ~ 0.68 μm . A significant dislocation density was found within the grains which led to highly blurred lines in the HOLZ patterns inside the grains and near the grain boundary. Due to this blurring in the pattern lines, the measurements of the strain were not possible in the sample pressed through eight passes. The high dislocation density can be seen in Fig. 4.9 in locations where a grain orientation allows the dislocations to be imaged.

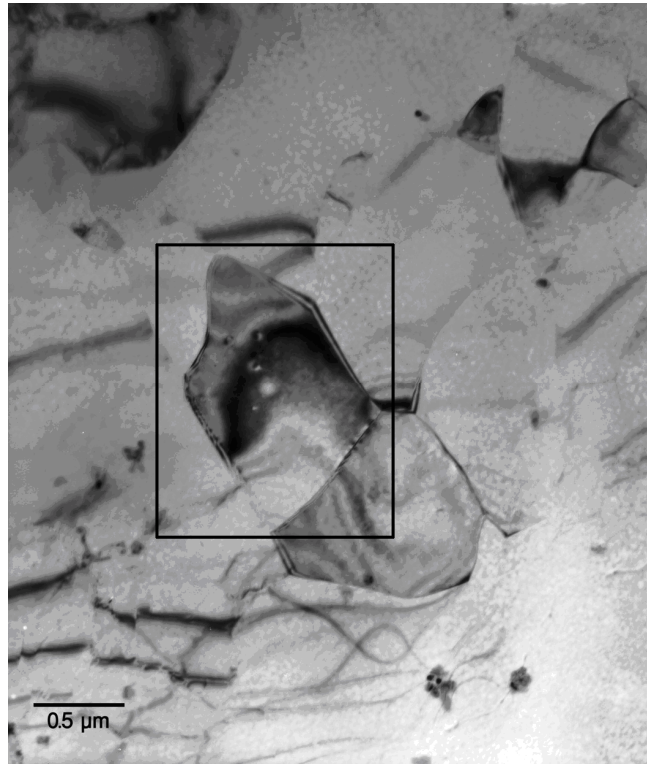


Fig. 4.6: TEM image of the grain used for taking the HOLZ pattern at the billet pressed through 4 passes.

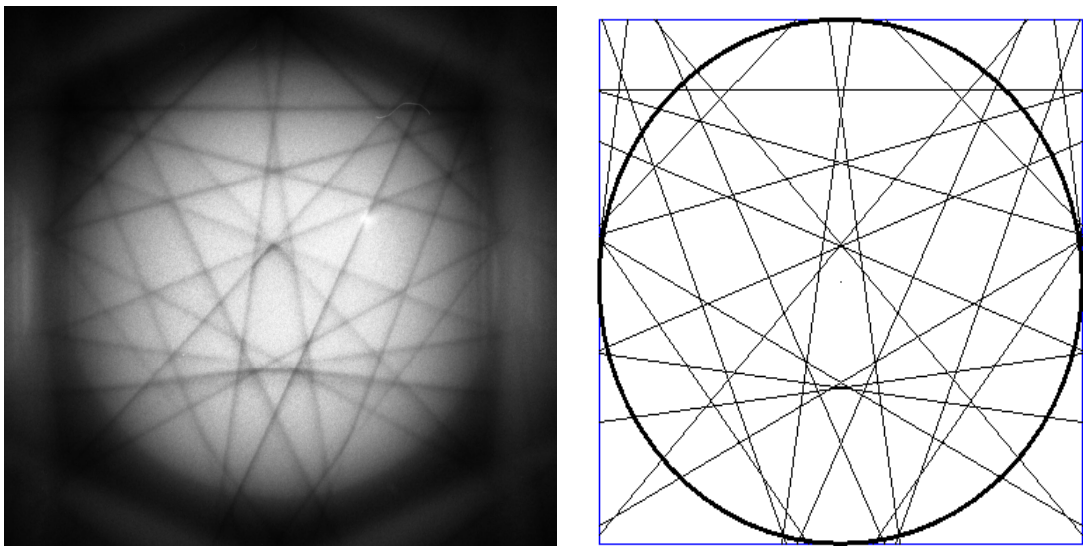


Fig. 4.7: The observed and the simulated HOLZ patterns taken from the centre of the grain after ECAP through four passes.

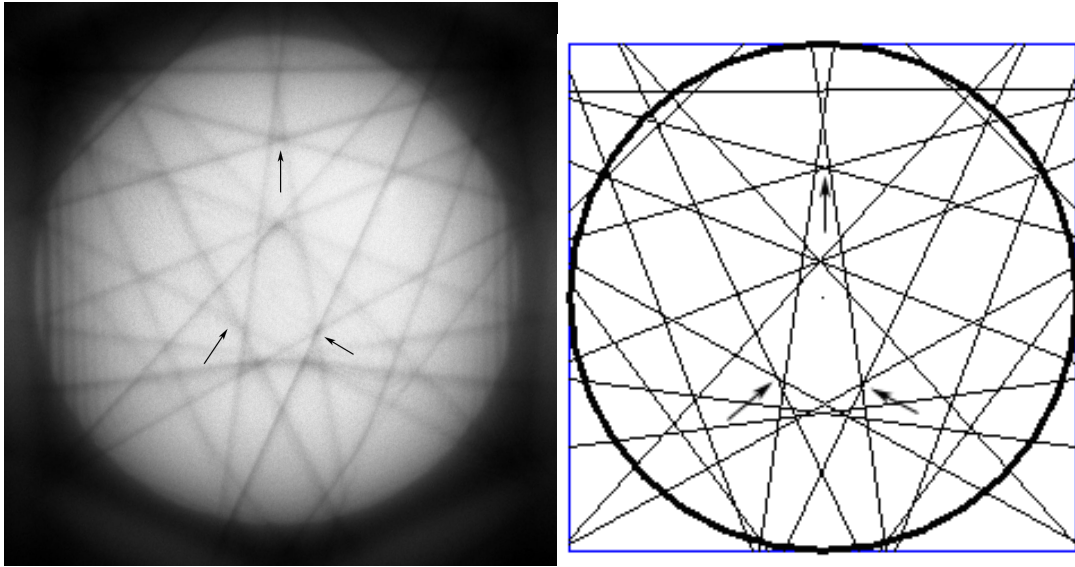


Fig. 4.8: The observed and the simulated HOLZ patterns taken near the grain boundary after ECAP through four passes. The arrows show the break in the symmetry.

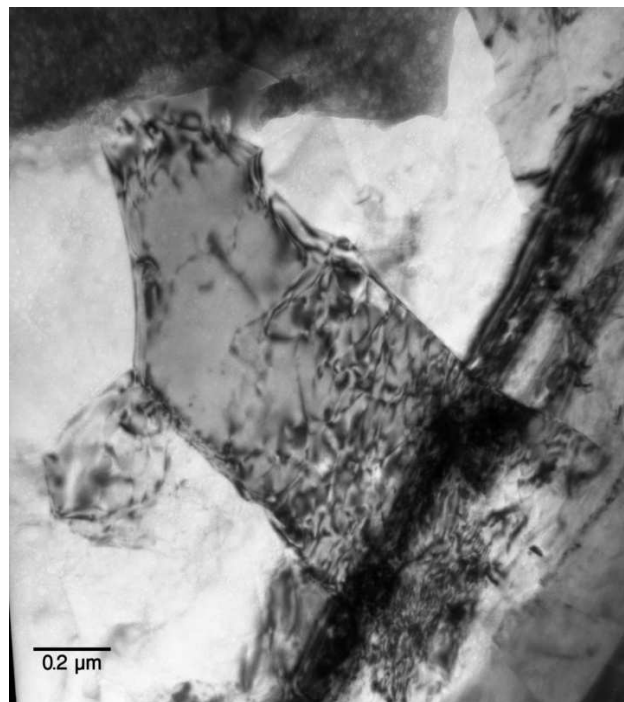


Fig. 4.9: TEM image of a single grain in the billet processed through 8 passes showing a dislocation network inside a typical grain.

4.4 Discussion

In the present investigation, billets of commercial purity aluminium (Al-1050) were pressed by ECAP through two, four and eight passes at room temperature using route B_c and pressing speed 0.5 mm/s. After pressing, a series of convergent beam electron diffraction (CBED) patterns were performed using a [114] zone axis. The patterns were obtained at 148.7 kV with a 20 nm diameter electron probe from dislocation-free regions close to and away from the grain boundaries in three different billets after ECAP through two and four passes and from the material in the as-received condition. The HOLZ patterns were taken after cooling the samples to 80 K to improve the visibility of the HOLZ lines.

There are two aspects regarding the lines of the HOLZ patterns: the sharpness and the position of the lines. The former can be affected by the increase in the density of dislocations. As was shown, the pattern of the material in the as-received condition was sharp which indicates that the interior of the grains in the as-received material was free from dislocations. It is known that a high density of dislocations is introduced into the material when processed by ECAP on each separate pass [9,118]. In addition, higher densities of dislocations are usually present in the zones adjacent to the grain boundaries where these boundaries are usually in a nonequilibrium state [9,119]. This can be noticed in the sharpness of the patterns taken after two and four passes both at the centre of the grains and near the grains boundary. After eight passes, the density of dislocations was extremely high at the centre and near the grain boundary which highly blurred the lines of the HOLZ patterns.

The second aspect is the position of the lines in the HOLZ CBED pattern. The lattice parameters of the strained lattice deviate from that in the unstrained lattice and this leads to shifts in the position of the HOLZ lines. The changes in the lattice parameter would indicate the presence of internal stresses [113,114]. This deviation can be measured from regions within 20 nm which is the probe size by comparing the patterns of the strained lattice to simulated patterns. The pattern of the material in the as-received condition was set as the reference pattern. The symmetry was preserved in the patterns taken from the interior of the grains after ECAP through two and four

passes which indicates that there were no detectable internal stresses in the interior of the grains. The patterns performed near the grain boundaries show different results in both samples. The lattice parameter c was reduced after two passes from 0.40329 nm to 0.40289 nm which indicates a compression strain of approximately 0.1%. This value of the lattice parameter c was the same after ECAP through four passes. These results indicate that the compression strains are introduced in the early stages of the ECAP processing when the sample is adjusting to the size of the channel and no more compression strains are accumulated with increasing number of passes. After two passes, the change in the angles α and β indicated a shear strain of approximately 0.044%. The shear strain increases after four passes of ECAP by a factor of four to reach 0.175%. These results are reasonable as the nature of the imposed deformation in the ECAP processing is simple shear which occurs as the billet passes through the channel angle.

In principle, CBED patterns contain three dimensional structure information. However, performing CBED using a single pattern only reduces the sensitivity of the technique. The FCC microstructure of the Al-1050 alloy consists of six lattice parameters which are the three lengths a , b and c and the three angles α , β and γ . The use of a single pattern only in the strain measurements reduces the sensitivity to three parameters only. Therefore, only the values of the parameter c and the angles α and β were used in the strain measurements and the values of the lattice parameters a , b and the angle γ were assumed to be at the unstrained condition in the simulations. A similar approach was adopted in many investigations used to measure the strain in semiconductors [120-122], in a titanium tri-aluminide intermetallic alloy [123] and in aluminium and copper alloys subjected to creep [114].

The results near the grain boundaries of the billets pressed through two and four passes indicate that the compression strain associated with the change in lattice parameter c is associated with a tetragonal deformation of the unit cell. The fact that both angles α and β are different indicates the strained unit cell is likely to be triclinic rather than tetragonal.

4.5 Summary and Conclusions

1. Billets of commercial purity aluminium (Al-1050) were pressed by ECAP through two, four and eight passes at room temperature using route B_c and a pressing speed of 0.5 mm/s.
2. A series of convergent beam electron diffraction (CBED) patterns were performed on the billets using a [114] zone axis. The patterns were obtained at 148.7 kV with a 20 nm diameter electron probe from dislocation-free regions close to and away from the grain boundaries. The pattern of the material in the as-received condition was set as the reference pattern. The HOLZ patterns were taken after cooling the samples to 80 K to improve the visibility of the HOLZ lines.
3. The results show that the inhomogeneous strain due to dislocations increased with increasing number of passes and increased near the grain boundaries by comparison with the interior of the grains. After ECAP through eight passes, the inhomogeneous strain was extremely high and the measurements of the lattice parameter changes (homogeneous strain) were not possible.
4. A homogeneous compression strain with a value of about 0.1% was introduced in the early stages of the ECAP processing when the sample is adjusting to the size of the channel and no more compression strains were accumulated in the following passes.
5. A shear strain with a value of about 0.044% was introduced after ECAP through two passes and it increased after four passes by a factor of four to reach 0.175%.
6. The strained unit cell near the grains boundaries is likely to be a triclinic unit cell.

CHAPTER 5

PROCESSING OF COMMERCIAL PURITY TITANIUM BY ECAP AT ROOM TEMPERATURE

5.1 Introduction

Processing by ECAP at low temperatures leads normally to the formation of microstructures with smaller grain sizes and higher fraction of high-angle boundaries [38]. However, for some hard materials such as titanium, performing ECAP experiments at room temperatures is not easy due to the high loads needed for pressing which may exceed the capacity of the press or lead to the formation of cracks and segmentations [33]. Therefore, most of the experiments for ECAP of CP Ti are performed at elevated temperatures which are higher than 473K [36,54-66,124]. Up to date, there is only one report of successfully performing the experiment of ECAP on CP Ti at room temperature [37]. According to this report, two conditions must be satisfied to perform ECAP on hard materials such as CP Ti at room temperature. First, increase the die channel angle (Φ) to 120 deg at least. Second, decrease the pressing speed to approximately 0.5 mm/s or less.

In this chapter, the possibility to perform ECAP experiments on CP Ti at room temperature will be investigated, taking into consideration the two conditions reported by Zhao et al. [37]. The microstructure and the microhardness of the processed billets will be analyzed.

5.2 Experimental Material and Procedures

A commercial purity titanium alloy (Grade 2) was used in this ECAP investigation and its chemical composition in weight percent (wt. %) is shown in Table 5.1. The

alloy was supplied in the form of a long bar having a diameter of 10.0 mm. Billets having a diameter of 10.0 mm and length of 65.0 mm were cut from the bar for the ECAP experiments.

Table 5.1: The chemical composition of CP Ti in wt. %:

Maximum composition in wt. %					
Fe	O	C	N	H	Ti
0.3	0.25	0.1	0.03	0.015	Balance

The experiments were conducted in air at room temperature using a DMG universal facility having a hydraulic press with a capacity of 200 tons. The photographs of the facility were shown in the chapter of ECAP of Al-1050. The experiments were conducted using a solid die and a plunger made from H13 tool steel material. The solid die contains a channel having a circular cross-section and the angle of the channel (Φ) was 135 deg and the angle of the outer arc of curvature (Ψ) was 20 deg. To calculate the equivalent imposed strain accumulated on each separate pass, the following equation were used [22]

$$\varepsilon_N = \frac{N}{\sqrt{3}} \left[2 \cot \left(\frac{\Phi}{2} + \frac{\Psi}{2} \right) + \Psi \operatorname{cosec} \left(\frac{\Phi}{2} + \frac{\Psi}{2} \right) \right]$$

$$\varepsilon_1 = \frac{1}{\sqrt{3}} \left[\left(2 \times \cot \left(\frac{135^\circ}{2} + \frac{20^\circ}{2} \right) \right) + \left(20^\circ \times \operatorname{cosec} \left(\frac{135^\circ}{2} + \frac{20^\circ}{2} \right) \right) \right]$$

$$= \mathbf{0.462}$$

So, the equivalent imposed strain accumulated on each separate pass was ~0.46. Before the ECAP experiments, the billets were annealed in air for 2h at a temperature of 993 K. To reduce the friction effect, a lubricant containing a suspension of molybdenum disulfide in a mineral oil was used on the billets, plunger and on the sides of the channel of the die before testing.

Billets were processed for one and two passes at two different pressing speeds; 0.5 mm/s and 0.05 mm/s. Route B was used where the billet was rotated by 90° between the first and the second passes. As mentioned in chapter 3, limited inherent back-pressure was applied on the billets from the preceding billet which stays in the die after pressing and this phenomenon is a feature of ECAP when using a solid die [53].

After ECAP, the billets were sectioned for optical microscopy (OM) and Vickers microhardness measurements. As shown in Fig. 5.1, for each billet, approximately 5.0 mm from the front edge was cut but it was not used in the analysis due to the severe distortion in the billets near the front and rear edges. Beside that, approximately 2.0 mm were cut and used for the optical microscopy and the cross-sectional plane microhardness measurements. The remaining part of the billets was sectioned into two halves along the central line of the billets, perpendicular to the upper surface, and one half was used for the optical microscopy and the vertical longitudinal plane microhardness measurements. The cutting process was performed by using 0.25 mm brass wire erosion with an electro-discharge machine.

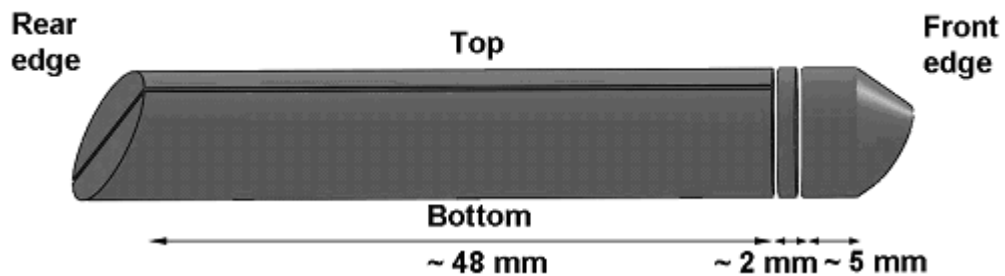


Fig. 5.1: Schematic illustration of a CP Ti billet after ECAP showing the cutting method and dimensions.

After cutting, samples from the annealed condition before ECAP and from the billets processed by ECAP through one and two passes at both pressing speeds were prepared for optical microstructural observations. The samples were polished electrochemically by using a solution consists of (25% H_2SO_4 + 15% HF + 60% CH_3COOH) at a voltage ranging between 14 and 17 V at room temperature. The polished surface of each billet was then etched using a solution consisting of (HF : HNO_3 : H_2O) in a volume percentage of (2 : 3 : 10) respectively.

For the Vickers microhardness measurements, H_v , the surface of both planes of each billet, the vertical longitudinal plane and the cross-sectional plane, were polished mechanically using 120, 600, 1200 and 4000 grit to a mirror-like finish. The measurements were then recorded using two instruments; MATSUZAWA 8033 Microhardness Tester and FUTURE-TECH FM-700 Microhardness Tester. For each measurement, a load of 300 gf was applied for a dwell time of 15 s. The MATSUZAWA 8033 Microhardness Tester was used on the annealed unpressed billet and on the billets pressed by ECAP through one and two passes using the pressing speed of 0.5 mm/s. The FUTURE-TECH FM-700 Microhardness Tester was used on the billets pressed by ECAP through one and two passes using the pressing speed of 0.05 mm/s. For comparison, the microhardness measurements of the billet in the annealed unpressed condition were also recorded using the FUTURE-TECH FM-700 Microhardness Tester.

For the cross-sectional plane, the microhardness measurements were recorded along two perpendicular lines, one lying vertically from the top surface to the bottom surface and the other lying horizontally from the right side to the left side, as shown in Fig. 5.2. All microhardness measurements on this plane were then recorded along these two lines at an increment of 1.0 mm between the data points. For the vertical longitudinal plane, the microhardness measurements were recorded along three traverses at distances of 1.0 mm from the top surface, at the centre, and at a distance of 1.0 mm from the bottom surface as shown in Fig. 5.3. All microhardness measurements on this plane were then recorded along these three lines at an increment of 3.0 mm between the data points. For each data point on both planes, as shown in Figs. 5.2 and 5.3, four measurements were taken; at the top, the bottom, the right and the left of the centre of the data point. Each measurement was positioned at

a distance of 0.15 mm from the centre of the data point. The total numbers of measurements on each cross-sectional plane were 68 and on each vertical longitudinal plane were 180.

For the cross-sectional plane, the individual microhardness measurements of the billets processed using the pressing speed of 0.5 mm/s were then plotted against the distance from the centre of the plane for both the vertical lines laying from top to bottom surfaces and the horizontal lines laying from the right to left sides. For the vertical longitudinal plane, the individual microhardness measurements of all billets were then plotted against the longitudinal axis of the billet. The microhardness of the alloy in the annealed unpressed condition was measured and recorded in the graphs to provide a comparison with the as-pressed billets.

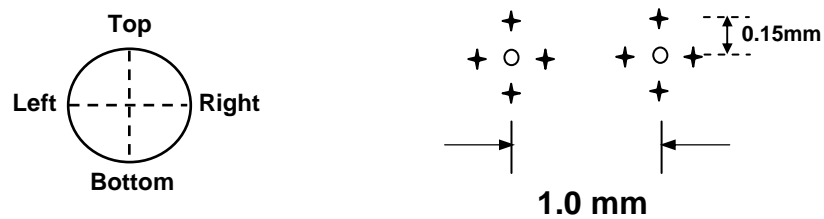


Fig. 5.2: Schematic illustrations of the cross-sectional plane showing the two lines defined for the microhardness measurements and the positions of the data points.

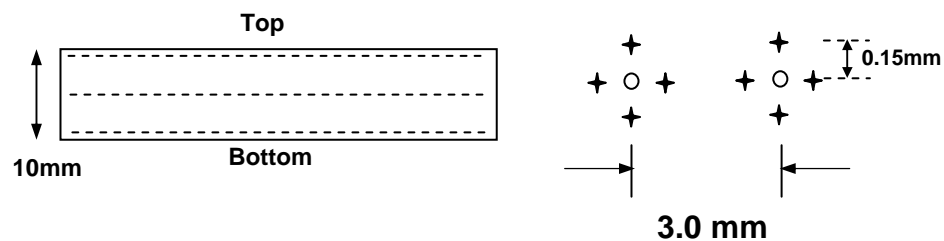


Fig. 5.3: Schematic illustrations of the vertical longitudinal plane showing the three lines defined for the microhardness measurements and the positions of the data points.

Statistical distribution measurements were then performed on the optical micrographs to define the twinning growth direction. The measurements were performed on the cross-sectional plane and the vertical longitudinal plane for both number of passes and both pressing speeds. The direction of the twinning growth starts at the grain boundary side of the twin to the end of the twin.

5.3 Experimental Results

In this research, CP Ti billets were processed by ECAP at room temperature at two pressing speeds; 0.5 mm/s and 0.05 mm/s. Firstly, two billets in the annealed condition were pressed through one and two passes at a pressing speed of 0.5 mm/s. The billets were successfully pressed through one pass without any visible cracks but after the second pass, a deep crack initiated across the middle of the billet. Secondly, two billets in the annealed condition were pressed through one and two passes at a pressing speed of 0.05 mm/s. The two billets performed a smooth flow and were successfully pressed through one and two passes without any visible cracks. The appearance of the billets after processing through one and two passes at room temperature under the pressing speeds of 0.5 mm/s and 0.05 mm/s is shown in Fig. 5.4. Another billet of CP Ti in the as-received condition was successfully pressed for one pass at a pressing speed of 0.5 mm/s.

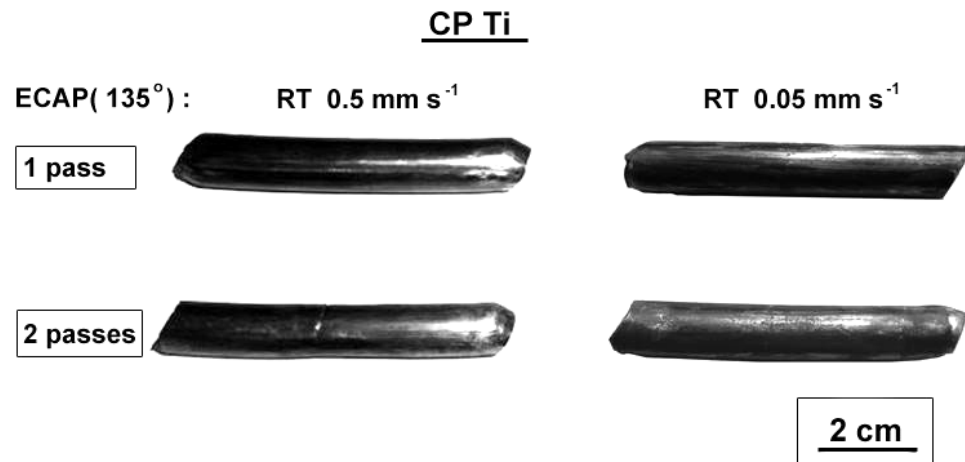


Fig. 5.4: Appearance of CP Ti billets after ECAP through one and two passes at room temperature using pressing speeds of 0.5 and 0.05 mm/s.

Since the microhardness measurements of the billets were recorded using two different instruments, the measurements of the billet in the annealed unpressed condition were recorded by both instruments to provide a comparison between them. The average value of the hardness was 169 Hv when the FUTURE-TECH FM-700 Microhardness Tester was used and this value was very close to the value recorded by the MATSUZAWA 8033 Microhardness Tester which was 174 Hv.

Fig. 5.5 shows the individual microhardness measurements recorded after processing by ECAP through one and two passes at a pressing speed of 0.5 mm/s on the cross-sectional planes at (a) the vertical line which is laying from the top to bottom surfaces and (b) the horizontal line which is laying from the right to left sides. In the figure, the clear points refer to pressing for one pass where the solid points refer to pressing for two passes. The bottom surface of the vertical lines and the right side of the horizontal lines lie on the right of the graphs. The microhardness measurements for the annealed unpressed alloy are also shown in the figure. The average microhardness measurements in the annealed unpressed alloy were approximately ~174. After one pass, the hardness increased on both lines; vertical and horizontal, to an average of approximately ~210. The hardness measured on both lines increased after two passes to an average of approximately ~230. For the vertical line which is lying from the top to bottom surfaces of the billet, as shown in Fig 5.5(a), the measurements after one pass were slightly lower than average near the centre of the billet. After two passes, the hardness increased along the line where it showed the maximum increase near the top and bottom surfaces. For the horizontal line which is lying from the right to left sides of the billet, as shown in Fig 5.5(b), the measurements after one pass were consistent along the measured axis except that in the centre which showed slight decrease in the value. After two passes, the hardness increased and continued to be consistent along the axis except the region near the left edge which showed higher hardness where it became approximately ~248.

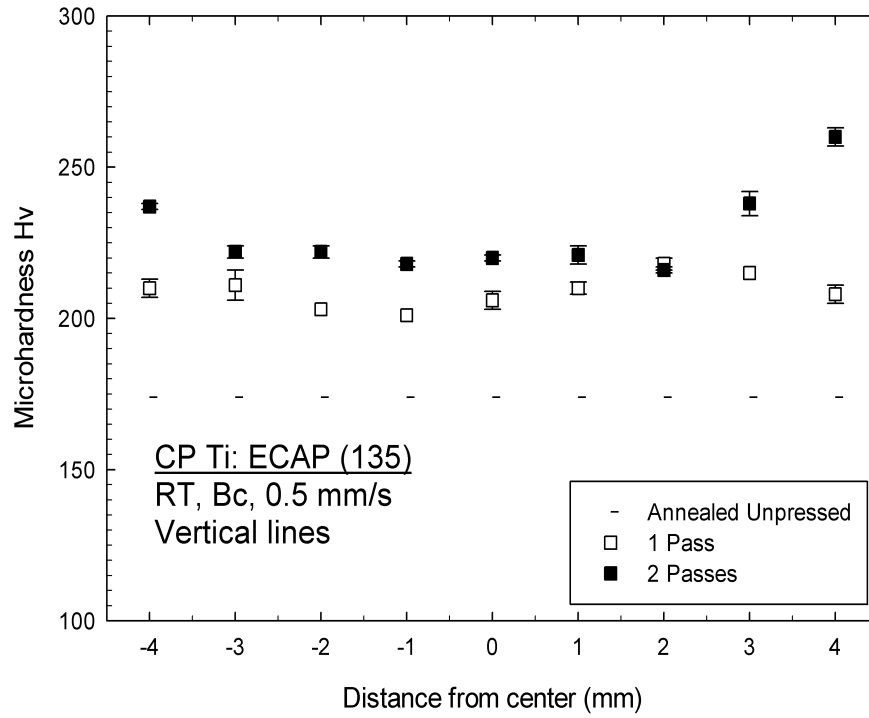


Fig. 5.5(a): Individual measurements of the microhardness, Hv, recorded along the vertical lines on the cross-sectional plane after 1 and 2 passes at a pressing speed of 0.5 mm/s. The bottom surface lies on the right of the graphs.

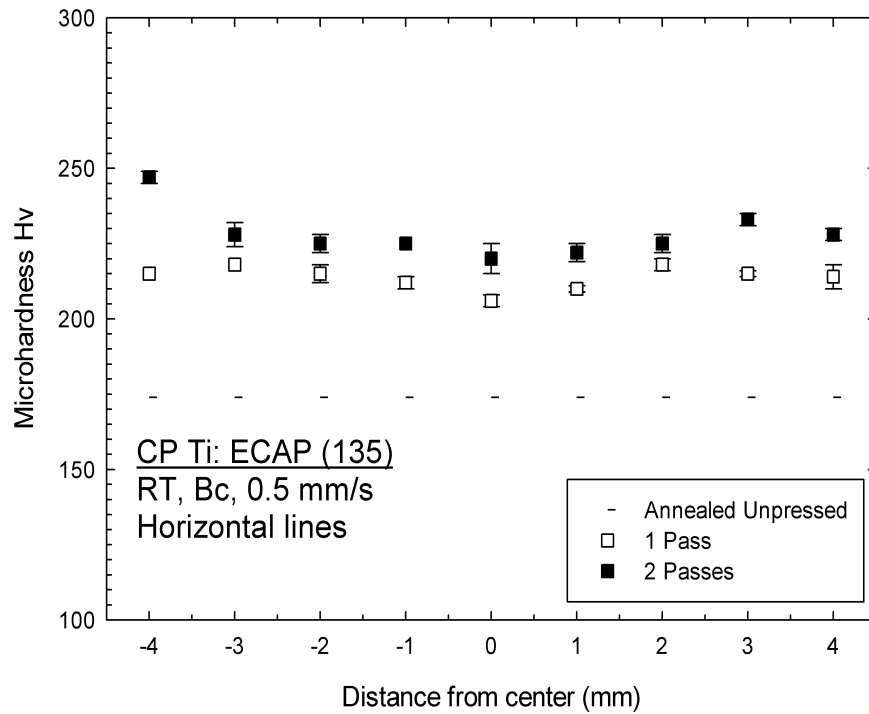


Fig. 5.5(b): Individual measurements of the microhardness, Hv, recorded along the horizontal lines on the cross-sectional plane after 1 and 2 passes at a pressing speed of 0.5 mm/s. The right side lies on the right of the graphs.

Fig. 5.6 shows the individual microhardness measurements, H_v , along the three traverses at the longitudinal axis; traverses at distances of 1.0 mm from the top and bottom surfaces and the central traverse, for the ECAP after (a) one pass at a speed of 0.5 mm/s, (b) two passes at a speed of 0.5 mm/s, (c) one pass at a speed of 0.05 mm/s and (d) two passes at a speed of 0.05 mm/s, respectively. The microhardness measurements for the annealed unpressed alloy are also shown and the front edge of the billets lies on the right of the graphs. As shown in Fig 5.6(a), the microhardness measurements from the billet pressed by ECAP through one pass at a pressing speed of 0.5 mm/s increased from ~174 in the annealed unpressed billet to ~220 for the three traverses. The variation between the microhardness measurements along the three traverses was relatively small. However, the hardness adjacent to the bottom surface towards the front edge was less than that at the centre and adjacent to the top surface. After two passes of ECAP at the same pressing speed (0.5 mm/s) as shown in Fig 5.6(b), the microhardness measurements increased at the traverse adjacent to the top surface and at the central traverse where it almost did not change at the traverse adjacent to the bottom surface at which the microhardness measurements were approximately ~220. The microhardness measurements were approximately ~250 at the traverse adjacent to the top surface and it was approximately ~235 at the central traverse. Fig. 5.6(c) shows the microhardness measurements after processing by ECAP through one pass at a pressing speed of 0.05 mm/s. The microhardness measurements near the bottom surface were slightly lower than that near the top surface and at the centre. The average hardness for all traverses was approximately ~230 which is somewhat higher than that attained after pressing through the same number of passes; i.e. one pass, at the higher pressing speed (0.5 mm/s). After two passes of ECAP at the same pressing speed (0.05 mm/s) as shown in Fig 5.6(d), the microhardness measurements increased in all traverses to a value of approximately ~245. The microhardness measurements were consistent along the longitudinal axis of the billet and also; to some extent, it was consistent along the vertical axis (i.e. at the three traverses).

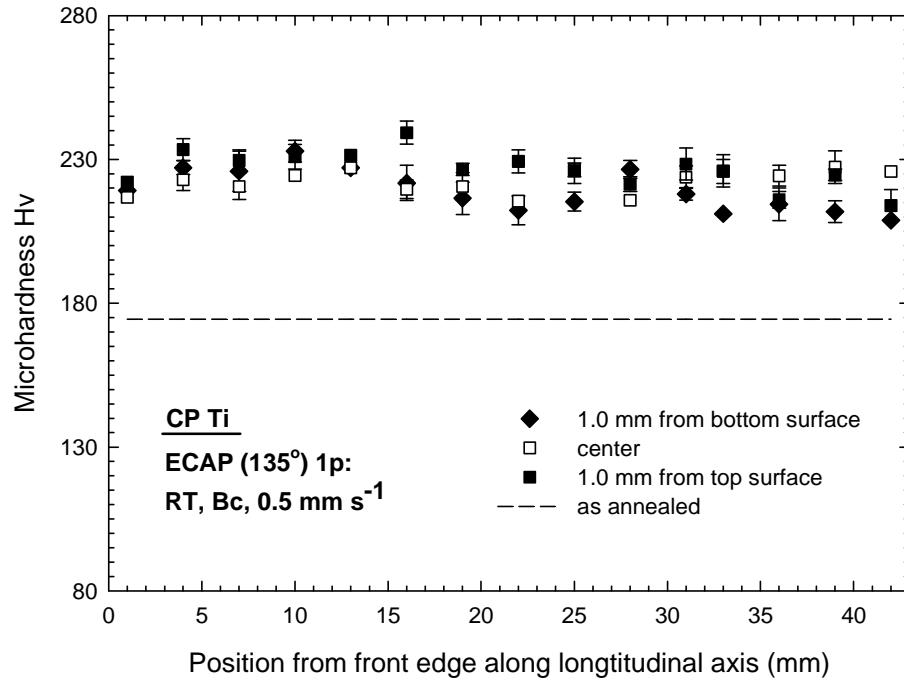


Fig. 5.6(a): Individual measurements of the microhardness, Hv, recorded along the vertical longitudinal plane at the central traverse and the traverses at 1.0mm from the top and bottom surfaces after ECAP through one pass at a pressing speed of 0.5 mm/s. The front edge lies on the right of the graphs.

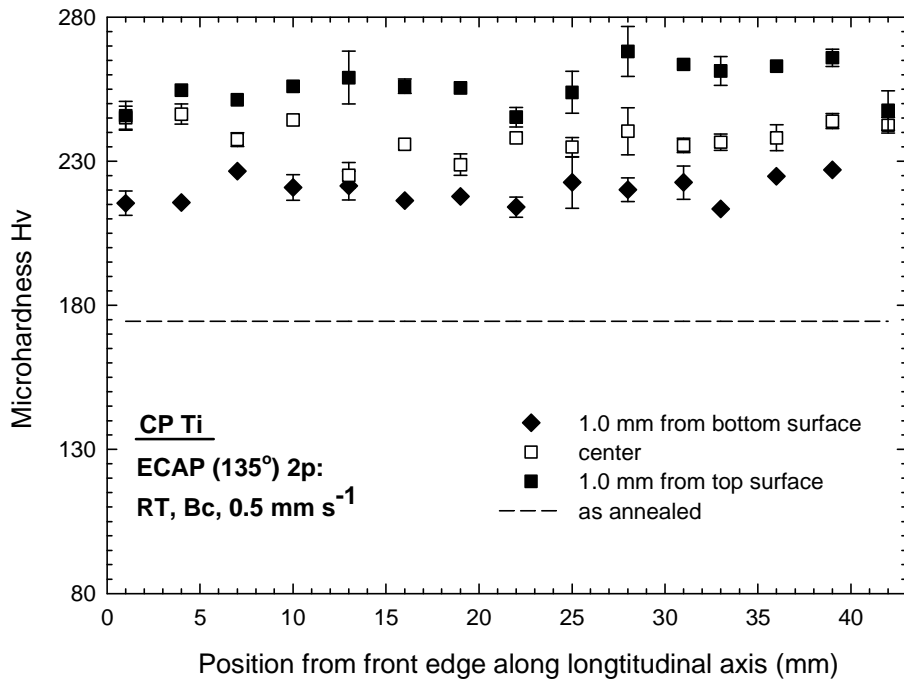


Fig. 5.6(b): Individual measurements of the microhardness, Hv, recorded along the vertical longitudinal plane at the central traverse and the traverses at 1.0mm from the top and bottom surfaces after ECAP through two passes at a pressing speed of 0.5 mm/s. The front edge lies on the right of the graphs.

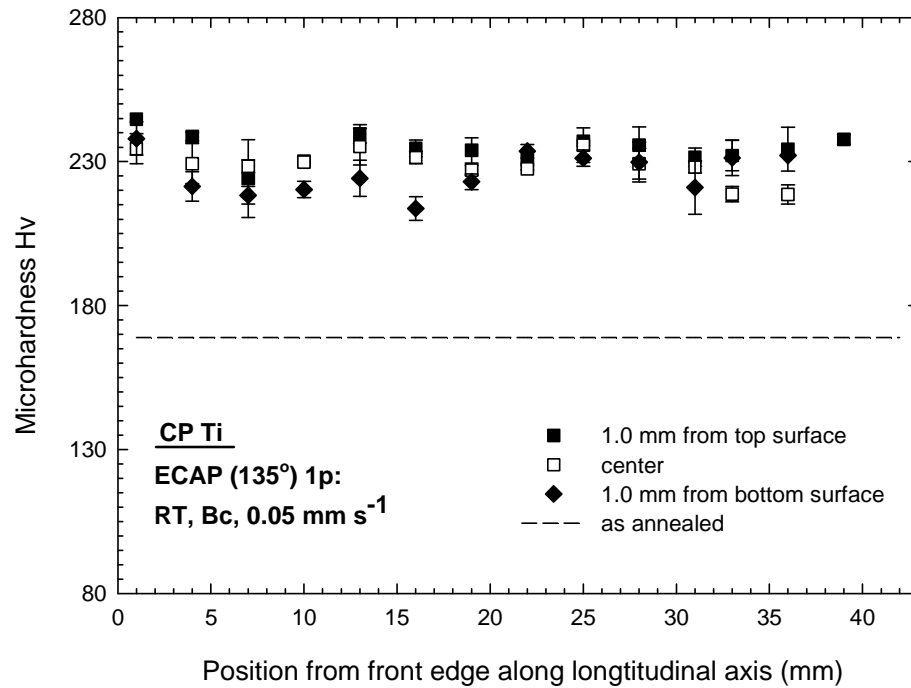


Fig. 5.6(c): Individual measurements of the microhardness, Hv, recorded along the vertical longitudinal plane at the central traverse and the traverses at 1.0mm from the top and bottom surfaces after ECAP through one pass at a pressing speed of 0.05 mm/s. The front edge lies on the right of the graphs.

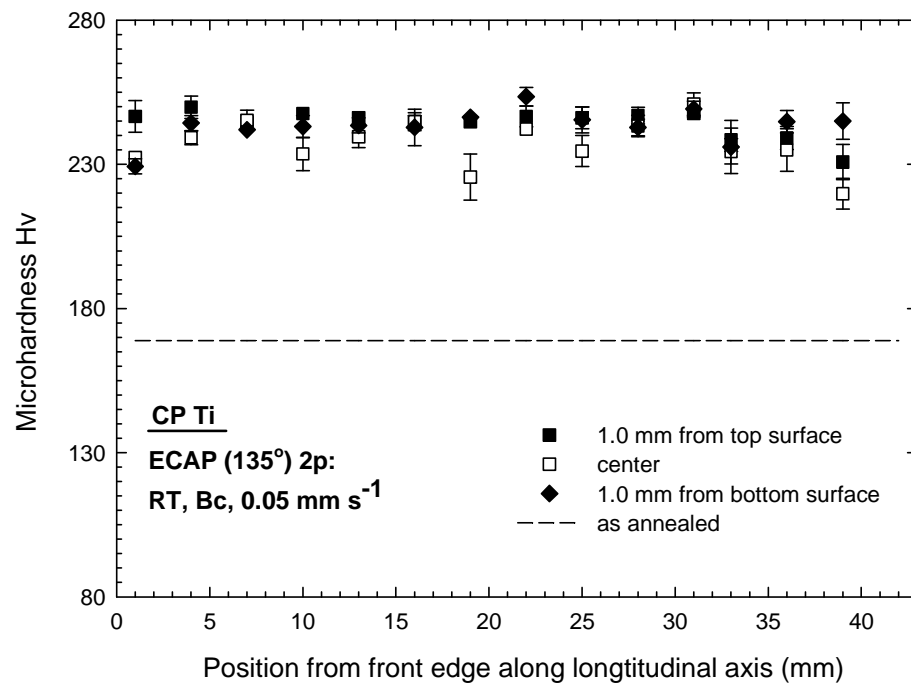


Fig. 5.6(d): Individual measurements of the microhardness, Hv, recorded along the vertical longitudinal plane at the central traverse and the traverses at 1.0mm from the top and bottom surfaces after ECAP through two passes at a pressing speed of 0.05 mm/s. The front edge lies on the right of the graphs.

Typical optical microstructure of CP Ti at the annealed unpressed condition is shown in Fig. 5.7. It is clear that the alloy in this condition is consisting of nearly equiaxed grains which have an average size of $\sim 10\ \mu\text{m}$. Fig. 5.8 shows the optical microstructures of CP Ti at the cross-sectional plane after processing by ECAP at room temperature using 135° die through (a) one pass at a pressing speed of 0.5 mm/s, (b) two passes at a pressing speed of 0.5 mm/s, (c) one pass at a pressing speed of 0.05 mm/s and (d) two passes at a pressing speed of 0.05 mm/s, respectively. The size of the nearly equiaxed grains did not change significantly after processing by ECAP. However, as shown in Fig. 5.8, a large fraction of twins were introduced into the equiaxed grain structures at both speeds and number of passes. However, as shown in Fig. 5.8, pressing through two passes does not increase the fraction of twins significantly. In addition, changing the pressing speed does not change the microstructure and the twin density significantly.

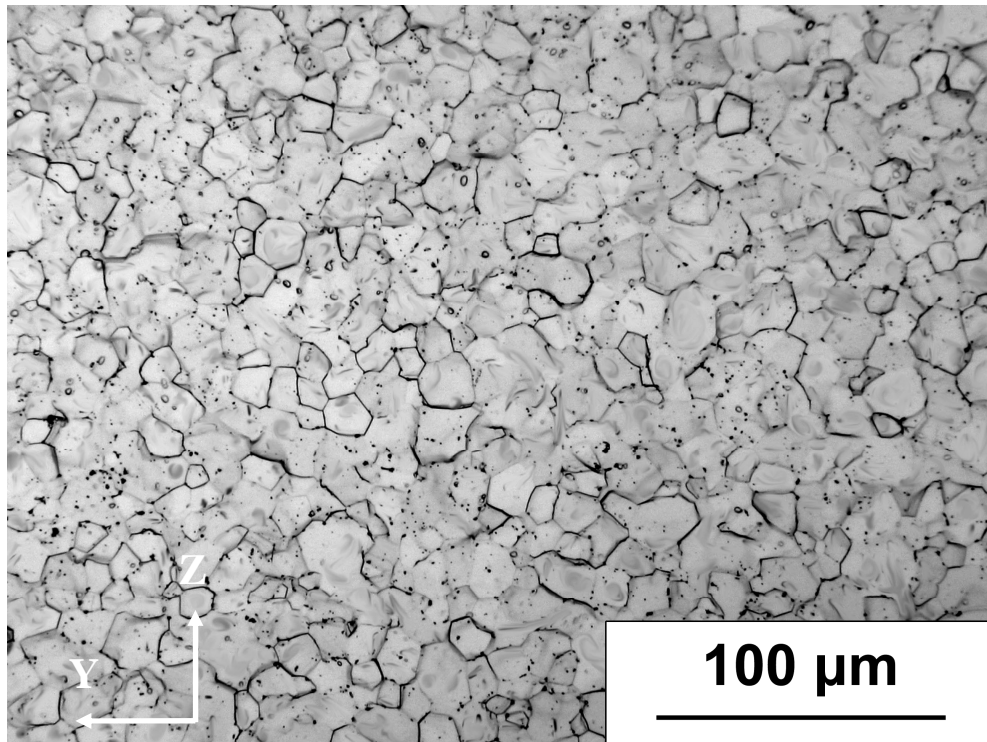


Fig. 5.7: Optical micrograph of the microstructure of CP Ti in as annealed unpressed condition.

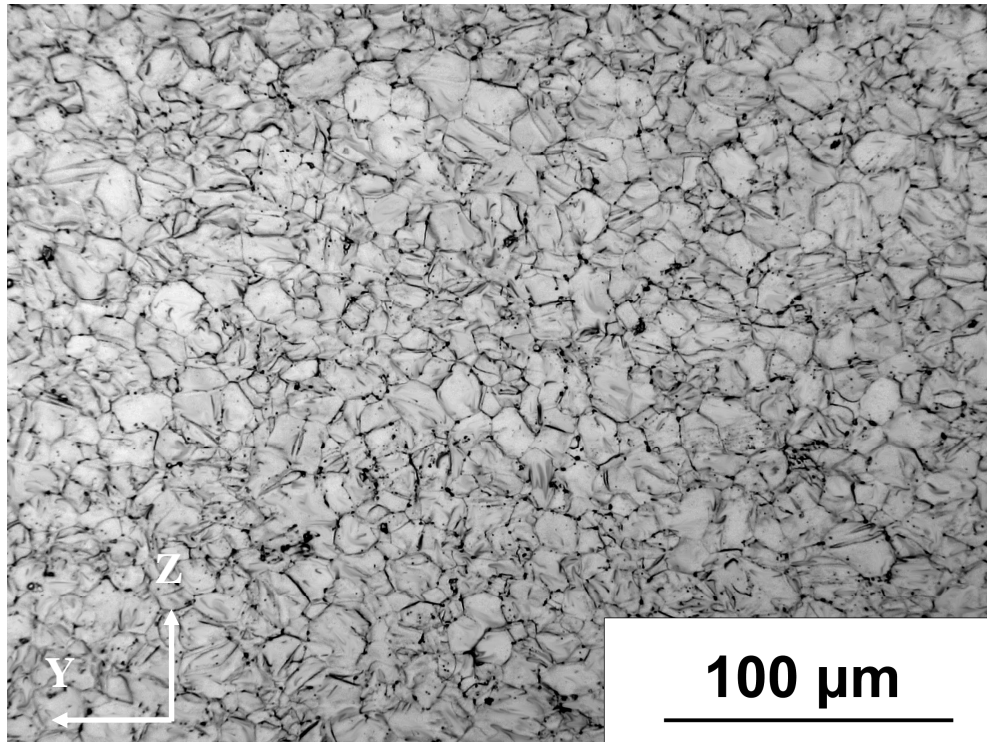


Fig. 5.8(a): Optical micrograph of the microstructure on the cross-sectional plane after ECAP at room temperature through one pass at a pressing speed of 0.5 mm/s.

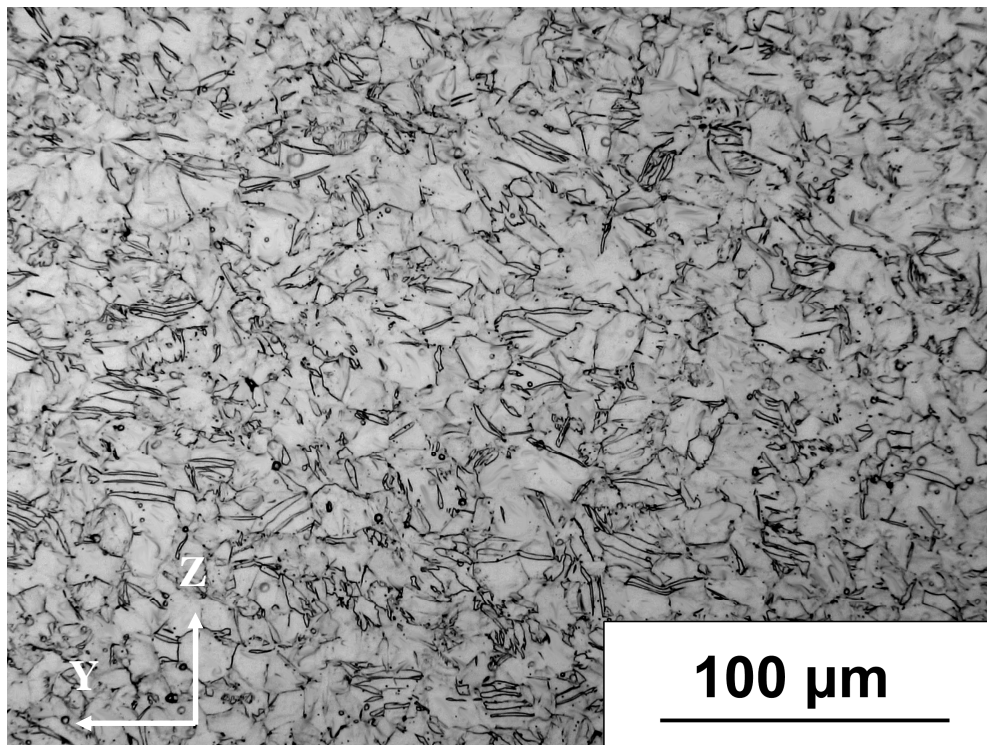


Fig. 5.8(b): Optical micrograph of the microstructure on the cross-sectional plane after ECAP at room temperature through two passes at a pressing speed of 0.5 mm/s.

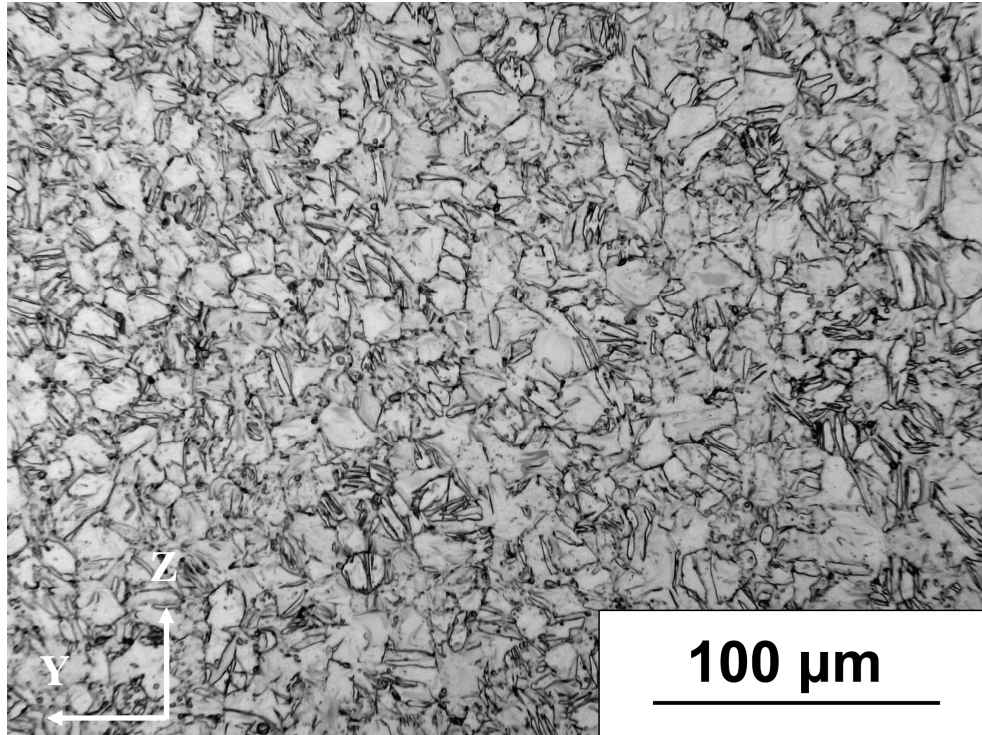


Fig. 5.8(c): Optical micrograph of the microstructure on the cross-sectional plane after ECAP at room temperature through one pass at a pressing speed of 0.05 mm/s.

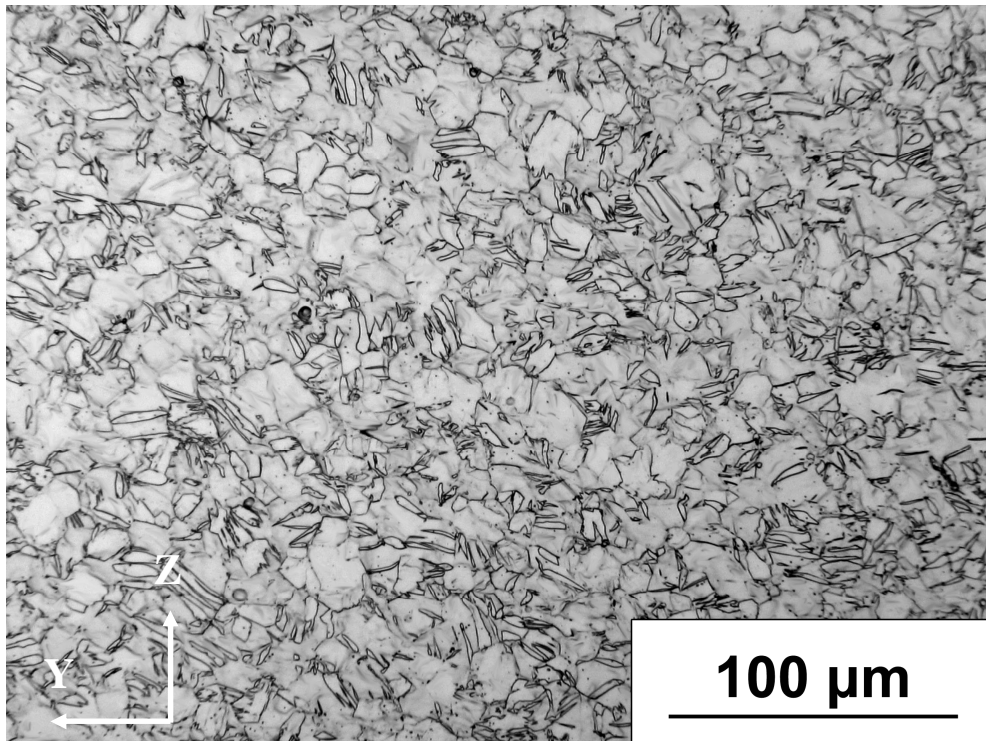


Fig. 5.8(d): Optical micrograph of the microstructure on the cross-sectional plane after ECAP at room temperature through two passes at a pressing speed of 0.05 mm/s.

Fig. 5.9 shows the optical microstructures of CP Ti at the vertical longitudinal plane after processing by ECAP at room temperature using 135° die through (a) one pass at a pressing speed of 0.5 mm/s, (b) two passes at a pressing speed of 0.5 mm/s, (c) one pass at a pressing speed of 0.05 mm/s and (d) two passes at a pressing speed of 0.05 mm/s, respectively. Elongated grains were introduced in the vertical longitudinal plane after one and two passes at both speeds of pressing. The long axis of these elongated grains inclined at approximately $\sim 40^\circ$ to the longitudinal axis. Twins, lying mostly in the direction of the elongated grains, were introduced after ECAP. From the figures, it is clear that the fraction of twins does not change significantly with the change in the number of passes or the pressing speed.

Fig. 5.10 shows the statistical distribution of twinning growth direction determined from the cross-sectional OM observations after processing by ECAP at room temperature through (a) one pass at a pressing speed of 0.5 mm/s, (b) two passes at a pressing speed of 0.5 mm/s, (c) one pass at a pressing speed of 0.05 mm/s and (d) two passes at a pressing speed of 0.05 mm/s, respectively. After pressing at a speed of 0.5 mm/s, as shown in Figs. 5.10(a) and (b), it can be noticed that higher fraction of twinning directions, compared to the pressing at a speed of 0.05 mm as in Figs. 5.10(c) and (d), concentrate around the 0° and $\pm 180^\circ$.

Fig. 5.11 shows the statistical distribution of twinning growth direction determined from the vertical longitudinal OM observations after processing by ECAP at room temperature through (a) one pass at a pressing speed of 0.5 mm/s, (b) two passes at a pressing speed of 0.5 mm/s, (c) one pass at a pressing speed of 0.05 mm/s and (d) two passes at a pressing speed of 0.05 mm/s, respectively. It is clear from the figures that the direction of the deformation twinning concentrated mainly at a degree ranging between $\sim 40^\circ$ and 50° or between $\sim -130^\circ$ and -140° .

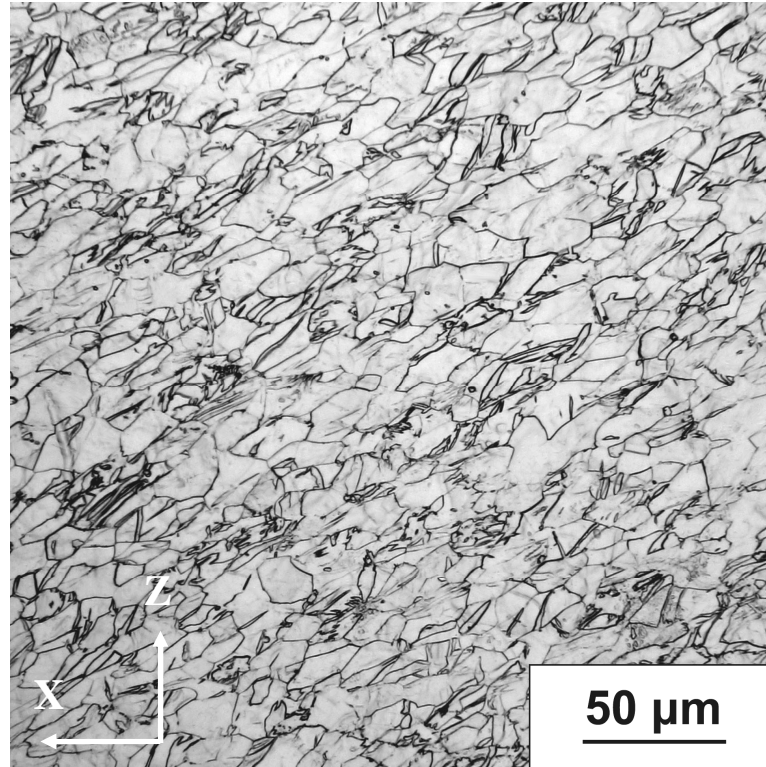


Fig. 5.9(a): Optical micrograph of the microstructure on the vertical longitudinal plane after ECAP at room temperature through one pass at a pressing speed of 0.5 mm/s.

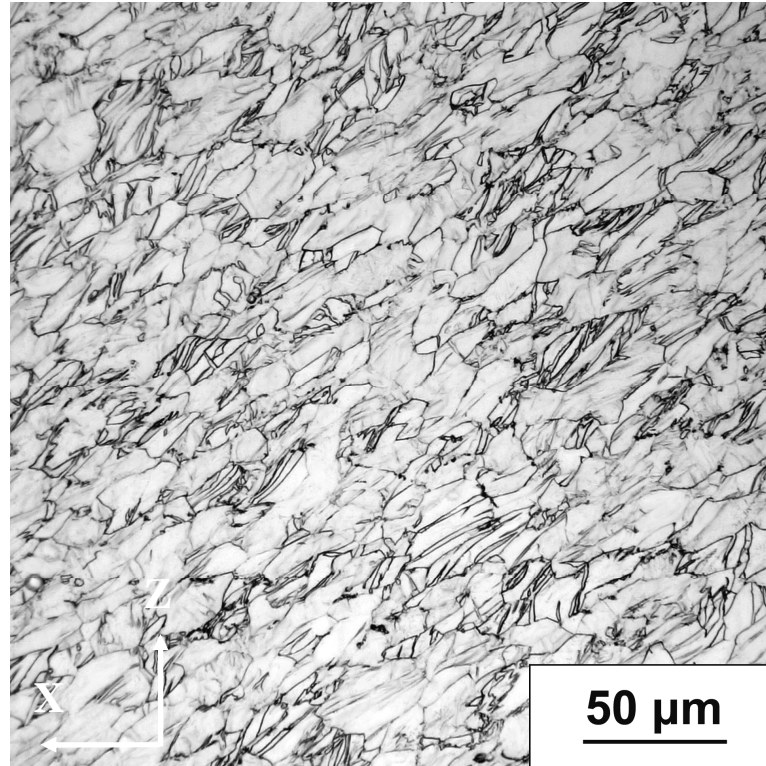


Fig. 5.9(b): Optical micrograph of the microstructure on the vertical longitudinal plane after ECAP at room temperature through two passes at a pressing speed of 0.5 mm/s.

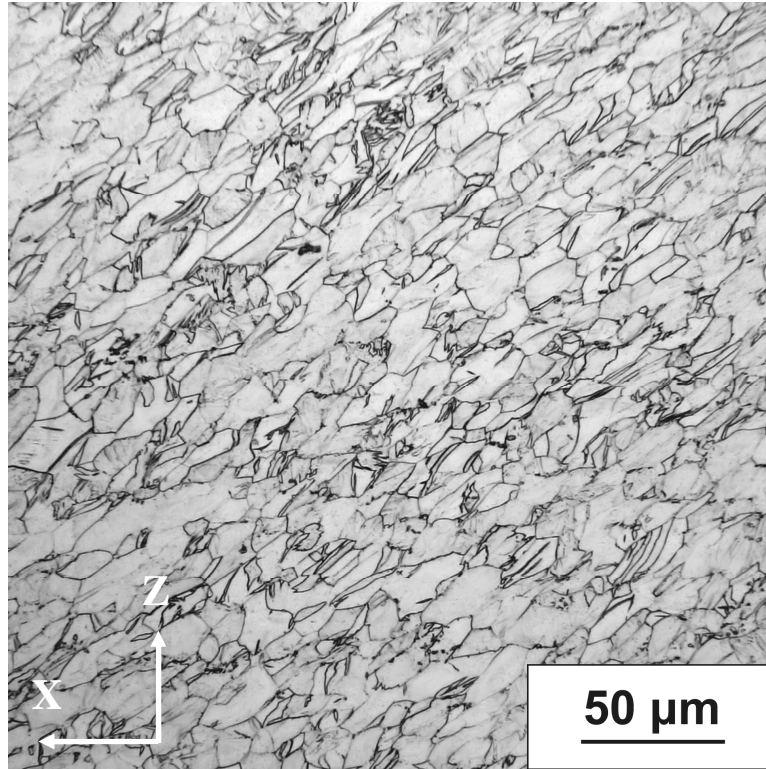


Fig. 5.9(c): Optical micrograph of the microstructure on the vertical longitudinal plane after ECAP at room temperature through one pass at a pressing speed of 0.05 mm/s.

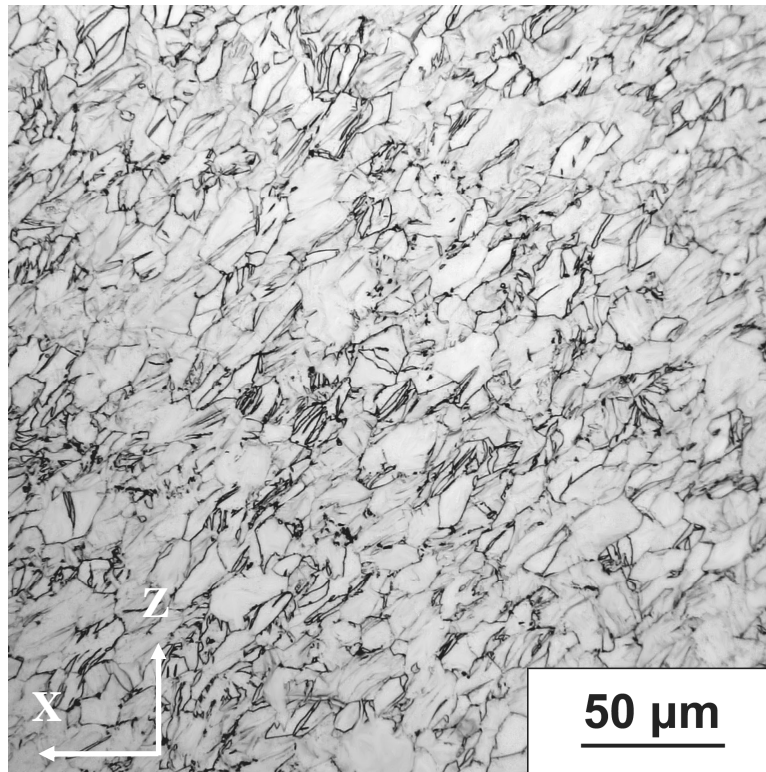


Fig. 5.9(d): Optical micrograph of the microstructure on the vertical longitudinal plane after ECAP at room temperature through two passes at a pressing speed of 0.05 mm/s.

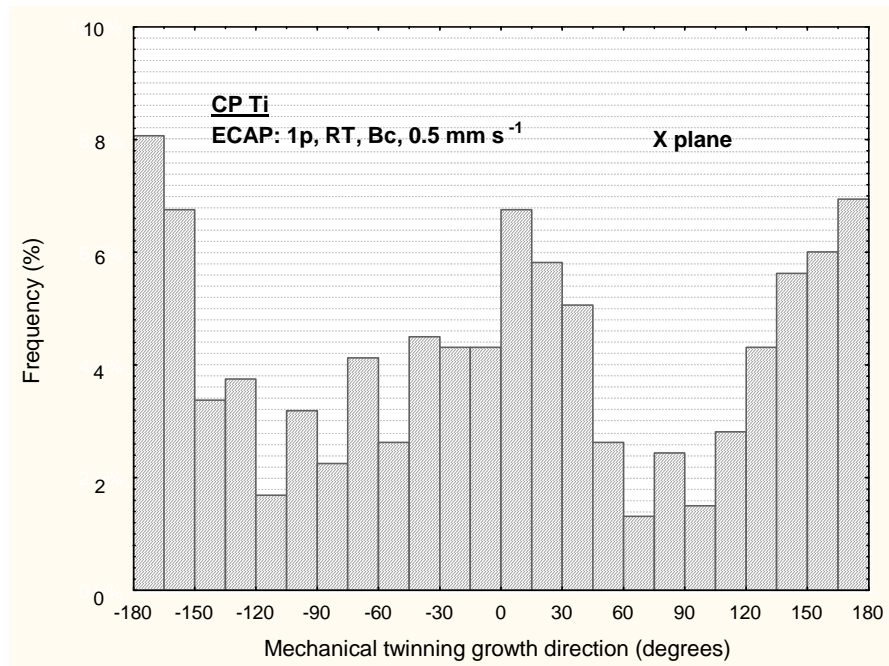


Fig. 5.10(a): Statistical distribution of twinning growth direction determined from the cross-sectional OM observations after pressing for one pass at a speed of 0.5 mm/s.

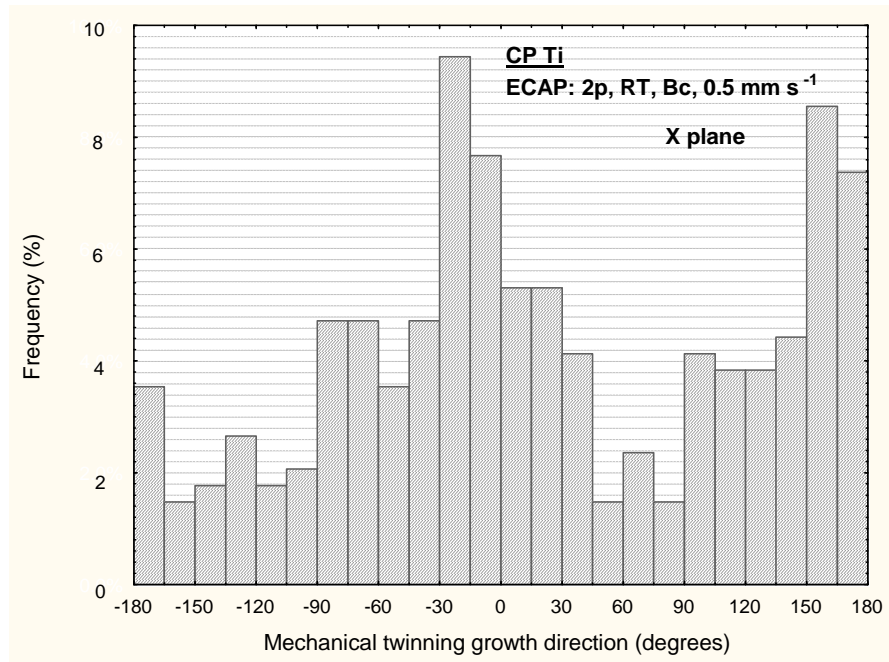


Fig. 5.10(b): Statistical distribution of twinning growth direction determined from the cross-sectional OM observations after pressing for two passes at a speed of 0.5 mm/s.

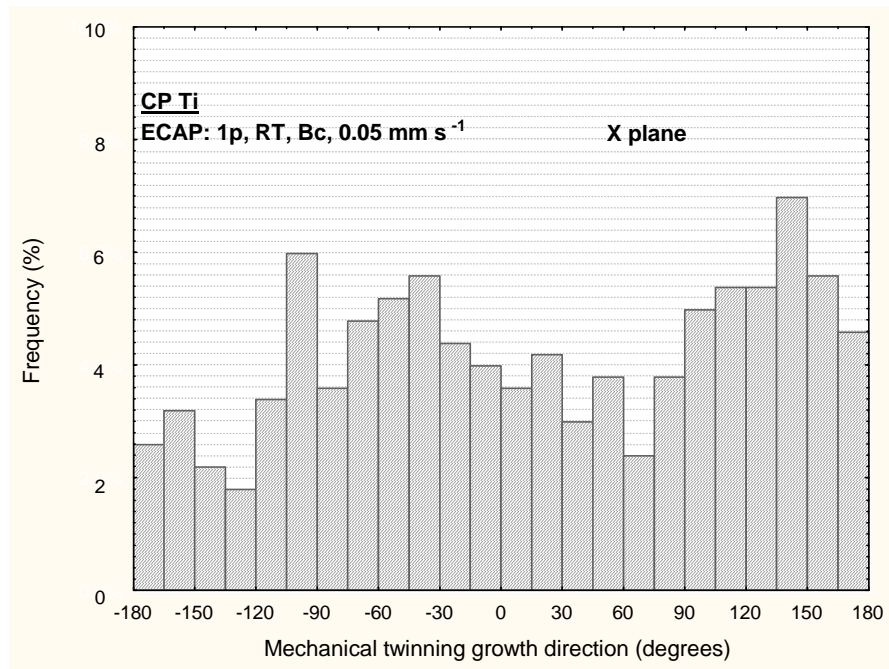


Fig. 5.10(c): Statistical distribution of twinning growth direction determined from the cross-sectional OM observations after pressing for one pass at a speed of 0.05 mm/s.

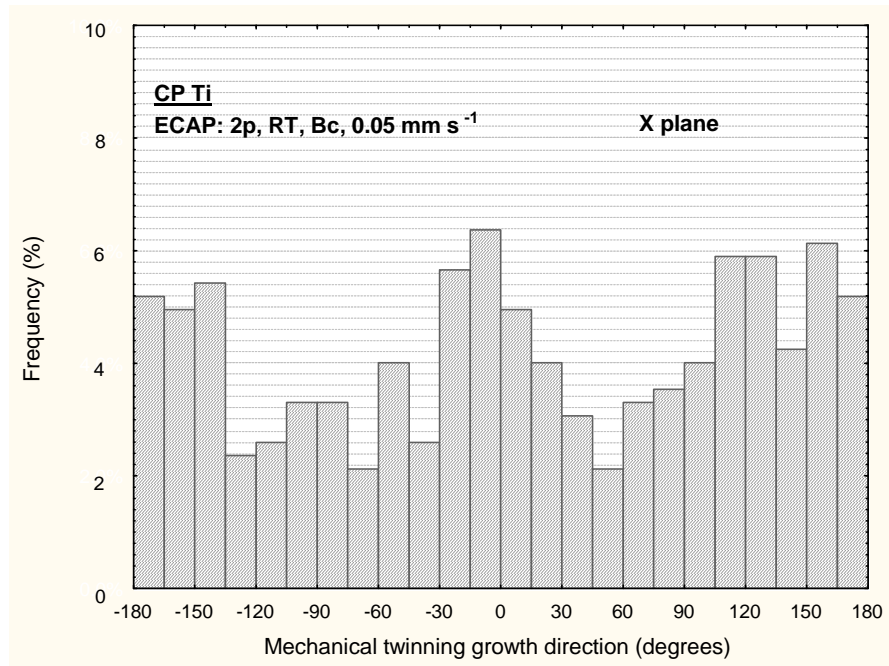


Fig. 5.10(d): Statistical distribution of twinning growth direction determined from the cross-sectional OM observations after pressing for two passes at a speed of 0.05 mm/s.

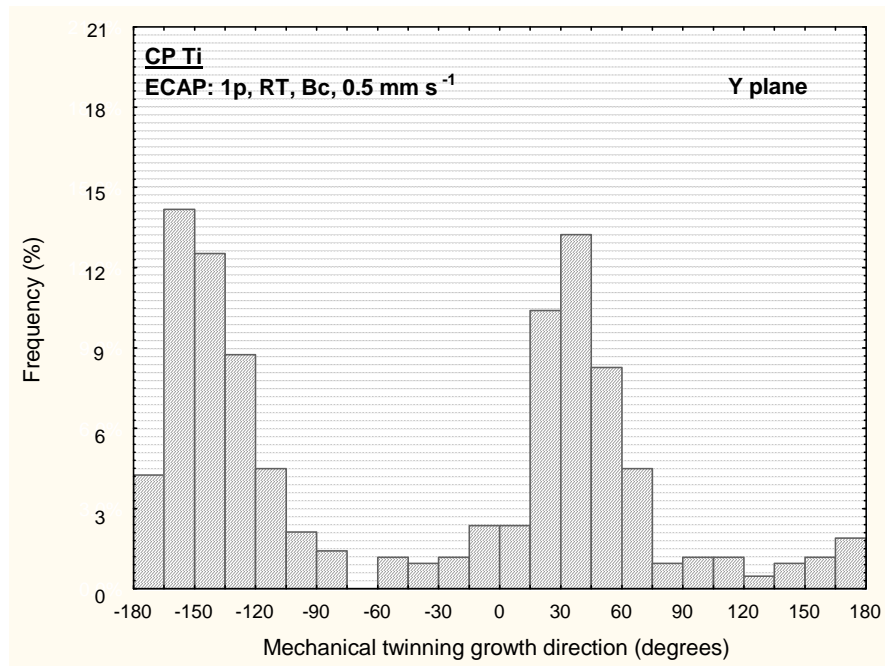


Fig. 5.11(a): Statistical distribution of twinning growth direction determined from the vertical longitudinal OM observations after pressing for one pass at a speed of 0.5 mm/s.

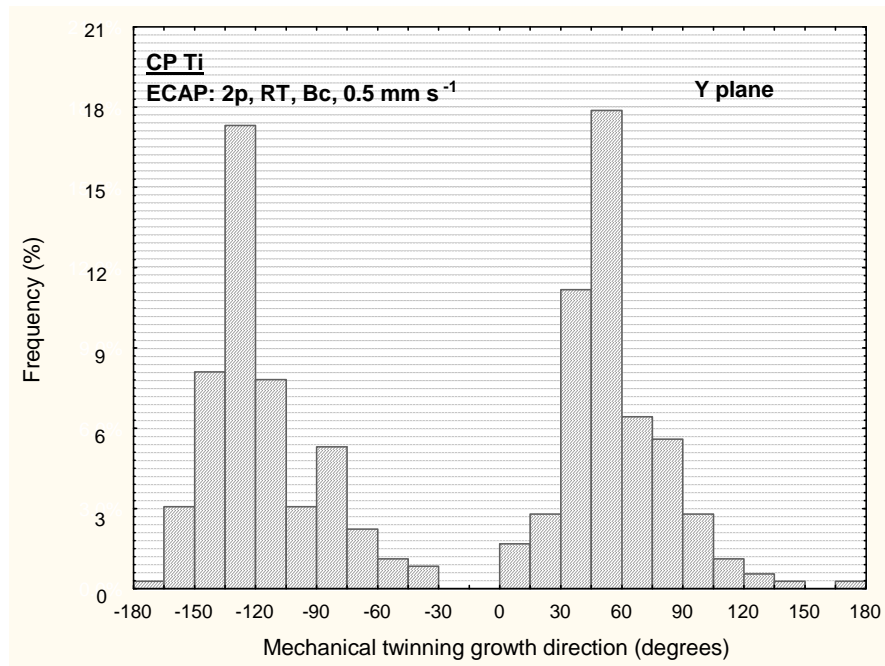


Fig. 5.11(b): Statistical distribution of twinning growth direction determined from the vertical longitudinal OM observations after pressing for two passes at a speed of 0.5 mm/s

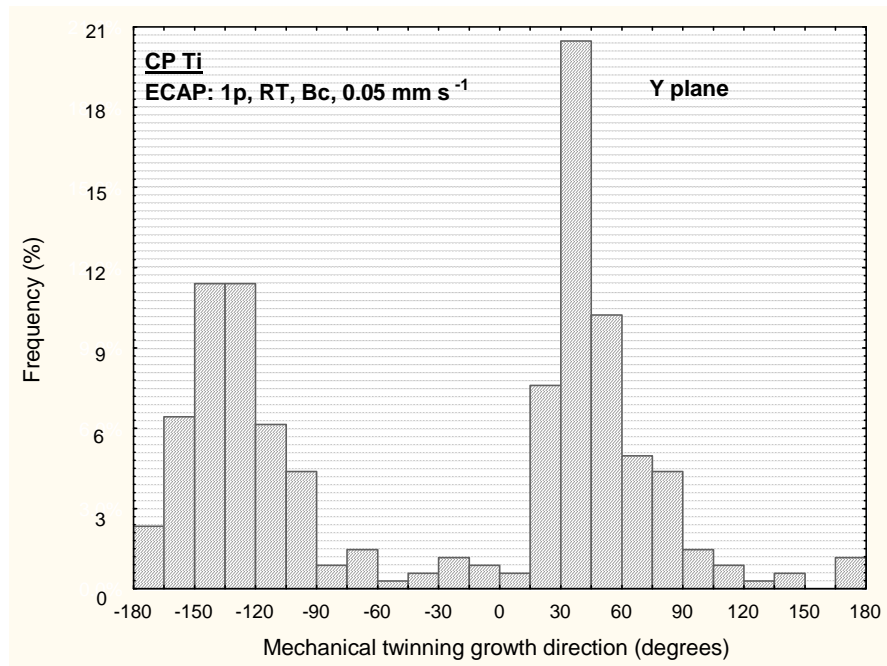


Fig. 5.11(c): Statistical distribution of twinning growth direction determined from the vertical longitudinal OM observations after pressing for one pass at a speed of 0.05 mm/s

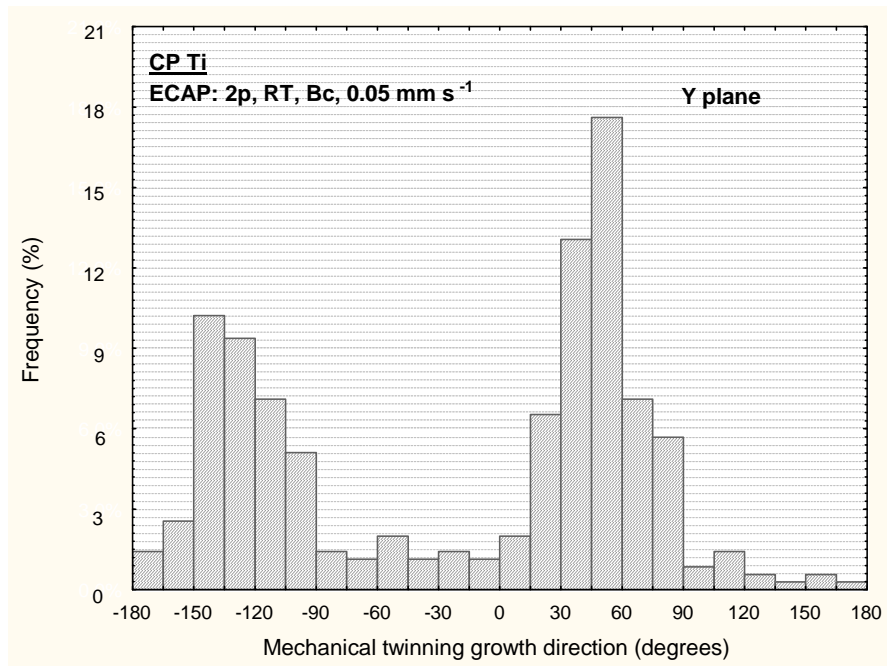


Fig. 5.11(d): Statistical distribution of twinning growth direction determined from the vertical longitudinal OM observations after pressing for two passes at a speed of 0.05 mm/s

5.4 Discussion

Processing materials at low temperatures leads to finer grain sizes and higher fractions of high angle boundaries, compared to processing at elevated temperatures which in turn enhances the mechanical properties of metals [125]. However, performing ECAP experiments at low temperatures (i.e. room temperature) for some hard to process materials like titanium is not easy and it is more convenient to process these materials at elevated temperatures. This difficulty initiated essentially from the increase in the load required by the press to process the material which may reach critical values that may damage some parts of the experimental facility. In addition, processing some hard to work materials such as titanium at low temperatures may lead to cracking and segmentation [33]. To avoid these limitations when processing these materials at room temperature, two conditions must be satisfied according to Zhao et al. [37]. First, the die channel angle (Φ) must be increased to at least 120 deg. Second, the pressing speed must be reduced to approximately 0.5 mm/s or less.

The most important conclusion for this investigation is proving the feasibility to process commercial purity titanium (CP Ti) by ECAP at room temperature. Considering the two conditions required to successfully processing CP Ti by ECAP at room temperature; increasing the die channel angle (Φ) to 135 deg led to successfully processing CP Ti at room temperature through two passes. For the second condition; reducing the pressing speed to 0.5 mm/s led to processing CP Ti at room temperature through one pass. But, when processing at the same speed through two passes, a crack was introduced in the middle of the billet. However, reducing the speed to a slower speed by one magnitude (i.e. 0.05 mm/s) led to processing CP Ti at room temperature through two passes successfully and without initiating any visible cracks. These results confirm the results established by Zhao et al. [37] and confirm the two conditions for successfully perform ECAP experiments on hard to work materials at room temperatures.

The results of the hardness recorded in this investigation were compared to results of other investigations [37,54,56,57], as in Table 5.2. The hardness was converted from

Hv to MPa by multiplying by the factor (9.807) and only the results of the billets that successfully introduced a smooth flow without visible cracking were considered in the table. It is clear from the table that the hardness after two passes of ECAP using a die which has an angle of 135 deg at room temperature at the slower speed of 0.05 mm/s is very close to the hardness after eight passes at elevated temperatures and it is even more than the hardness after seven passes at elevated temperatures. It is also very close to the hardness after ECAP using a die which has an angle of 120 deg after one pass; taking into consideration that performing ECAP using 135 deg die angle is easier and more convenient than performing the experiments using 120 deg die angle.

Table 5.2: The hardness of CP Ti at this and earlier investigations:

	ECAP conditions				Hardness (MPa)
	Angle (Φ)	Temp. (K)	N	Pressing Speed (mm/s)	
This investigation					
Annealed unpressed	-	-	-	-	1710
After ECAP	135°	R.T.	1	0.5	2160
	135°	R.T.	1	0.05	2260
	135°	R.T.	2	0.05	2400
Earlier investigations					
Stolyarov et al. [54]	90°	723-773	7	-	2350
Stolyarov et al. [56]	90°	673-723	8	6	2610-2830
Stolyarov et al. [57]	90°	673-723	8	-	2700-2810
Zhao et al. [37]	120°	R.T.	1	0.5	2430

The microstructures introduced in this investigation after ECAP through one and two passes at room temperature, which are covered by high fraction of deformation twins, are consistent with the microstructures found in earlier investigations when processing CP Ti by ECAP [37,55,59,60,66]. It was suggested always that the limited slip system in hexagonal close packed (hcp) systems such as CP Ti is assisted by the formation of the deformation twins. The density of the deformation twins does not change after pressing through two passes from that after one pass and this result

is consistent with earlier investigation of processing CP Ti for one and two passes at elevated temperatures [60]. It was shown in the investigation by Shin et al [60] that the density of the twins did not change much after two passes compared to pressing for one pass but, on the other hand, the density of dislocations increased significantly. It was concluded that the essential deformation mechanism in the first pass of ECAP for CP Ti was the deformation twinning and in the second pass was dislocation slip. It was suggested that the microstructural changes such as grain-size refinement and texture formation which occurred during the first pass increased the critical resolved shear stress (CRSS) for deformation twinning over that for dislocation slip.

5.5 Summary and Conclusions

1. Commercial purity titanium (CP Ti) billets were processed by ECAP at room temperature through one and two passes using a die which have a channel angle of 135 deg. Two pressing speeds were used in this investigation; 0.5 and 0.05 mm/s, and the processing route was route B.
2. The billets were successfully pressed through two passes using a pressing speed of 0.05 mm/s without having any visible crack. Processing the billets using the higher speed of 0.5 mm/s was successfully done through one pass. However, a crack in the middle of the billet was initiated when processing by the higher speed through two passes.
3. The results of this investigation confirm the conclusion of a previous study established by Zhao et al. [37] establishing that two conditions must be satisfied for performing ECAP on the hard to process materials at room temperature; increase the die angle to 120 deg or more and reduce the pressing speed to 0.5 mm/s or less.
4. The resultant hardness after two passes of ECAP at room temperature using 135 die angle was very close, or even slightly better in some cases, to the hardness after ECAP through seven and eight passes at elevated temperatures. The resultant hardness in this investigation after two passes using 135 deg die angle was similar to the hardness after ECAP through one pass using 120 deg die angle.
5. The essential deformation mechanism after one pass of ECAP for CP Ti is the deformation twinning. After two passes, the dominant deformation mechanism becomes the dislocation slip.

CHAPTER 6

THE EVOLUTION OF HOMOGENEITY IN ALUMINIUM DURING PROCESSING BY HPT

6.1 Introduction

The theoretical shear strain imposed during torsional straining is given by $(2 \pi N r / h)$ where N , r and h are the number of turns, the radial distance from the centre and the thickness of the disk, respectively. Accordingly, at least theoretically with the assumption that the thickness of the disk remains constant, the shear strain increases linearly with the increase in the radius and the strain must be zero at the centre of the disk. The reports up to date which analyze the shear along the radial distance show some contradiction. Some reports agree with the theoretical shear strain relationship and show that the values of the microhardness along the diameter of disks processed by high pressure torsion (HPT) vary significantly with low values in the centre and high values near the edge of the disks [85-87]. On the other hand, most of the reports up to date show that this relationship is not valid at high pressures and number of turns where the microhardness values become reasonably homogeneous along the diameter of the disks processed by HPT [71,88-94]. A clear contradiction with this relationship is shown by Xu et al. [95] where the hardness at the centre of high purity aluminium disks processed by HPT is higher than that near the edge of the disk and with increasing number of turns the hardness become homogeneous along the diameter of the disk.

In this chapter, the microhardness will be recorded across the surfaces of two aluminium alloys; Al-1%Mg and Commercial purity aluminium (Al-1050), after processing by HPT for up to five turns. The evolution of the microhardness homogeneity, and hence the internal microstructure homogeneity as mentioned

previously, and the validity of the theoretical shear strain relationship for the two materials under high pressure and different number of turns will be investigated.

6.2 Experimental Materials and Procedures

The HPT experiments were conducted using disks cut from two aluminium alloys. The first was Aluminium -1.0 wt. % Magnesium (Al-1.0%Mg) alloy which has 0.003% Si and 0.001% Fe as minor impurities. The second was commercial purity aluminium alloy (Al-1050) with a weight percent of at least 99.5% aluminium and with a chemical composition in weight percent (wt. %) as shown previously in Table 3.1. Both alloys were supplied in the form of billets having a length of 65.0 mm and a diameter of 10.0 mm.

The HPT experiments were conducted in air at room temperature using a facility as shown in the photographs in Figs. 6.1-6.3. Fig. 6.1 shows a photograph of the HPT facility illustrating the high pressure press and the control panel. Fig. 6.2 shows the control panel with the pressure gauges. Fig. 6.3 shows the high pressure torsion facility illustrating the upper and lower anvils. The HPT process is illustrated schematically in Fig. 6.4. The facility consists of an upper and lower anvil made from high-strength tool steel. A spherical cavity having a diameter of 10.0 mm was machined at the centre of each anvil. The surfaces of both anvils were roughened and hardened using shot peening process. As illustrated schematically in Fig. 6.4, the experiments were performed under a quasi-constrained condition in which a limited material is flowing outward between the two anvils. The alloy disk was fitted in the cavity on the lower anvil which is then moved upward. The two anvils were then brought together to impose a pressure on the disk. After achieving the full contact between the disk and the surfaces of the two anvils and applying the pressure on the disk, the rotation was made concurrently with the compression. The lower anvil was rotated at a speed of one r.p.m.



Fig 6.1: HPT facility showing the two sets: the control panel and the high pressure press.



Fig 6.2: The control panel and the pressure gauges.



Fig 6.3: The high pressure torsion facility showing the upper and lower anvil.

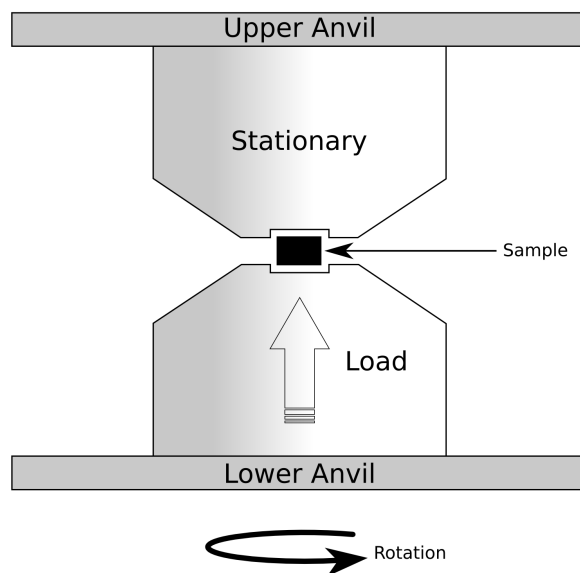


Fig. 6.4: Illustration of the HPT facility showing the sample under pressure and rotation.

The disks of each material were subjected to HPT for totals of quarter, one and five turns, respectively. The applied load used in these experiments was 48 tons which is corresponding to an imposed pressure, P , of 6.0 GPa. The conversion calculations used to convert the load in tons into pressure in GPa are:

$$\begin{aligned}
 \text{Load} &= 48 \text{ ton} = 48000 \text{ kg} \\
 \text{Force} = F &= \frac{48000 \text{ kg}}{0.102 \text{ kg/N}} = 470588.2 \text{ N} \\
 \text{Area} = A &= \pi r^2 = \pi (5 \times 10^{-3})^2 = 7.854 \times 10^{-5} \text{ m}^2 \\
 \text{Pressure} = P &= \frac{F}{A} = \frac{470588.2 \text{ N}}{7.854 \times 10^{-5} \text{ m}^2} = 6 \times 10^9 \text{ N/m}^2 \\
 &= 6 \text{ GPa}
 \end{aligned}$$

There was a very small reduction in the thickness of the disk noticed after processing due to the very high pressure used in the experiments.

After the HPT process, the disks were mounted using a cold-setting resin based on two fluid epoxy components and then carefully polished using 120, 600, 1200 and 4000 grit to a mirror-like finish. Microhardness measurements, H_v , were then taken on the disks using a Matsuzawa Seiki MHT-1 microhardness tester equipped with a Vickers indenter. For each measurement, a load of 50 gf was applied for a dwell time of 15 seconds. Three procedures were used for taking the microhardness measurements. First, 33 points across the diameter of each disk were selected to take the measurements at them and at each point four measurements were taken as shown in Fig. 6.5. The measurements started at the centre of the disk (i.e. at 5.0 mm from the edge) at an increment of 0.3 mm between each point and the adjacent point. The distance between the first data point and the edge of the disk was 0.2 mm and the same distance was managed between the last data point and the edge of the disk. At each data point, four measurements were taken; at the top, the bottom, the left and the right. The distance between each measurement of these four measurements and the centre of the data point was 0.15 mm. The total number of microhardness measurements for each diameter line was 100 data points. Graphs were then plotted where the data points show error bars which were calculated by the statistical method

explained later. Second, microhardness measurements were taken across the surface of each disk with an increment of 0.6 mm between the data points on both axes, X and Y. The total number of microhardness measurements covering the surface of each disk was 227 data points. Colour-coded contour maps were then performed for each disk showing the distributions of the microhardness, Hv, on the surface of the HPT disks after quarter, one and five turns for both alloys. Third, three-dimensional representations were performed for the individual microhardness measurements of all disks with the Hv microhardness lying on one axis and the axes X and Y lying on the other two axes.

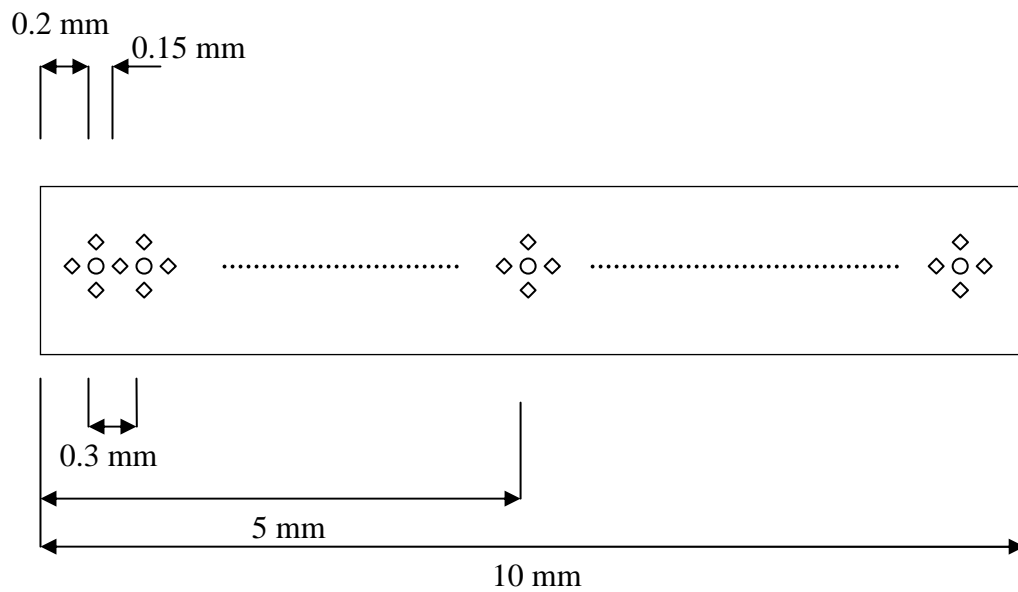


Fig. 6.5: Illustration of the process used for taking the data points along the diameter of the disks after HPT.

Error Bars Calculations Based on the Experimental Data [126]:

Calculating the error bars about the mean begins with calculating the *sample standard deviation* s :

$$\text{mean} = \bar{C} = \sum_{i=1}^N C_i / N$$

$$\text{sample standard deviation} = s = \left\{ \sum_{i=1}^N (C_i - \bar{C})^2 / (N-1) \right\}^{1/2}$$

where N is the number of measurements. The sample standard deviation s is the best guess for the standard deviation of the distribution. The confidence limits for the mean (error bars) are obtained by the following expression:

$$\text{Error Bars} : \pm \frac{t s}{\sqrt{N}}$$

In this expression, the value of (t) is determined from Table 6.1 by two parameters:

1. *The number of degrees of freedom in the measurement.* With N measurements, the number of degrees of freedom is $N-1$. In this experiment, the number of data measurements in each point (N) was four. So, there are three degrees of freedom.
2. *The size of the desired confidence limits.* The confidence limit used in this investigation was 95%.

From Table 6.1, the value of (t) which was used in this investigation is 3.182.

Table 6.1: The factor (t) used in calculating the error bars:

	Confidence Limit				
Degrees Of freedom	90%	95%	98%	99%	99.9%
1	6.314	12.706	31.821	63.657	636.619
2	2.920	4.303	6.965	9.925	31.598
3	2.353	3.182	4.541	5.841	12.941
4	2.132	2.776	3.747	4.604	8.610
5	2.015	2.571	3.365	4.032	6.859
6	1.943	2.447	3.143	3.707	5.959
7	1.895	2.365	2.998	3.499	5.405
8	1.860	2.306	2.896	3.355	5.041
9	1.833	2.262	2.821	3.250	4.781
10	1.812	2.228	2.764	3.169	4.587
20	1.725	2.086	2.528	2.845	3.850
30	1.697	2.042	2.457	2.750	3.646
40	1.684	2.021	2.423	2.704	3.551
60	1.671	2.000	2.390	2.660	3.460
120	1.658	1.980	2.364	2.617	3.373
∞	1.645	1.960	2.326	2.576	3.291

6.3 Experimental Results

In this research, HPT experiments were performed on two aluminium alloys (Al-1%Mg and Al-1050) for 1/4, 1 and 5 turns under a pressure of 6 GPa, then the measurements of the Vickers microhardness, Hv, were recorded using three different methods. First, the individual measurements of the Vickers microhardness, Hv, were recorded across the diameter of each disk. Second, the individual microhardness measurements were recorded on the surface of each disk to give colour-coded contour maps. Third, the individual microhardness measurements were recorded on the surface of each disk to give three-dimensional representations.

6.3.1 Al-1% Mg alloy:

Fig. 6.6 shows the individual microhardness measurements recorded along the diameter after HPT under a pressure of 6.0 GPa for (a) 1/4, (b) one and (c) five turns, respectively. The microhardness measurements for alloy in the as-received unprocessed condition are also shown. As shown in Fig. 6.6(a), the microhardness values increased after processing by HPT for 1/4 turn from an initial value of ~31.5 in the as-received unprocessed material to values ranging between ~47 at the centre of the disk and ~92 near the edge of the disk. The increment in the microhardness values near the edge of the disk is approximately 300%. The microhardness measurements near the centre of the disk were small and increased almost linearly with increasing distance from the centre. After one turn, as shown in Fig. 6.6(b), the microhardness measurements at the centre of the disk increased slightly to reach ~54 and it reached near the edges of the disk ~120 which is approximately 400% increment than that in the as-received unprocessed material. The microhardness values started to become slightly constant beyond a distance of ~3.0 mm from the centre of the disk where the values are ranging between ~110-120. After five turns, as shown in Fig. 6.6(c), the microhardness values at the centre of the disk increased to a value of approximately ~70 and remained constant near the edges of the disk with approximately ~120. After a distance of ~0.7 mm from the centre of the disk, the microhardness values started to become slightly constant where the values are ranging between ~110-122. The distance of approximately constant microhardness

values was larger compared to the distance after one turn of HPT. It is also noticed from the figure that the error in the microhardness measurements taken near the centre of the disk was remarkably higher than that away from the centre.

Fig. 6.7 compares the individual microhardness measurements recorded along the diameter after HPT under a pressure of 6.0 GPa for 1/4, one and five turns, respectively. The microhardness measurements for the alloy in the as-received unprocessed condition are also shown. As shown in the figure, the microhardness measurements increased with increasing number of turns until reaching a saturation value of approximately ~120 near the edges of the disk. This saturation value starts to move inwards with increasing number of turns until it covers the whole length of the diameter of the disk processed for five turns except for a distance of 0.7 mm from the centre of the disk on both sides.

Fig. 6.8 shows the colour-coded contour maps of the microhardness measurements across the surface of the Al-1%Mg disks after HPT under a pressure of 6.0 GPa for (a) 1/4, (b) one and (c) five turns, respectively. The significance of the colours is shown by the scale lying on the right of the figures where the increments of the microhardness values are 10. After HPT for 1/4 turn, as shown in Fig. 6.8(a), the microhardness values were totally inhomogeneous and range between ~50 near the centre of the disk and ~90 near the edges of the disk. After one turn, as shown in Fig. 6.8(b), the microhardness became homogeneous with values of approximately ~110-120 beyond a circle of a radius of approximately ~2.5 mm from the centre of the disk while it was low inside this circle with values between 60 and 100. As shown in Fig. 6.8(c), the microhardness became homogeneous across the surface of the disk processed for five turns with values ranging between 110 and 130 except for a very small circle with a radius of approximately ~0.5 mm around the centre of the disk where the microhardness values were less than 100.

Fig. 6.9 shows the three-dimensional representations of the microhardness measurements across the surface of the Al-1%Mg disks after HPT under a pressure of 6.0 GPa for (a) 1/4, (b) one and (c) five turns, respectively. The significance of the colours is shown by the scale lying on the right of the figures where the increments of the microhardness values are 10. As shown in Fig. 6.9(a), the microhardness

values were totally inhomogeneous after HPT for 1/4 turn where it was low at the centre of the disk where the microhardness was ~50 and increased gradually to become ~90 near the edges of the disk. After one turn, as shown in Fig. 6.9(b), the microhardness values near the edges of the disk became homogeneous with values of approximately ~120 and dropping in the centre of the disk to reach values of approximately 60. As shown in Fig. 6.9(c), the microhardness values became homogeneous across the surface of the disk processed for five turns with values ranging between 120 and 130 and dropping again in the centre of the disk to reach values of about 70.

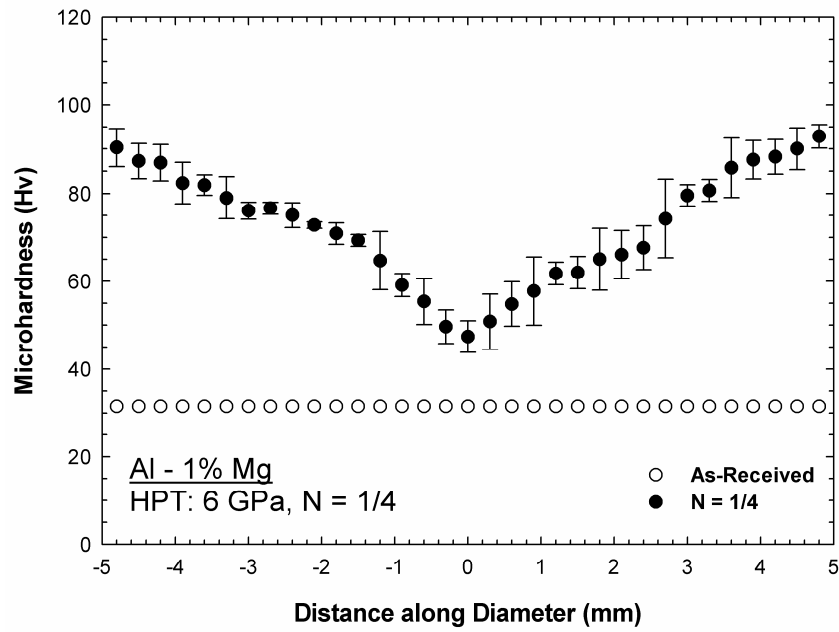


Fig. 6.6(a): Individual measurements of the microhardness, Hv, recorded along the diameter of Al-1%Mg disk after HPT under a pressure of 6.0 GPa for 1/4 turn. The microhardness measurements for alloy in the as-received unprocessed condition are also shown.

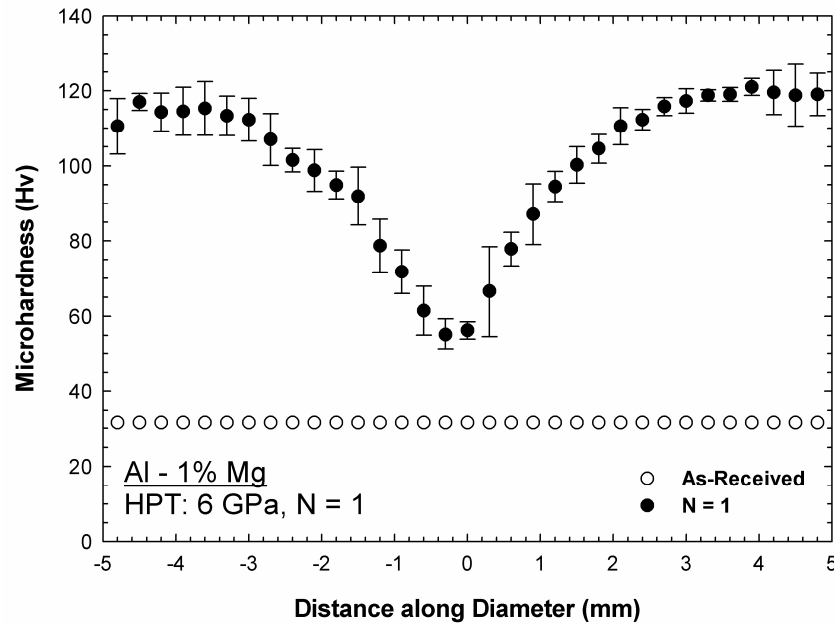


Fig. 6.6(b): Individual measurements of the microhardness, Hv, recorded along the diameter of Al-1%Mg disk after HPT under a pressure of 6.0 GPa for 1 turn. The microhardness measurements for alloy in the as-received unprocessed condition are also shown.

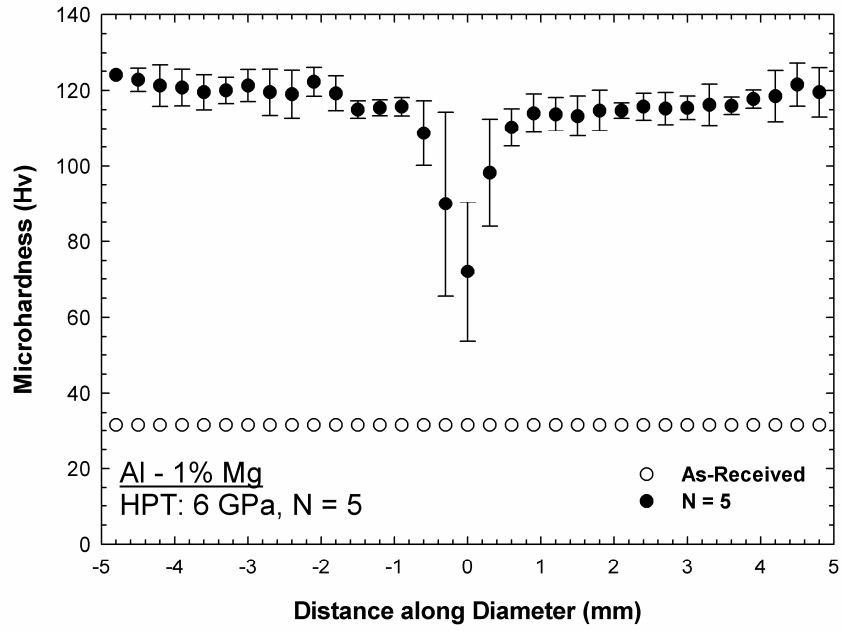


Fig. 6.6(c): Individual measurements of the microhardness, Hv, recorded along the diameter of Al-1%Mg disk after HPT under a pressure of 6.0 GPa for 5 turns. The microhardness measurements for alloy in the as-received unprocessed condition are also shown.

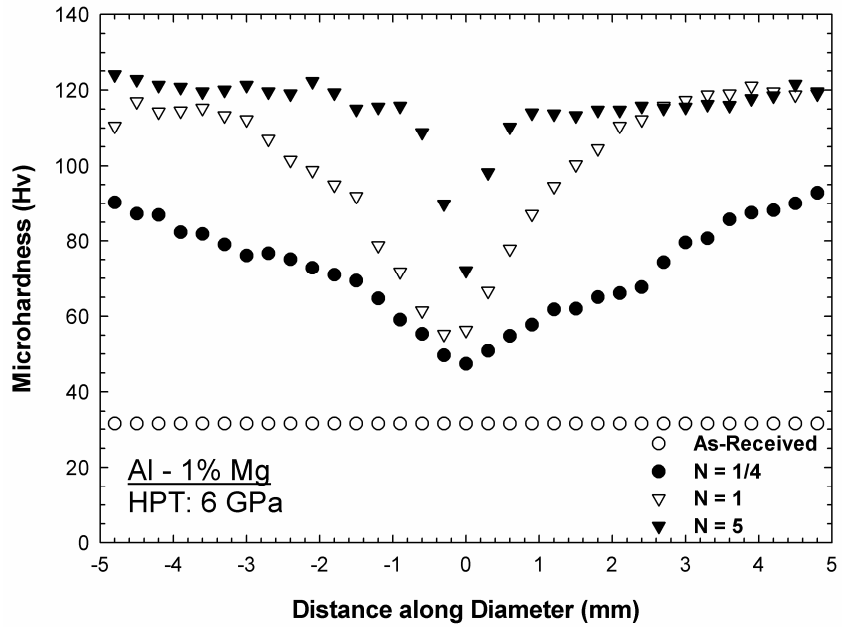


Fig. 6.7: Individual microhardness measurements recorded along the diameter of Al-1%Mg disks after HPT under a pressure of 6.0 GPa for 1/4, 1 and 5 turns. The microhardness measurements for alloy in the as-received unprocessed condition are also shown.

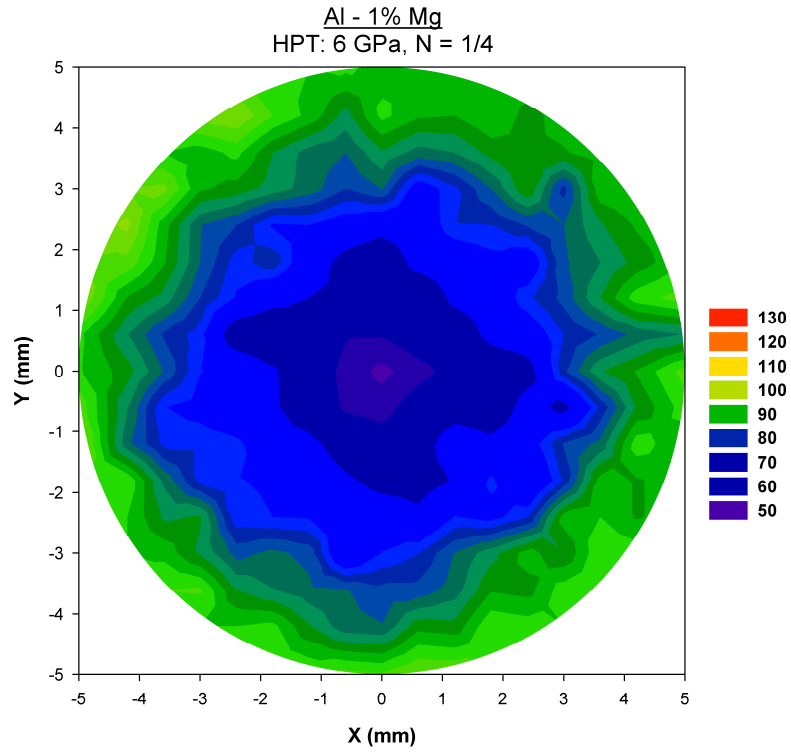


Fig. 6.8(a): The colour-coded contour maps of the microhardness measurements along the surface of Al-1% Mg disk after HPT under a pressure of 6.0 GPa for 1/4 turn. The significance of the colours is shown by the scale lying on the right of the figures.

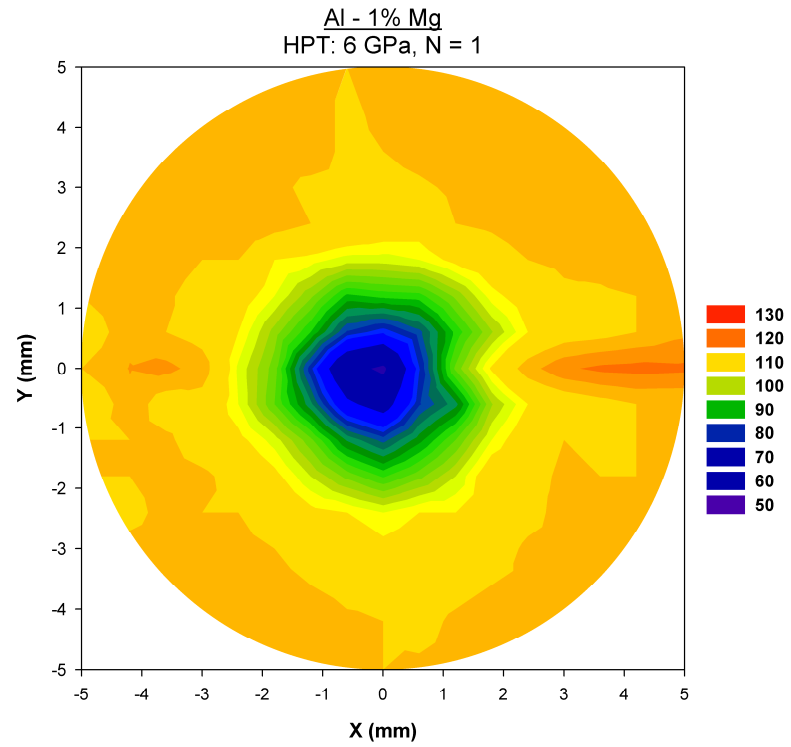


Fig. 6.8(b): The colour-coded contour maps of the microhardness measurements along the surface of Al-1%Mg disk after HPT under a pressure of 6.0 GPa for 1 turn. The significance of the colours is shown by the scale lying on the right of the figures.

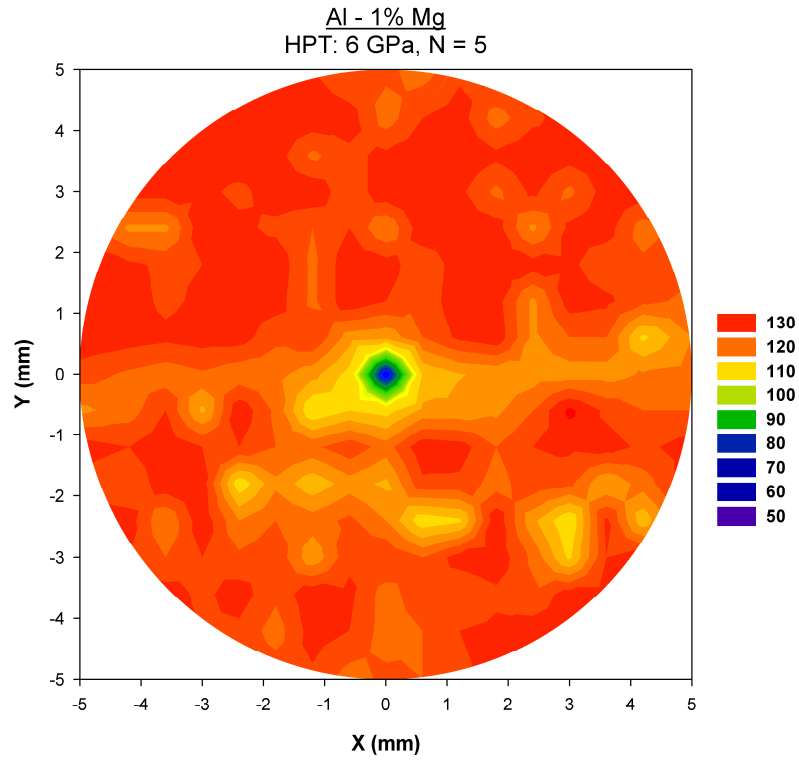


Fig. 6.8(c): The colour-coded contour maps of the microhardness measurements along the surface of Al-1%Mg disk after HPT under a pressure of 6.0 GPa for 5 turns. The significance of the colours is shown by the scale lying on the right of the figures.

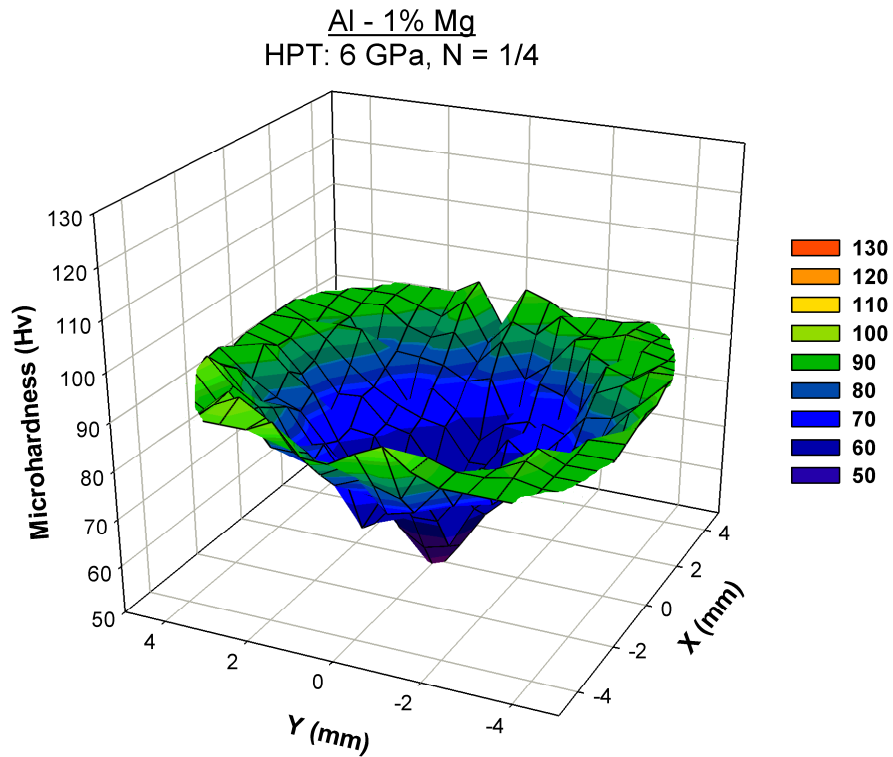


Fig. 6.9(a): Three-dimensional representation of the hardness measurements on the surface of Al-1%Mg disk after HPT under a pressure of 6.0 GPa for 1/4 turn: the significance of the colours is shown on the right.

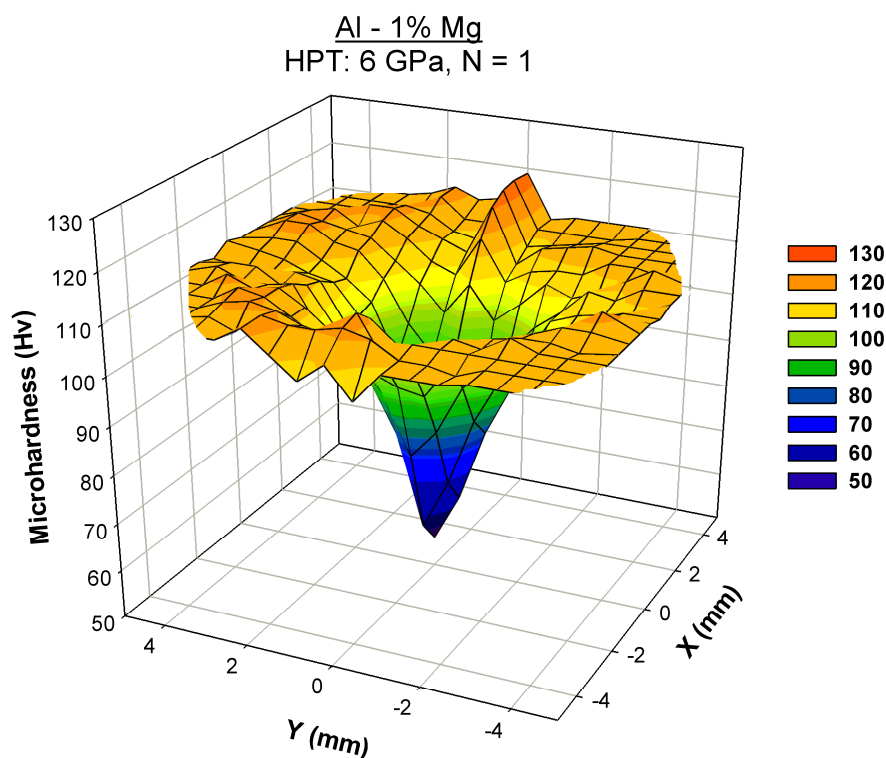


Fig. 6.9(b): Three-dimensional representation of the hardness measurements on the surface of Al-1%Mg disk after HPT under a pressure of 6.0 GPa for 1 turn: the significance of the colours is shown on the right.

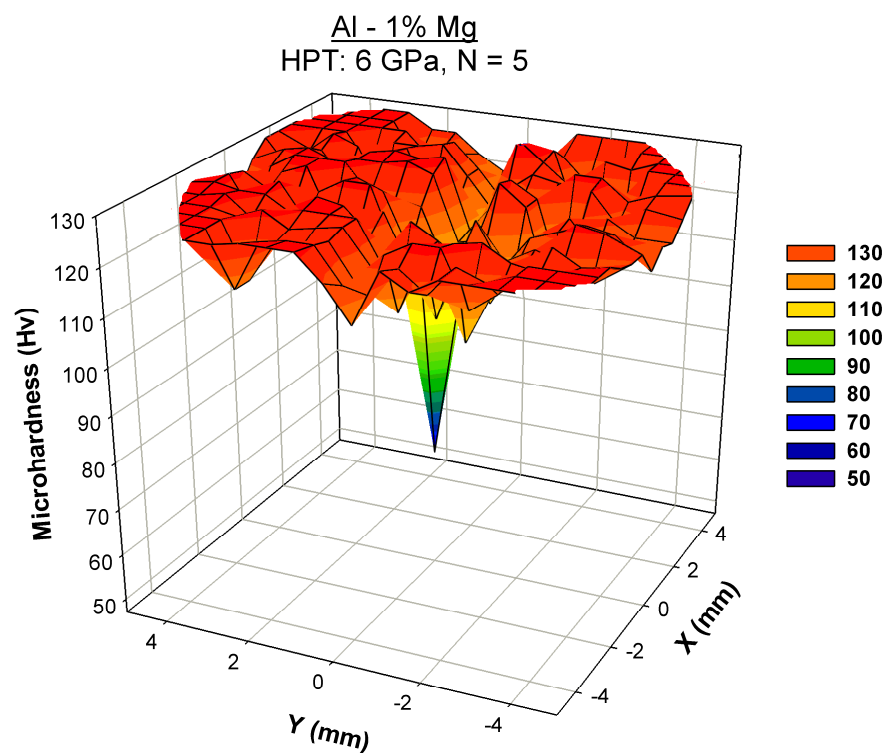


Fig. 6.9(c): Three-dimensional representation of the hardness measurements on the surface of Al-1%Mg disk after HPT under a pressure of 6.0 GPa for 5 turns: the significance of the colours is shown on the right.

6.3.2 Al-1050 alloy:

Fig. 6.10 shows the individual microhardness measurements recorded along the diameter after HPT under a pressure of 6.0 GPa for (a) 1/4, (b) one and (c) five turns, respectively. The microhardness measurements for the alloy in the as-received unprocessed condition are also shown. As shown in Fig. 6.10(a), the microhardness values increased after processing by HPT for 1/4 turn from an initial value of ~27 in the as-received unprocessed material to values ranging between ~41 at the centre of the disk and ~61 near the edge of the disk. The increment in the microhardness values near the edge of the disk is approximately 225%. The microhardness measurements reached a constant value of about ~60 after a distance of 2.0 mm from the centre of the disk on both sides. After one turn, as shown in Fig. 6.10(b), the microhardness measurements at the centre of the disk increased slightly to reach ~45 and remained constant near the edges of the disk where the values were approximately ~62. The microhardness values started to become constant beyond a distance of ~1.0 mm from the centre of the disk. It is also noticed that the error in the microhardness measurements taken near the centre of the disk was high compared to the error in the measurements away from the centre. After five turns, as shown in Fig. 6.10(c), the microhardness values became constant along the entire length of the diameter where the values of the microhardness were approximately ~62.

A comparison between the three cases is shown in Fig. 6.11 where the individual microhardness measurements are recorded after HPT under a pressure of 6.0 GPa for 1/4, one and five turns, respectively. The microhardness measurements for the alloy in the as-received unprocessed condition are also shown. As shown in the figure, the microhardness measurements reached a saturation value of approximately ~60 near the edges of the disk after 1/4 turn. This saturation value started at the edges and continued to a length of 3.0 mm from the edges after 1/4 turn. It continued to a length of 4.0 mm from the edges after 1 turn and it continued along the entire length of the diameter after five turns.

The colour-coded contour maps of the microhardness measurements across the surface of the Al-1050 disks after HPT under a pressure of 6.0 GPa for (a) 1/4, (b) one and (c) five turns, respectively, are shown in Fig. 6.12. The significance of the

colours is shown by the scale lying on the right of the figures where the increments of the microhardness values are 5. After HPT for 1/4 turn, as shown in Fig. 6.12(a), the microhardness values were slightly homogeneous with values of approximately ~60-65 beyond a circle of a radius of approximately ~2.0 mm from the centre of the disk while it was low inside this circle with values between 40 and 55. After one turn, as shown in Fig. 6.12(b), the microhardness became reasonably homogeneous with values of approximately ~60-65 across the entire surface except a small circle having radius of approximately ~1.0 mm around the centre of the disk where the microhardness values were less than 55. As shown in Fig. 6.12(c), the microhardness became totally homogeneous across the entire surface of the disk processed for five turns where the microhardness values were approximately ~65.

The three-dimensional representations of the microhardness measurements across the surface of the Al-1050 disks after HPT under a pressure of 6.0 GPa for (a) 1/4, (b) one and (c) five turns, respectively, are shown in Fig. 6.13. The significance of the colours is shown by the scale lying on the right of the figures where the increments of the microhardness values are 5. After HPT for 1/4 turn, as shown in Fig. 6.13(a), the microhardness values near the edges of the disk were homogeneous with values ranging between 60 and 65. The microhardness dropped in the centre of the disk to reach values of approximately 40. After one turn, as shown in Fig. 6.13(b), the homogeneity of the microhardness measurements increased compared to the disk processed for 1/4 turn where the values were approximately 65. However, the microhardness measurements dropped near the centre of the disk to reach values of about 45. The microhardness values became totally homogeneous across the entire surface of the disk processed for five turns with values of approximately 65, as shown in Fig. 6.13(c).

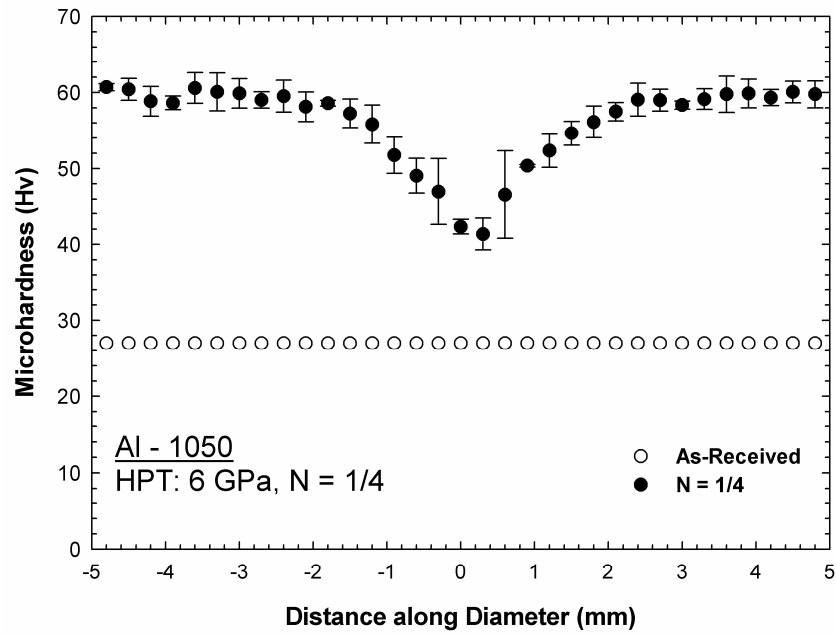


Fig. 6.10(a): Individual measurements of the microhardness, Hv, recorded along the diameter of Al-1050 disk after HPT under a pressure of 6.0 GPa for 1/4 turn. The microhardness measurements for alloy in the as-received unprocessed condition are also shown.

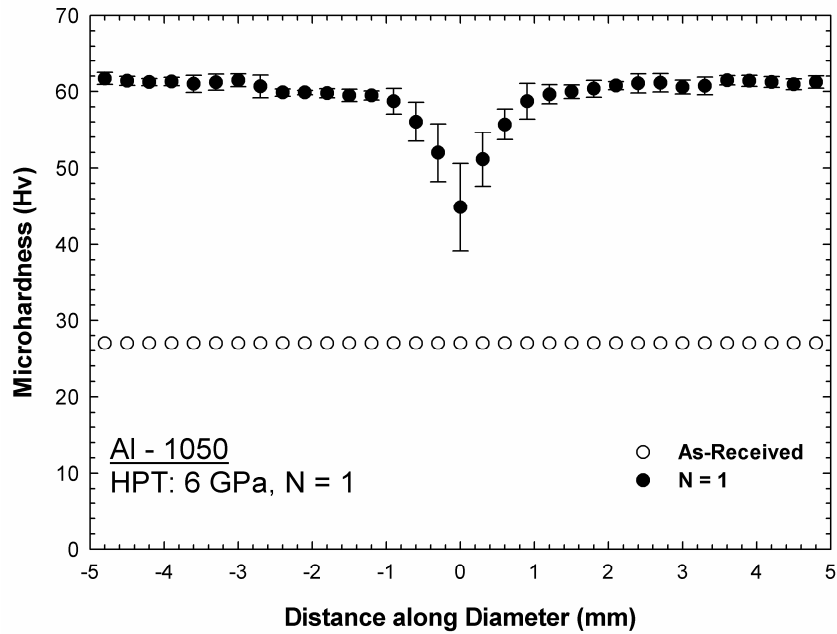


Fig. 6.10(b): Individual measurements of the microhardness, Hv, recorded along the diameter of Al-1050 disk after HPT under a pressure of 6.0 GPa for 1 turn. The microhardness measurements for alloy in the as-received unprocessed condition are also shown.

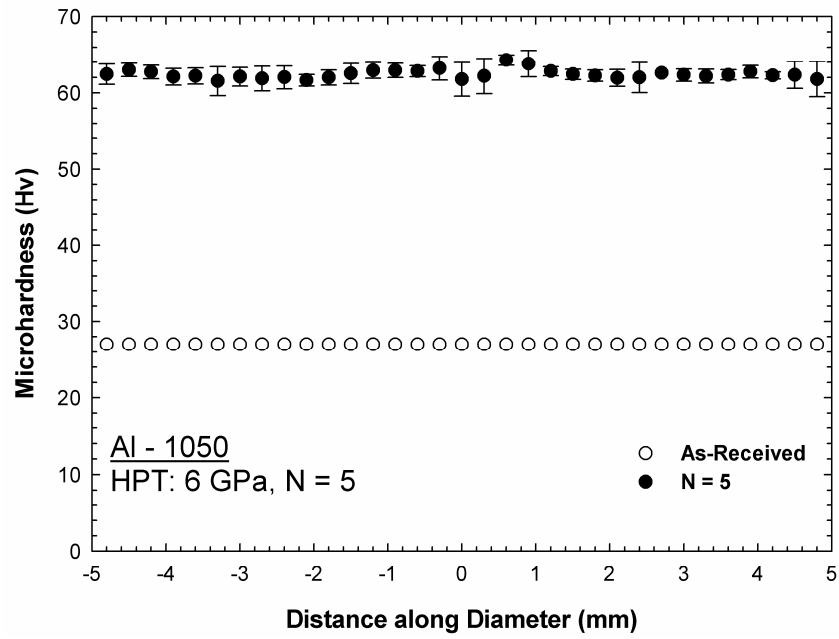


Fig. 6.10(c): Individual measurements of the microhardness, Hv, recorded along the diameter of Al-1050 disk after HPT under a pressure of 6.0 GPa for 5 turns. The microhardness measurements for alloy in the as-received unprocessed condition are also shown.

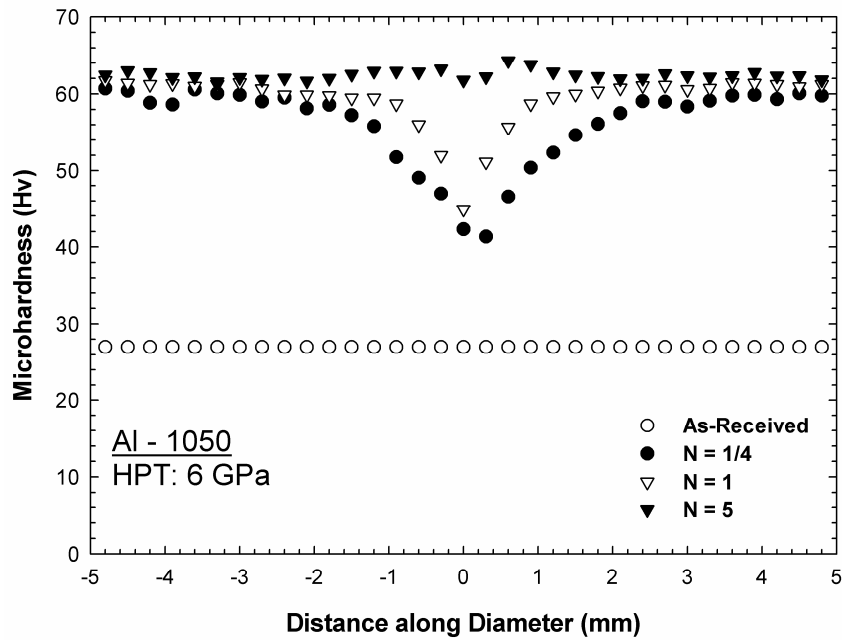


Fig. 6.11: Individual microhardness measurements recorded along the diameter of Al-1050 disks after HPT under a pressure of 6.0 GPa for 1/4, 1 and 5 turns. The microhardness measurements for alloy in the as-received unprocessed condition are also shown.

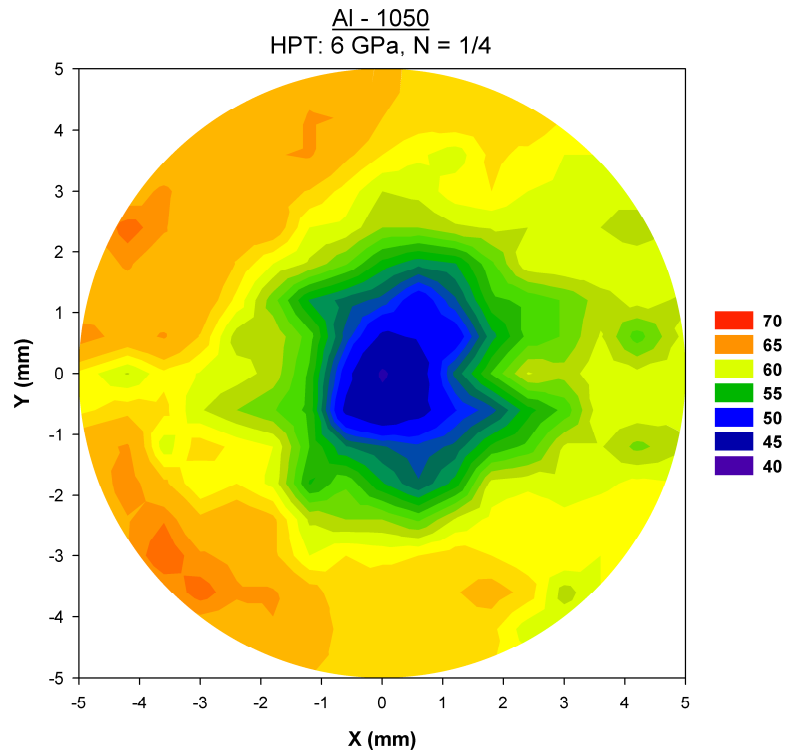


Fig. 6.12(a): The colour-coded contour maps of the microhardness measurements along the surface of Al-1050 disk after HPT under a pressure of 6.0 GPa for 1/4 turn. The significance of the colours is shown by the scale lying on the right of the figures.

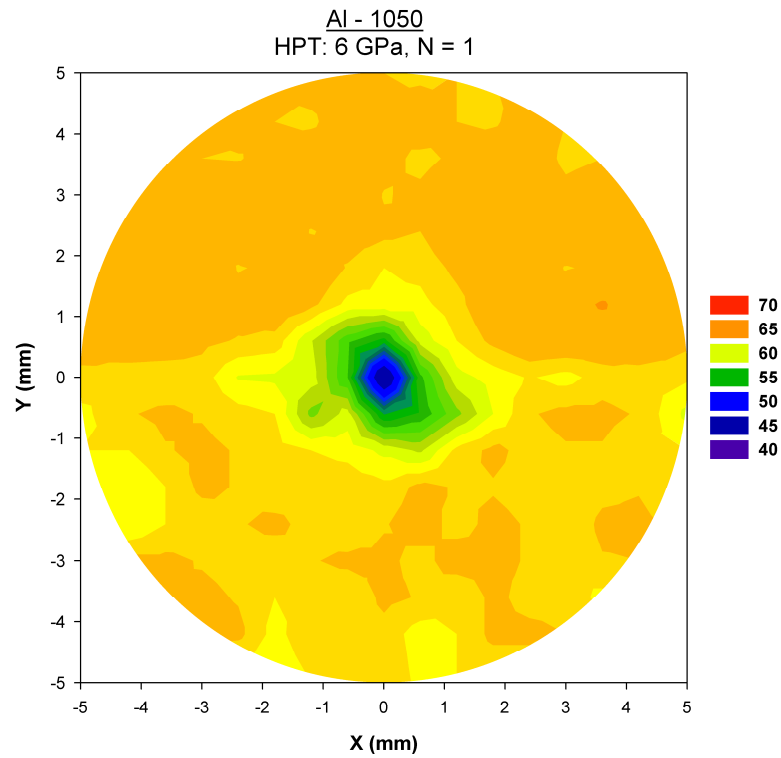


Fig. 6.12(b): The colour-coded contour maps of the microhardness measurements along the surface of Al-1050 disk after HPT under a pressure of 6.0 GPa for 1 turn. The significance of the colours is shown by the scale lying on the right of the figures.

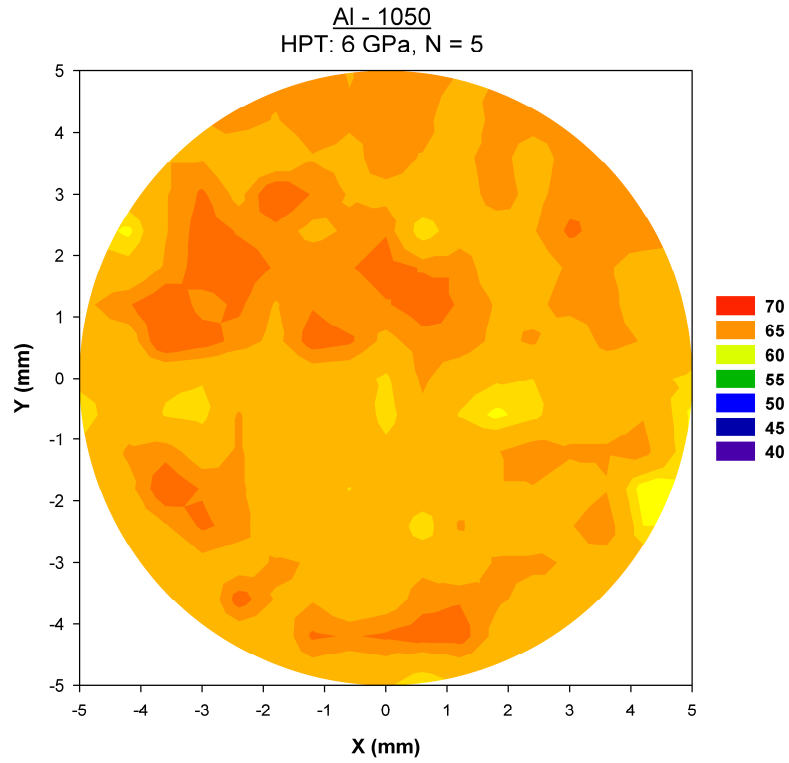


Fig. 6.12(c): The colour-coded contour maps of the microhardness measurements along the surface of Al-1050 disk after HPT under a pressure of 6.0 GPa for 5 turns. The significance of the colours is shown by the scale lying on the right of the figures.

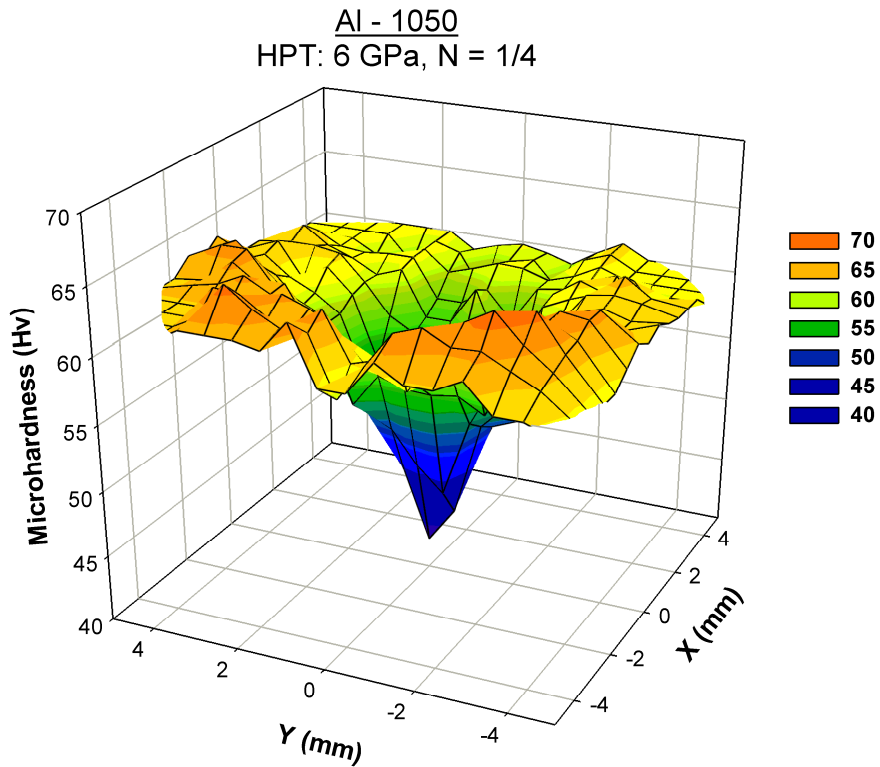


Fig. 6.13(a): Three-dimensional representation of the hardness measurements on the surface of Al-1050 disk after HPT under a pressure of 6.0 GPa for 1/4 turn: the significance of the colours is shown on the right.

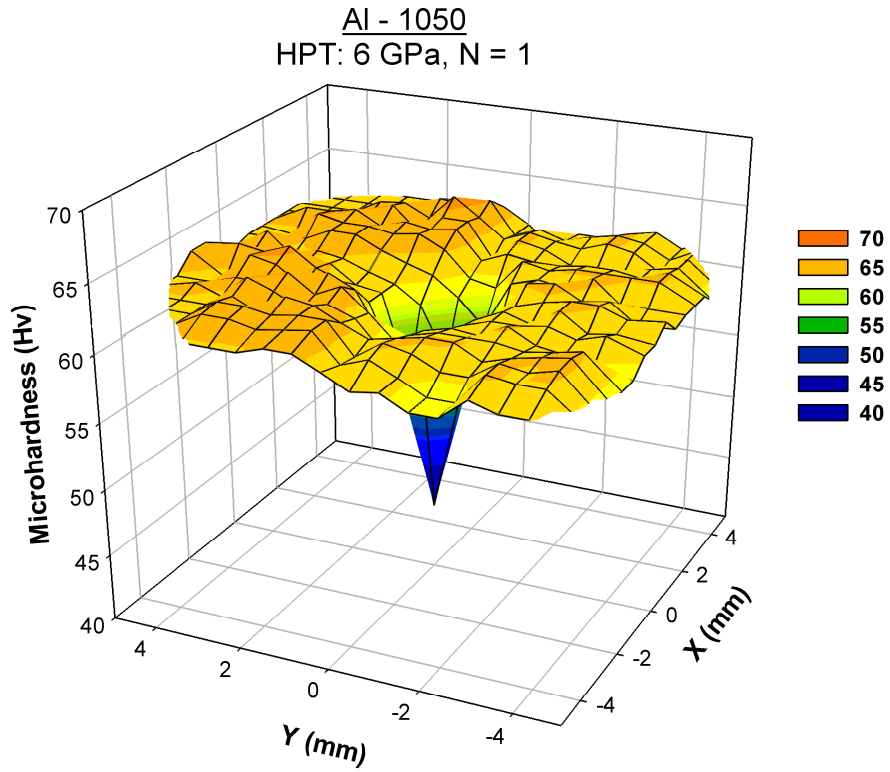


Fig. 6.13(b): Three-dimensional representation of the hardness measurements on the surface of Al-1050 disk after HPT under a pressure of 6.0 GPa for 1 turn: the significance of the colours is shown on the right.

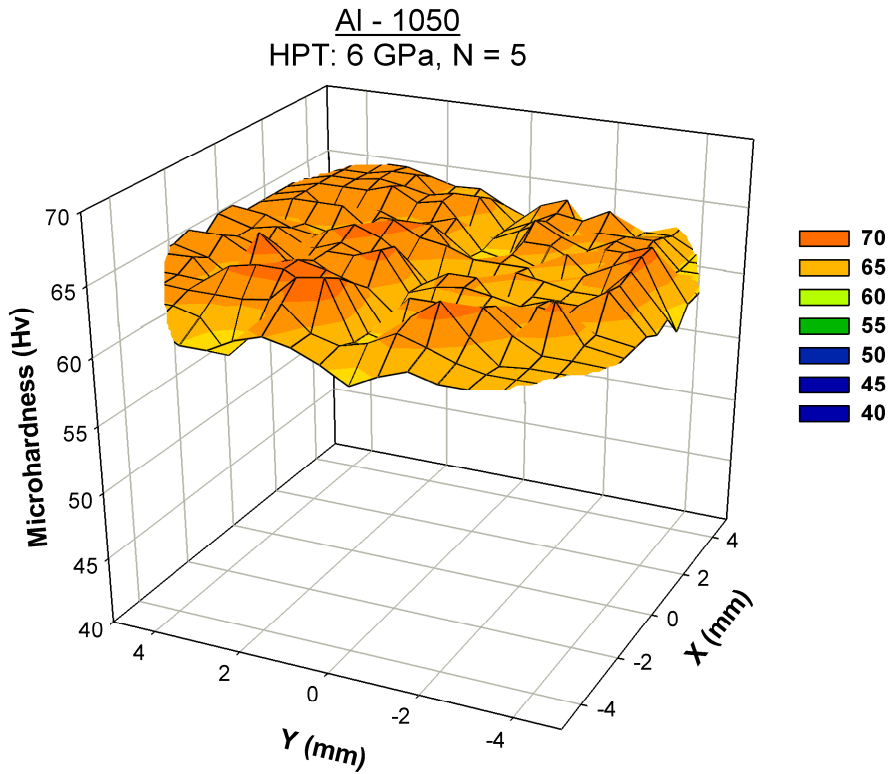


Fig. 6.13(c): Three-dimensional representation of the hardness measurements on the surface of Al-1050 disk after HPT under a pressure of 6.0 GPa for 5 turns: the significance of the colours is shown on the right.

6.4 Discussion

The Vickers microhardness, Hv, measurements were recorded on the surface of Al-1%Mg and Al-1050 alloys after HPT for different number of turns using three different methods. First, the individual measurements were recorded across the diameter of each disk. Second, colour-coded contour maps were plotted across the surface of each disk. Third, three-dimensional representations were plotted for the surface of each disk.

The most important conclusion from these measurements lies in providing a clear demonstration that evolution of hardness homogeneity occurs in both alloys with increasing numbers of turns. However, the evolution in the commercial purity aluminium (Al-1050) occurs more rapidly than that in the Al-1%Mg alloy. After five turns of HPT at room temperature under a pressure of 6.0 GPa, the hardness was totally homogeneous in the Al-1050 alloy while there is still a small region of lower hardness at the centre of the Al-1%Mg disk. The Al-1%Mg alloy needs more than five turns under the pressure of 6.0 GPa to become totally homogeneous. It is worth noticing, as stated previously, that the microhardness measurements exhibit the internal microstructure of metal alloys and the homogeneity of the microstructure of metal alloys can be identified by studying the microhardness measurements of these alloys [52,78,95,103].

This result is consistent with an earlier report for pure aluminium and two aluminium-magnesium alloys processed by equal-channel angular pressing (ECAP) [72]. In the ECAP report, the results showed that additional passes of ECAP are required in the aluminium-magnesium alloys compared to the pure aluminium in order to achieve a reasonably homogeneous microstructure. This is because, as suggested, the slower rate of recovery in the aluminium-magnesium alloy compared to the pure aluminium. Similar results were found when processing high purity aluminium and Al-6061 alloy by HPT [94].

Another important conclusion from the results of this investigation is confirming that the theoretical shear strain relationship which states that the shear strain imposed

during torsional straining is given by $(2 \pi N r / h)$ is not valid at high pressures and number of turns, at least for these two aluminium alloys. In the relationship, N , r and h are the number of turns, the radial distance from the centre and the thickness of the disk, respectively. In the Al-1050 alloy, even at the lower number of turns used in this investigation (i.e. 1/4 turn), the microhardness shows some homogeneity in the outer region of the disk and this result contradicts the theoretical shear strain relationship. On the other hand, in Al-1%Mg, the microhardness at the lower number of turns varies linearly with the distance from the centre of the disk and this agrees with the relationship. However, after one turn, the microhardness starts to become homogeneous in the outer region of the disk and the relationship becomes invalid. Therefore, it is better, as suggested, to specify the strain imposed during the processing by HPT in terms of the numbers of turns imposed on the disk [11].

The error in the microhardness measurements taken near the centre of the Al-1050 disk after one turn of HPT was high compared to the error in the measurements away from the centre. These high values of error at the centre indicate the instability in the hardness at the centre of the disk within very small distances. The error became consistent along the diameter of the disk after five turns. On the other hand, this observation of high error values near the centre of the disk was delayed in the Al-1%Mg alloy and it was noticed only after five turns of HPT. It is concluded from this observation that the hardness near the centre of disks processed by HPT becomes highly instable within very small distances prior to becoming consistent with the values of the hardness along the diameter of the disk. The same observation can be noticed in high purity aluminium processed by HPT under the same pressure (i.e. 6.0 GPa) [95]. In that experiment, the error was high near the centre after one turn and it became consistent along the diameter after three and five turns when the hardness became consistent along the entire length of the diameter.

6.5 Summary and Conclusions

1. Vickers microhardness, Hv, measurements were taken along the diameter and across the surface of Al-1.0% Mg and Al-1050 alloy disks after HPT at room temperature under a pressure of 6.0 GPa and a rotation speed of 1 rpm for 1/4, 1, and 5 turns.
2. Three methods of recording the microhardness measurements were used in this investigation to provide a clear demonstration for the evolution of microhardness. These methods were recording the individual measurements along the diameter of each disk, plotting colour-coded contour maps across the surface of each disk and plotting three-dimensional representations for the surface of each disk.
3. The most important conclusion in this investigation was illustrating the evolution of hardness homogeneity that occurs in both alloys with increasing numbers of turns.
4. The evolution of hardness homogeneity in the commercial purity aluminium (Al-1050) occurs more rapidly than in the Al-1%Mg alloy. This is due to the slower rate of recovery in Al-1%Mg alloy compared to Al-1050.
5. Five turns of HPT was enough to get complete homogeneity of the hardness across the entire surface of Al-1050 alloy while this number of turns was not enough for Al-1%Mg alloy to become totally homogeneous.
6. The theoretical shear strain relationship which states that the shear strain imposed during torsional straining is given by $(2 \pi N r / h)$ is not valid when processing aluminium alloys by HPT. It is more reasonable to specify the strain imposed during the processing by HPT in terms of the numbers of turns.

7. The hardness near the centre of disks processed by HPT became unstable within very small distances immediately prior to become consistent with the values of the hardness along the entire diameter of the disk.

CHAPTER 7

THE EFFECT OF STRAIN REVERSAL ON ALUMINIUM AND TITANIUM ALLOYS DURING PROCESSING BY HPT

7.1 Introduction

The high pressure torsion (HPT) process is termed as a continuous process where the sample remains between the two anvils during the entire experiment. This continuity of the processing operation has limited the initiating of many processing routes. By comparison, the equal-channel angular pressing (ECAP) process is termed as a discontinuous process where this discontinuity allowed the establishing of four different and distinct processing routes where each one of these four routes lead to different microstructure [29,96]. However, changing the direction of rotation in the HPT process, without removing the pressure, can produce different processing routes. This technique produced two HPT processes; the first is termed the monotonic HPT (m-HPT) process where the sample is strained in the same direction during the entire experiment and the second is termed the cyclic HPT (c-HPT) process where the direction of rotation is altered during the process.

There are few reports up to date investigating the effect of strain path on the structure and the mechanical properties of some materials such as Al-3% Mg-0.2% Sc [90], high-purity Al [97], Armco iron [98], high-purity Ni [98], 900A pearlitic rail steel [99] and low carbon steel (Fe-0.03C) [100]. The results in all these reports showed that the rate of increase of the hardness was higher in the disks processed by m-HPT than that processed by c-HPT. The only exception was the CP Ti alloy [100], where the results showed that the rate of increase of hardness was higher in c-HPT than that in m-HPT.

In this chapter, the microhardness will be recorded along the diameters of four alloys; commercial purity aluminium (Al-1050), Al-1%Mg, commercial purity titanium and Ti-6Al-4V, after processing by HPT monotonically and cyclically for up to two turns. The evolution of the microhardness measurements, and hence the internal microstructure as mentioned previously, will be investigated under the two paths. Also in this chapter, the existence of any slippage between the surface of the disks and the surface of the upper or lower anvils during the processing will be investigated, since the existence of the slippage will affect the accuracy of the results [127].

7.2 Experimental Materials and Procedures

Four different alloys were used in this HPT investigation. The first was commercial purity aluminium (Al-1050) alloy with a weight percent of at least 99.5% aluminium and with a chemical composition in weight percent (wt. %) as shown previously in Table 3.1. The second was Aluminium - 1.0 wt. % Magnesium (Al-1.0%Mg) alloy which has 0.003% Si and 0.001% Fe as minor impurities. The third was commercial purity titanium (CP Ti) alloy with a weight percent of at least of 99.2% titanium and with a chemical composition in weight percent (wt. %) as shown previously in Table 5.1. The fourth was Titanium - 6.0 wt. % Aluminium - 4.0 wt. % Vanadium (Ti-6Al-4V) alloy which has 0.25% Fe and 0.20% O as minor impurities. All materials were supplied in the form of long circular bars with a diameter of 10.0 mm.

The HPT experiments were conducted in air at room temperature using a facility as shown previously in chapter 6. The process of HPT was described in detail in chapter 6. In the present HPT experiments, two sets of disks were used from the four alloys. All disks were cut using 0.25 mm brass wire erosion with an electro-discharge machine to a thickness of 1.6 mm. The thickness of each disk was then reduced to 0.8 mm by mechanical polishing using 120, 600 and 1200 grit SiC papers. For the first set of disks, a forward direction was used to strain the disks monotonically (m-HPT) for totals of 1/2, 3/4, 1 and 2 turns, respectively. For the second set of disks,

the direction of straining was changed forward and backward during the processing to perform a cyclic rotation process (c-HPT), as shown in Fig. 7.1. The change in direction was attained by stopping the lower anvil and then starting again within less than two seconds in the opposite direction. The disks were subjected to c-HPT for $+1/4 -1/4$, $+1/4 -1/4 +1/4$, $+1/4 -1/4 +1/4 -1/4$ and $+1 -1$ which gave totals of $1/2$, $3/4$, 1 and 2 turns, respectively. The applied load used in these experiments was 48 tons which is corresponding to an imposed pressure, P , of 6.0 GPa. The speed of the forward and backward rotation was 1 r.p.m. Due to conducting the experiments under a high pressure and a quasi-constrained condition, there was a limited flow of the material outside the anvils which leads to a small reduction in the thickness of the disks after processing.

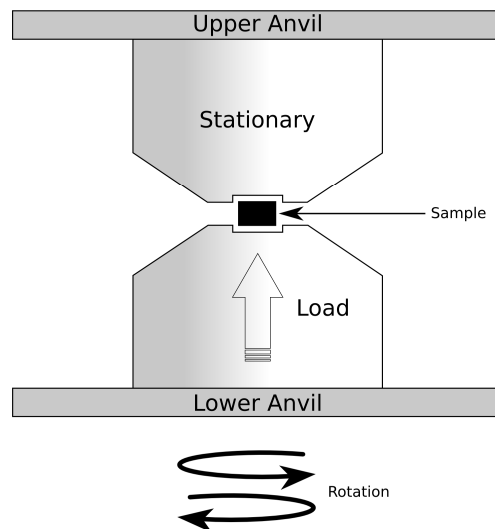


Fig. 7.1: Illustration of the HPT facility showing the sample under pressure and cyclic rotation.

Before performing the experiments, a straight line was marked along the diameter of one side of each disk and a parallel line was marked along the diameter of the other side of the disk. The marking was performed using a permanent black marker. These lines were used to study the existence of any slippage between the surface of the disk and the surface of the upper or lower anvils during the straining. This can be performed by comparing the angle between the two lines after straining with the anticipated angle. For example, after straining for $1/2$ turn, the anticipated angle between the two lines is zero. So, if the measured angle between the two lines is zero, then there was no slippage. If there was slippage between the surface of the disk and the surface of the upper or lower anvils, then the measured angle between the two lines must be different than zero. To investigate the effect of the strain reversal, it is important to know that the two sets were subjected to the same number of turns.

After HPT straining, the angle between the lines on both sides of each disk was measured and compared with the corresponding anticipated angle. After that, all disks were mounted using a cold-setting resin based on two fluid epoxy components and then carefully polished using 120, 600, 1200 and 4000 grit SiC papers to a mirror-like finish. Microhardness measurements, H_v , were then taken on the disks using a Matsuzawa Seiki MHT-1 microhardness tester equipped with a Vickers indenter. For the aluminium alloys, the measurements were taken by applying a load of 50 gf for a dwell time of 15 seconds. For the titanium alloys, the measurements were taken by applying a load of 300 gf for a dwell time of 15 seconds. The procedure of taking the measurements was explained in chapter 6 where 33 points across the diameter of each disk were selected to take the measurements at them and at each point 4 measurements were taken as shown in Fig. 6.5. The total number of microhardness measurements taken on the diameter of each disk was 100 data points. The graph of each disk was then plotted where the data points showing the error bars which is denoting an estimated 95% confidence limits and calculated by the statistical method explained previously in chapter 6. Graphs showing the evolution of microhardness measurements of each alloy monotonically and cyclically were then plotted without the error bars for simplicity.

7.3 Experimental Results

In this research, monotonic and cyclic HPT experiments were performed on four materials, two aluminium alloys (Al-1050 and Al-1%Mg) and two titanium alloys (CP Ti and Ti-6Al-4V) for totals of 1/2, 3/4, 1 and 2 turns under a pressure of 6.0 GPa. Two objectives were cited for this research, the first is to determine the existence of any slippage between the surface of the disks and the surface of the upper or lower anvils. The second objective is to perform the measurements of the Vickers microhardness, H_v , along the diameter of each disk and to compare the results of the m-HPT with the c-HPT.

7.3.1 The existence of slippage:

After the preparation of all disks and before performing the HPT experiments monotonically and cyclically, two parallel lines were marked on the surfaces of each disk, one on each surface. After the experiments, the lines were drawn on white paper and the measurements were taken for the angle between the two lines for each disk. The total numbers of disks were 8 disks for each one of the four alloys, four processed monotonically and four processed cyclically. For the disks processed for totals of 1/2, 1 and 2 turns, the anticipated angle between the two lines was 0° while the anticipated angle for the disk processed for a total of 3/4 turn was 90° . The results for all alloys and all disks processed monotonically and cyclically showed that the difference between the measured and the anticipated angles was zero or very close to zero.

7.3.2 The microhardness measurements:

The individual microhardness measurements, H_v , were recorded for each alloy along the diameter of four disks processed by m-HPT for 1/2, 3/4, 1 and 2 turns, respectively, and another four disks processed by c-HPT for +1/4-1/4, +1/4-1/4+1/4, +1/4-1/4+1/4-1/4 and +1-1 turns, respectively. The individual measurements plotted on the figures were the average of four measurements recorded around each data point. Error bars correspond to the 95% confidence limits of the four measurements

which taken around the data point were drawn in the figures. Figures showing the evolution of the microhardness in each alloy processed monotonically and cyclically were also plotted.

7.3.2.1 Al-1050 alloy:

Fig. 7.2 shows the individual microhardness measurements recorded along the diameter of the commercial purity aluminium (Al-1050) alloy after m-HPT under a pressure of 6.0 GPa for (a) 1/2, (b) 3/4, (c) one and (d) two turns, respectively. The microhardness measurements for the alloy in the as-received unprocessed condition are also shown. After processing by HPT for 1/2 turn, as shown in Fig. 7.2(a), the microhardness values increased from an initial value of ~27 in the as-received unprocessed material to values ranging between ~40 at the centre of the disk and ~60 near the edge of the disk. The increment in the microhardness values near the edge of the disk is approximately 220%. The microhardness measurements reached a constant value of about ~60 after a distance of 2.0 mm from the centre of the disk on both sides. The error bars at and near the centre of the disk are high compared to that after a distance of approximately 1.0 mm from the centre of the disk on both sides. After processing for 3/4 turn, as shown in Fig. 7.2(b), the microhardness measurements at the centre of the disk increased slightly compared to processing for 1/2 turn to reach ~47 and near the edge of the disk the values were approximately ~61. The microhardness values started to become constant beyond a distance of ~1.0 mm from the centre of the disk on both sides. It is also noticed, as in the disk processed for 1/2 turn, that the error in the microhardness measurements taken near the centre of the disk was high compared to the error in the measurements away from the centre. After processing for one turn, as shown in Fig. 7.2(c), the microhardness measurement at the centre of the disk was approximately ~45 and near the edge of the disk the values were approximately ~62. The microhardness values started to become constant beyond a distance of ~0.9 mm from the centre of the disk on both sides. The error bars at and near the centre of the disk were also high compared to that away from the centre. After processing for two turns, as shown in Fig. 7.2(d), the microhardness measurement at the centre of the disk increased to reach approximately ~50 and near the edge of the disk the values were approximately ~60. The microhardness values started to become constant beyond a distance of ~0.6 mm

from the centre of the disk on both sides. The error bars at and near the centre of the disk were also high compared to that away from the centre, as in the other disks processed for 1/2, 3/4 and 1 turn.

The microhardness measurements along the diameter of the Al-1050 disks after c-HPT under a pressure of 6.0 GPa for (a) +1/4-1/4, (b) +1/4-1/4+1/4, (c) +1/4-1/4+1/4-1/4 and (d) +1-1 turns, respectively, are shown in Fig. 7.3. After processing by HPT cyclically for +1/4-1/4 for a total of 1/2 turn, as shown in Fig. 7.3(a), the microhardness values increased from an initial value of ~27 in the as-received unprocessed material to values ranging between ~40 at the centre of the disk and ~59 near the edge of the disk. The microhardness measurements increased gradually from the centre to reach a constant value of about ~59 after a distance of approximately 3.5 mm from the centre of the disk on both sides. Similar to that in the disks processed monotonically, the error bars at and near the centre of the disk are high compared to that away from the centre of the disk on both sides. After processing for +1/4-1/4 +1/4 for a total of 3/4 turn, as shown in Fig. 7.3(b), the microhardness measurements at the centre were approximately ~40 and near the edge of the disk the values were approximately ~61. The microhardness values started to become constant beyond a distance of ~2.5 mm from the centre of the disk on both sides. It is also noticed, as in all other disks, that the error in the microhardness measurements taken near the centre of the disk was high compared to the error in the measurements away from the centre. After processing for +1/4-1/4 +1/4-1/4 for a total of one turn, as shown in Fig. 7.3(c), the microhardness measurement at the centre of the disk remained constant at a value of approximately ~40 and near the edge of the disk the values were approximately ~60. The microhardness values increased gradually from the centre and started to become relatively constant beyond a distance of ~3.0 mm from the centre of the disk on both sides. The error bars at and near the centre of the disk were also high compared to that away from the centre. After processing for +1-1 for a total of two turns, as shown in Fig. 7.3(d), the microhardness measurement at the centre of the disk increased to reach approximately ~49 and near the edge of the disk the values were approximately ~61. The microhardness values started to become constant beyond a distance of ~0.9 mm from the centre of the disk on both sides. The error bars at and near the centre of the disk were also high compared to that away from the centre, as in the other disks processed monotonically or cyclically.

The microhardness measurements along the diameter of the Al-1050 disks after m-HPT and c-HPT under a pressure of 6.0 GPa for (a) 1/2, (b) 3/4, (c) 1 and (d) 2 turns, respectively, are shown in Fig. 7.4. The microhardness measurements for the alloy in the as-received unprocessed condition are also shown. The evolution of the microhardness measurements in the disks processed by m-HPT was faster than that in the disks processed by c-HPT. This can be clearly seen in the disks processed for totals of 1/2, 3/4 and 1 turn, as shown in Figs. 7.4(a), (b) and (c), respectively. In the disks processed for a total of 2 turns, as shown in Fig. 7.4(d), the evolution of the microhardness measurements was similar when processing by m-HPT or c-HPT. In the disk processed by c-HPT for a total of 2 turns, the strain was imposed for 1 turn in each cycle where it was 1/4 in each cycle in the disks processed for totals of 1/2, 3/4 and 1 turn.

The variation of the microhardness measurements along the diameter of the Al-1050 disks after m-HPT and c-HPT under a pressure of 6.0 GPa for totals of 1/2, 3/4, 1 and 2 turns, respectively, are shown in Fig. 7.5. The microhardness measurements for the alloy in the as-received unprocessed condition are also shown. As shown in Fig. 7.5(a), the microhardness measurements increased in the centre of the disks processed monotonically with increasing number of turns and it reached a saturation value of approximately ~60. This saturation value started at the edges and continued to a length of 3.0 mm from the edges after 1/2 turn. It continued to a length of 4.0 mm from the edges after 3/4 and 1 turn and it also continued to a length of 4.5 mm after two turns. As shown in Fig. 7.5(b), the evolution of the microhardness values was nearly similar in the disks processed cyclically for +1/4-1/4, +1/4-1/4+1/4 and +1/4-1/4+1/4-1/4 which give totals of 1/2, 3/4 and 1 turn, respectively. After processing for +1-1 for a total of two turns, the microhardness values increased in the centre and reached the saturation value of approximately ~60 faster. By comparing the two graphs, it is noticed that the evolution of the microhardness values were faster when the disks are processed monotonically.

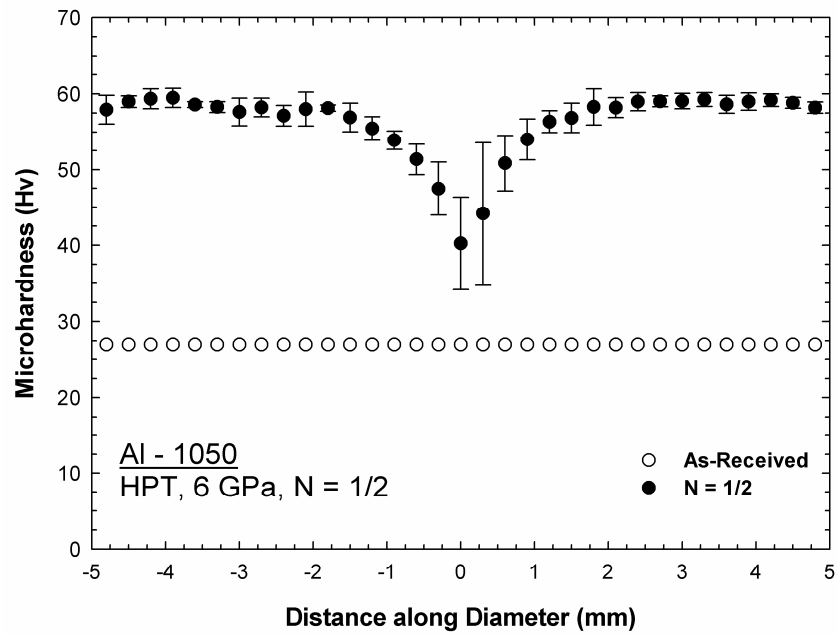


Fig. 7.2(a): The average of the microhardness measurements, Hv, recorded along the diameter of Al-1050 disk after m-HPT under a pressure of 6.0 GPa for 1/2 turn. The microhardness measurements for alloy in the as-received unprocessed condition are also shown.

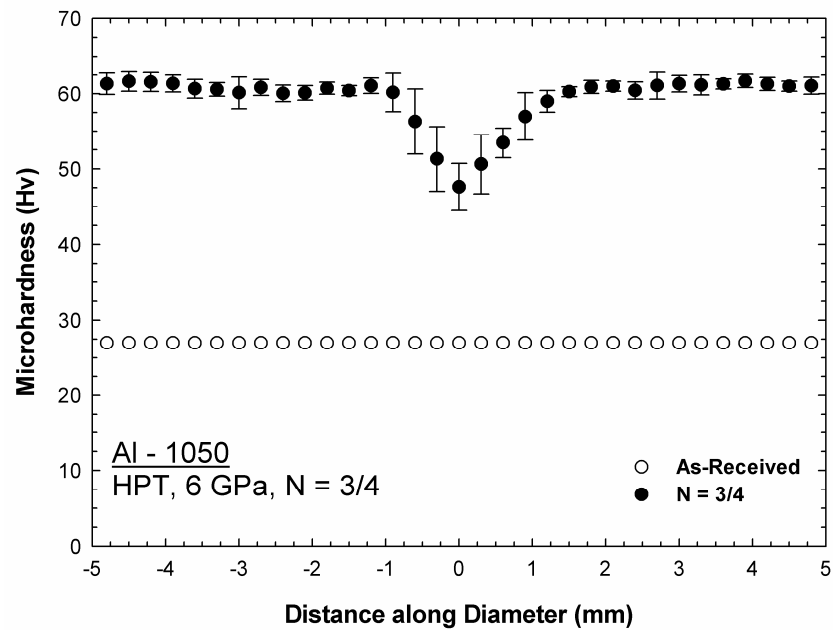


Fig. 7.2(b): The average of the microhardness measurements, Hv, recorded along the diameter of Al-1050 disk after m-HPT under a pressure of 6.0 GPa for 3/4 turn. The microhardness measurements for alloy in the as-received unprocessed condition are also shown.

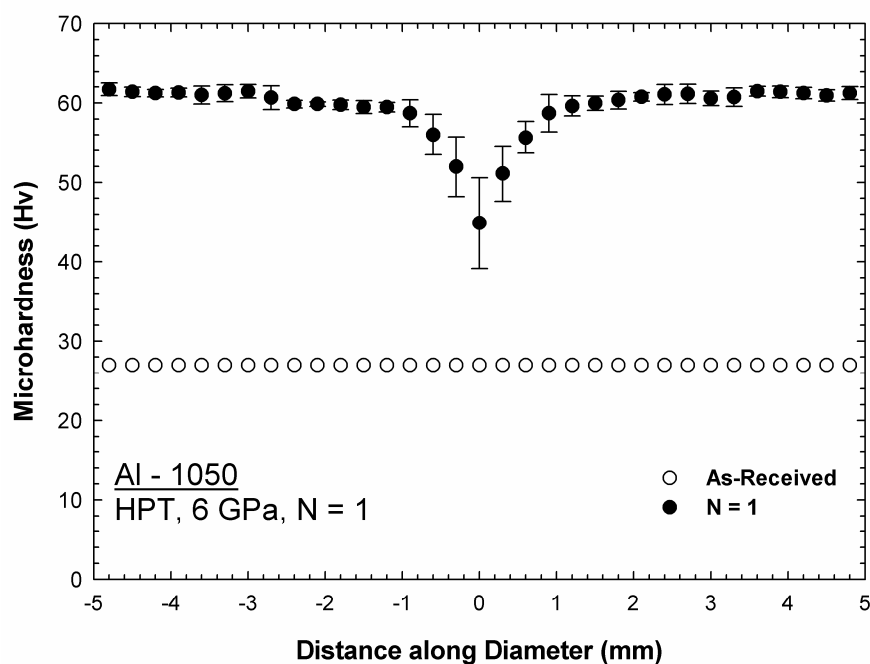


Fig. 7.2(c): The average of the microhardness measurements, Hv, recorded along the diameter of Al-1050 disk after m-HPT under a pressure of 6.0 GPa for 1 turn. The microhardness measurements for alloy in the as-received unprocessed condition are also shown.

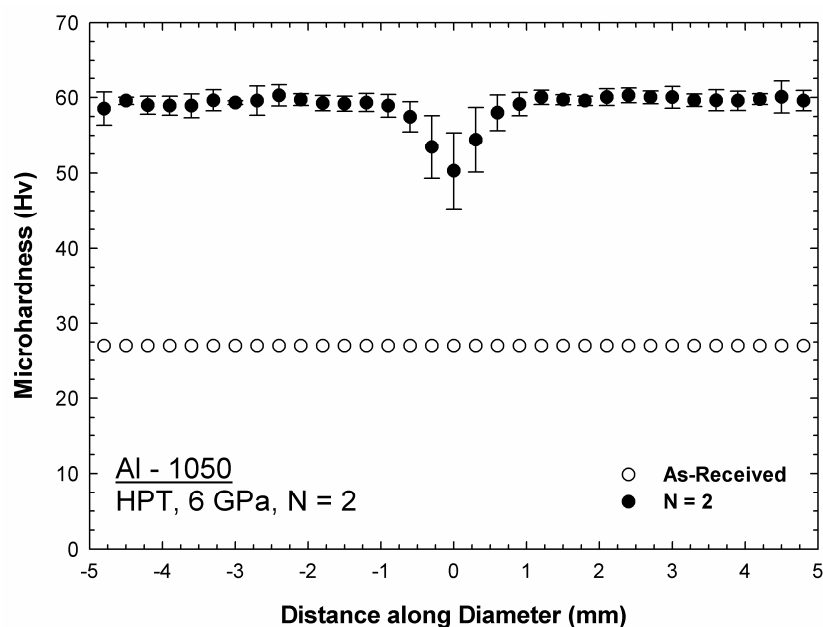


Fig. 7.2(d): The average of the microhardness measurements, Hv, recorded along the diameter of Al-1050 disk after m-HPT under a pressure of 6.0 GPa for 2 turns. The microhardness measurements for alloy in the as-received unprocessed condition are also shown.

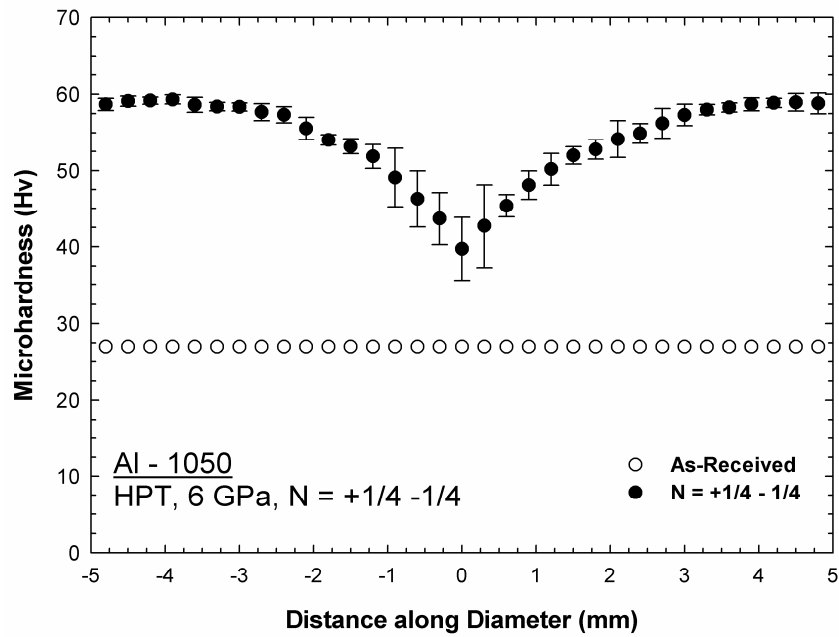


Fig. 7.3(a): The average of the microhardness measurements, Hv, recorded along the diameter of Al-1050 disk after c-HPT under a pressure of 6.0 GPa for +1/4 -1/4 turn. The microhardness measurements for alloy in the as-received unprocessed condition are also shown.

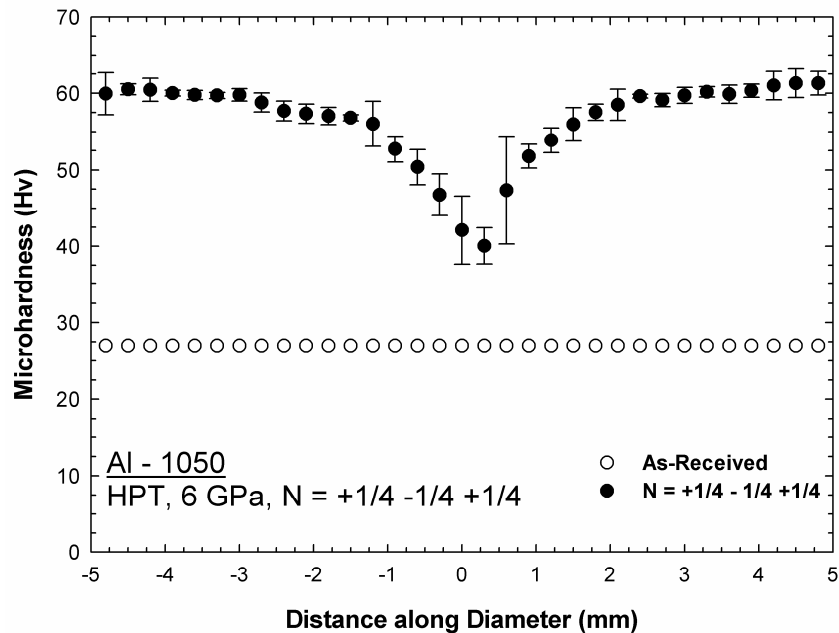


Fig. 7.3(b): The average of the microhardness measurements, Hv, recorded along the diameter of Al-1050 disk after c-HPT under a pressure of 6.0 GPa for +1/4 -1/4 +1/4 turn. The microhardness measurements for alloy in the as-received unprocessed condition are also shown.

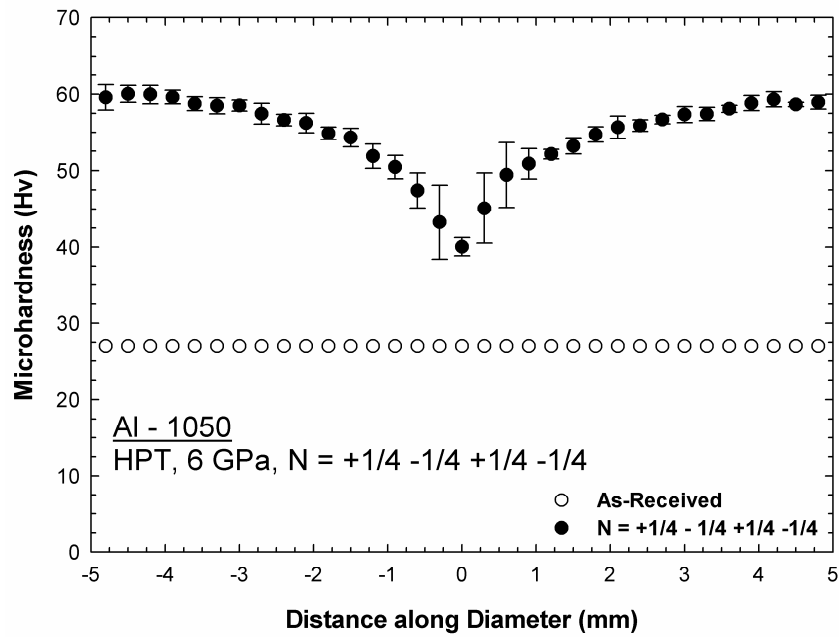


Fig. 7.3(c): The average of the microhardness measurements, Hv, recorded along the diameter of Al-1050 disk after c-HPT under a pressure of 6.0 GPa for +1/4 -1/4 +1/4 -1/4 turn. The microhardness measurements for alloy in the as-received unprocessed condition are also shown.

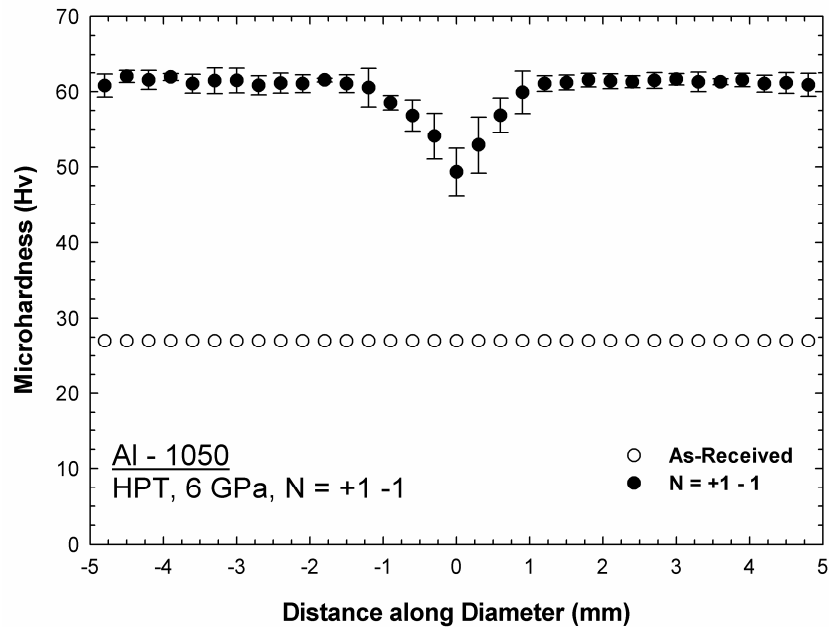


Fig. 7.3(d): The average of the microhardness measurements, Hv, recorded along the diameter of Al-1050 disk after c-HPT under a pressure of 6.0 GPa for +1 -1 turn. The microhardness measurements for alloy in the as-received unprocessed condition are also shown.

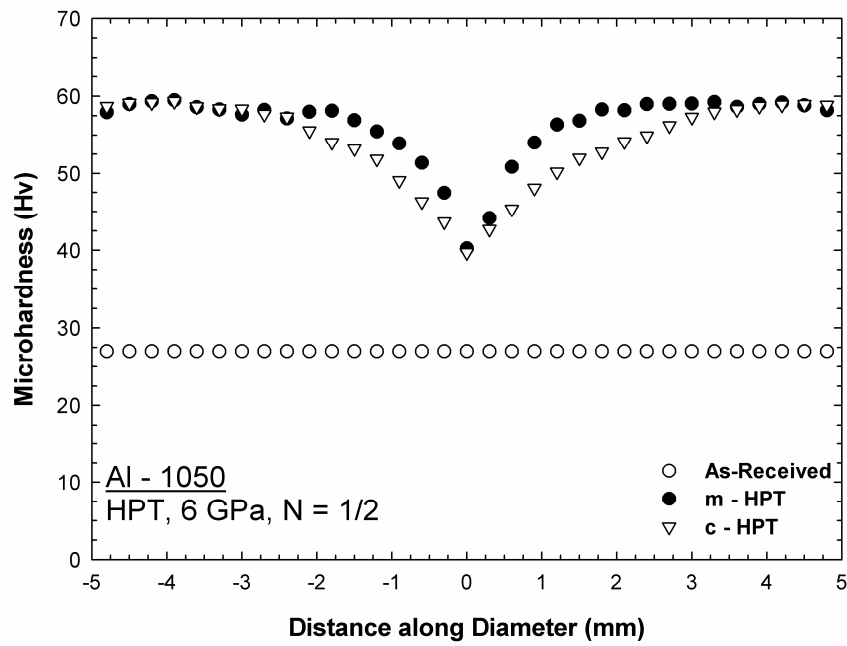


Fig. 7.4(a): The average of the microhardness measurements, Hv, recorded along the diameter of Al-1050 disks after m-HPT and c-HPT under a pressure of 6.0 GPa for 1/2 turn. The microhardness measurements for alloy in the as-received unprocessed condition are also shown.

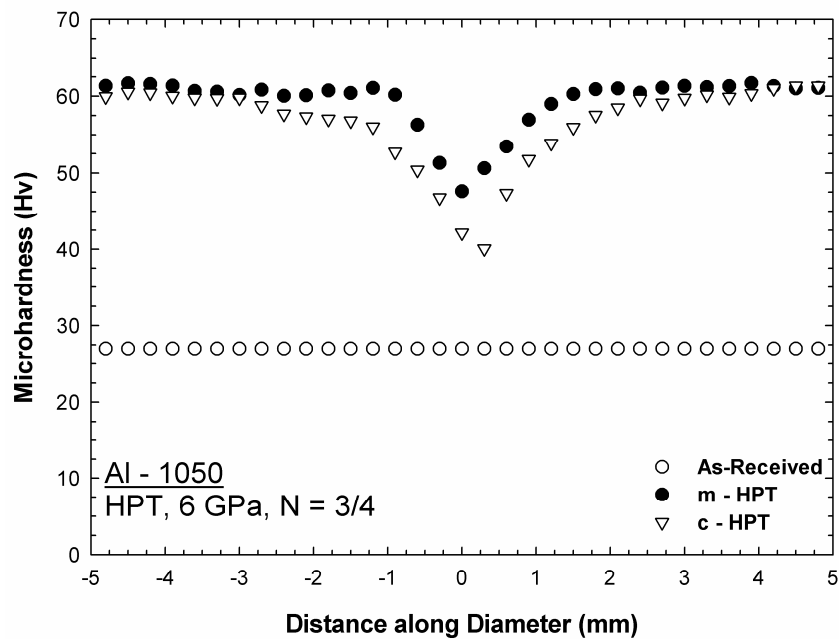


Fig. 7.4(b): The average of the microhardness measurements, Hv, recorded along the diameter of Al-1050 disks after m-HPT and c-HPT under a pressure of 6.0 GPa for 3/4 turn. The microhardness measurements for alloy in the as-received unprocessed condition are also shown.

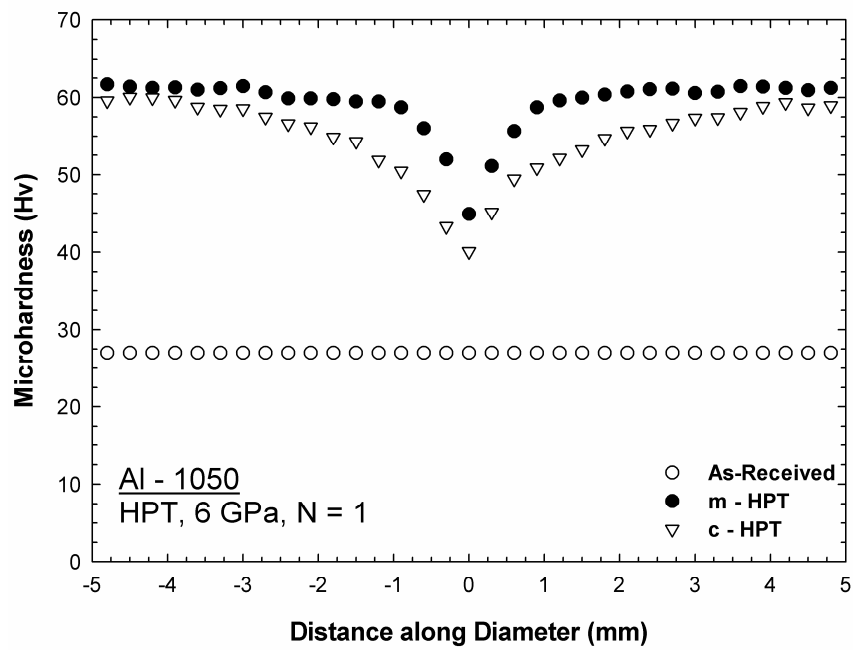


Fig. 7.4(c): The average of the microhardness measurements, Hv, recorded along the diameter of Al-1050 disks after m-HPT and c-HPT under a pressure of 6.0 GPa for 1 turn. The microhardness measurements for alloy in the as-received unprocessed condition are also shown.

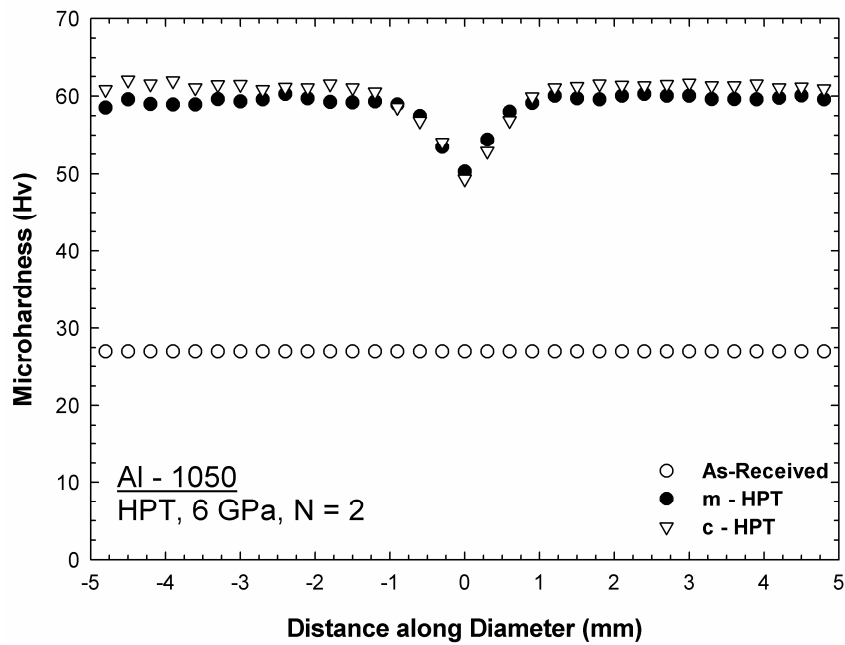


Fig. 7.4(d): The average of the microhardness measurements, Hv, recorded along the diameter of Al-1050 disks after m-HPT and c-HPT under a pressure of 6.0 GPa for 2 turns. The microhardness measurements for alloy in the as-received unprocessed condition are also shown.

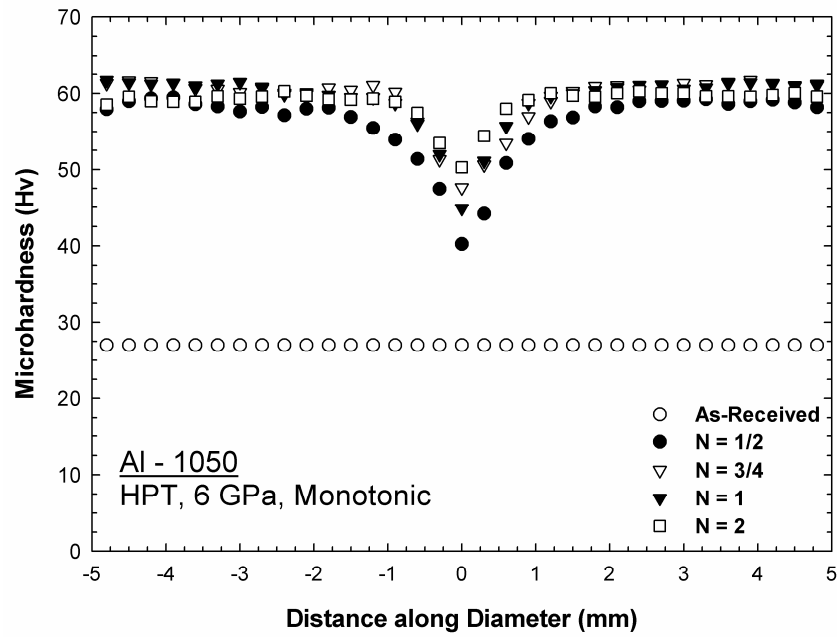


Fig. 7.5(a): The average microhardness measurements, Hv, recorded along the diameter of Al-1050 disks after m-HPT under a pressure of 6.0 GPa for 1/2, 3/4, 1 and 2 turns. The microhardness measurements for alloy in the as-received unprocessed condition are also shown.

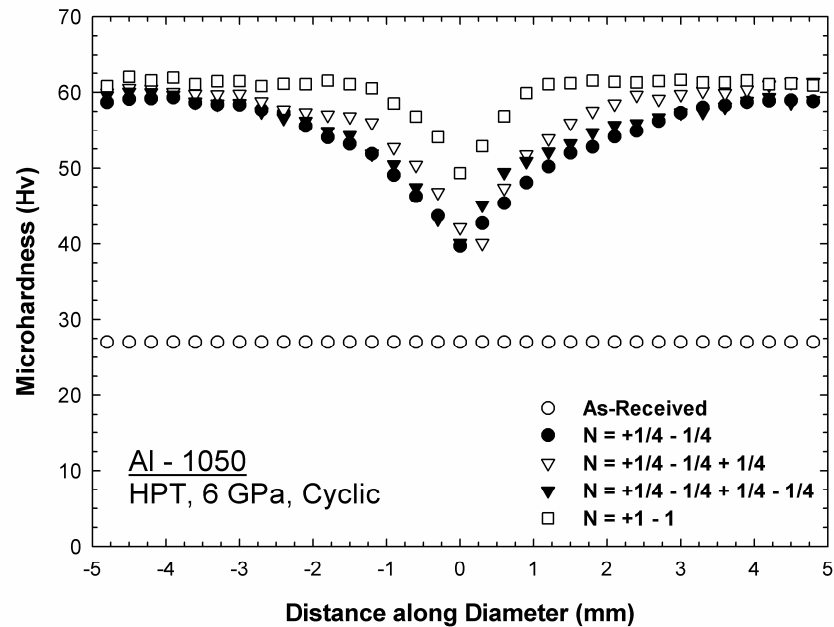


Fig. 7.5(b): The average microhardness measurements, Hv, recorded along the diameter of Al-1050 disks after c-HPT under a pressure of 6.0 GPa for +1/4-1/4, +1/4-1/4+1/4, +1/4-1/4+1/4-1/4 and +1-1 turns. The microhardness measurements for alloy in the as-received unprocessed condition are also shown.

7.3.2.2 Al-1%Mg alloy:

Fig. 7.6 shows the individual microhardness measurements recorded along the diameter of the Al-1%Mg alloy after m-HPT under a pressure of 6.0 GPa for (a) 1/2, (b) 3/4, (c) one and (d) two turns, respectively. The microhardness measurements for the alloy in the as-received unprocessed condition are also shown. After processing by HPT for 1/2 turn, as shown in Fig. 7.6(a), the microhardness values increased from an initial value of ~31.5 in the as-received unprocessed material to values ranging between ~56 at the centre of the disk and ~110 near the edge of the disk. The increment in the microhardness values near the edge of the disk is approximately 350%. The microhardness measurements increased linearly from the low values at the centre to the high values near the edges of the disk on both sides. The error bars at and near the centre of the disk are high compared to that away from the centre. After processing for 3/4 turn, as shown in Fig. 7.6(b), the microhardness measurements at the centre of the disk were approximately ~53 and near the edge of the disk the values were approximately ~115. The microhardness values increased linearly from the low values at the centre to a distance of 2.5 mm from the centre then the slope of increment decreased to the edges of the disk on both sides. It is also noticed, as in the disk processed for 1/2 turn, that the error in the microhardness measurements taken near the centre of the disk was high compared to the error in the measurements away from the centre. After processing for one turn, as shown in Fig. 7.6(c), the microhardness measurement at the centre of the disk was approximately ~56 and near the edge of the disk the values were approximately ~119. The microhardness values started to become constant beyond a distance of ~3.0 mm from the centre of the disk on both sides. The error bars were relatively high both near the centre of the disk and away from the centre. After processing for two turns, as shown in Fig. 7.6(d), the microhardness measurement at the centre of the disk increased to reach approximately ~66 and near the edge of the disk the values were approximately ~120. The microhardness values started to become constant beyond a distance of ~1.5 mm from the centre of the disk on both sides. The error bars at and near the centre of the disk were high compared to that away from the centre on one side where it were high near the other edge of the disk.

The microhardness measurements along the diameter of the Al-1%Mg disks after c-HPT under a pressure of 6.0 GPa for (a) $+1/4-1/4$, (b) $+1/4-1/4+1/4$, (c) $+1/4-1/4+1/4-1/4$ and (d) $+1-1$ turns, respectively, are shown in Fig. 7.7. After processing by HPT cyclically for $+1/4-1/4$ for a total of $1/2$ turn, as shown in Fig. 7.7(a), the microhardness values increased from an initial value of ~ 31.5 in the as-received unprocessed material to values ranging between ~ 50 at the centre of the disk and ~ 106 near the edge of the disk. The microhardness measurements increased linearly from the low values at the centre to the high values near the edges of the disk on both sides. Similar to that in the disks processed monotonically for $1/2$, $3/4$ and 2 turns, the error bars at and near the centre of the disk are high compared to that away from the centre of the disk on both sides. After processing for $+1/4-1/4 +1/4$ for a total of $3/4$ turn, as shown in Fig. 7.7(b), the microhardness measurements at the centre increased slightly to reach approximately ~ 54 and near the edge of the disk the values also increased slightly to reach approximately ~ 109 . The microhardness measurements also increased linearly from the low values at the centre to the high values near the edges of the disk on both sides. It is also noticed, as in the other disks, that the error in the microhardness measurements taken near the centre of the disk was high compared to the error in the measurements away from the centre. After processing for $+1/4-1/4 +1/4-1/4$ for a total of one turn, as shown in Fig. 7.7(c), the microhardness measurement at the centre of the disk increased slightly to reach a value of approximately ~ 57 and near the edge of the disk the values were approximately ~ 110 . The microhardness values also increased linearly from the centre to the edges of the disk on both sides. The error bars at and near the centre of the disk were also high compared to that away from the centre. After processing for $+1-1$ for a total of two turns, as shown in Fig. 7.7(d), the microhardness measurement at the centre of the disk increased again slightly to reach a value of approximately ~ 61 and near the edge of the disk the values were approximately ~ 120 . The microhardness values started to become constant on a value of ~ 120 beyond a distance of ~ 3.0 mm from the centre of the disk on both sides. The error bars at and near the centre of the disk were also high compared to that away from the centre, as in the other disks processed monotonically or cyclically except the disk processed monotonically for one turn.

The microhardness measurements along the diameter of the Al-1%Mg disks after m-HPT and c-HPT under a pressure of 6.0 GPa for (a) 1/2, (b) 3/4, (c) 1 and (d) 2 turns, respectively, are shown in Fig. 7.8. The microhardness measurements for the alloy in the as-received unprocessed condition are also shown. The evolution of the microhardness measurements in the disks processed by m-HPT was faster than that in the disks processed by c-HPT. This can be clearly seen in all disks processed for totals of 1/2, 3/4, 1 and 2 turns, as shown in Figs. 7.8(a), (b), (c) and (d), respectively.

The variation of the microhardness measurements along the diameter of the Al-1%Mg disks after m-HPT and c-HPT under a pressure of 6.0 GPa for totals of 1/2, 3/4, 1 and 2 turns, respectively, are shown in Fig. 7.9. The microhardness measurements for the alloy in the as-received unprocessed condition are also shown. As shown in Fig. 7.9(a), the microhardness measurements increased gradually in the disks processed monotonically with increasing number of turns and it reached a saturation value of approximately ~120. This saturation value started at the edges of the disk processed for one turn and it continued to a length of ~2.0 mm from the edges and after two turns, this saturation continued to a length of ~3.5 mm from the edges of the disk. As shown in Fig. 7.9(b), the evolution of the microhardness values was nearly similar in the disks processed cyclically for +1/4-1/4, +1/4-1/4+1/4 and +1/4-1/4+1/4-1/4 which give totals of 1/2, 3/4 and 1 turn, respectively. This trend in the evolution of the microhardness was identical to that in the commercial purity aluminium (Al-1050) alloy in the three disks processed cyclically for totals of 1/2, 3/4 and 1 turn. The maximum value reached by these three disks was approximately ~110 near the edges of the disks and this value was less than the saturation value which is approximately ~120. After processing for +1-1 for a total of two turns, the microhardness values remarkably increased and reached the saturation value of approximately ~120 beyond a distance of ~3.0 mm from the centre of the disk. By comparing the two graphs, it is noticed that, as in the commercial purity aluminium (Al-1050) alloy, the evolution of the microhardness values was faster when the disks are processed monotonically.

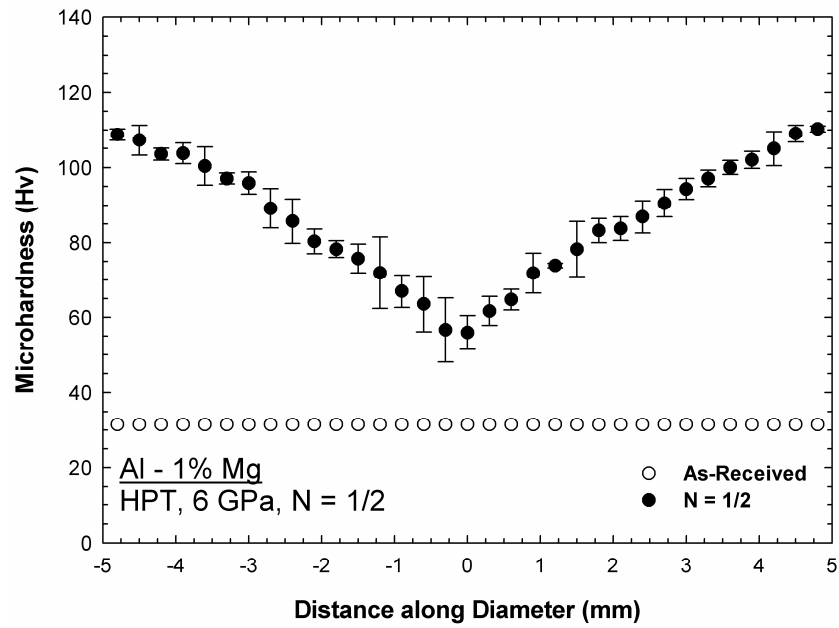


Fig. 7.6(a): The average of the microhardness measurements, Hv, recorded along the diameter of Al-1% Mg disk after m-HPT under a pressure of 6.0 GPa for 1/2 turn. The microhardness measurements for alloy in the as-received unprocessed condition are also shown.

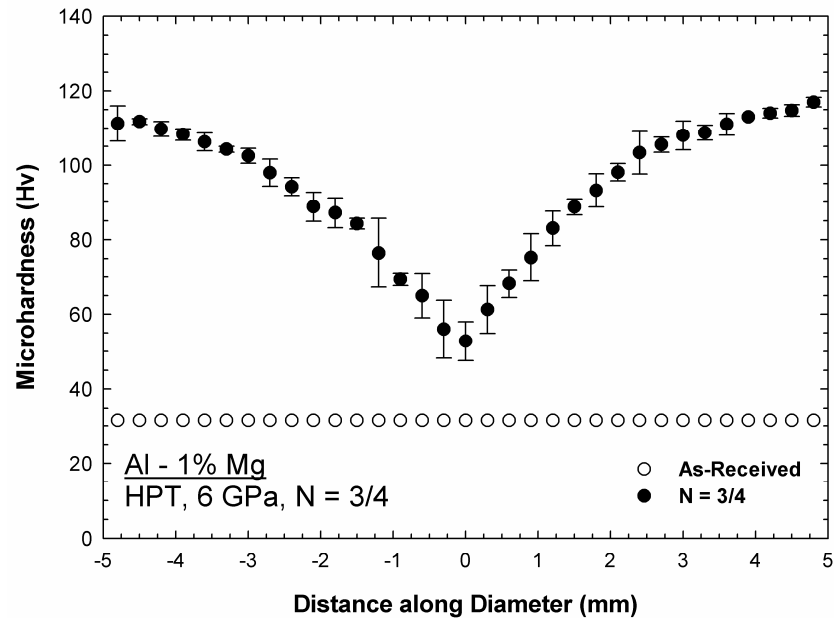


Fig. 7.6(b): The average of the microhardness measurements, Hv, recorded along the diameter of Al-1% Mg disk after m-HPT under a pressure of 6.0 GPa for 3/4 turn. The microhardness measurements for alloy in the as-received unprocessed condition are also shown.

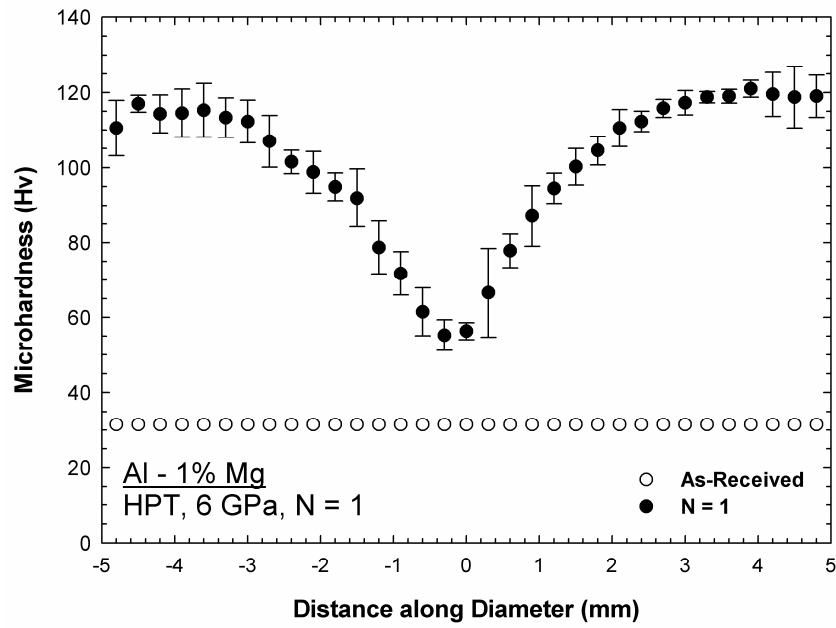


Fig. 7.6(c): The average of the microhardness measurements, Hv, recorded along the diameter of Al-1% Mg disk after m-HPT under a pressure of 6.0 GPa for 1 turn. The microhardness measurements for alloy in the as-received unprocessed condition are also shown.

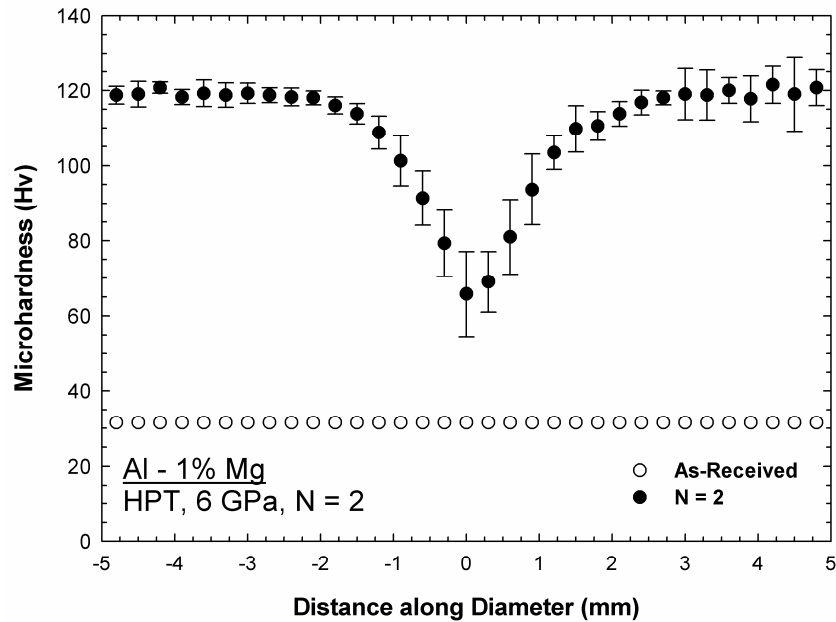


Fig. 7.6(d): The average of the microhardness measurements, Hv, recorded along the diameter of Al-1% Mg disk after m-HPT under a pressure of 6.0 GPa for 2 turns. The microhardness measurements for alloy in the as-received unprocessed condition are also shown.

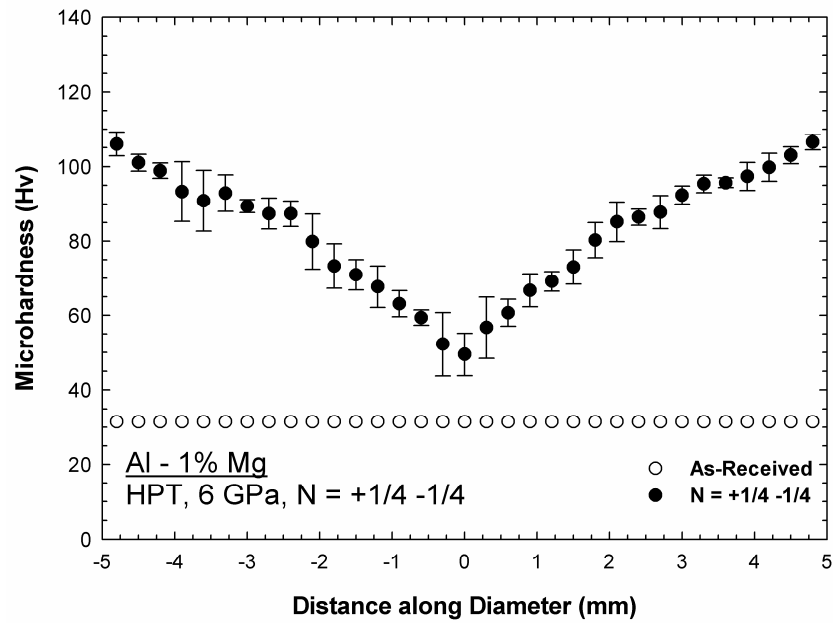


Fig. 7.7(a): The average of the microhardness measurements, Hv, recorded along the diameter of Al-1% Mg disk after c-HPT under a pressure of 6.0 GPa for +1/4 -1/4 turn. The microhardness measurements for alloy in the as-received unprocessed condition are also shown.

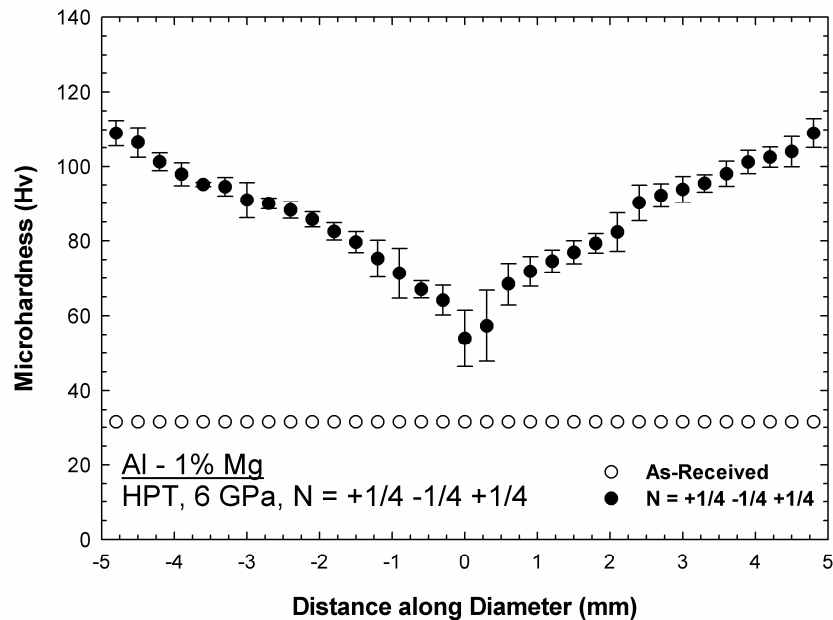


Fig. 7.7(b): The average of the microhardness measurements, Hv, recorded along the diameter of Al-1% Mg disk after c-HPT under a pressure of 6.0 GPa for +1/4 -1/4 +1/4 turn. The microhardness measurements for alloy in the as-received unprocessed condition are also shown.

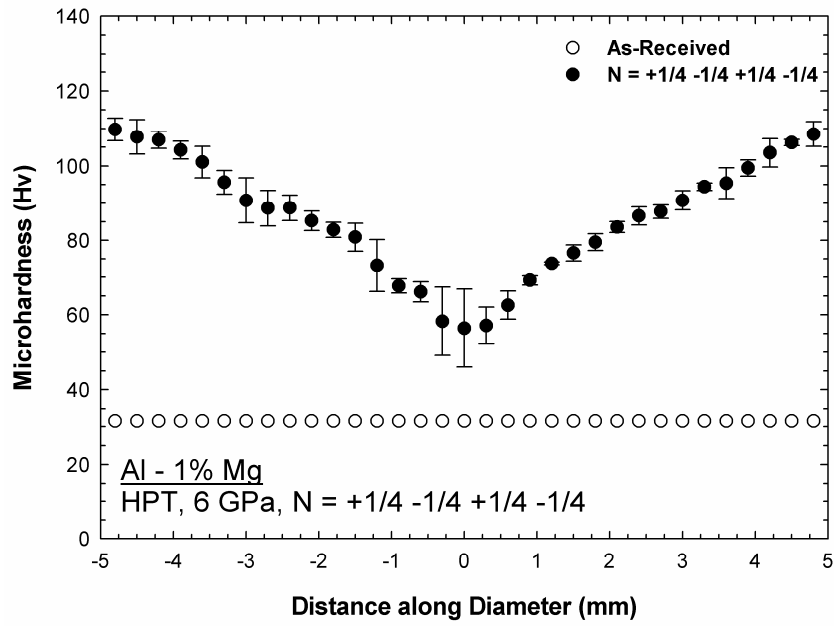


Fig. 7.7(c): The average of the microhardness measurements, Hv, recorded along the diameter of Al-1% Mg disk after c-HPT under a pressure of 6.0 GPa for +1/4 -1/4 +1/4 -1/4 turn. The microhardness measurements for alloy in the as-received unprocessed condition are also shown.

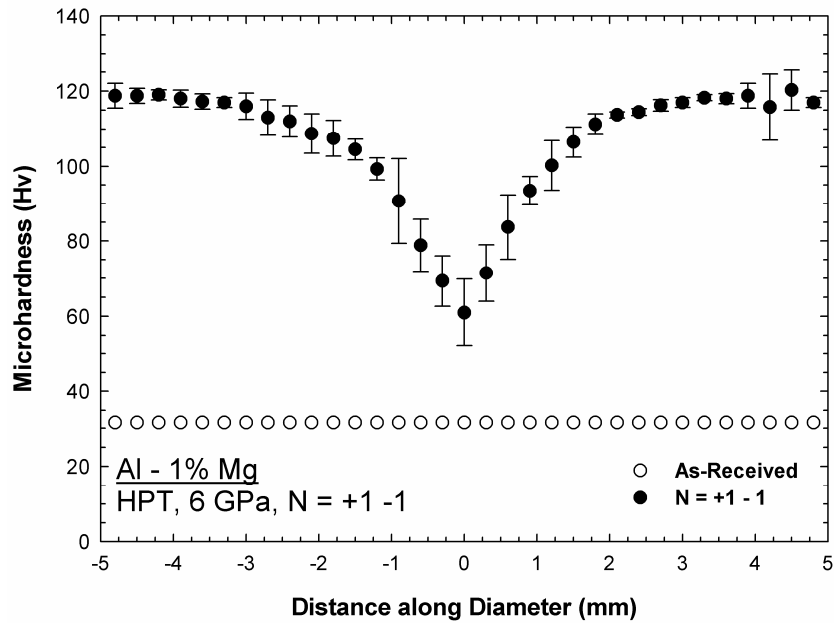


Fig. 7.7(d): The average of the microhardness measurements, Hv, recorded along the diameter of Al-1% Mg disk after c-HPT under a pressure of 6.0 GPa for +1 -1 turn. The microhardness measurements for alloy in the as-received unprocessed condition are also shown.

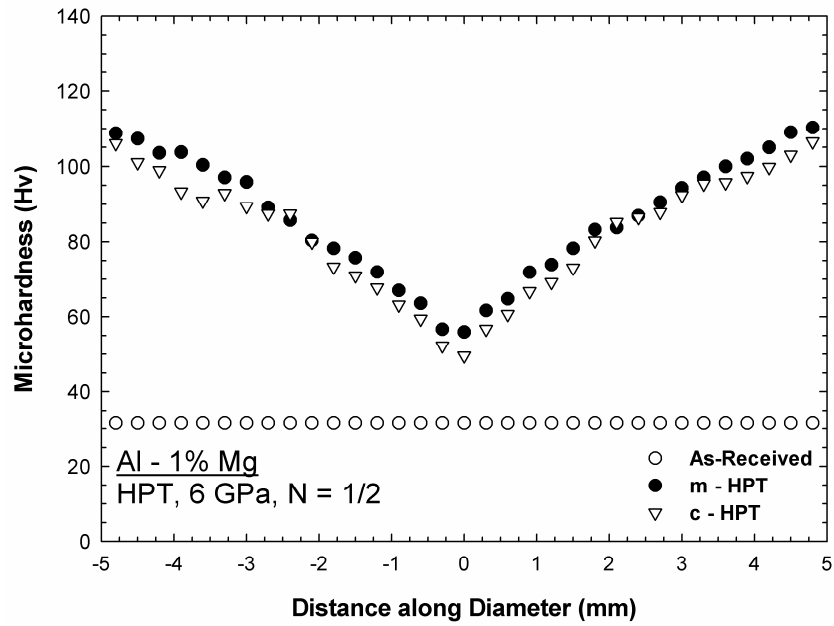


Fig. 7.8(a): The average of the microhardness measurements, Hv, recorded along the diameter of Al-1%Mg disks after m-HPT and c-HPT under a pressure of 6.0 GPa for 1/2 turn. The microhardness measurements for alloy in the as-received unprocessed condition are also shown.

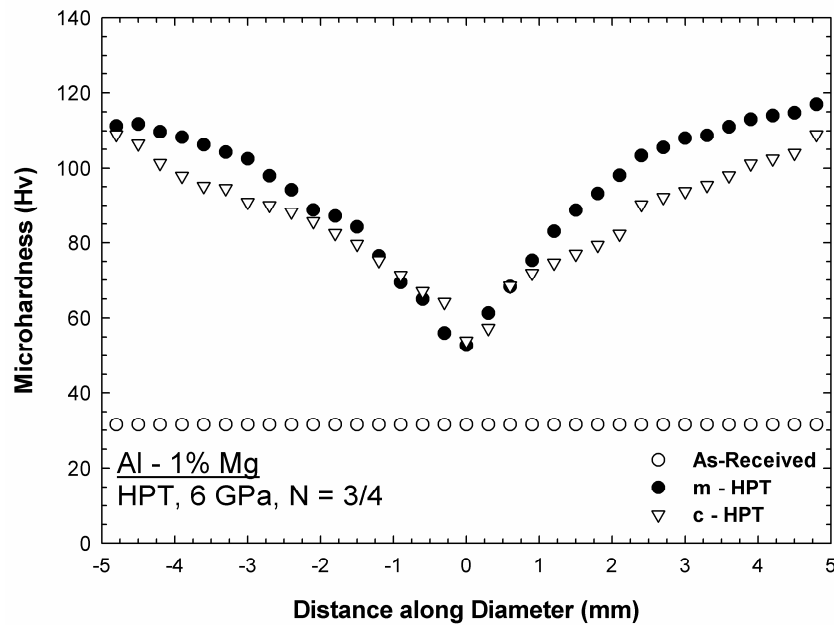


Fig. 7.8(b): The average of the microhardness measurements, Hv, recorded along the diameter of Al-1%Mg disks after m-HPT and c-HPT under a pressure of 6.0 GPa for 3/4 turn. The microhardness measurements for alloy in the as-received unprocessed condition are also shown.

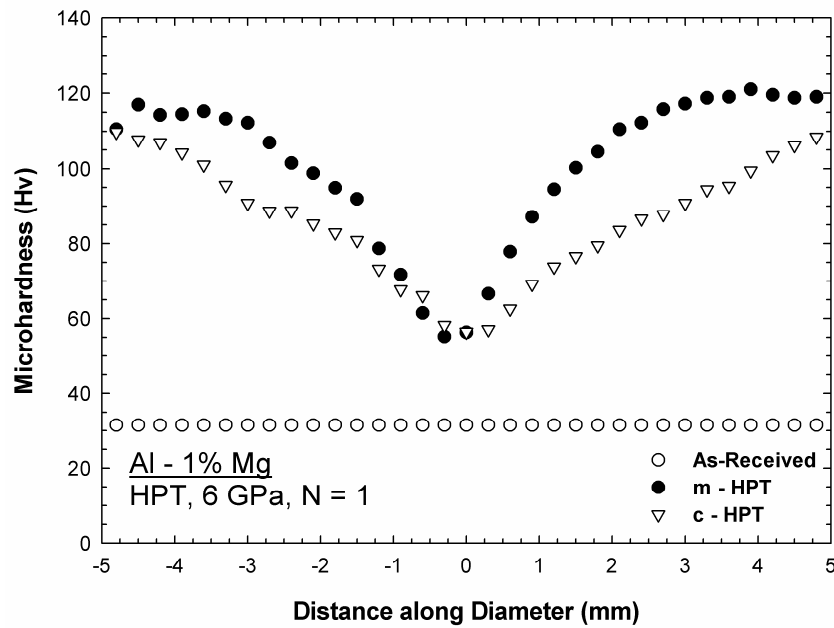


Fig. 7.8(c): The average of the microhardness measurements, Hv, recorded along the diameter of Al-1%Mg disks after m-HPT and c-HPT under a pressure of 6.0 GPa for 1 turn. The microhardness measurements for alloy in the as-received unprocessed condition are also shown.

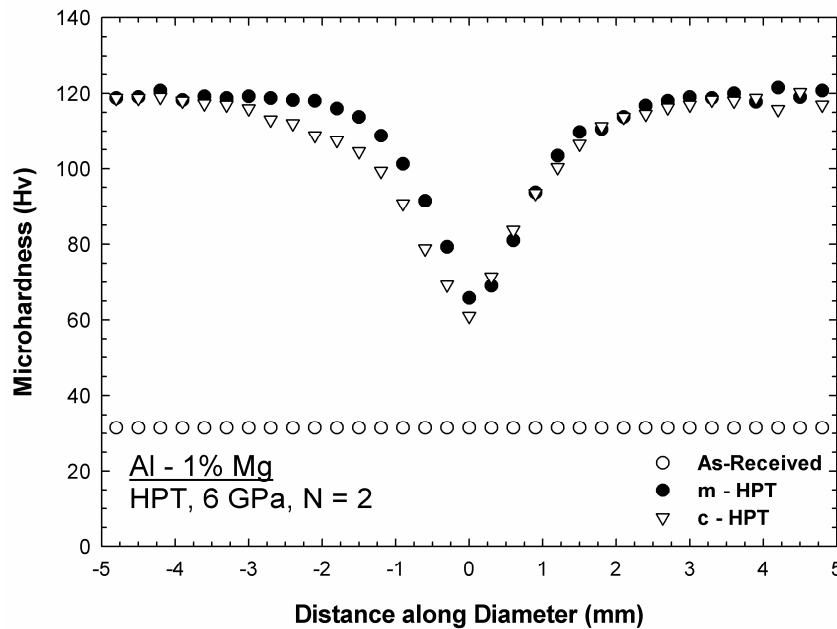


Fig. 7.8(d): The average of the microhardness measurements, Hv, recorded along the diameter of Al-1%Mg disks after m-HPT and c-HPT under a pressure of 6.0 GPa for 2 turns. The microhardness measurements for alloy in the as-received unprocessed condition are also shown.

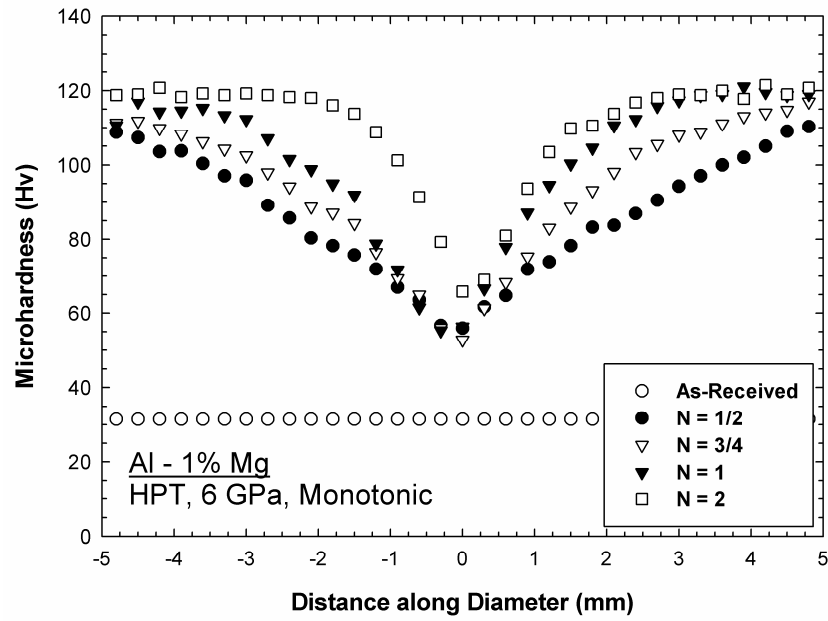


Fig. 7.9(a): The average microhardness measurements, Hv, recorded along the diameter of Al-1% Mg disks after m-HPT under a pressure of 6.0 GPa for 1/2, 3/4, 1 and 2 turns. The microhardness measurements for alloy in the as-received unprocessed condition are also shown.

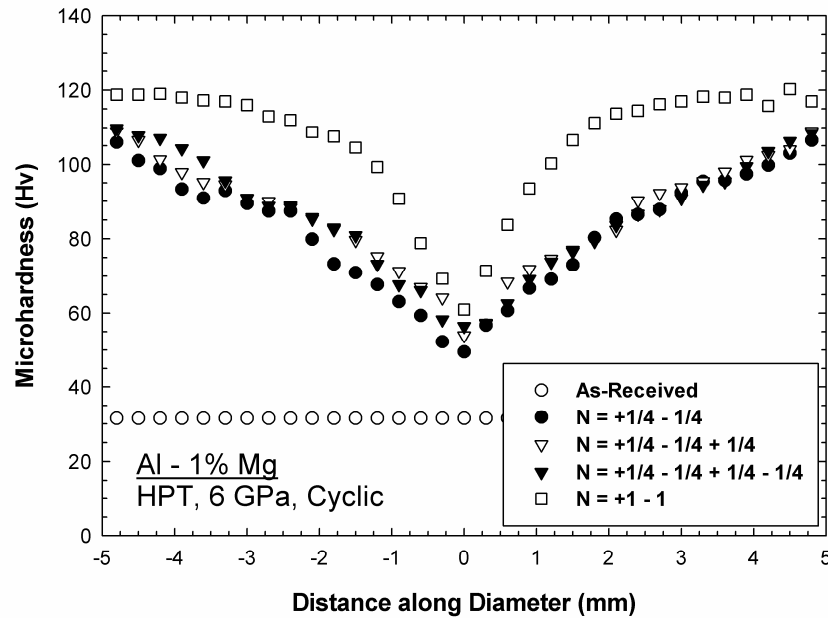


Fig. 7.9(b): The average microhardness measurements, Hv, recorded along the diameter of Al-1% Mg disks after c-HPT under a pressure of 6.0 GPa for +1/4-1/4, +1/4-1/4+1/4, +1/4-1/4+1/4-1/4 and +1-1 turns. The microhardness measurements for alloy in the as-received unprocessed condition are also shown.

7.3.2.3 CP Ti alloy:

Fig. 7.10 shows the individual microhardness measurements recorded along the diameter of the commercial purity titanium (CP Ti) alloy after m-HPT under a pressure of 6.0 GPa for (a) 1/2, (b) 3/4, (c) one and (d) two turns, respectively. The microhardness measurements for the alloy in the as-received unprocessed condition are also shown. After processing by HPT for 1/2 turn, as shown in Fig. 7.10(a), the microhardness values increased from an initial value of ~172 in the as-received unprocessed material to values ranging between ~248 at the centre of the disk and a maximum of approximately ~320 beyond a distance of ~2.0 mm from the centre of the disk before dropping to a value between 280 and 310 adjacent to the edges of the disk. The error bars were relatively high near the centre and the edges of the disk on both sides. After processing for 3/4 turn, as shown in Fig. 7.10(b), the microhardness measurements at the centre of the disk were approximately ~244 and near the edge of the disk the values were approximately ~310-320. The microhardness values started to become constant beyond a distance of ~2.0 mm from the centre of the disk on both sides and it dropped near the edge of one side to reach a value of approximately ~280. It is also noticed, as in the disk processed for 1/2 turn, that the error in the microhardness measurements taken near the centre and the edges of the disk was relatively high. After processing for one turn, as shown in Fig. 7.10(c), the microhardness measurement at the centre of the disk was approximately ~252 and it reached a constant values of approximately ~310-320 beyond a distance of ~2.0 mm from the centre on both sides of the disk before dropping to values of approximately ~280-300 near the edge of the disk. As in the other two disks, the error in the microhardness measurements taken near the centre and the edges of the disk was relatively high. After processing for two turns, as shown in Fig. 7.10(d), the microhardness measurement at the centre of the disk increased to reach approximately ~265 and it reached constant values of approximately ~300-310 beyond a distance of ~1.5 mm from the centre on both sides of the disk before dropping to values less than 300 in the vicinity of the edges of the disk. The error in the microhardness measurements taken near the centre and the edges of the disk was also relatively high, as in the other disks processed for 1/2, 3/4 and 1 turn.

The microhardness measurements along the diameter of the CP Ti disks after c-HPT under a pressure of 6.0 GPa for (a) $+1/4-1/4$, (b) $+1/4-1/4+1/4$, (c) $+1/4-1/4+1/4-1/4$ and (d) $+1-1$ turns, respectively, are shown in Fig. 7.11. After processing by HPT cyclically for $+1/4-1/4$ for a total of $1/2$ turn, as shown in Fig. 7.11(a), the microhardness values increased from an initial value of ~ 172 in the as-received unprocessed material to values of ~ 226 at the centre of the disk and it reached a relatively constant values of approximately $\sim 280-290$ beyond a distance of ~ 1.8 mm from the centre on both sides of the disk before dropping to values of approximately $\sim 260-270$ near the edges of the disk. Similar to that in the disks processed monotonically, the error bars near the centre and the edges of the disk were relatively high. After processing for $+1/4-1/4 +1/4$ for a total of $3/4$ turn, as shown in Fig. 7.11(b), the microhardness measurements at the centre increased to reach a value of approximately ~ 237 . The microhardness increased rapidly to reach values of approximately ~ 290 at a distance of ~ 1.0 mm from the centre of the disk and beyond that it increased gradually to reach a maximum of ~ 320 before dropping again to values of $\sim 280-290$ near the edges of the disk. It is also noticed that the error in the microhardness measurements taken near the centre of the disk was high compared to the error in the measurements away from the centre. After processing for $+1/4-1/4 +1/4-1/4$ for a total of one turn, as shown in Fig. 7.11(c), the microhardness measurement at the centre of the disk remained constant at a value of approximately ~ 237 and it increased rapidly to reach values above 290 at a distance of ~ 0.8 mm from the centre of the disk and beyond that it remained relatively constant at values about ~ 300 before dropping again to values of ~ 280 near the edges of the disk. The error bars at and near the centre of the disk were also high compared to that away from the centre. After processing for $+1-1$ for a total of two turns, as shown in Fig. 7.11(d), the microhardness measurement at the centre of the disk increased to reach approximately ~ 270 and it increased rapidly to reach values above 300 at a distance of ~ 0.5 mm from the centre of the disk. Beyond that, the microhardness values increased gradually to reach values about $\sim 310-325$ and remained constant before dropping again to values of $\sim 280-290$ near the edges of the disk. The error bars at and near the centre of the disk were also high compared to that away from the centre.

The microhardness measurements along the diameter of the CP Ti disks after m-HPT and c-HPT under a pressure of 6.0 GPa for (a) $1/2$, (b) $3/4$, (c) 1 and (d) 2 turns,

respectively, are shown in Fig. 7.12. The microhardness measurements for the alloy in the as-received unprocessed condition are also shown. After processing for a total of 1/2 turn, as shown in Fig. 7.12(a), the microhardness measurements were higher in the disk processed by m-HPT compared to that processed by c-HPT. In the disks processed for totals of 3/4 and 1 turn, as shown in Figs. 7.12(b) and (c), the evolution of the microhardness measurements was approximately similar when processing by m-HPT or c-HPT. After processing for a total of 2 turns, as shown in Fig. 7.12(d), the microhardness measurements were slightly higher in the disk processed by c-HPT compared to that processed by m-HPT.

The variation of the microhardness measurements along the diameter of the CP Ti disks after m-HPT and c-HPT under a pressure of 6.0 GPa for totals of 1/2, 3/4, 1 and 2 turns, respectively, are shown in Fig. 7.13. The microhardness measurements for the alloy in the as-received unprocessed condition are also shown. As shown in Fig. 7.13(a), the microhardness measurements were low in the centre of the disks processed monotonically and it increased with increasing distance from the centre to reach a saturation value of approximately ~300-320 before dropping again near the edges of the disks. The microhardness values reached the saturation value faster with increasing in the number of turns. The saturation value of the disk processed for two turns was less than that for the disks processed for fewer numbers of turns, although it was more consistent along the length of the diameter. As shown in Fig. 7.13(b), the microhardness values for the disks processed cyclically for +1/4-1/4, +1/4-1/4+1/4, +1/4-1/4+1/4-1/4 and +1-1 increased gradually with increasing numbers of turns. All disks had the same trend where the microhardness values were low at the centre of the disks and increased to reach a saturation values then dropped near the edges of the disks. The maximum saturation value was for the disk processed for +1-1 turns and it was higher than all saturation values can be reached by processing monotonically. By comparing the two graphs, it is noticed that the rate of increase in the microhardness values were faster when the disks are processed cyclically.

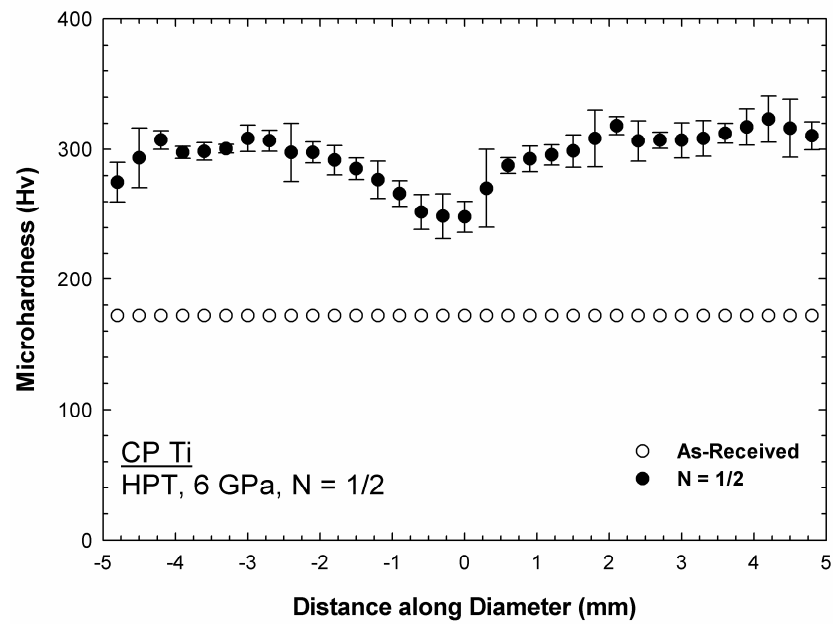


Fig. 7.10(a): The average of the microhardness measurements, Hv, recorded along the diameter of CP Ti disk after m-HPT under a pressure of 6.0 GPa for 1/2 turn. The microhardness measurements for alloy in the as-received unprocessed condition are also shown.

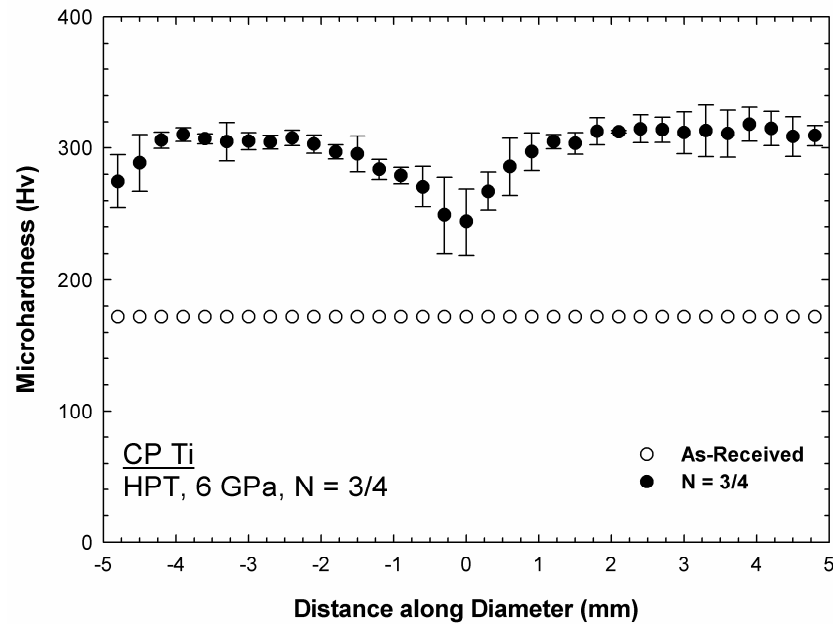


Fig. 7.10(b): The average of the microhardness measurements, Hv, recorded along the diameter of CP Ti disk after m-HPT under a pressure of 6.0 GPa for 3/4 turn. The microhardness measurements for alloy in the as-received unprocessed condition are also shown.

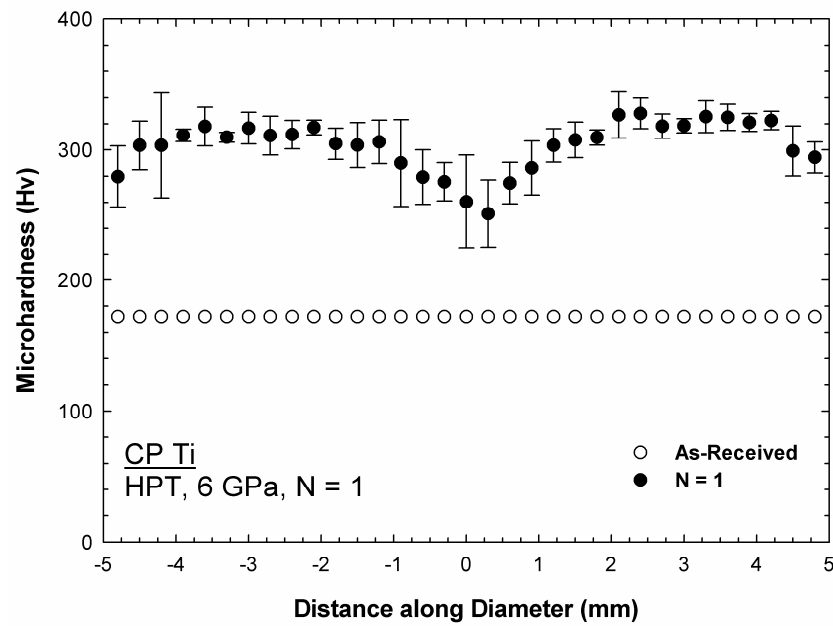


Fig. 7.10(c): The average of the microhardness measurements, Hv, recorded along the diameter of CP Ti disk after m-HPT under a pressure of 6.0 GPa for 1 turn. The microhardness measurements for alloy in the as-received unprocessed condition are also shown.

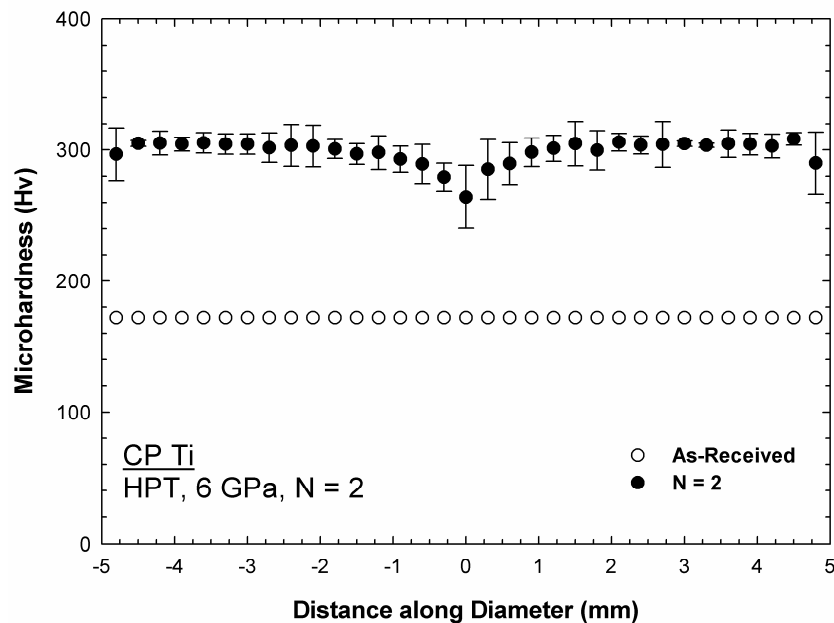


Fig. 7.10(d): The average of the microhardness measurements, Hv, recorded along the diameter of CP Ti disk after m-HPT under a pressure of 6.0 GPa for 2 turns. The microhardness measurements for alloy in the as-received unprocessed condition are also shown.

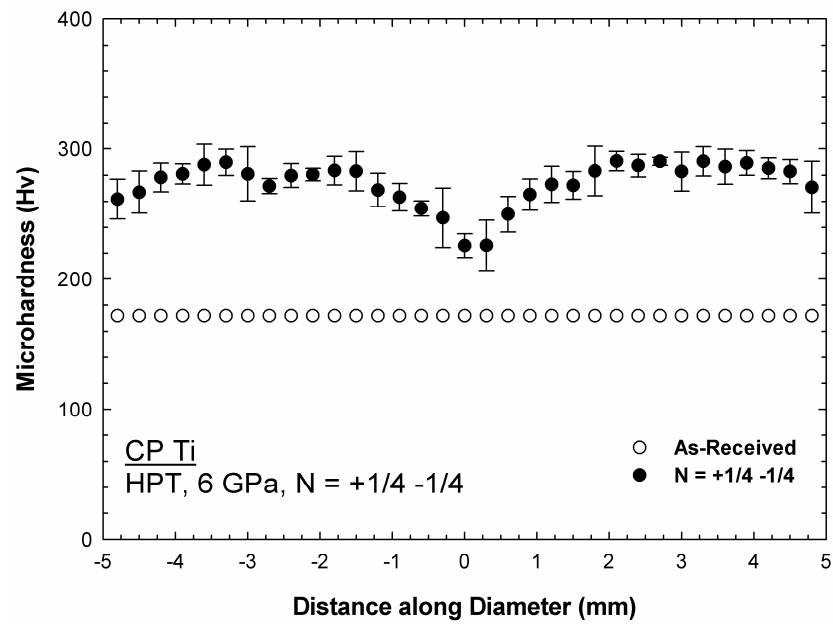


Fig. 7.11(a): The average of the microhardness measurements, Hv, recorded along the diameter of CP Ti disk after c-HPT under a pressure of 6.0 GPa for +1/4 -1/4 turn. The microhardness measurements for alloy in the as-received unprocessed condition are also shown.

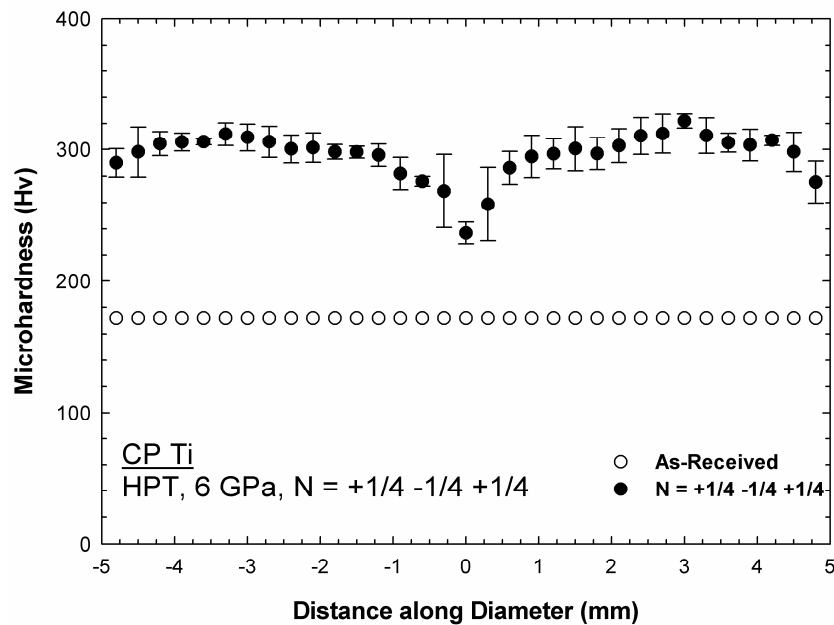


Fig. 7.11(b): The average of the microhardness measurements, Hv, recorded along the diameter of CP Ti disk after c-HPT under a pressure of 6.0 GPa for +1/4 -1/4 +1/4 turn. The microhardness measurements for alloy in the as-received unprocessed condition are also shown.

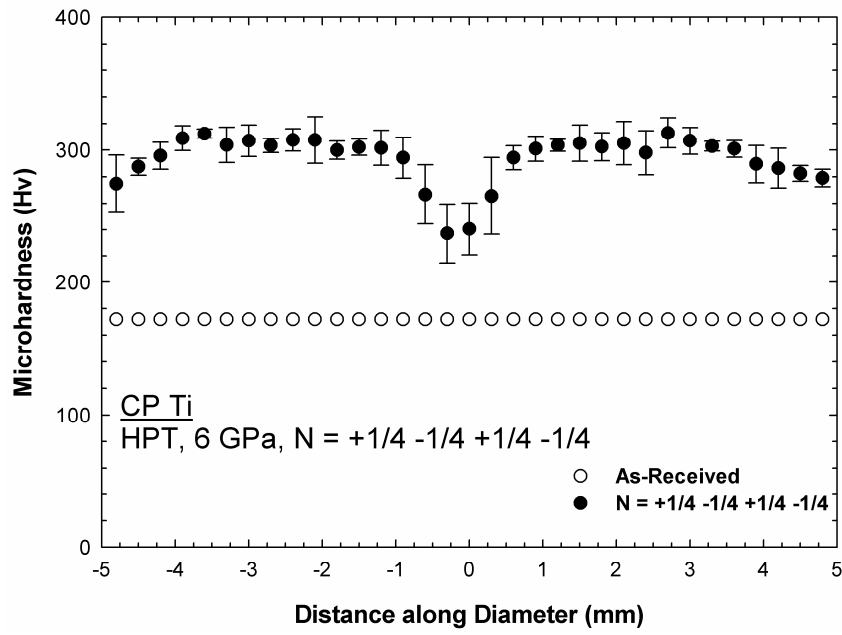


Fig. 7.11(c): The average of the microhardness measurements, Hv, recorded along the diameter of CP Ti disk after c-HPT under a pressure of 6.0 GPa for +1/4 -1/4 +1/4 -1/4 turn. The microhardness measurements for alloy in the as-received unprocessed condition are also shown.

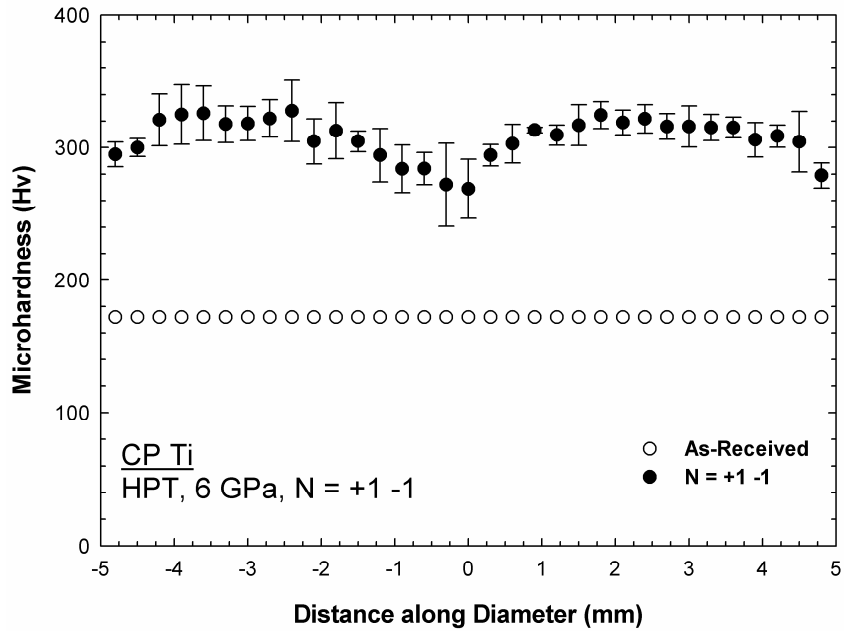


Fig. 7.11(d): The average of the microhardness measurements, Hv, recorded along the diameter of CP Ti disk after c-HPT under a pressure of 6.0 GPa for +1 -1 turn. The microhardness measurements for alloy in the as-received unprocessed condition are also shown.

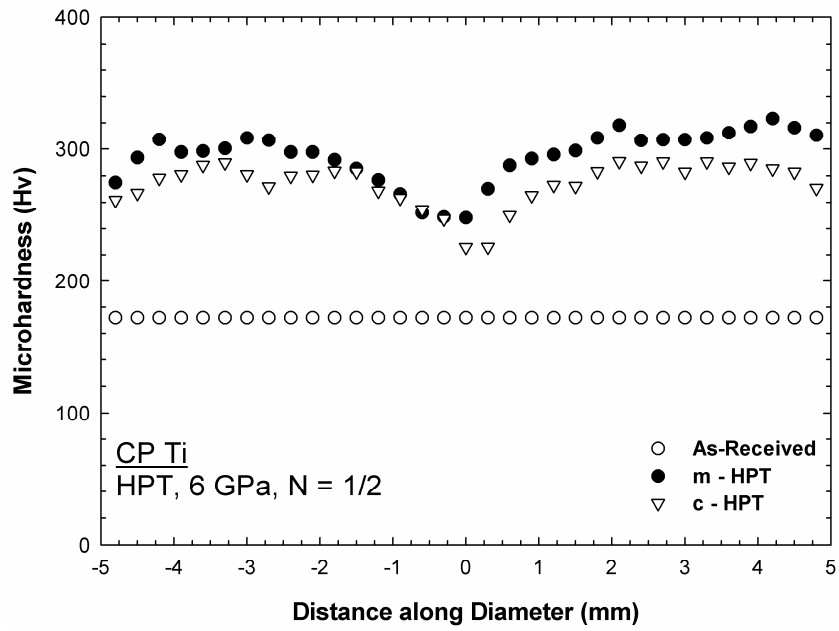


Fig. 7.12(a): The average of the microhardness measurements, Hv, recorded along the diameter of CP Ti disks after m-HPT and c-HPT under a pressure of 6.0 GPa for 1/2 turn. The microhardness measurements for alloy in the as-received unprocessed condition are also shown.

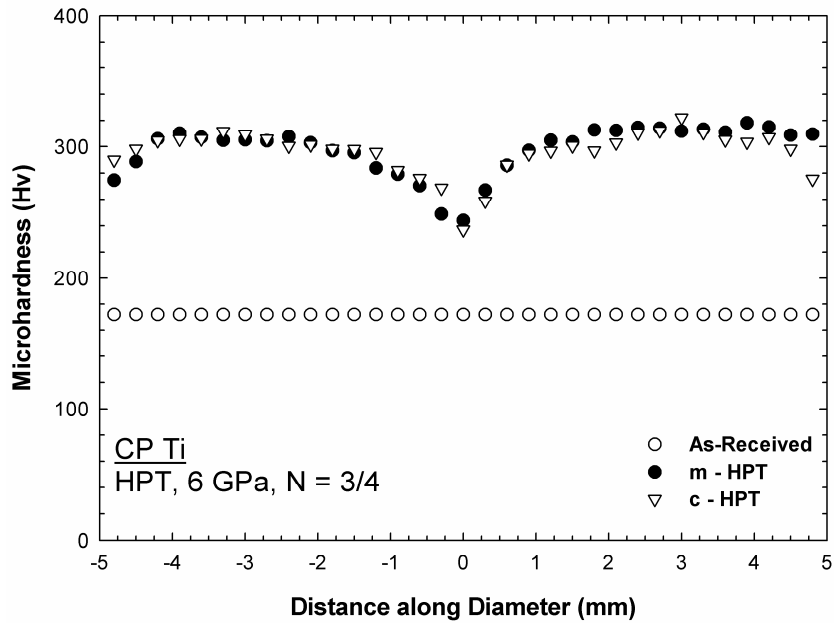


Fig. 7.12(b): The average of the microhardness measurements, Hv, recorded along the diameter of CP Ti disks after m-HPT and c-HPT under a pressure of 6.0 GPa for 3/4 turn. The microhardness measurements for alloy in the as-received unprocessed condition are also shown.

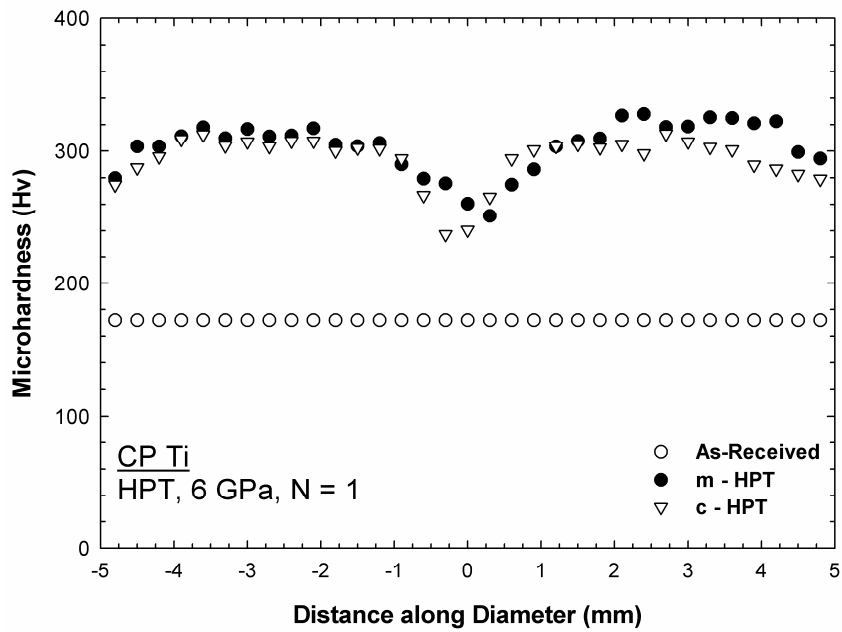


Fig. 7.12(c): The average of the microhardness measurements, Hv, recorded along the diameter of CP Ti disks after m-HPT and c-HPT under a pressure of 6.0 GPa for 1 turn. The microhardness measurements for alloy in the as-received unprocessed condition are also shown.

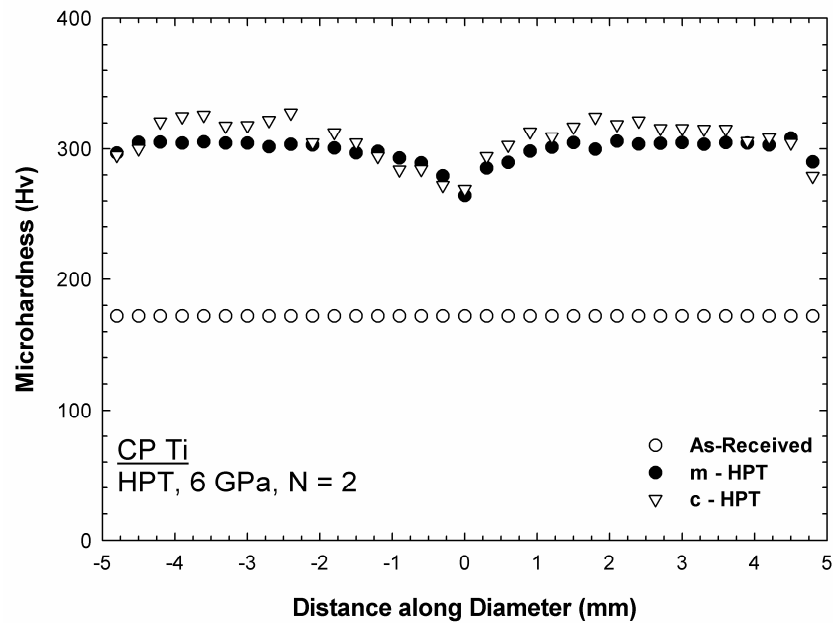


Fig. 7.12(d): The average of the microhardness measurements, Hv, recorded along the diameter of CP Ti disks after m-HPT and c-HPT under a pressure of 6.0 GPa for 2 turns. The microhardness measurements for alloy in the as-received unprocessed condition are also shown.

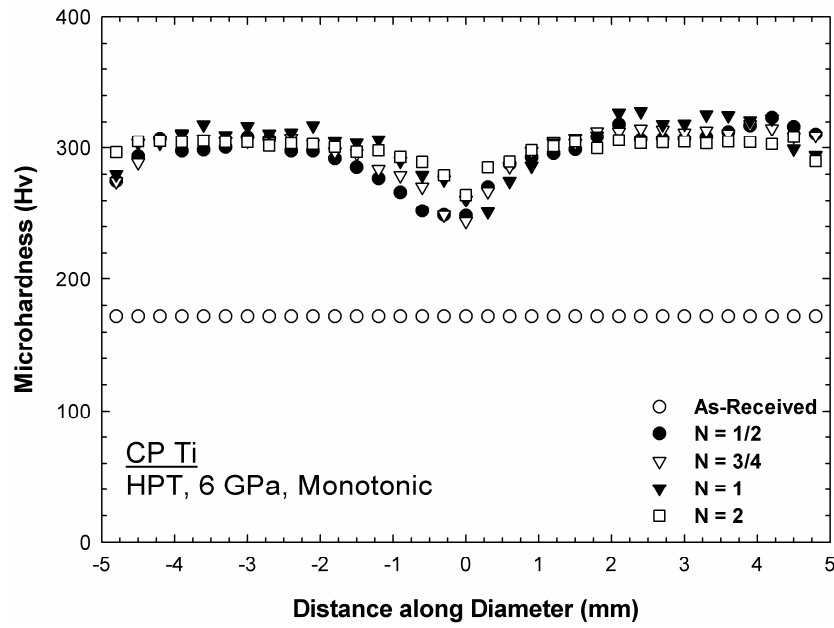


Fig. 7.13(a): The average microhardness measurements, Hv, recorded along the diameter of CP Ti disks after m-HPT under a pressure of 6.0 GPa for 1/2, 3/4, 1 and 2 turns. The microhardness measurements for alloy in the as-received unprocessed condition are also shown.

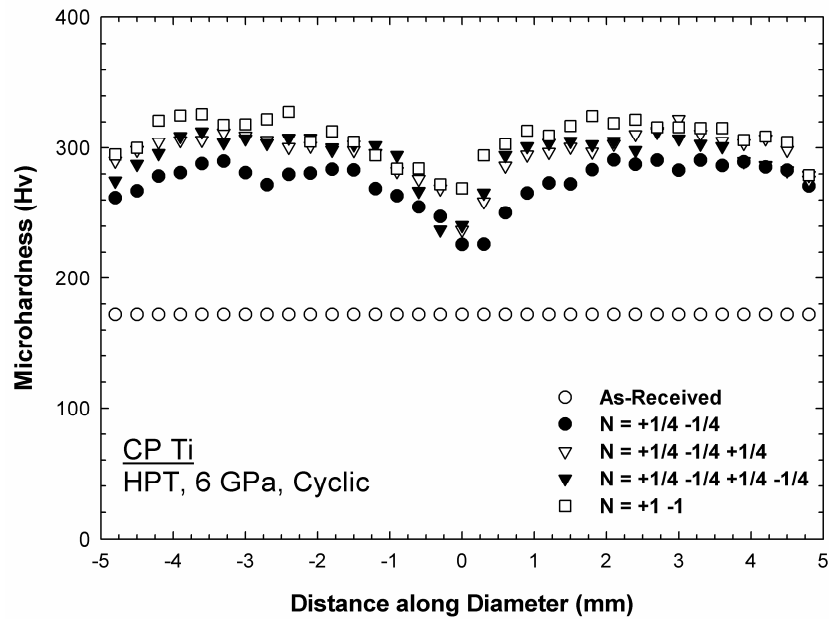


Fig. 7.13(b): The average microhardness measurements, Hv, recorded along the diameter of CP Ti disks after c-HPT under a pressure of 6.0 GPa for +1/4-1/4, +1/4-1/4+1/4, +1/4-1/4+1/4-1/4 and +1-1 turns. The microhardness measurements for alloy in the as-received unprocessed condition are also shown.

7.3.2.4 Ti - 6Al - 4V alloy:

Fig. 7.14 shows the individual microhardness measurements recorded along the diameter of the Ti-6Al-4V alloy after m-HPT under a pressure of 6.0 GPa for (a) 1/2, (b) 3/4, (c) one and (d) two turns, respectively. The microhardness measurements for the alloy in the as-received unprocessed condition are also shown. After processing by HPT for 1/2 turn, as shown in Fig. 7.14(a), the microhardness values increased from an initial value of ~290 in the as-received unprocessed material to values about ~312 at the centre of the disk and increased gradually with increasing distance from the centre before reaching a saturation value of approximately ~340 at a distance of ~1.5 from the centre. The microhardness measurements adjacent to the edges of the disk increased to reach values of approximately ~360-370. The error bars were relatively low along the diameter except the measurements near the edge of the disk on one side. After processing for 3/4 turn, as shown in Fig. 7.14(b), the microhardness measurements at the centre of the disk were approximately ~310 and it increased gradually to reach a maximum of approximately ~360 near the edges of the disk. There were some saturation values intervals along the diameter of the disk where the measurements reached a saturation value for a limited length then gradually increased to another saturation value. The first saturation value was approximately ~330 which started at a distance of ~1.0 mm from the centre of the disk and ended at a distance of ~2.5 mm from the centre of the disk. The second one was approximately ~360 which started at a distance of ~3.3 mm from the centre of the disk and continued to the edges of the disk on both sides. It is also noticed, as in the disk processed for 1/2 turn, that the error in the microhardness measurements was low along the diameter of the disk except the measurements taken near the edge of the disk on one side. After processing for one turn, as shown in Fig. 7.14(c), the microhardness measurement at the centre of the disk was approximately ~293 and it was different on both sides of the disk. On one side, the microhardness measurements increased gradually from the centre to reach a maximum of ~400 at a distance of 3.0 mm from the centre then dropped to a saturation value of about ~375 to the edge of the disk. On the second side, the microhardness increased gradually to reach a saturation value of approximately ~330 at a distance between ~1.0 mm and 3.0 mm from the centre of the disk and increased again gradually to reach a second saturation value of approximately ~360 at a distance of ~3.8 mm from the centre of

the disk to the edge of the disk. The trend of the microhardness evolution on the second side of the disk was similar to that in the disk processed for 3/4 turn. The error in the microhardness measurements taken on the second side of the disk was low compared to that taken on the first side. After processing for two turns, as shown in Fig. 7.14(d), the evolution of the microhardness measurements was similar to that of the disk processed for one turn. The microhardness at the centre of the disk increased to reach approximately ~304 and on one side it gradually increased to reach a maximum value of ~420 at a distance of ~4.0 mm from the centre then decreased beyond that to a value of approximately ~390 in the vicinity of the edge of the disk. On the second side, the microhardness increased gradually to reach a saturation value of approximately ~335 at a distance between ~0.8 mm and 2.5 mm from the centre of the disk and increased again gradually to reach a second saturation value of approximately ~365 at a distance of ~3.0 mm from the centre of the disk to the edge of the disk. Similar to that in the disk processed for one turn, the error in the microhardness measurements taken on the second side of the disk was low compared to that taken on the first side.

The microhardness measurements along the diameter of the Ti-6Al-4V disks after c-HPT under a pressure of 6.0 GPa for (a) +1/4-1/4, (b) +1/4-1/4+1/4, (c) +1/4-1/4+1/4-1/4 and (d) +1-1 turns, respectively, are shown in Fig. 7.15. After processing by HPT cyclically for +1/4-1/4 for a total of 1/2 turn, as shown in Fig. 7.15(a), the microhardness values near the centre of the disk were approximately ~296 which is close to that in the as-received unprocessed material. It increased gradually with increasing the distance from the centre to reach values of approximately ~365 near the edges of the disk. On one side, there was dropping in the microhardness values then increase again to reach the value of ~365 near the edge. The error bars were relatively low along the diameter except some isolated points. After processing for +1/4-1/4 +1/4 for a total of 3/4 turn, as shown in Fig. 7.15(b), the microhardness measurements at the centre increased to reach a value of approximately ~309. The microhardness increased gradually to reach values of approximately ~335 at a distance of ~1.5 mm from the centre of the disk on both sides of the disk and beyond that it remained almost constant on one side to the edge of the disk. On the second side, the measurements were ranging between ~330 and ~340 to a distance of ~3.0 mm from the centre then the measurements beyond that increased gradually to reach

a maximum of ~ 370 near the edge of the disk. The error bars were relatively low along the diameter except some isolated points and near the edge of the second side of the disk where the microhardness values were high. After processing for $+1/4-1/4$ for a total of one turn, as shown in Fig. 7.15(c), the microhardness measurement at the centre of the disk increased to reach a value of approximately ~ 315 and it increased gradually to reach values of ~ 370 on one side and ~ 400 on the second side before dropping near the edges to values of ~ 360 on the first side and ~ 380 on the second side. The error bars were relatively high near the edges of the disk. After processing for $+1-1$ for a total of two turns, as shown in Fig. 7.15(d), the microhardness measurement at the centre of the disk was approximately ~ 304 . The microhardness increased gradually to reach values of approximately ~ 365 at a distance of ~ 1.8 mm from the centre of the disk on both sides of the disk and beyond that it remained almost constant on one side to the edge of the disk. On the second side, the microhardness measurements increased near the edge of the disk to reach values of ~ 385 . The error bars were relatively low along the diameter except some isolated points.

The microhardness measurements along the diameter of the Ti-6Al-4V disks after m-HPT and c-HPT under a pressure of 6.0 GPa for (a) $1/2$, (b) $3/4$, (c) 1 and (d) 2 turns, respectively, are shown in Fig. 7.16. The microhardness measurements for the alloy in the as-received unprocessed condition are also shown. After processing for totals of $1/2$ and $3/4$ turn, as shown in Figs. 7.16(a) and (b), the microhardness measurements were higher in the disk processed by m-HPT compared to that processed by c-HPT. In the disks processed for totals of 1 and 2 turns, as shown in Figs. 7.16(c) and (d), the evolution of the microhardness measurements was approximately similar when processing by m-HPT or c-HPT.

The variation of the microhardness measurements along the diameter of the Ti-6Al-4V disks after m-HPT and c-HPT under a pressure of 6.0 GPa for totals of $1/2$, $3/4$, 1 and 2 turns, respectively, are shown in Fig. 7.17. The microhardness measurements for the alloy in the as-received unprocessed condition are also shown. In the disks processed monotonically, as shown in Fig. 7.17(a), the microhardness measurements were low in the centre of the disks and it increased gradually and almost linearly with increasing distance from the centre to reach maximum values near the edges of the

disks. The increase in the microhardness values with increasing number of turns was very small. There was instability in the measurements near the edge of one side. As shown in Fig. 7.17(b), the microhardness values for the disks processed cyclically for $+1/4-1/4$, $+1/4-1/4+1/4$, $+1/4-1/4+1/4-1/4$ and $+1-1$ increased gradually with increasing numbers of turns. All disks had the same trend where the microhardness values were low at the centre of the disks and increased gradually to reach a saturation values at a distance of approximately ~ 1.8 mm which continued to the edge of the disk. The saturation value increased with increasing number of turns. On one side, there was some increase in the microhardness near the edge of the disk. It is noticed, by comparing the two graphs, that the rate of increase in the microhardness values, when the instability near the edge of one side of the disks processed monotonically was neglected, were faster when the disks are processed cyclically.

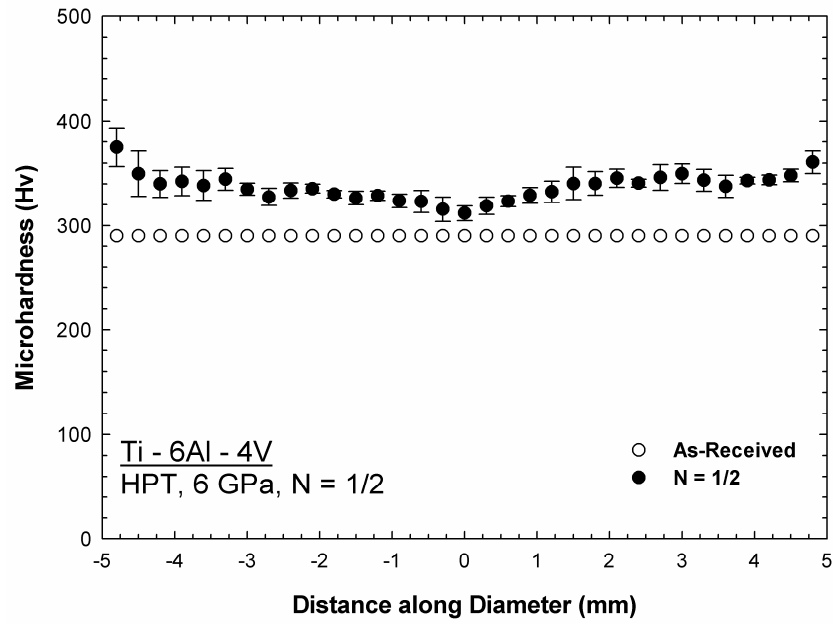


Fig. 7.14(a): The average of the microhardness measurements, Hv, recorded along the diameter of Ti-6Al-4V disk after m-HPT under a pressure of 6.0 GPa for 1/2 turn. The microhardness measurements for alloy in the as-received unprocessed condition are also shown.

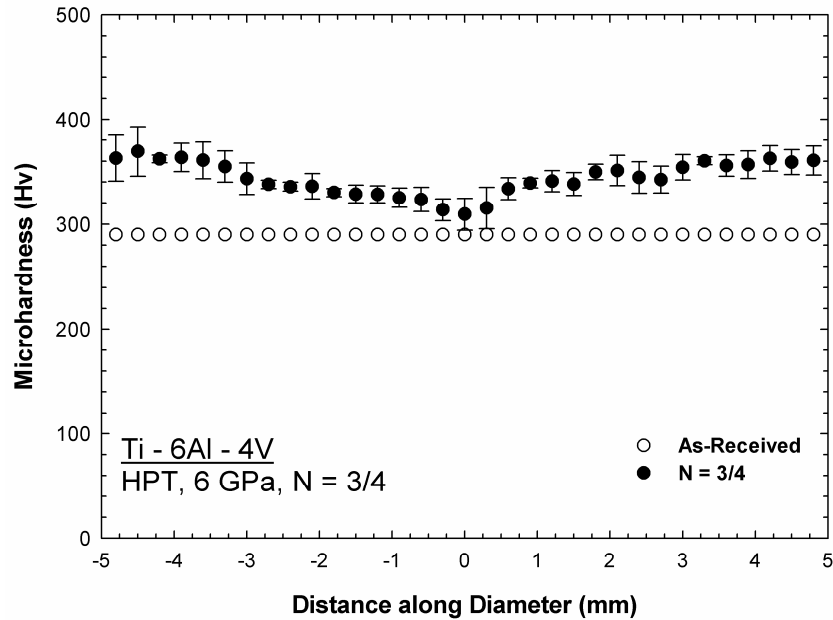


Fig. 7.14(b): The average of the microhardness measurements, Hv, recorded along the diameter of Ti-6Al-4V disk after m-HPT under a pressure of 6.0 GPa for 3/4 turn. The microhardness measurements for alloy in the as-received unprocessed condition are also shown.

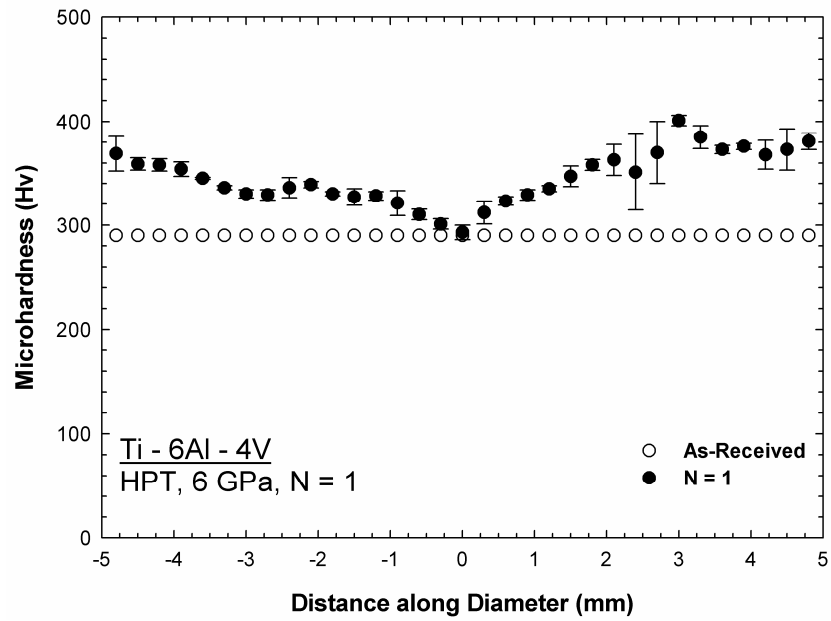


Fig. 7.14(c): The average of the microhardness measurements, Hv, recorded along the diameter of Ti-6Al-4V disk after m-HPT under a pressure of 6.0 GPa for 1 turn. The microhardness measurements for alloy in the as-received unprocessed condition are also shown.

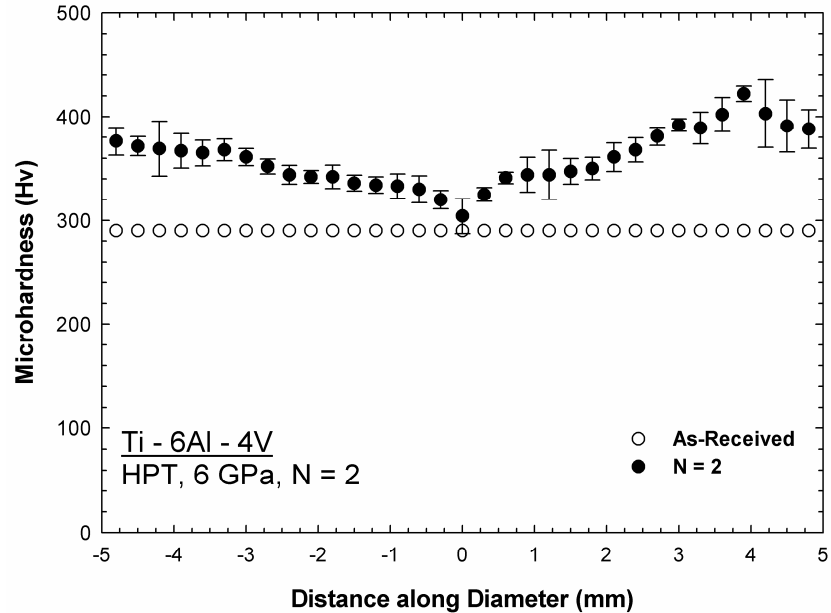


Fig. 7.14(d): The average of the microhardness measurements, Hv, recorded along the diameter of Ti-6Al-4V disk after m-HPT under a pressure of 6.0 GPa for 2 turns. The microhardness measurements for alloy in the as-received unprocessed condition are also shown.

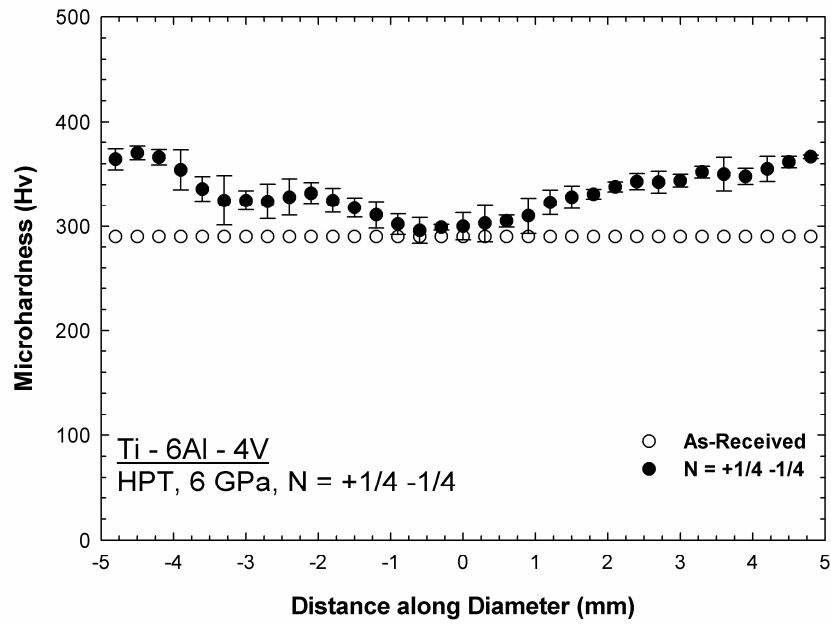


Fig. 7.15(a): The average of the microhardness measurements, Hv, recorded along the diameter of Ti-6Al-4V disk after c-HPT under a pressure of 6.0 GPa for +1/4 -1/4 turn. The microhardness measurements for alloy in the as-received unprocessed condition are also shown.

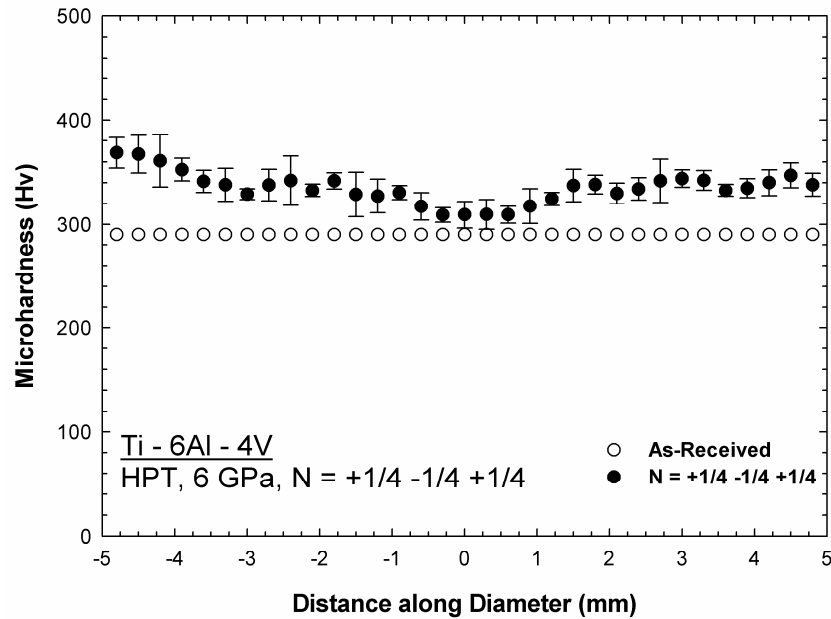


Fig. 7.15(b): The average of the microhardness measurements, Hv, recorded along the diameter of Ti-6Al-4V disk after c-HPT under a pressure of 6.0 GPa for +1/4 -1/4 +1/4 turn. The microhardness measurements for alloy in the as-received unprocessed condition are also shown.

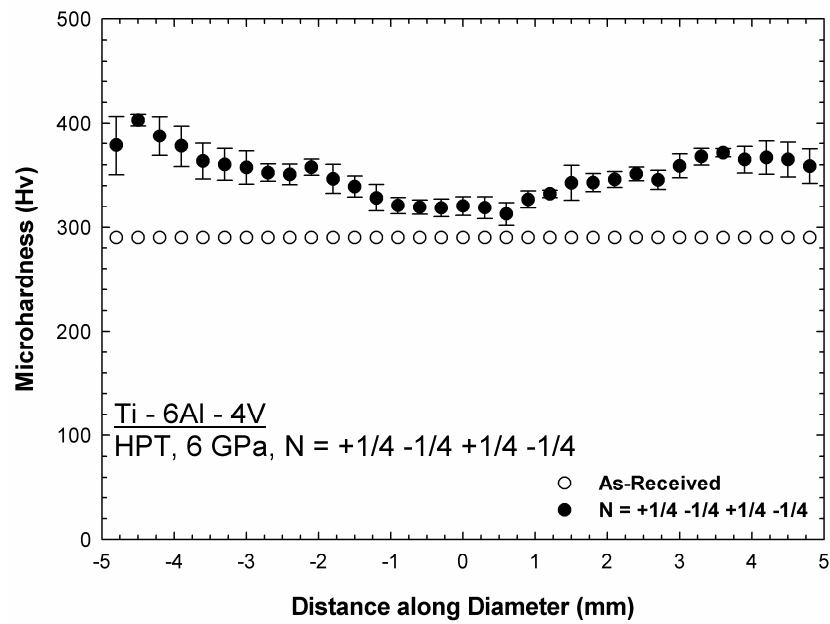


Fig. 7.15(c): The average of the microhardness measurements, Hv, recorded along the diameter of Ti-6Al-4V disk after c-HPT under a pressure of 6.0 GPa for +1/4 -1/4 +1/4 -1/4 turn. The microhardness measurements for alloy in the as-received unprocessed condition are also shown.

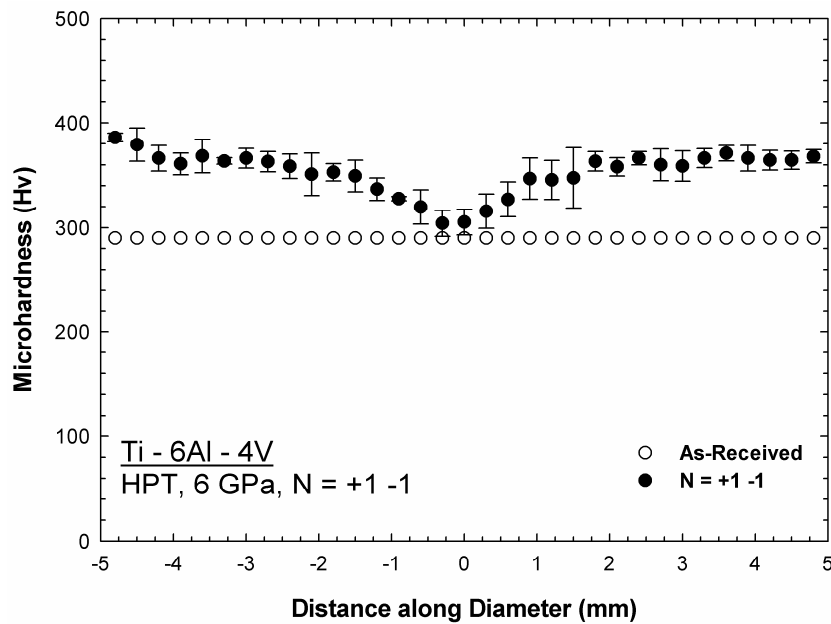


Fig. 7.15(d): The average of the microhardness measurements, Hv, recorded along the diameter of Ti-6Al-4V disk after c-HPT under a pressure of 6.0 GPa for +1 -1 turn. The microhardness measurements for alloy in the as-received unprocessed condition are also shown.

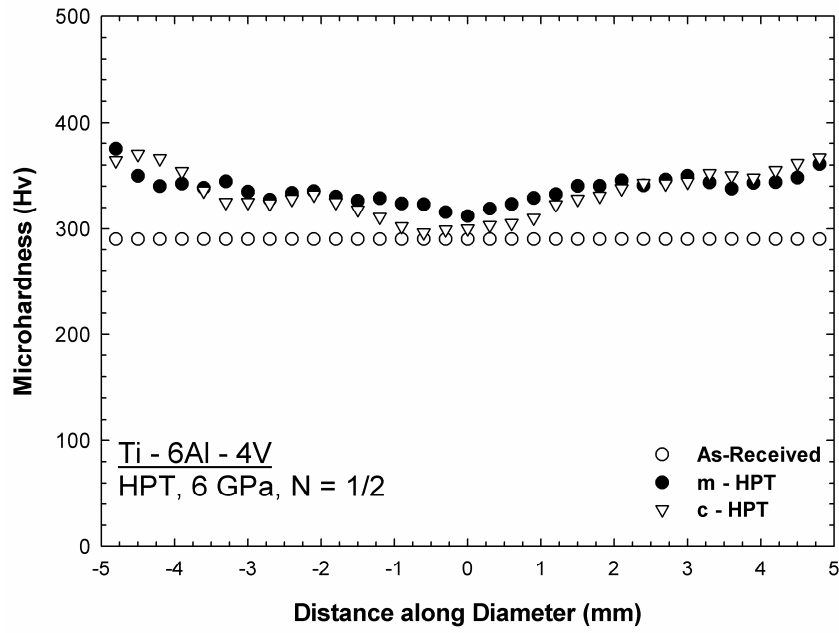


Fig. 7.16(a): The average of the microhardness measurements, Hv, recorded along the diameter of Ti-6Al-4V disks after m-HPT and c-HPT under a pressure of 6.0 GPa for 1/2 turn. The microhardness measurements for alloy in the as-received unprocessed condition are also shown.

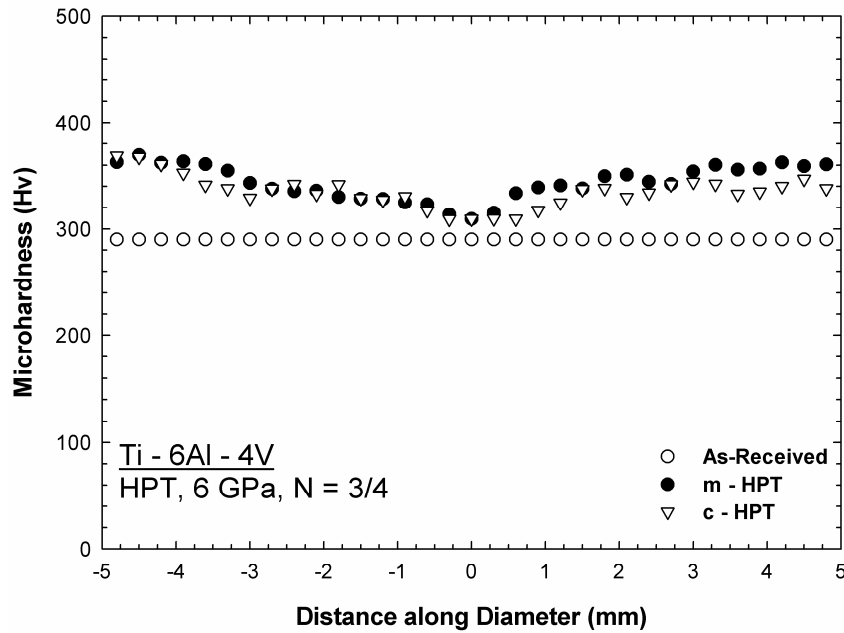


Fig. 7.16(b): The average of the microhardness measurements, Hv, recorded along the diameter of Ti-6Al-4V disks after m-HPT and c-HPT under a pressure of 6.0 GPa for 3/4 turn. The microhardness measurements for alloy in the as-received unprocessed condition are also shown.

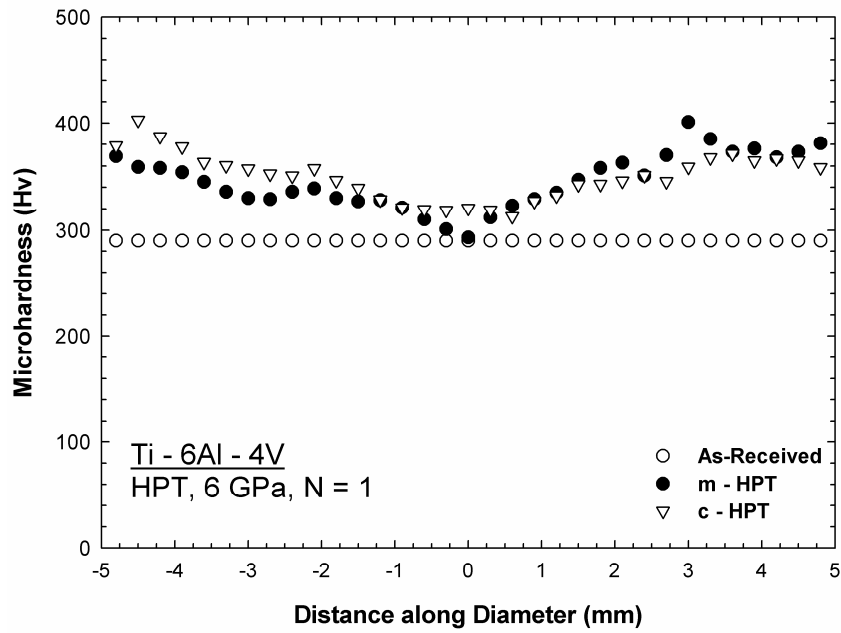


Fig. 7.16(c): The average of the microhardness measurements, Hv, recorded along the diameter of Ti-6Al-4V disks after m-HPT and c-HPT under a pressure of 6.0 GPa for 1 turn. The microhardness measurements for alloy in the as-received unprocessed condition are also shown.

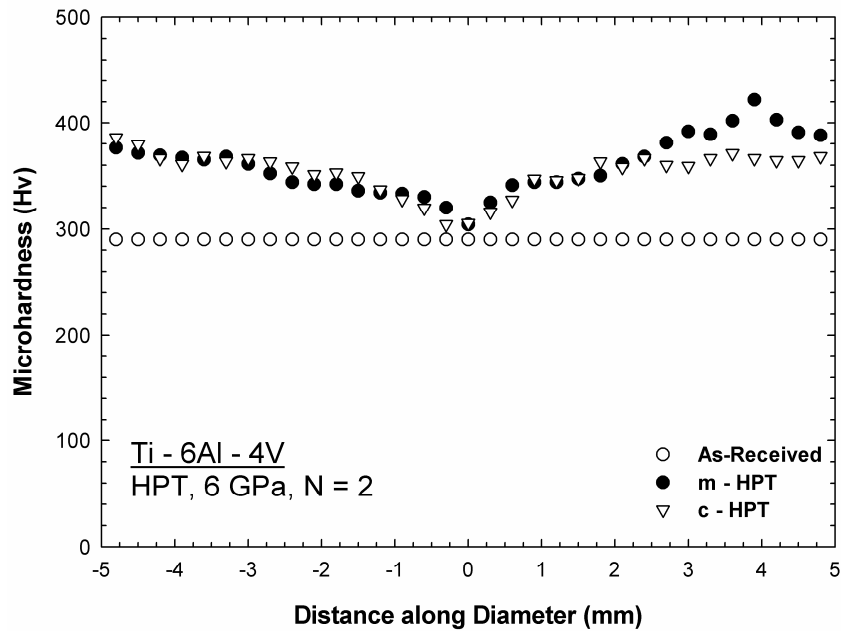


Fig. 7.16(d): The average of the microhardness measurements, Hv, recorded along the diameter of Ti-6Al-4V disks after m-HPT and c-HPT under a pressure of 6.0 GPa for 2 turns. The microhardness measurements for alloy in the as-received unprocessed condition are also shown.

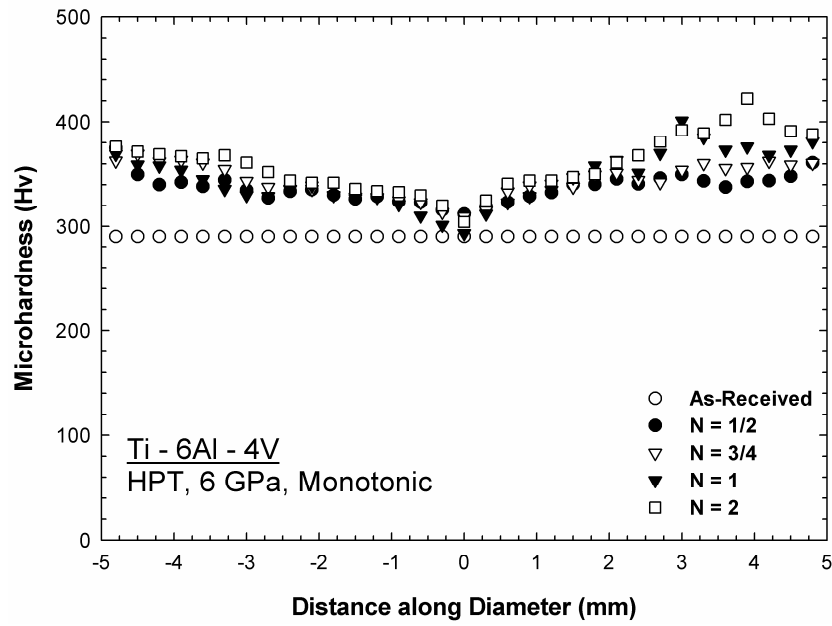


Fig. 7.17(a): The average microhardness measurements, Hv, recorded along the diameter of Ti-6Al-4V disks after m-HPT under a pressure of 6.0 GPa for 1/2, 3/4, 1 and 2 turns. The microhardness measurements for alloy in the as-received unprocessed condition are also shown.

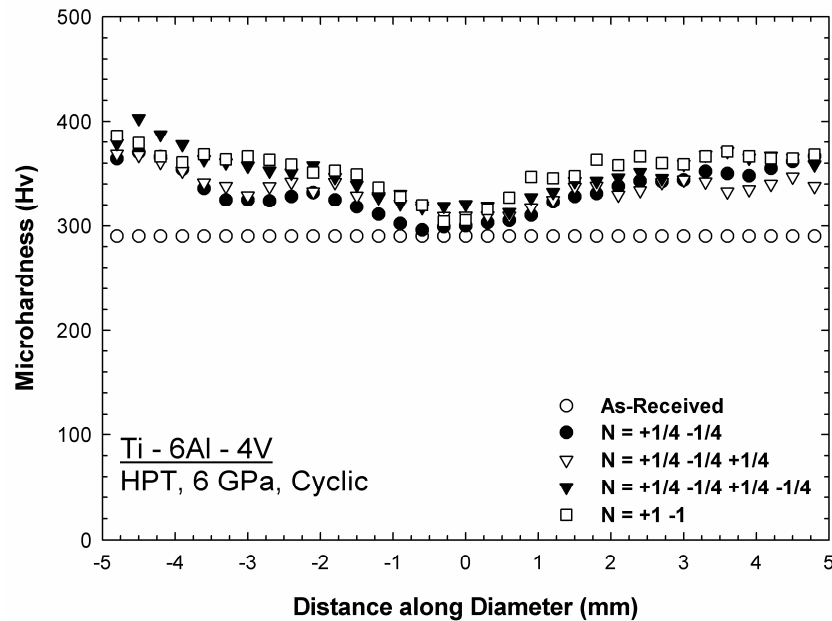


Fig. 7.17(b): The average microhardness measurements, Hv, recorded along the diameter of Ti-6Al-4V disks after c-HPT under a pressure of 6.0 GPa for +1/4-1/4, +1/4-1/4+1/4, +1/4-1/4+1/4-1/4 and +1-1 turns. The microhardness measurements for alloy in the as-received unprocessed condition are also shown.

7.4 Discussion

The main objective of this research was to evaluate the effect of strain reversal on the evolution of the microhardness along the diameter of four different alloys. The alloys used in this investigation were commercial purity aluminium, Al-1%Mg, commercial purity titanium and Ti-6Al-4V. To perform this two sets of disks were used, one set processed monotonically for 1/2, 3/4, 1 and 2 turns and the second processed cyclically for +1/4-1/4, +1/4-1/4+1/4, +1/4-1/4+1/4-1/4 and +1-1 which gave totals of turns similar to that used for m-HPT processing.

To evaluate the effect of strain reversal correctly, it was important to measure that the same numbers of turns were achieved in the two cases, m-HPT and c-HPT, for the four alloys. This can be achieved by assuring that the external rotation which imposed during processing is similar to the straining applied on the disks. In this case, it was important to know that the experiments were performed in absence of any slippage between the disks surfaces and the surfaces of the upper or lower anvils. Although, the possibility of experience slippage under high pressures such as the pressure used in this investigation which was 6.0 GPa is small [127]. To study the existence of slippage, two parallel lines were drawn on the two surfaces of each disk. After straining, the angle between the two lines was measured and compared to the anticipated angle of the corresponding rotation. The results showed that the difference between the measured and the anticipated angles of all cases was zero or very close to zero in some cases which can be linked to the manual operation of the experiments.

The results of the microhardness measurements after m-HPT and c-HPT for the four alloys showed low values at the centre of the disks and high values near the edges. These results are consistent with all previous reports on different materials which processed by HPT technique, except the processing of high purity aluminium alloy which showed high values of microhardness at the centre of the disks and low values near the edges which was due to, as suggested, the high stacking fault of high purity aluminium [95]. In the two aluminium alloys (Al-1050 and Al-1%Mg) which processed by m-HPT, there was a gradual increase towards the homogeneity and

consistency of the microhardness values along the diameter of the disks with increasing in the number of turns. On the other hand, when the two alloys were processed by c-HPT, the evolution of microhardness in the first three disks which processed for $+1/4-1/4$, $+1/4-1/4+1/4$ and $+1/4-1/4+1/4-1/4$ with totals of $1/2$, $3/4$ and 1 turn, respectively, was very small. Only the evolution of the microhardness of the disk which processed for $+1-1$ with a total of 2 turns was very close to that processed by m-HPT for 2 turns. It is concluded from these results that the rate of the evolution towards the homogeneity of microhardness along the diameter of the disks in the aluminium alloys is higher when the disks are processed by m-HPT rather than processing by c-HPT. This result is consistent with the results of some materials such as Al-3%Mg-0.2%Sc [90], high purity Al [97], Armco iron [98], high purity Ni [98], 900A pearlitic rail steel [99] and low carbon steel (Fe-0.03C) [100]. It is also concluded that increasing the amount of strain imposed in each separate rotation will increase the rate of evolution of the microhardness along the diameter. This can be proven by the big difference between the evolution of the microhardness of the disks processed by c-HPT through the rotation of $1/4$ turn increments and that of the disk processed by c-HPT through the rotation of 1 turn increments. The later result is consistent with the results of the reversal straining of high purity aluminium alloy which showed that the rate of evolution of the microhardness is dependent on the amount of strain imposed in each rotation and the total number of strain imposed on the disk [97]. In both alloys processed by either m-HPT or c-HPT, the error in the microhardness measurements which taken near the centre was generally high compared to that away from the centre. These high values of error at the centre indicate the instability in the hardness at the centre of the disks within very small distances. Away from the centre, the error became small and consistent along the diameter of the disk. It is concluded from this observation that the hardness near the centre of disks processed by HPT is highly instable within very small distances while it is stable and consistence along the diameter of the disks away from the centre.

In the two titanium alloys (CP Ti and Ti-6Al-4V), the results were different than the aluminium alloys. The increase in the microhardness values with increasing numbers of turn during processing by m-HPT was very small. Furthermore, the microhardness values of the CP Ti disk processed for two turns were less than that processed for one turn, although it was more consistent along the diameter. On the other hand, there

was a gradual increase in the microhardness values with increasing number of turns for both alloys during processing by c-HPT. It is concluded from these results that the rate of the evolution of the microhardness in the titanium alloys was higher when the disks are processed by c-HPT rather than processing by m-HPT. This result is consistent with a previous result of commercial purity titanium (CP Ti) which showed that the rate of increase of hardness in CP Ti was higher in c-HPT than that in m-HPT [100]. This contradiction between the results of the titanium alloys and the results of all other alloys processed by reversal straining is due to, as suggested, the different internal microstructure of the titanium alloys which is hexagonal closed packed (hcp) where the alloy initiating new slip systems on each reverse of the straining direction [97]. In the CP Ti alloy processed by either m-HPT or c-HPT, the error in the microhardness measurements which taken near the centre for most of the disks and near the edges for some disks was generally high. As mentioned for the aluminium alloys, these high values of error indicate the instability in the hardness at the centre of the disks and near the edges within very small distances. In the Ti-6Al-4V alloy, the error in the microhardness measurements along the diameter was generally small for the two cases, m-HPT and c-HPT. This might be due to the small increments of the microhardness along the diameter of the disks where the overall increase in the hardness of this alloy after processing by HPT for up to two turns was relatively small.

7.5 Summary and Conclusions

1. HPT processing were performed monotonically and cyclically on two aluminium alloys (Al-1050 and Al-1.0%Mg) and two titanium alloys (CP Ti and Ti-6Al-4V) under a pressure of 6.0 GPa for totals of 1/2, 3/4, 1 and 2 turns.
2. The processing was performed under the absence of any slippage between the surfaces of the disks of all alloys and the surface of the upper or lower anvils.
3. Microhardness measurements were taken along the diameter at 33 points and the average of four measurements was recorded with the error bars corresponding to 95% confidence limits.
4. In the two aluminium alloys, the rate of the evolution towards the homogeneity of microhardness along the diameter of the disks which processed by m-HPT is higher than that processed by c-HPT.
5. Increasing the amount of strain imposed in each separate rotation during c-HPT will increase the rate of the evolution of the microhardness.
6. In the two titanium alloys, opposing the results of the aluminium alloys, the rate of increase of the microhardness values in the disks which processed by c-HPT is higher than that processed by m-HPT.
7. For most of the disks, the error was relatively high near the centre which indicates that the hardness at this region is highly instable within very small distances.

CHAPTER 8

SUMMARY AND FUTURE WORK

8.1 Summary and Conclusions

8.1.1 The evolution of homogeneity after processing by ECAP and HPT:

The study of the microhardness values of Al-1050 alloy after processing by ECAP showed an inhomogeneous increase in the hardness of the alloy after processing through one pass of ECAP. The ECAP experiments were conducted at room temperature at a pressing speed of 0.5 mm/s and through up to six passes. After one pass, high values of microhardness were recorded in the central region of the billet and low values near the top and bottom surfaces. With increasing number of passes, the values of the hardness increased slightly and started to become more homogeneous. After six passes of ECAP, the lower values near the top surface disappeared and that near the bottom surface remained, although it became less pronounced. The values of the hardness after six passes of ECAP were in the range of approximately ~56 and the billet was completely homogeneous except the region adjacent to the bottom surface especially towards the front edge. Better results were approached when processing the same material by HPT. The HPT experiments were conducted at room temperature at a pressure of 6.0 GPa and for up to five turns. After 1/4 turn, the hardness increased inhomogeneously with lower values at the centre of the disk and higher values near the edges. With increasing numbers of turns, the values of the hardness increased slightly and started to become more homogeneous. After five turns, the hardness was completely homogeneous across the entire surface and it was approximately ~65. A comparison between the results performed by processing Al-1050 alloy by ECAP and by HPT shows clearly that better homogeneity and higher hardness was achieved by using the HPT process. As mentioned previously, the degree of homogeneity of the microhardness

measurements reveals the homogeneity of the internal microstructure of metals as stated in many previous reports [52,78,95,103]. The results of higher hardness after processing by HPT compared to processing by ECAP are consistent with the results showing that the grains produced by HPT are smaller in sizes compared to that produced by ECAP. Processing Al-3%Mg alloy by HPT produced grains with sizes of ~90 nm whereas that produced by ECAP had sizes of ~270 nm [72,73]. The sizes of the Al-5%Fe alloy grains after processing by HPT were ~100 nm whereas after ECAP they were ~300 nm [74]. In high purity Ni, the grain sizes after processing by HPT were ~170 nm and after processing by ECAP were ~350 nm [75]. In pure Ti, the grain sizes which were ~300 nm after processing by ECAP can be reduced to ~200 nm by processing by HPT after the ECAP [54]. In addition to the reduction in the grain sizes, the fraction of high angle boundaries were higher in high purity Ni alloy after processing by HPT compared to that in the alloy processed by ECAP [75,76].

Another important conclusion were found by investigating the evolution of microhardness of Al-1050 alloy and Al-1%Mg alloy after processing by HPT at room temperature under a pressure of 6 GPa for up to five turns. In both alloys, the results showed an increase in the microhardness with increasing numbers of turns. However, the evolution of the microhardness homogeneity occurs more rapidly in the commercial purity aluminium (Al-1050) alloy compared to that in the Al-1%Mg alloy. The hardness was totally homogeneous in the Al-1050 alloy after five turns of HPT while there is still small region of lower hardness at the centre of Al-1%Mg disk after the same number of turns. It was clear that the Al-1%Mg alloy needs more than five turns under the pressure of 6.0 GPa to become totally homogeneous. The higher rate of evolution of the hardness in the commercial purity aluminium (Al-1050) alloy was due to the higher rate of recovery compared to that of the Al-1%Mg alloy.

8.1.2 Strain measurements by CBED in Al-1050 processed by ECAP:

A series of [114] convergent beam electron diffraction (CBED) zone axis patterns were obtained at 148.7 kV with a 20 nm diameter electron probe from dislocation-

free regions close to and away from the grain boundaries in the billets processed by ECAP through two and four passes after cooling to 80 K. There are two issues regarding the lines in the HOLZ patterns; these are the sharpness and the position of the lines. The first concerns line blurring due to a possible increase in the dislocation density, i.e. the presence of inhomogeneous strains. The lines in the [114] pattern taken from the centre of a grain in the material in the as-received condition were sharp which indicates that the interiors of the grains in the as-received material are free from dislocations. The sharpness of the lines was decreased with increasing numbers of passes and after eight passes of ECAP the lines were highly blurred both at the centre of grains and near the grain boundaries. This was due to the high density of dislocations in the interior and near the boundaries of the grains of the billet processed through eight passes. In addition, the HOLZ lines near the grain boundaries in the billets processed through two and four passes were less sharp compared to that at the centre of the grains. These results are consistent with the fact that a high density of dislocations is introduced into the material when processed by ECAP on each separate pass and higher densities of these dislocations are usually present in the zones adjacent to the grain boundaries as these boundaries are usually in a non-equilibrium state [9,73,118].

The second issue is the position of the lines in the HOLZ CBED pattern. The deviation of the measured HOLZ lines from the reference position is an indication of changes of the lattice parameters of the processed billets which in turn indicates the presence of the internal stresses [113,114]. The pattern from the material in the as-received condition was set as the reference pattern. The symmetry was preserved in the patterns taken from grain centres after ECAP through two and four passes and this indicates that there are no detectable internal stresses in the interior of the grains. The patterns obtained at the regions near the grain boundaries give similar lattice parameter results for both the billets processed through two and four passes but with increased levels of strain in the latter. The lattice parameter c was reduced after two passes from 0.40329 nm to 0.40289 nm which indicates a compressive strain of approximately 0.1%. This value of the lattice parameter c was the same after ECAP through four passes. This indicates that this compressive strain is introduced in the early stages of the ECAP processing when the sample is adjusting to the size of the die and that no more compressive strains are accumulated with increasing numbers

of passes above one or two. After two passes, the change in the angles α and β indicated a shear strain of approximately 0.044%. The shear strain increases after four passes of ECAP by a factor of four to reach 0.175%. These results are expected as the nature of the imposed deformation in the ECAP processing is simple shear which occurs as the billet passes through the channel angle. These changes in the lattice parameter c and the angles α and β suggest that the strained unit cell is likely to be triclinic for both billets.

8.1.3 Processing of CP Ti by ECAP at room temperature:

The results of this investigation verified the feasibility to process commercial purity titanium (CP Ti) by ECAP at room temperature. It was shown previously that processing of hard materials such as titanium at room temperature requires the application of two conditions [37]. First, the die channel angle (Φ) must be increased to at least 120 deg. Second, the pressing speed must be reduced to approximately 0.5 mm/s or less. In this research, the processing of CP Ti was performed at a die channel angle (Φ) of 135 deg and at two different speeds. At a speed of 0.5 mm/s, the pressing was successfully performed for only one pass of ECAP. The CP Ti billet experienced a crack in the middle when the pressing was performed for the second pass. However, when the pressing speed was reduced to 0.05 mm/s the billet was successfully pressed for two passes without having any visible cracks.

The results of the hardness measurements after two passes of ECAP at room temperature using 135 die angle were comparable to the hardness after ECAP through seven and eight passes at elevated temperatures using 90 deg die angle and after ECAP through one pass at room temperature using 120 die angle [37,54,56,57]. After one pass of ECAP, the essential deformation mechanism in CP Ti alloy is the deformation twinning while the dominant deformation mechanism after two passes is the dislocation slip.

8.1.4 The effect of strain reversal in Al and Ti alloys during processing by HPT:

The results of the microhardness measurements after m-HPT and c-HPT for the four alloys; Al-1050, Al-1%Mg, CP Ti and Ti-6Al-4V, showed low values at the centre of the disks and high values near the edges which is consistent with all previous reports on different materials processed by HPT, except high purity aluminium alloy. In the two aluminium alloys (Al-1050 and Al-1%Mg) which processed by m-HPT and c-HPT for totals of 1/2, 3/4, 1 and 2 turns, the results showed that the rate of the evolution towards the homogeneity of microhardness along the diameter of the disks in the aluminium alloys is higher when the disks are processed by m-HPT rather than processing by c-HPT. In addition, it was also concluded that increasing the amount of strain imposed in each separate rotation will increase the rate of evolution of the microhardness along the diameter.

In the two titanium alloys (CP Ti and Ti-6Al-4V), the results were different than the aluminium alloys where it was shown that the rate of the evolution of the microhardness in the titanium alloys was higher when the disks are processed by c-HPT rather than processing by m-HPT. This contradiction between the results of the titanium alloys and the results of all other alloys processed by reversal straining is due to the different internal microstructure of the titanium alloys which is hexagonal closed packed (hcp) where the alloy initiating new slip systems on each reverse of the straining direction [97]. The error in most of the disks, both aluminium and titanium alloys, was relatively high near the centre which indicates that the hardness at this region is highly instable within very small distances.

8.2 Future work

Many aspects related to processing by ECAP and HPT were investigated in the present work and extensive data was collected. However, in performing these studies several paths of further studies have been opened. Some of the experimental and modeling future work is as follows:

- Billets of the commercial purity aluminium (Al-1050) alloy will be processed by ECAP under different pressing speeds in order to study the effect of changing the pressing speeds of the ECAP on the evolution of homogeneity of the microhardness measurements and thus the microstructure of Al-1050 alloy. The results will be compared with the existing results which performed at a pressing speed of 0.5 mm/s.
- The present investigation of the evolution of homogeneity during the processing of commercial purity aluminium (Al-1050) alloy by ECAP has used extensive microhardness measurements to evaluate the homogeneity of the microstructures on the longitudinal vertical plane and the cross sectional plane in the as-pressed billets. The next step will be using these measurements in order to get similar results by computational modeling. In addition, the microhardness measurements of the aluminium alloys (Al-1050 and Al-1%Mg) after processing by HPT will be used in initiating a computational modeling to study the evolution of the microhardness across the surfaces of the disks.
- The titanium transforms from the hexagonal close packed α -phase which is the normal phase at ambient conditions into the simple hexagonal ω -phase when processing at high pressures. At room temperature, this transformation occurs at a pressure of approximately ~ 2.0 GPa. An investigation will be carried out on two disks of CP Ti which processed by HPT for five turns at two different pressures. The first pressure will be 1.0 GPa which is below the transformation anticipated pressure and the second will be 6.0 GPa which is above the transformation anticipated pressure. TEM and microhardness measurements will be taken on both billets to study the effect of the transformation on the microstructure and properties of the alloy.

REFERENCES

1. Hall EO. Proc Roy Soc B 1951;64:747.
2. Petch NJ. J Iron Steel Inst 1953;174:25.
3. Langdon TG. Metall Trans 1982;13A:689.
4. Valiev RZ, Estrin Y, Horita Z, Langdon TG, Zehetbauer MJ, Zhu YT. JOM 2006;58(4):33.
5. Zhu YT, Lowe TC, Langdon TG. Scripta Mater 2004;51:825.
6. Gleiter H. In: Hansen N, Horsewell A, Leffers T, Lilholt H, editors. Deformation of polycrystals: Mechanisms and microstructures. Roskilde, Denmark: Risø National Laboratory; 1981. p. 15.
7. Erb U, El-Sherik AM, Palumbo G, Aust KT. Nanostruct Mater 1993;2:383.
8. Koch CC, Cho YS. Nanostruct Mater 1992;1:207.
9. Valiev RZ, Langdon TG. Prog Mater Sci 2006;51:881.
10. Saito Y, Tsuji N, Utsunomiya H, Sakai T, Hong RG. Scripta Mater 1998;39:1221.
11. Zhilyaev AP, Langdon TG. Prog Mater Sci 2008;53:893.
12. Valiev RZ, Islamgaliev RK, Alexandrov IV. Prog Mater Sci 2000;45:103.
13. Bridgman PW. J Appl Phys 1943;14:273.
14. Segal VM. USSR Patent No. 575892, 1977.
15. Segal VM, Reznikov VI, Drobyshevskiy AE, Kopylov VI. Russian Metall 1981;1:99.
16. Segal VM. Mater Sci Eng 1995;A197:157.
17. Valiev RZ, Krasilnikov NA, Tsenev NK. Mater Sci Eng 1991;A137:35.
18. Valiev RZ, Korznikov AV, Mulyukov RR. Mater Sci Eng 1993;A168:141.
19. Berbon PB, Furukawa M, Horita Z, Nemoto M, Langdon TG. Metall Mater Trans 1999;30A:1989.
20. Iwahashi Y, Horita Z, Nemoto M, Langdon TG. Acta Mater 1997;45:4733.
21. Nakashima K, Horita Z, Nemoto M, Langdon TG. Mater Sci Eng 2000;A281:82.
22. Iwahashi Y, Wang J, Horita Z, Nemoto M, Langdon TG. Scripta Mater 1996;35:143.
23. Wu Y, Baker I. Scripta Mater 1997;37:437.
24. Shan A, Moon IG, Ko HS, Park JW. Scripta Mater 1999;41:353.
25. Nemoto M, Horita Z, Furukawa M, Langdon TG. Metals Mater 1998;4:1181.
26. Horita Z, Furukawa M, Nemoto M, Langdon TG. Mater Sci Tech 2000;16:1239.
27. Furukawa M, Horita Z, Langdon TG. Metals Mater 2003;9:141.
28. Furukawa M, Horita Z, Nemoto M, Langdon TG. J Mater Sci 2001;36:2835.
29. Furukawa M, Iwahashi Y, Horita Z, Nemoto M, Langdon TG. Mater Sci Eng 1998;A257:328.
30. Iwahashi Y, Horita Z, Nemoto M, Langdon TG. Acta Mater 1998;46:3317.
31. Oh-ishi K, Horita Z, Furukawa M, Nemoto M, Langdon TG. Metall Mater Trans 1998;29A:2011.

32. Nakashima K, Horita Z, Nemoto M, Langdon TG. *Acta Mater* 1998;46:1589.
33. Semiatin SL, Segal VM, Goforth RE, Frey ND, DeLo DP. *Metall. Mater. Trans.* 1999;30A:1425.
34. Aleksandrov IV, Raab GI, Shestakova LO, Kil'mametov AR, Valiev RZ. *Phys Met Metallogr* 2002;93:493.
35. Yamaguchi D, Horita Z, Nemoto M, Langdon TG. *Scripta Mater* 1999;41:791.
36. Kim IY, Kim JY, Shin DH, Park JT. *Metall Mater Trans* 2003;34A:1555.
37. Zhao X, Fu W, Yang X, Langdon TG. *Scripta Mater* 2008;59:542.
38. Yamashita A, Yamaguchi D, Horita Z, Langdon TG. *Mater Sci Eng* 2000;A287:100.
39. Utsunomiya H, Saito Y, Hayashi T, Sakai T. *J Mater Eng Perform* 1997;6:319.
40. Saito Y, Utsunomiya H, Suzuki H, Sakai T. *Scripta Mater* 2000;42:1139.
41. Lee JC, Seok HK, Han JH, Chung YH. *Mater Res Bull* 2001;36:997.
42. Han JH, Seok HK, Chung YH, Shin MC, Lee JC. *Mater Sci Eng* 2002;A323:342.
43. Lee JC, Seok HK, Suh JY, Han JH, Chung YH. *Metall Mater Trans* 2002;33A:665.
44. Nam CY, Han JH, Chung YH, Shin MC. *Mater Sci Eng* 2003;A347:253.
45. Lee JC, Suh JY, Ahn JP. *Metall Mater Trans* 2003;34A:625.
46. Suh JY, Han JH, Oh KH, Lee JC. *Scripta Mater* 2003;49:185.
47. Park JW, Kim JW, Chung YH. *Scripta Mater* 2004;51:181.
48. Utsunomiya H, Hatsuda K, Sakai T, Saito Y. *Mater Sci Eng* 2004;A372:199.
49. Raab GJ, Valiev RZ, Lowe TC, Zhu YT. *Mater Sci Eng* 2004;A382:30.
50. Huang Y, Prangnell PB. *Scripta Mater.* 2007;56:333.
51. Xu C, Langdon TG. *J Mater Sci* 2007; 42:1542.
52. Xu C, Furukawa M, Horita Z, Langdon TG. *Mater Sci Eng* 2005;A398:66.
53. Prell M, Xu C, Langdon TG. *Mater Sci Eng* 2008; A480:449.
54. Stolyarov VV, Zhu YT, Lowe TC, Islamgaliev RK, Valiev RZ. *Nanostruct Mater* 1999;11:947.
55. Kim I, Jeong WS, Kim J, Park KT, Shin DH. *Scripta Mater* 2001;45:575.
56. Stolyarov VV, Zhu YT, Alexandrov IV, Lowe TC, Valiev RZ. *Mater Sci Eng* 2001;299A:59.
57. Stolyarov VV, Zhu YT, Lowe TC, Valiev RZ. *Mater Sci Eng* 2001;303A:82.
58. Jia D, Wang YM, Ramesh KT, Ma E, Zhu YT, Valiev RZ. *Appl Phys Lett* 2001;79:611.
59. Shin DH, Kim I, Kim J, Zhu YT. *Mater Sci Eng* 2002;334A:239.
60. Shin DH, Kim I, Kim J, Kim YS, Semiatin SL. *Acta Mater* 2003;51:983.
61. Kim I, Kim J, Shin DH, Liao XZ, Zhu YT. *Scripta Mater* 2003;48:813.
62. Stolyarov VV, Zhu YT, Alexandrov IV, Lowe TC, Valiev RZ. *Mater Sci Eng* 2003;343A:43.
63. Zhu YT, Kolobov YR, Grabovetskaya GP, Stolyarov VV, Girsova NV, Valiev RZ. *J Mater Res* 2003;18:1011.
64. Zhu YT, Huang JY, Gubicza J, Ungár T, Wang YM, Ma E, Valiev RZ. *J Mater Res* 2003;18:1908.
65. Ko YG, Shin DH, Park KT, Lee CS. *Scripta Mater* 2006;54:1785.

66. Kim I, Kim J, Shin DH, Lee CS, Hwang SK. *Mater Sci Eng* 2003;342A:302.
67. Figueiredo RB, Cetlin PR, Langdon TG. *Acta Mater* 2007;55:4769.
68. Lee BJ, Ahzi S, Asaro RJ. *Mech Mater* 1995;20:1.
69. Smirnova NA, Levit VI, Pilyugin VI, Kuznetsov RI, Davydova LS, Sazonova VA. *Fiz Metal Metalloved* 1986;61(6):1170.
70. Valiev RZ, Kaibyshev OA, Kuznetsov RI, Musalimov RSh, Tsenev NK. *Proc USSR Acad Sci* 1988;301:864.
71. Zhilyaev AP, Nurislamova GV, Kim BK, Baro' MD, Szpunar JA, Langdon TG. *Acta Mater* 2003;51:753.
72. Iwahashi Y, Horita Z, Nemoto M, Langdon TG. *Metall Mater Trans* 1998;29A:2503.
73. Horita Z, Smith DJ, Furukawa M, Nemoto M, Valiev RZ, Langdon TG. *J Mater Res* 1996;11:1880.
74. Stolyarov V, Valiev RZ, in: Zehetbauer MJ, Valiev RZ (Eds.), *Nanomaterials by Severe Plastic Deformation*, Wiley-VCH, Weinheim, Germany 2004;125.
75. Zhilyaev AP, Kim BK, Nurislamova GV, Baro' MD, Szpunar JA, Langdon TG. *Scripta Mater* 2002;48:575.
76. Zhilyaev AP, Kim BK, Szpunar JA, Baro' MD, Langdon TG. *Mater Sci Eng* 2005;391A:377.
77. Valiev RZ, Ivanisenko YuV, Rauch EF, Baudelet B. *Acta Mater* 1996;44:4705.
78. Wetscher F, Vorhauer A, Stock R, Pippan A. *Mater Sci Eng A* 2004;387–389:809.
79. Wetscher F, Pippan R, Sturm S, Kauffmann F, Scheu C, Dehm G. *Metall Mater Trans* 2006;37A:1963.
80. Polakowski NH, Ripling EJ. *Strength and structure of engineering materials*. Englewood Cliffs, NJ: Prentice-Hall; 1966.
81. Degtyarev MV, Chashchukhina TI, Voronova LM, Davydova LS, Pilyugin VP. *Phys Metal Metall* 2000;90:604.
82. Efros BM, Pilyugin VP, Patselov AM, Beygelzimer YY, Efros NB. In: Zhu YT, Langdon TG, Mishra RS, Semiatin SL, Saran MJ, Lowe TC, editors. *Ultrafine grained materials II*. Warrendale, PA: The Minerals, Metals and Materials Society; 2002. p. 193.
83. Degtyarev MV, Chashchukhina TI, Voronova LM, Patselov AM, Pilyugin VP. *Acta Mater* 2007;55:6039.
84. Zhilyaev AP, McNelley TR, Langdon TG. *J Mater Sci* 2007;42:1517.
85. Vorhauer A, Pippan R. *Scripta Mater* 2004;51:921.
86. Jiang H, Zhu YT, Butt DP, Alexandrov IV, Lowe TC. *Mater Sci Eng* 2000;A290:128.
87. Yang Z, Welzel U. *Mater Lett* 2005;59:3406.
88. Zhilyaev AP, Oh-ishi K, Langdon TG, McNelley TR. *Mater Sci Eng* 2005;A410–411:277.
89. Sakai G, Horita Z, Langdon TG. *Mater Sci Eng* 2005;A393:344.
90. Horita Z, Langdon TG. *Mater Sci Eng* 2005;A410–411:422.
91. Zhilyaev AP, Lee S, Nurislamova GV, Valiev RZ, Langdon TG. *Scripta Mater* 2001;44:2753.
92. Xu C, Horita Z, Langdon TG. *J Mater Sci* 2008;55:203.

93. Lugo N, Llorca N, Cabrera JM, Horita Z. Mater Sci Eng 2008;A477:366.
94. Xu C, Langdon TG. Mater Sci Eng 2009;A503:71.
95. Xu C, Horita Z, Langdon TG. Acta Mater 2007; 55:203.
96. Furukawa M, Horita Z, Langdon TG. Mater Sci Eng 2002;332A:97.
97. Kawasaki M, Langdon TG. Mater Sci Eng 2008;498A:341.
98. Wetscher F, Pippan R. Phil Mag 2006;86:5867.
99. Wetscher F, Tian B, Stock R, Pippan R. Mater Sci Forum 2006;503-504:455.
100. Todaka Y, Umemoto M, Yamazaki A, Sasaki J, Tsuchiya K. Mater Trans 2008;49:47.
101. Orlov D, Todaka Y, Umemoto M, Tsuji N. Mater Sci Eng 2009;499A:427.
102. Orlov D, Bhattacharjee PP, Todaka Y, Umemoto M, Tsuji N. Scripta Mater 2009;60:893.
103. Xu C, Xia K, Langdon TG. Acta Mater 2007;55:2351.
104. Qiao XG, Starink MJ, Gao N. Mater Sci Eng 2009;513-514A:52.
105. Semiatin SL, DeLo DP, Shell EB. Acta Mater 2000;48:1841.
106. Kim HS. Mater Sci Eng 2001;A315:122.
107. El-Danaf EA, Soliman MS, Almajid AA, El-Rayes MM. Mater Sci Eng A 2007;458:226.
108. Horita Z, Fujinami T, Langdon TG. Mater Sci Eng 2001;A318:34.
109. Xu C, Langdon TG. Scripta Mater 2003;48:1.
110. Kim HS, Seo MH, Hong SI. Mater Sci Eng 2000;A291:86.
111. Kim HS, Seo MH, Hong SI. J Mater Proc Tech 2002;130–131:497.
112. Randle V, Barker I, Ralph B. J Elect Micr Tech 1989;13:51.
113. Straub S, Blum W, Maier HJ, Ungar T, Borberly A, Renner H. Acta Mater 1996;44:4337.
114. Kassner ME, Pe'rez-Prado MT, Long M, Vecchio KS. Metall Mater Trans 2002;33A:311.
115. Houdellier F, Roucau C, Clement L, Rouviere JL, Casanove MJ. Ultramicrosc 2006;106:951.
116. Li XZ. Journ of Mater Educ 2007;29(3-4):177.
117. Straumanis ME and Woodard CL. Acta Cryst 1971;27A:549.
118. Langdon TG. Mater Sci Eng 2007;462A:3.
119. Horita Z, Smith DJ, Nemoto M, Valiev RZ, Langdon TG. J Mater Res 1998;13:446.
120. Balboni R, Frabboni S, Armigliato A. Philos Mag 1998;77A:67.
121. Toda A, Ikarashi N, Ono H. J Crys Growth 2000;210:341.
122. Kim M, Zuo JM, Park G-S. App Phys Lett 2004;84(12): 2181.
123. Rossouw CJ, Tsuda K, Forwood CT, Gibson MA, Tanaka M. J Elect Micr 2000;49(5):589.
124. Stolyarov VV, Shuster LSh, Migranov MSh, Valiev RZ, Zhu YT. Mater Sci Eng 2004;A371:313.
125. Valiev RZ. Nature Mater 2004;3:511.
126. Alder HL, Roessler EB. Introduction to probability and statistics. Third Edition. San Francisco and London: W. H. Freeman and Company; 1964.
127. Edalati K, Horita Z, Langdon TG. Scripta Mater 2009;60:9.